APPLICATIONS OF STATISTICAL METHODS IN COMPUTATIONAL FLUID DYNAMICS FOR PRECIPITATION AND COMBUSTION

by

Alexander William Abboud

A dissertation submitted to the faculty of
The University of Utah
in partial fulfillment of the requirements for the degree of

Doctor of Philosophy

Department of Chemical Engineering

The University of Utah

August 2015

The University of Utah Graduate School

STATEMENT OF DISSERTATION APPROVAL

The dissertation of **Alexander William Abboud**

has been approved by the following supervisory committee members:

Sean Smith	, Chair	**5/22/2015** Date Approved
Philip Smith	, Member	**5/22/2015** Date Approved
James Sutherland	, Member	**5/22/2015** Date Approved
Terry Ring	, Member	Date Approved
David Lignell	, Member	**5/22/2015** Date Approved

and by **Milind Deo** , Chair/Dean of

the Department/College/School of **Chemical Engineering**

and by David B. Kieda, Dean of The Graduate School.

ABSTRACT

The development of models for use in computational fluid dynamics often rely on a set of assumptions, as resolving the full set of length and timescales is often unfeasible in terms of computational cost for applied flow regimes. Many models rely on statistical formulations as the method for development. In large-eddy simulation, the prescription of inlet conditions affect the overall outcome of the results. Two turbulent inlet methods are implemented into computational fluid dynamics code and simulations are run to compare results to a stationary inlet for an experimental coaxial jet flow configuration. Both of the methods rely on the recreation of first- and second-order statistics – the mean and variance – in the derivations. A flamelet model is presented that accounts for nonequilibrium effects in combustion systems. Subgrid effects of the model are accounted for with a presumed probability density function method for mixture fraction and scalar dissipation rates. The flamelet library approach is extended from past flamelet studies to include five independent variables: extent of reaction, mixture fraction, scalar dissipation rate, scalar variance, and heat loss.

For dispersed multiphase flow simulations, transporting the moments of a population balance equation can often provide good results. Moments methods rely on tracking the statistical properties of a particle size distribution. Utilizing an Eulerian moment method provides a computationally cheaper way to track particles than using a Lagrangian method. The quadrature method of moments is used for the simulation of the particle size distribution of calcium carbonate precipitation. Two sets of simulations are run, the first set uses an idealized geometry with an increasing Reynolds number, the second set of simulations uses pilot scale reactors. The mixing rates that occur in each of these simulation sets affect the outcome of the particle size distributions of the precipitate particles. The conditional quadrature method of moments is used to simulate inert particles of nonnegligible Stokes number. These larger particles require using velocities as an internal coordinate. Simple cases are set up to show the implementation of the method showing proper behavior with particle trajectory crossing and wall interaction cases. A comparison of the method with experimental results of inert particle flow for monodisperse and polydisperse particle size

distributions is shown for coaxial jet flow. The method is shown to be extendable to any arbitrary number of internal coordinates, which should make it useful in modeling of complex multivariate particle systems.

"Every mathematician believes that he is ahead of the others. The reason none state this belief in public is because they are intelligent people."

– Andrei Kolmogorov

CONTENTS

LIST OF FIGURES

LIST OF TABLES

ACKNOWLEDGMENTS

First and foremost, I would like to thank my parents for all of their support. They convinced me to apply for graduate school when I was at a low point in my career. Without them, I never would have conceived of earning a doctorate degree.

I would like to thank Dr. James Sutherland, who originally hired me on and gave me this unique opportunity. Of course, I would like to thank my adviser, Dr. Sean Smith, who took me under his wing as his first graduate student. I would also like to thank the rest of my committee – Dr. Philip Smith, Dr. David Lignell, and Dr. Terry Ring – for many insightful discussions and other guidance.

I would like to thank both Dr. Tony Saad and Dr. Jeremy Thornock for their help in code development and debugging. While I never worked directly with either, I would also like to thank Dr. Julien Pedel and Dr. Charles Reid for their work in implementing the DQMOM models. Without this groundwork, it would not have been possible to complete the development of CQMOM in the time frame that I planned.

While earning my undergraduate degree at the University of California, Davis there were several professors who gave me the motivation to succeed; Dr. Brian Higgans, who demonstrated to me the amazing usefulness of computer science applications in chemical engineering; Dr. Pieter Stroeve for teaching the fundamental mass and fluid transfer that is central to everything; and Dr. Roland Fäller for his amazing enthusiasm in teaching thermodynamics.

And of course, I would like to thank the great support staff that we have at the University of Utah. Catrina Wilson, Jeri Schryver, Christina Bushman, Ribana Milas and Rachelle Reed help the program run smoothly, and allow the graduate students to focus more time on their research and less on the bureaucratic issues of the university.

CHAPTER 1

INTRODUCTION

This research covers several broad topics in multiphase flow modeling of precipitation and combustion systems. The techniques researched throughout this dissertation rely heavily on core probability theory. In terms of a general set of rules for probability, it is a relatively new mathematical field when compared to older mathematical techniques such as calculus. In the 1930s a pioneer in this field, Andrey Kolmogorov, developed a well defined set of basic probabilistic axioms. A much less rigorous definition of probability was defined prior to his work. It was developed as: a need for definitive axioms of probability, in much the same way that calculus, algebra and geometry have a set of definitions that one abides by (to paraphrase Kolmogorov) [81]. In this way, Kolomogorv developed axioms of probability that have been used to further develop probability methods.

Simple stochastic processes model the time evolution of a system of random variables over time. The simplest such approach can be to model a random walk such as the Brownian motion. Stochastic processes can be modeled using techniques such as Monte Carlo methods. Monte Carlo techniques rely on repeated random sampling of a process to obtain results. These techniques require averaging over a large amount of random data samples. As the number of samples increase, then the accuracy of the set of random data will also increase, but only as the square root of N. Thus, it becomes prohibitively more expensive to run Monte Carlo methods when high accuracy of the results is of concern. Most of the work done here is based on further extensions of probability theory in a way that full random sampling is unneeded. Some techniques rely on simple statistical measures that can be sufficient to describe a population.

Rather than using a full random data set to prescribe a stochastic process, the evolution of the probability distribution function (PDF) is another alternative. For a continuous variable the PDF describes that relative probability that the variable of interest lies in a given range of values. In the mathematical sense, the PDF is defined such that it is nonnegative for the entire ranges of the given variable, and that the integral of the PDF is

equal to one. If a PDF is applied to a physical distribution such that the total population is greater than one, it can be referred to as a number density function (NDF).

Using a method to calculate the evolution of the PDF and the associated equations is often referred to the a population balance equation (PBE) approach. Often, the PBE approach is applied to particles in multiphase flows. The PBE can be used to track many aspects of particles such as physical properties: size, mass, volume, surface area; or chemical properties: moisture, elemental composition, species composition. When the PBE is applied with specific interest in the particle size, then the PBE can be said to represent the particle size distribution (PSD) of the set of particles.

When the PBE approach is used for the evolution of a set of particles, several different techniques can be used. One is to create a set of equations to track the PBE with the moments of the distribution. The moments of the distribution are specific quantitative measures of the shape of the distribution. The first couple of moments describe well-known quantities: the zeroth moment of the distribution is the total number density, the first moment is the mean, and the second moment is the variance. The next moments help describe the shape of the distribution. The third moment is the skewness, which describes the lopsidedness of the distribution. The fourth moment is the kurtosis, which describes how much of the distribution lies in the tails versus the peak. The higher order moments of the system continue to refine the shape of the PDF, but are usually irrelevant unless an exact reconstruction of the PDF is desired.

Statistical approaches utilizing PDFs have many applications in science and engineering. In particular, for chemical engineering processes that involve particle flow, the size of the particles can have a large effect on the kinetic rates of the system. For some applications, it is desirable to tightly control the width of the PSD, so that reactions occur near homogeneously throughout the domain. Often, the experimental analysis of a PSD must be done over the entire stream, rather than just a portion, to capture particles which cover all ranges of Stokes numbers, some of which may not follow fluid streamlines. The analysis of some chemical processes, such as pulverized coal combustion show a wide PSD and modeling the process to accurately portray that large and small particles evolve differently can require using a PBE method.

Pollution of the environment is a primary topic of interest in the scientific community. The continued increase in the required energy needs of society results in an increase in various pollutants in the environment. One of the primary concerns recently is the build-up of green house gases in the atmosphere, specifically carbon dioxide emissions from fossil fuel

combustion. The increase in carbon dioxide levels in the atmosphere is a large contributing factor to the current climate change phenomena. While the continued development of green energy sources may be a solution to the build-up of green house gases, many obstacles in the scale-up of these technologies exist. The improvement or refinements of current fossil fuel combustion systems is another way that may help combat climate change.

In order to combat the build-up of carbon dioxide in the atmosphere, the separation of carbon dioxide for sequestration from combustion processes has become a large research area. There are two primary issues in the research, the first being the separation of carbon dioxide from the flue gas, and the second being the actual storage of the carbon dioxide. One such way to store carbon dioxide is through mineral sequestration, this process could be done by either long-term geological storage or through short-term chemical processes. When carbon dioxide is dissolved into water, the molecule will form carbonate ions in solution. When the solution of carbonate ions is mixed with a brine stream containing other positive ions, precipitation reactions can occur that effectively transform carbon dioxide into mineral matter. One way to represent this system in a simpler form is to represent the two streams with saturated salt solutions. A stream of aqueous calcium chloride can be used to represent the brine stream, and a stream of aqueous sodium carbonate can be used to represent the carbon dioxide. As these two streams are mixed, calcium carbonate precipitates and the carbon dioxide is effectively sequestered in this mineral phase.

Another concern for environmental pollution is the minor species of combustion processes such as nitrogen oxides and sulfur oxides. These species are typically hard to model, as simple approaches with equilibrium chemistry do not account for their formation. By accurately modeling combustion processes, the prediction of these species can be improved, and improvements to processes can be made to lessen the formation of harmful species. The improvement in combustion models for these processes must include nonequilibrium effects. In well characterized combustion systems where the general chemical reaction mechanisms are known, models can be developed for these nonequilibrium effects. Specifically, a simple gaseous combustion system such as natural gas has a well defined mechanism that can be used in flamelet modeling.

More complex combustion systems do not have a well defined mechanism for the system of chemical reactions. Coal in particular proceeds to give off energy through nonconventional sets of reactions due to the vast number of known and unknown chemical species that are involved. Coal is one of the cheapest and abundant sources of energy available, so modeling its complexities is of large importance as it becomes the go-to resource for energy needs in

developing nations. As shown in Figure 1.1, the emissions from coal are the most abundant source of carbon dioxide production for electricity generation in the US [177].

This dissertation examines various physical applications of probability, and implements these techniques into large-eddy simulation (LES) code and discusses the resulting computational fluid dynamics (CFD) simulations. The simulations included here consist of both theoretical and validation cases.

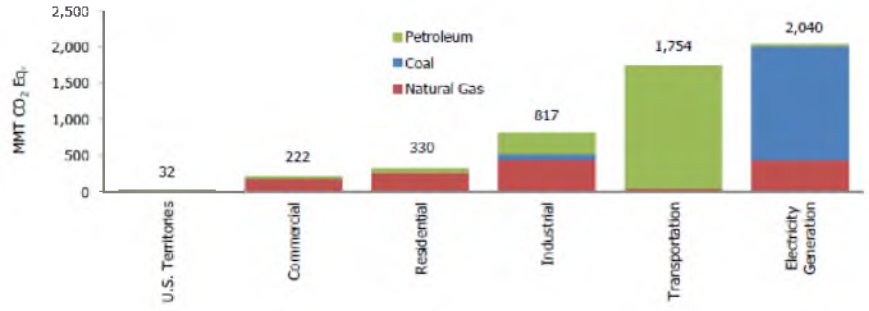

Figure 1.1: Carbon dioxide emissions from fossil fuel combustion. The right most bar shows the emissions specifically from electricity generation. This plot is used from the EPA report [177]: U.S Environmental Protection Agency, *Inventory of U.S. greenhouse has emissions and sinks: 1900-2013, tech. rep., 2015.*

CHAPTER 2

OVERVIEW

This section will cover the scientific methods that are utilized to solve the problems mentioned in the previous chapter with much more depth. As computational processing power has continued to increase, computational fluid dynamics (CFD) has emerged as an important tool as for analyzing both reactive and nonreactive flow systems. CFD separates the Navier-Stokes equations of fluid dynamics into a discretized system of partial differential equations that can be used to solve for the flow field of a given system. This tool can be used as a validation to experimental results, or to gain insight into flow and reaction regimes that are not well defined. There are a vast array of methods used in CFD modeling spanning differing length and timescales in their applications.

The most accurate CFD method is direct numerical simulation (DNS), which resolves all of the length and timescales of the flow. As all of the scales are resolved, this method is very computationally expensive and is limited to a low Reynolds number. The computational cost scales as Re^3, which implies that the method is limited to small scale flows. A commonly used method that ignores the full resolution of the flow field is referred to as Reynolds-averaged Navier Stokes (RANS). This method only solves for the mean velocity field, which can ignore many relevant turbulent mixing effects. A method known as large-eddy simulation (LES) fits between these two previous methods on the CFD spectrum in terms of resolution. In LES, only the large length and timescales are fully resolved, while the length scales smaller than the grid size are modeled as subgrid effects [146].

All of the CFD simulations conducted here are done using large-eddy simulation with the in-house Uintah framework [176]. Both the ARCHES [57] and Wasatch [159] components of the framework are utilized. In all of the simulations which are run, the ARCHES portion of the code is used for the fluid flow solution. The Wasatch component of the framework is utilized for the moment equations in the precipitation set of simulations, other simulations use the ARCHES code exclusively.

Uintah provides large-scale parallelization tools for physics components [13, 31, 127].

The Uintah code is maintained in a repository, which takes care of regression tests and allows for free distribution [176]. The ARCHES component solves the conservative, finite-volume, low-Mach formulation of the Navier-Stokes equations with a pressure projection that includes the effect of variable density, reaction and heat transfer models in the gas phase [57]. The Uintah code uses a Cartesian mesh with an equally spaced grid. The code was originally developed to provide accurate simulations of turbulent flow fields of fires and flames [169]. For LES, the constant density-filtered continuity and Navier-Stokes equations are given by [160]

$$\frac{\partial \bar{u}_i}{\partial x_i} = 0 \,, \tag{2.1}$$

and

$$\frac{\partial \bar{u}_i}{\partial t} + \frac{\partial}{\partial x_j}(\bar{u}_i \bar{u}_j) = -\frac{1}{\rho}\frac{\partial \bar{p}}{\partial x_i} + 2\nu \frac{\partial}{\partial x_j}\bar{S}_{ij} - \frac{\partial \tau_{ij}}{\partial x_j} \,, \tag{2.2}$$

with

$$\bar{S}_{ij} = \frac{1}{2}\nu\left(\frac{\partial \bar{u}_i}{\partial x_j} + \frac{\partial \bar{u}_j}{\partial x_i}\right) \,, \tag{2.3}$$

and

$$\tau_{ij} = \overline{u_i u_j} - \bar{u}_i \bar{u}_j \,. \tag{2.4}$$

Here u_i is the i^{th} velocity component, ρ is the density, ν is the kinematic viscosity, $\bar{S}_{ij}$ is the rate-of-strain tensor, and τ_{ij} is the residual stress tensor. For subgrid modeling of τ_{ij} the dynamic Smagorinsky model was used from Germano et al. [54].

The dissertation contains several separate research aspects in CFD, and is ordered as follows. First, the implementation of turbulent inlet conditions in the ARCHES codebase is discussed and comparisons with experimental data are made. The turbulent inlet conditions become important for the improvement of the overall accuracy of the LES. Next, the precipitation study using the quadrature method of moments for tracking the evolution of the PSD for calcium carbonate is presented with both simple and complex geometries. While no experimental data exist for the complex geometries, the turbulent inlet method is utilized for those simulations. As the geometries are truncated from the actual size, the proper development of turbulence prior to the mixing of two streams would not occur without the use of the inlet condition. After this, a new formulation for a flamelet library is shown, along with some discussion of the method applied to natural gas combustion. The flamelet library utilizes some of the development in the precipitation research for subgrid modeling of LES flow, dictated by the local scalar dissipation rates. In addition, coding work done to improve the chemistry library for the precipitation research was able to be utilized for the flamelet library. Finally, the implementation of the conditional quadrature method of

moments will be discussed, along with its extension into multiple-scalar internal coordinates, as well as comparisons with experimental data of inert particles. These simulations also utilize the turbulent inlet method to improve the near-field LES results.

2.1 Turbulent Inlet Conditions

The first portion of this research is centered on improving boundary conditions in the LES through the implementation of a turbulent inlet condition. In CFD, poor selection of the boundary conditions can have significant effect on the outcome of the solution. For outlet boundary conditions, these effects can often be mitigated by placing the outlet sufficiently far from the field of interest. The inlet of the domain then becomes the main boundary condition to be prescribed. In the context of RANS simulation, this inlet can often be set as a stationary velocity along with prescribed length scale and turbulent kinetic energy profiles. For example, with a channel-flow inlet in RANS, a stationary power-law profile is sufficient. For LES, setting a fully developed power-law profile with constant velocity is not sufficient to characterize the properties of the turbulent flow. This insufficiency is due to an absence of fluctuations in the resolved velocity. One method to approximate fully developed inlet flow in LES is to use a periodic boundary condition, but this is limited to simple geometries such as constant-cross-section channels. For other cases, inlet flow conditions need to be investigated.

Several different types of turbulent inlet conditions have been demonstrated in the technical literature, a naive approach consists of superimposing time-dependent random data to a stationary velocity profile. However, this approach yields poor results since the uncorrelated fluctuations are quickly dissipated [172]. The inlet condition in LES must be prescribed in a way to produce physically realistic velocity structures. Coherence of structures downstream from the inlet have been shown in two categories of inlet turbulence: synthetically generated turbulence [66, 97, 113, 79]; and generation of data with a precursor simulation [188, 8, 164]. Alternative implementations for inlet conditions can be found in the review by Tabor and Baba-Ahmadi [172]. Tabor and Baba-Ahmadi [172] acknowledge that synthetic methods can be inherently less accurate as they only provide turbulent-like properties to the inlet. Other methods exist which are not specific to LES, but rather related to hybrid LES/RANS codes [11]. Synthetic inlet methods do provide an easy way to specify the desired parameters of turbulence, and are quick to generate. Precursor simulation methods generate true turbulent structures, and are thus inherently more accurate than synthetic methods. While using data from precursor simulations can

be simple to implement, it may be argued that this approach is undesirable for large-scale codes. A precursor simulation may be undesirable for problems with complex geometry. In addition, the computational cost associated with a large-scale precursor simulation for an LES inlet is often not justifiable. Due to these arguments, the choice of implementation (in our specific academic codebase) is a synthesized turbulent inlet.

The studies by Pedel et al. have been performed with the same research LES code used in this study [129, 130, 131]. The papers by Pedel et al. compared the results of LES simulations for circular coaxial jets with the experimental results of Budilarto [16]. The focus of those studies was on the particle-fluid interactions. While the simulations performed reasonably well, there were some discrepancies between the experimental data and the results in the fluid flow. Those simulations were run using a stationary velocity inlet condition. This study introduces to the ARCHES codebase an implementation of a generalized turbulent inlet condition for use in arbitrary geometries and inlets. Furthermore, this study applies the synthesized turbulent inlet to the conditions of the previous simulations in order to provide more accurate fluid-phase results in relation to the experimental data from Budilarto [16].

The research presented here focuses on external jets. These types of flow fields are important in many combustion applications – notably flares, burners and boilers. Velocity fields in turbulent free-flow jets have been studied for several decades, allowing for a good definition of the characteristics [191, 19, 22]. These characteristics include features such as a core region in the central jet (where the velocity decay occurs slowly), the entrainment of an annular jet decreasing the centerline velocity, and the downstream development of a self-preserving profile. Early LES studies have examined the flow of these single circular jets [125, 6]. Hassel et al. [60] and Tkatchenko et al. [174] have run simulations using both RANS and LES codes for comparison between the methods in a coaxial jet mixer. Another LES study showing how varying the Reynolds number can affect the growth of the shear layer in the near field region has been performed in Kim and Choi [78]. Zhdanov et al. [199] have experimentally measured confined coaxial jets to study the recirculation zone development. Jung et al. [70] have carried out experiments for single circular turbulent jets at very high Reynolds numbers. Comparisons between experimental data and RANS simulations of other reacting flows in a confined coaxial jet have also been studied [23]. Kornev et al. [82] have studied the development of scalar fields in experiments with weakly confined coaxial jets.

Recent data have also been produced with significantly more information in the velocities

and fluctuations for a single circular jet and under two strong coflow conditions [16]. In addition to experimental data in recent years, many CFD results of these types of flows have been produced, which give better insight into the fine structures of these flows [5, 129, 130, 131].

The experiment used for comparison in this paper does not utilize a swirl generator, however, we point out significant developments in this area. Experimental results in weak coaxial jets have been produced with an impeller to generate a swirl condition in Petersson et al. [135]. Other inlet methods in LES have been developed based on using a swirl condition at the inlet first used in Pierce and Moin [137] and shown to work well in coaxial flow of combustion [5], and in combustion reactors to mix the air and fuel streams [139]. Another development of a swirl inlet condition was created by Baba-Ahmadi and Tabor [7] to remap data from the domain to the inlet.

This paper examines the effects of using the synthesized turbulence inlet condition with comparison against experimentally measured flow statistics of a circular coaxial jet. For reference, comparison is made to a stationary velocity inlet. A few additional configurational options were investigated with results being summarized in the text. Another study, which is similar to the current work, compared three inlet conditions for channel flow simulations [74]. The size of the domain in that paper was much smaller than that presented here. Two of the methods presented in the Keating et al. paper are based on the approach of using prior results over a periodic domain. Again, these methods are usually not desirable for a large-scale simulation or complex geometry. The Keating paper also presents one method based on the generation of turbulence with a near-wall momentum source term. In contrast, the simulation presented in the current study is a free-flow jet with little wall interaction. The Keating et al. paper only compares a few different simulation results and neglects any inclusion of experiment data.

Only two inlet types are examined in this study: the digital filter method suggested by Klein et al. [79] and the synthetic eddy method of Jarrin et al. [66]. The digital filter generation method was used for a few major reasons. First, it is easy to adapt for arbitrary geometry inlets, second the simple algorithm does not require much adaptation to fit within our specific LES codebase. In addition, the relative computational cost of this method with a pregenerated table is small. The digital filter method was first shown to work well in DNS plane jets [80], and has been demonstrated to closely match DNS data of a plane jet when utilized in LES [34]. Veloudis et al. [180] have also shown a variation of the method to work well in channel flow for LES. The synthetic eddy method has been shown to work

well in channel flows [66, 68, 67]. With a small adaption the synthetic eddy method can be constructed with the same advantages that the digital filter method has.

2.2 Flamelet Modeling

One representation of modeling combustion reactions is known as a flamelet model. This model was developed specifically for nonpremixed combustion simulations. The model accounts for subgrid effects of combustion involving nonequilibrium mixing effects. The flamelet model was first developed by Peters [132, 133]. The flamelet model assumes that the chemical timescales are fast enough that reactions occur on a length scale that is smaller than the small turbulent length scales [140].

The small flamelet scales are assumed to remain laminar, and diffusive transport is assumed to occur normal to the flame front. This allows for an analytical transformation of the scalar transport equations. The mixture fraction of the system is changed into the only independent coordinate, and the set of scalar equations can be solved as a function of the mixture fraction only [134]. The steady state formulation of the flamelet model couples the nonequilibrium chemistry to the mixture fraction and the scalar dissipation rate [133]. The solution to the transformed scalar equations can be precomputed and tabulated in terms for the scalar dissipation rate and mixture fraction. This approach was used in early studies in LES combustion modeling [26, 29]. The steady-state model is used in LES because its simplicity only requires two dependent variables and has shown improvements in simulations over equilibrium chemistry assumptions [76, 150, 75].

An unsteady flamelet model can be used instead to improve the flamelet model accuracy in certain flows where slow chemical or physical processes have to be considered. These processes include formation of pollutants and radiative heat transfer [141]. An improvement to the steady-state flamelet model is to add an additional variable to the tabulation, as a reaction progress variable. Known as the flamelet progress variable approach, this method was developed by Pierce and Moin for specific use in LES combustion applications [138, 139]. To model this a filtered transport equation for the reaction progress variable is solved. This variable can be defined as the sum of the mass fractions of CO_2, H_2O, CO, and H_2. This model can potentially give a better description of local extinction and ignition events [140].

The flamelet library of the digital analysis of reacting systems (DARS) tool is utilized here [27] in conjunction with the Gas Research Institute (GRI) mechanism for natural gas combustion [167]. This produces a wide range of outputs that can be retooled to be usable in the ARCHES codebase. The flamelet approach used here is modified from the progress variable approach of Pierce and Moin [142, 65]. The data are tabulated over five

independent variables of the system, and do not use the same definition for the reaction progress variable. These variables are the mixture fraction, a transformed reaction extent, the heat loss – a normalized version of the enthalpy – the scalar dissipation rate, and the normalized scalar variance.

2.3 Quadrature Method of Moments

In order to track the evolution of a distribution of particles, a population-balance equation approach (PBE) can be used [151]. Moment methods have first been proposed for use by Hulbert and Katz [64] as a way to track these PBEs. Using a method of moments can give a general statistical description of a particle size distribution (PSD) using a low number of scalar equations. Moment methods have traditionally been used for aerosol applications to model the evolution of the PSD even with complex source terms such as nucleation, growth, condensation and coagulation [48, 108, 47, 147].

However, using moment methods often requires some sort of closure estimation, as the dependence of source terms can require a seemingly infinite number of moments. For more recent applications, quadrature based moment methods (QBMM) have been used in order to provide estimation of moments for the closure problem. The first method proposed to accomplish this is the quadrature method of moments (QMOM) developed by McGraw [107]. The method is a univariate method that utilizes the product difference algorithm [56] to create a set of linear systems with the known moments to generate a set of weights and abscissas that are delta functions of a distribution. These delta function distributions can then be used to estimate the moments needed to close the set. The method here is done for aerosols, but presented in a general enough sense that it proves that it can be used for any problem that requires the evolution of a univariate distribution function.

In order to demonstrate QMOM, an example is shown graphically in Figure 2.1 with a log-normal distribution. Log-normal distributions often occur as a PDF in particle size applications. In Figure 2.1(a), the basic log-normal distribution is shown, and Figure 2.1(b) shows the weights and abscissas that are calculated when QMOM is applied to the moments of this PDF. The area of the PDF, which is the zeroth moment, is equivalent to the summation of the weights of these quadrature nodes, so the total number density of the distribution is preserved. This example utilizes three quadrature nodes, which can be used to calculate the following statistical properties: mean, variance, skewness and kurtosis. For the analysis conducted in the studies here, the main variables of concern are the number density and mean values.

In some cases, it may be desirable to represent a PBE with two variables describing

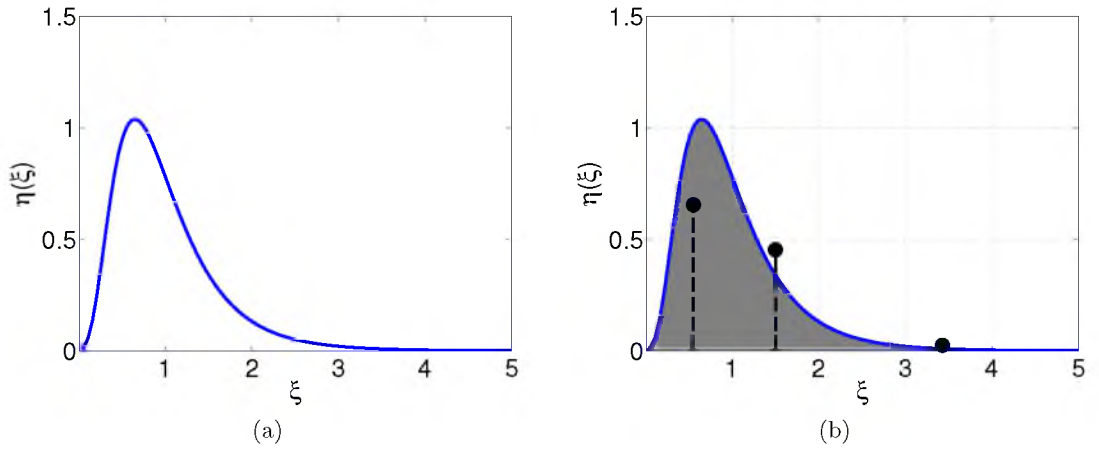

Figure 2.1: A log-normal distribution function (a) with the calculated quadrature nodes shown (b).

the particle distribution; these particle variables can be referred to as internal coordinates. The QMOM method has been extended to be used in multivariate particle PBE problems for the use of internal coordinates of particle area and particle volume for the simultaneous coagulation and sintering of a PSD [190]. Rosner et al. have also proposed extensions of the QMOM bivariate method to specify principal components for the calculation of quadrature nodes for comparison with Monte Carlo random sampling techniques [156]. Other tools for the closure of moment methods have been developed and applied to coagulating aerosols that develop self-preserving distributions such as the Jacobian matrix transformation [109]. The principal component version has been applied to multivariate populations of aerosols that include condensation in addition to the coagulation [193, 194]. The QMOM framework that was generalized has been adaptable for the use in CFD codes for aggregation and breakage [104]. The coupling of a quadrature based moment method has been further developed for full fluid-particle interactions with velocities included as internal coordinates [128].

2.4 The Use of Particle Size Distributions to Simulate Precipitation

In precipitation applications, it can be considered for the PBE to be represented as a univariate population with the radius as the sole internal coordinate. The system will undergo various physical parameters which are analogous to the terms first used to describe aerosol in McGraw [107]. The specific system that is examined is the precipitation of calcium carbonate. The precipitation of calcium carbonate is used as a stand-in for a system of carbon-dioxide mineral sequestration. Sodium carbonate and calcium chloride are highly soluble in water. When aqueous streams with these two chemicals are mixed a

supersaturated solution of calcium carbonate is formed, and rapid precipitation proceeds. Calcium carbonate can exist as many different polymorphs based on the state of the system. Here, only normal conditions are considered, and as such the only polymorphs to be considered will be: amorphous calcium carbonate (ACC), vaterite, aragonite and calcite, listed in the order of increasing stability at room temperature [144].

The ACC phase is so unstable that its solubility is orders of magnitude lower than the other polymorphs, and it only exists for a few minutes in solution. It is theorized that this phase rapidly precipitates and redissolves back into solution once its supersaturation ratio drops [121], but the direct transformation of ACC into other polymorphs has also been considered as a possible mechanism [122, 162]. For the simplicity of the formulation in this study, only the dissolution of the ACC phase is modeled. The solubilities of the remaining polymorphs are affected by the temperature of the system, which has the strongest effect on the long-term results of the abundance of the metastable vaterite and aragonite or the stable phase of calcite. As the simulations here are run at room temperature, calcite should be the most stable phase in the long term, and ACC the most abundant phase in the short term.

A population balance approach is utilized for tracking the PSD of the polymorphs. The formulation of the PBE will allow for the influence of appropriate physical models to be accounted for in the modeling. Each of the four solid phases of calcium carbonate is given a separate PBE. There is difficulty in obtaining the solutions to PBEs with complex source terms due to the problem of moment closure. PBEs that are cast in a simple enough way can be solved with equations using transformation techniques [63], which can sometimes be limited to treat specific kernels such as growth and nucleation or aggregation [106, 35, 158]. Discretization techniques applied to the function of the particle size distribution have been one way to model the complex PBEs with nucleation, growth and aggregation terms [86, 114, 87]. PBEs have been used to successfully model a variety of other generalized particle size distributions [99, 98], along with extensions of PBE solutions into multiple dimensions [58]. In this study, QMOM is used to circumvent the challenges of solving PBEs directly [107]. By using the QMOM version of the PBE approach, Schroeder et al. [165] have shown that experimental results of calcium-carbonate precipitation from Ogino et al. [121] can be accurately modeled for a spatially homogeneous problem.

To construct the source terms for the PBEs, kinetic rates of the various precipitation mechanics are required, an overview of many of these for general precipitation can be found in Nielsen [117] and Dirksen and Ring [36]. The main source to be considered is the birth rate

of the polymorphs. In the short timescale that is examined in a LES simulation this becomes by far the most important of the sources. There are two main types of birth mechanisms in precipitation, homogeneous and heterogeneous nucleation. Homogeneous nucleation assumes that the particles spontaneously nucleate as embryonic clusters of molecules become larger than a given critical size and are stabilized. Heterogeneous nucleation allows particles to nucleate on any other already-present particles or surfaces, either induced by seed particles or occurring as secondary nucleation on precipitated solute particles [36, 72]. The process here assumes that the incoming streams are unseeded and nucleation occurs entirely through the homogeneous process. Many different growth terms exist for particles after nucleation occurs, some of these are monosurface nucleation, monopoly crossover, polysurface nucleation, screw dislocation and bulk diffusion [36]. The high supersaturation ratios that occur in the system here lead to bulk diffusion as the dominant growth mechanism [73]. Other relevant models that are included in the modeling here are the aggregation of particles [104, 105] and the death of small particles [195].

The effects of mixing when the PSD is implemented into a CFD code is examined. There are two effects that are studied at different scales. The first is the implementation of a subgrid mixing model into the LES code. The second effect is the larger macroscale mixing effects that a CFD simulation will have on the system. This is first examined by using a temporal jet and changing the Reynolds number of the system to look at the influence that the mixing rate has on the reactions in the turbulent shear layer. This simple layout has been studied in DNS flows by Riley et al. [154, 153] and more recently by Pantano et al. [126]. The use of a turbulent mixing layer has also been used in more complex reactive systems with soot formation [92] and flame extinction [91]. Another CFD method called one-dimensional turbulence (ODT) has utilized this simple geometry for ODT/DNS comparisons for flame extinction [149] and soot formation [93]. In the context of LES, the use of an idealized temporal jet has been used to study different subgrid fluid models [185], and to examine an elementary reaction the the turbulent mixing layer with a filtered density function LES formulation [25].

The second way the macroscale mixing is examined is in the application of a pilot scale industrial reactor. With the collaboration of an industrial partner [18], the geometry of a pilot scale system was provided. A reactor that is often seen in precipitation literature was adapted from Liu and Fox [96] and Johnson and Prud'homme [69], and was scaled up by an order of magnitude in size to match the flow rate seen in the Calera reactor. This reactor is referred to as a confined impinging jet reactor and has been shown to work well

in many other CFD studies for nano-precipitation [50, 95, 178] and competing reactions of different timescales [49, 100], both of which are important in pharmaceutical production. In order provide a good comparison of the mixing without the Reynolds number effects of the temporal jet, the inlet velocity and pipe diameter were set to the same values for both reactor cases.

2.5 Further Development of Quadrature Based Moment Methods

There are a couple of disadvantages that QMOM exhibits. The first is that the simplicity and efficiency of QMOM is lost when applied to multivariate distributions, and the second is that strong coupling between velocities and other internal coordinates can be unrealistic. The direct quadrature method of moments (DQMOM) was formulated to address these concerns. DQMOM tracks the weights and abscissas of the PSD directly, rather than using the raw moments of the PSD [101]. The method has been shown to be extendable into the multivariate regime and the bivariate extension of DQMOM has been compared to the coagulation and sintering particle case of Wright et al. [190] by Fox [43] with good agreement.

With the development of the DQMOM method, several applications in CFD codes have been shown to work well. In commercial CFD code, the monovariate case with soot formation in ethylene flame [200] and the extension of the soot formation to a bivariate case [201] has been compared with traditional Monte Carlo approaches with good results. These cases have included nucleation, molecular growth and Brownian aggregation. To ensure numerical stability, the use of DQMOM requires the selection of a particular set of moments to be used in the matrix calculations. DQMOM has also been shown to work with multivariate cases where the velocity is included as an internal coordinate of the PSD, such as with particle flow in a fluidized bed using size regimes where the polydispersity plays an important role [38, 37].

Although the use of DQMOM has produced many studies, there are some issues with the technique. As shown in Desjardins et al. [33], traditional Eulerian quadrature methods can only handle particle trajectory crossing in simplified cases. In complex fluid flow, as would occur in large-scale LES, there can be a breakdown in the DQMOM model by forcing abscissas to cross each other in the internal coordinate space. There are various techniques to avoid singularities in the required matrix inversion [101].

Higher order quadrature methods have been proposed for the solution of the PBE when applied to the kinetic equations of particles by using rotated central moments to calculate

closure terms [45]. However, the rotated central moments can be subjected to large round off errors when the mean velocity is much larger than the RMS velocity. The development of these methods has led to increased improvement in the required flux limiters for higher order schemes [182, 181]. The method developed should be applicable to any kinetic equation that is closed in the velocity distribution, such as Boltzmann collision [45], the Williams spray equation [32, 46], and fluid-particle flows with finite Stokes number [161, 33, 44]. Further development of quadrature methods has led to the extended quadrature method of moments (EQMOM), which was developed to increase the accuracy of moment closures at low cost by introducing a parameter to give variance to the sum of distributions that is used in regular QMOM [196].

2.6 The Conditional Quadrature Method of Moments and Application in Coal

Further development of QBMM have resulted in the development of the conditional quadrature method of moments (CQMOM) [195]. This method transports the mixed moments of the system, but calculates the weights and abscissas needed for the closure problem in a different way than in a multivariate QMOM approach. The abscissas are solved for one internal coordinate at a time, then the abscissas for the next internal coordinate are solved conditioned on the nodes being located at the first solution, and so forth for each additional internal coordinate. The basis for the math behind the node calculations is in separating the multivariate PDF into a series of conditional PDFs by applying simple properties of conditional probabilities. In Marchisio and Fox [103], CQMOM has been compared to multivariate QMOM approaches, and shown to be more robust than brute force or tensor-product methods. The set of moments to use in CQMOM is determined by a subset of the optimal set [46].

Several studies in the literature have utilized CQMOM for passive scalar systems, where the particles have a low Stokes number. CQMOM has been utilized for two internal coordinates of particle size and oxygen composition in a CFD simulation of mass transfer in a stirred tank [136]. Flash precipitation modeling with CQMOM has been performed with two internal coordinates for the particle composition in unimers and organic molecules [20]. The use of CQMOM has been compared to direct Monte Carlo simulations and DQMOM results for gas-liquid systems and shown to be more accurate than DQMOM in comparison to MC results [17], and results in much lower computational time than a Monte Carlo method. In calculating the internal coordinates to use for the kinetic equations of the particles, the full optimal moment set is required to maintain accuracy [195]. When used

for internal coordinates as the velocities of the particles, CQMOM exhibits a unique trait for Eulerian approaches for particle transport. The use of CQMOM allows for the solution of a particle trajectory crossing problem that would normally require a Lagrangian method to solve. The use of the adaptive Wheeler algorithm in CQMOM [189] also avoids some of the singularities that can occur in the matrix inversion of other QBMM.

For the application of CQMOM to the kinetic equations of the particles, several test cases are set up to show the particle trajectory crossing cases working in the ARCHES codebase, as well as comparisons to the behavior of the DQMOM implementation. While the available literature only demonstrates the extension of the CQMOM method into three internal coordinates for the velocities of particles, the basis for its derivation can be used to continue to expand the use of the method into M-dimensional internal coordinate space. The extension to higher order dimensional space can be achieved through a simplification in the number of nodes that are added. Once the internal coordinate order reaches five, only one quadrature node is allowed for the additional variables. However, this simplification requires that these higher order internal coordinates are directly dependent on the lower order internal coordinates, and not on each other.

DQMOM has been used to model many different internal coordinates in coal combustion. In Pedel et al. [129, 130], DQMOM was utilized to model coal with seven different internal coordinates. These coordinates were the three velocity directions, the particle diameter, the mass of raw coal, the mass of char and the enthalpy of the particle. While not used as internal coordinates, it is also mentioned that the moisture in the coal and the mass of ash could also be modeled in the coal with DQMOM. However, the ash is inert and assumed as constant, and the moisture was assumed to be evaporated and was added to the gas inlet stream.

All of the same internal coordinates will be addressed here. The first internal coordinates to be implemented will be the particle velocities. The applications for CQMOM in a coal simulation will be in the complex geometry of a coal boiler. Due to the complexities of flow in this regime, it is possible that the particle trajectory crossing problem that is solved by CQMOM will improve the flow results of the particles.

The simulation of coal in LES requires the implementation of various models for the internal coordinates. To describe the evolution of the internal coordinates time derivative models can be used. For example, for the devolatilization of the raw coal there are the FLASHCHAIN [118], the chemical percolation devolatilization [41], the Yamamoto one step reaction [192], and the distributed activation energy model [112]. Another important

aspect to coal modeling is the oxidation of char, which is the material left after the volatiles have been burned off. In a homogeneous mechanism the combustion of the volatiles in the particle vicinity are important, however, in heterogeneous mechanisms the influence of volatile matter is neglected and the heat generation is the primary driving force for oxidation [59]. The enthalpy of the particle can be utilized to calculate the temperature of a coal particle, rather than just using the gas phase temperature for kinetic rates. Models for the particles heat capacity can be constructed and the heat flux to the particle can be calculated through both radiative and convective heat transfer [110, 168].

While the work here has not been fully developed for a full coal model, the CQMOM framework developed in the LES should allow for continued development to complete the implementation for application purposes. As there is high dependency of the internal coordinates of coal on the radius of the particles, the internal coordinates are not expected to be entirely independent distributions – i.e., the covariance of the distributions is high. This dependency allows for the use of a low number of quadrature nodes in the transport space, rather than the exponential scaling that would be required for independent distributions of the variables.

The development of wall models for CQMOM should allow for the easy adoption of ash deposits on the wall. The ash deposits on the wall can be expressed as a fraction of a deposit striking a wall that sticks as a function of the temperature and composition of the coal [186, 15]. As the composition and temperature will be known via internal coordinates, CQMOM will track this information and simply adding a multiplier to the wall boundary condition should accomplish deposit modeling.

CHAPTER 3

TURBULENT INLET CONDITIONS[1]

This chapter will discuss the implementation and testing of turbulent inlet conditions into the LES ARCHES code. Two inlet conditions were examined. As stated earlier, only methods that use a synthetic generation of turbulence were examined. The digital filter generator of Klein et al. [79] and the the synthetic eddy method of Jarrin et al. [66] were used. Each of these methods was used in a way that created a table prior to the simulations. This table is then loaded into the ARCHES code upon the start of the simulation. The data from each of these tables are convected through the inlet at a fixed reference velocity according to Taylor's frozen turbulence hypothesis [173].

One of the main reasons a pregenerated table of values was utilized was to limit any MPI calls between the processors in large-scale simulations. If an inlet crosses multiple patch boundaries and the random field exists on the grid layout, then the processors must provide more information to each other than just one layer of the bounding "ghost cells" when the summations that appear later in Eq. (3.9) and Eq. (3.16) are computed. In the way variables are stored in the ARCHES code, it would also create issues in cases where an inlet is located at the edge of the domain. In these cases, there is no easy way to store the random data as a grid variable, as no patch exists. In contrast, the entire computation could be done on one processor before each time-step, but this would add to the computation time. In addition, creating a table that is separate from the simulation allows for easy verification of the prescribed first and second-order statistics, as well as the transformations of a cylindrically specified velocity or a prescribed velocity that is angled from the inlet plane.

---

[1]Reprinted from publication A.W. Abboud and S.T. Smith, *Large eddy simulation of a coaxial jet with a synthetic turbulent inlet*, International Journal of Heat and Fluid Flow, 50 (2014), pp. 240-253, copyright 2014 with permission from Elsevier.

3.1 Digital Filter Inlet

The specification of a synthetic turbulent inlet requires the recreation of the flow statistics. The digital filter method presented by Klein et al. [79] has been proven to adequately reproduce a prescribed averaged-velocity profile and the correlation tensor profile for second-order statistics. The filtering operation in the method forces spatial and temporal correlations between random data, which allows for the propagation of the turbulent properties downstream from the inlet. If random data are used without any correlation, the fluctuations quickly dampen out and the result is similar to a constant velocity inlet [164, 79]. The digital filter method was implemented into the ARCHES code, and a brief overview is presented here. For the following $\overline{(\cdot)}$ is a simple averaging procedure. The following set of equations is simply a reprint of those in Klein et al. [79]. Let r_m be a set of random data such that $\overline{r_m} = 0$ and $\overline{r_m r_m} = 1$. The convolution or digital linear nonrecursive filter is defined by

$$u_m = \sum_{n=-N}^{N} b_n r_{m+n} \ , \tag{3.1}$$

where N is the support of the filter, and b_n is the set of filter coefficients. From Eq. (3.1) it can be shown that

$$\frac{\overline{u_m u_{m+k}}}{\overline{u_m u_m}} = \sum_{j=-N+k}^{N} b_j b_{j-k} \Big/ \sum_{j=-N}^{N} b_j^2 \ . \tag{3.2}$$

For extending filter coefficients to three dimensions, a simple convolution of the three one-dimensional filters is used

$$b_{ijk} = b_i \cdot b_j \cdot b_k \ . \tag{3.3}$$

Now consider a fully developed flow. An approximation for the autocorrelation function in homogeneous turbulence can be expressed as [10]

$$R_{uu}(r) = \exp\left(-\frac{\pi r^2}{4L^2}\right) \quad \left(\text{with } L = L(t) = (2\pi\nu(t - t_0))^{1/2}\right) \ , \tag{3.4}$$

where L is the integral length scale. If the grid spacing is Δx, then the length scale can be set as $L = n\Delta x$, the coordinate can be substituted as $r = k\Delta x$, and the discrete autocorrelation function is then

$$R_{uu}(k\Delta x) = \exp\left(-\frac{\pi(k\Delta x)^2}{4(n\Delta x)^2}\right) = \exp\left(-\frac{\pi k^2}{4n^2}\right) \ . \tag{3.5}$$

Now Eq. (3.2) is applied to relate the discrete autocorrelation function to the filter coefficients

$$R_{uu}(k\Delta x) = \frac{\overline{u_m u_{m+k}}}{\overline{u_m u_m}} = \sum_{j=-N+k}^{N} b_j b_{j-k} \Big/ \sum_{j=-N}^{N} b_j^2 = \exp\left(-\frac{\pi k^2}{4n^2}\right) \ . \tag{3.6}$$

The approximate solution to the filter coefficients is then given by

$$b_k \approx \tilde{b}_k \Big/ \left(\sum_{j=-N}^{N} \tilde{b}_j^2 \right)^{1/2} \quad \text{with} \quad \tilde{b}_k = \exp\left(-\frac{\pi k^2}{2n^2} \right) , \tag{3.7}$$

which is a valid approximation as long the filter support is sufficiently large, $N \geq 2n$. This maintains that the support of the filter is large enough to capture twice the length scale. The error in this approximation for the filter coefficients is

$$\max_k \left| \exp\left(-\frac{\pi k^2}{4n^2} \right) - \sum_{j=-N+k}^{N} b_j b_{j-k} \Big/ \sum_{j=-N}^{N} b_j^2 \right| \leq 0.001 \quad \text{for} \quad N \geq 2n \, . \tag{3.8}$$

Next, three fields of random numbers, $\mathscr{R}_\alpha$, are generated of dimensions $[-N_x : N_x, -N_y - 1 : M_y + N_y, -N_z + 1 : M_z + N_z]$, where N_α is specified by the length scale for each α direction and M_y and M_z are the grid dimensions of the inlet flow plane. The filter coefficients are applied to these random fields of data as

$$\mathscr{U}_\alpha(j,k) = \sum_{i'=-N_x}^{N_x} \sum_{j'=-N_y}^{N_y} \sum_{k'=-N_z}^{N_z} b(i',j',k') \mathscr{R}_\alpha(i', j+j', k+k') \, , \tag{3.9}$$

which yields two-dimensional arrays of spatially correlated data. In order to match the second order statistics, these arrays are transformed and added to the mean statistics as

$$u_i = \overline{u}_i + a_{ij} \mathscr{U}_j \, , \tag{3.10}$$

where the transformation matrix is given by Lund et al. as [97]

$$a_{ij} = \begin{pmatrix} (R_{11})^{1/2} & 0 & 0 \\ R_{21}/a_{11} & \left(R_{22} - a_{21}^2\right)^{1/2} & 0 \\ R_{31}/a11 & (R_{32} - a_{21}a_{31})/a_{22} & \left(R_{33} - a_{31}^2 - a_{32}^2\right)^{1/2} \end{pmatrix} \, . \tag{3.11}$$

Here R_{ij} is the correlation tensor, for a more in-depth derivation, the reader should refer to the original paper [79]. It should be noted that the specifications of the correlation tensor has the following restrictions to maintain real numbers in the transformation matrix

$$\begin{aligned} R_{11} &> 0 \\ R_{22} - a_{21}^2 &> 0 \\ R_{33} - a_{31}^2 - a_{32}^2 &> 0. \end{aligned} \tag{3.12}$$

In order to reduce computational time in ARCHES, the procedure here was adapted to generate a list of velocities of size N_t (number of time-steps) by M_y (cells in y-direction) by

M_z (cells in z-direction) that is periodic in the flow direction prior to the simulation, and then to convect this through the inlet plane via a table lookup.

For the specification of the turbulent inlet condition, it was assumed that the integral length scales have a constant value of $1/4\ D$, where D is the jet diameter. For the simulation cases, three different inlet conditions were used for each of the velocity ratios and grid resolutions. The first inlet maintained a constant velocity profile at the inlet based on the data from Budilarto [16]. The second inlet enforced the use of a constant stress profile of $\langle u'u' \rangle = \langle v'v' \rangle = \langle w'w' \rangle = 0.02 * U_0^2$, where U_0 is the initial centerline velocity. For the digital filter inlet, this is the magnitude of the stresses that is used in the original implementation of the method [79]. For the velocity ratio of 1.5, the annular region fluctuations were based on the maximum velocity in the annulus. The third inlet made use of the experimental profiles for the fluctuations from Budilarto [16]. These experimental data are listed as radial data for V_r and v_r', so this was transformed into y-direction and z-direction velocity components of the Cartesian mesh used in the CFD code, with zero values assumed for the tangential velocity and fluctuations. This results in a 90 degree shift in the $\langle v'v' \rangle$ and $\langle w'w' \rangle$ profiles.

3.2 Synthetic Eddy Method

The other synthetic method that was tested here was the synthetic eddy method (SEM) of Jarrin et al. [66]. This method creates coherent structures to be generated over the inlet plane, which are shaped by a function to encompass the structures spatial and temporal characteristics. Instead of generating random data and applying a filter, the space is randomly filled with eddy locations.

The one-dimensional case is as follows. A shape function, $f_L(x)$, needs to be defined on the interval $[a, b]$ such that it meets a normalization condition

$$\frac{1}{\Delta} \int_{-\Delta/2}^{\Delta/2} f_L^2(x) \mathrm{d}x = 1. \tag{3.13}$$

Here, $\Delta = b - a + 2L$, and L is the support of the shape function – essentially the length scale of the turbulent structures. Each turbulent location, i, has a position, x_i, that is random on the interval $[a - L, b + L]$. Each spot is assigned a sign, ϵ_i, that is randomly assigned as ± 1. The contribution of each individual eddy on the velocity field is

$$u^{(i)}(x) = \epsilon_i f_L(x - x_i). \tag{3.14}$$

Summing over all of the N eddys in the system gives a contribution to the velocity field as

$$u(x) = \frac{1}{\sqrt{N}} \sum_{i=1}^{N} \epsilon_i f_L(x - x_i). \tag{3.15}$$

The number of eddys on the domain is set to $N = (b-a)/L$ to ensure the plane is well covered with turbulent locations. The extension to three dimensions is straight forward, as now the eddy locations are simply randomized in three-dimensional space in the domain of $[a_x - L, b_x + L]$ by $[a_y - L, b_y + L]$ by $[a_z - L, a_z + L]$. The contribution of each of the eddy locations is the given by the convolution of three tent functions. For each eddy k, the position of the eddy is randomized into the space at location $\mathbf{x}_{i,k}$. The intensity of the fluctuation, $\epsilon_{i,k}$, is then randomized to ± 1 as before. Then the base fluctuations are calculated as

$$\mathscr{U}_i(\mathbf{x}) = \sqrt{\frac{1}{N}} \sum_{k=1}^{N} \epsilon_{i,k} f_L(x_1 - x_{1,k}) f_L(x_2 - x_{2,k}) f_L(x_3 - x_{3,k}), \tag{3.16}$$

where f_L is a tent function such that

$$f_L(r) = \sqrt{\frac{3}{2L}} \left(1 - \left|\frac{r}{L}\right|\right). \tag{3.17}$$

Here, L is the same length scale used in the digital filter method. Now the data exist as correlated fluctuations with a mean of 0 and variance of 1. As with the digital filter method, the transformation matrix from Lund et al. [97] in Eq. (3.11) and Eq. (3.10) is applied to enforce the prescribed mean and fluctuations of the data. As with the digital filter method, two cases are tested here: an isotropic value of $\langle u'u' \rangle = \langle v'v' \rangle = \langle w'w' \rangle = 0.02 * U_{\mathrm{J}}^2$, and the prescribed experimental data fluctuation profile from Budilarto [16].

3.3 Experimental Data Set

The experimental data that are used for comparison are from the dissertation of Budilarto [16]. Air and particles were injected at room temperature into a 0.4752 by 0.4752 by 0.4752 meter chamber. The experiments measured the flow field and particle motion based on different conditions for the inlet velocity. Laser Doppler velocimetry and phase Doppler anemometry were used in order to get accurate measurements of time-averaged velocities. The velocity ratio (VR) of the coaxial jet, defined as the ratio of the annular maximum velocity to the center inlet's maximum velocity, $VR = U_a/U_0$, was varied for the experiments as 0.0, 1.0 and 1.5.

The velocity of the center jet was 11.7 m/s, with a central inlet of 0.014224 meters in diameter. The Reynolds number based on the maximum velocity for the central jet was 11,000. The annular inlet had an inner diameter of 0.015875 meters and an outer diameter of 0.031852 meters. There is a vast amount of experimental data, for multiple cases with and without particles [16]. These data include the centerline velocities and fluctuations for

all cases, as well as radially positioned velocities at various axial positions downstream from the inlet. The inlet profiles for the velocity and the fluctuations are shown in Figure 3.1 to Figure 3.3, with a line for the isotropic fluctuation profile that was discussed in Section 3.1 included. One should note that the isotropic fluctuation profiles are smaller in magnitude than those of the experiment. These were prescribed in this way to mirror a profile that one might use in the absence of experimental data.

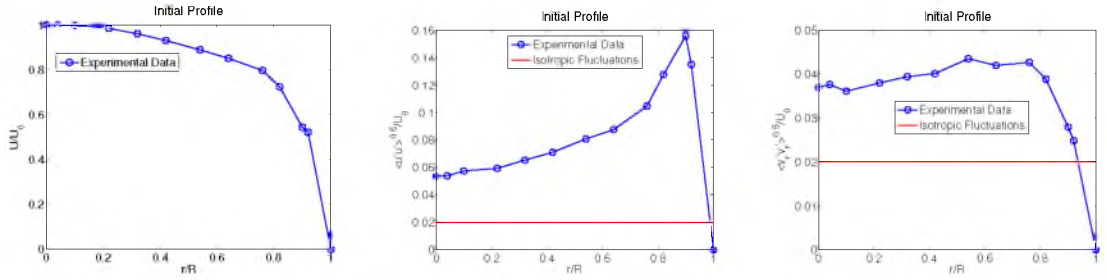

(a) (b) (c)

Figure 3.1: Initial profiles of velocity (a) and fluctuations (b,c) for VR 0.0.

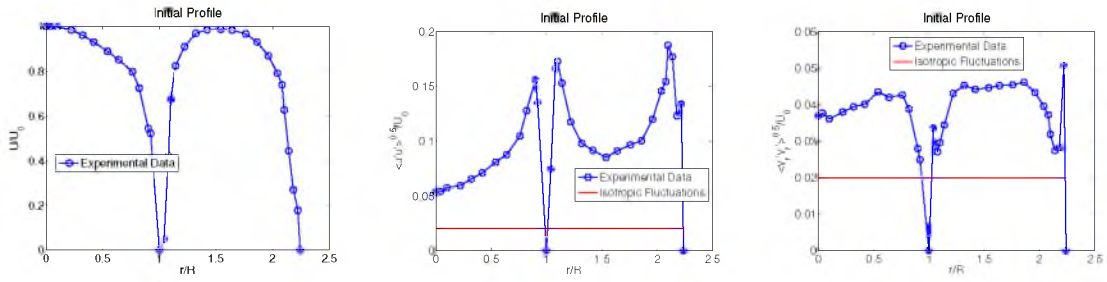

(a) (b) (c)

Figure 3.2: Initial profiles of velocity (a) and fluctuations (b,c) for VR 1.0.

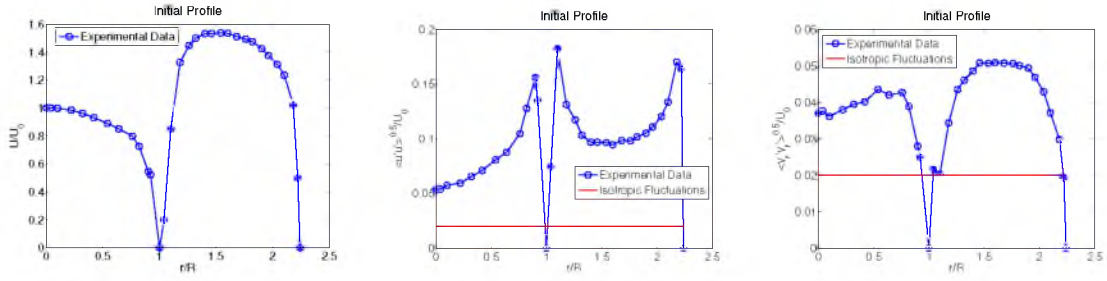

(a) (b) (c)

Figure 3.3: Initial profiles of velocity (a) and fluctuations (b,c) for VR 1.5.

3.4 Simulation Setup

The following chapter details the setup of the simulation in the ARCHES CFD codebase. The results of the simulations when compared to the experimental data of Budilarto [16] are discussed. The code uses the finite-volume method with a mesh of Cartesian coordinates. The computational domain, a slice of which is shown in Figure 3.4a, is a cubic box of 0.28 meters with the jet nozzle centrally located on one face. The face at the inlet (other than the circular inlet itself) is specified as a wall. The four lateral boundaries are zero gradient boundaries, and the face opposite the inlet is a convective outflow condition. The domain was truncated from the experimental size to improve grid resolution, but kept large enough to allow for proper jet spreading and to encompass all of the physical data. The large lateral boundaries of the domain should also dampen effects of these boundary conditions. The inlet pipes are excluded from the domain because the experimental results were reported at the pipe outlet. The simulation contains 8 million cells with equal grid spacing such that $\Delta x = 0.0014$ meters, and it was run in parallel on 512 processors. A more resolved simulation was also run with the same box dimensions but with 22 million cells such that $\Delta x = 0.001$ meters – a slightly higher resolution than that used in Pedel et al. [131]. Of particular interest, the higher resolution case results in a better resolved area between the circular jet and the annulus. Figure 3.4b and c illustrate this difference, where white areas are wall cells and grey are inlet cells. The academic code utilized in the study uses constant grid resolution throughout the domain, as it was built for computational speed and scalability and does not allow for the use of mesh refinement near the inlet. Spatially, a second order central scheme was utilized, and a second order, strong stability preserving time integrator was used.

The constant density filtered continuity and Navier-Stokes equations are used as the basis for LES [160]. For subgrid modeling of the stress tensor, the dynamic Smagorinsky model was used [54]. In Pedel et al. [131], a simple power law was used to set the velocities as constant values for both the circular inlet and the annular inlet

$$u(r) = u_{\max}(1 - r/R)^{1/7} \ . \tag{3.18}$$

This inlet was not adopted for this paper. Due to the way the synthetic turbulent inlet was implemented, a specified profile can be set in ARCHES. The velocities used were the experimental data interpolated onto the grid points. While the data are close to a power law correlation, there are some discrepancies, specifically where the annular region has a profile skewed towards the center axis. To keep consistency, the constant velocity cases shown in Pedel et al. [131] were regenerated with this condition.

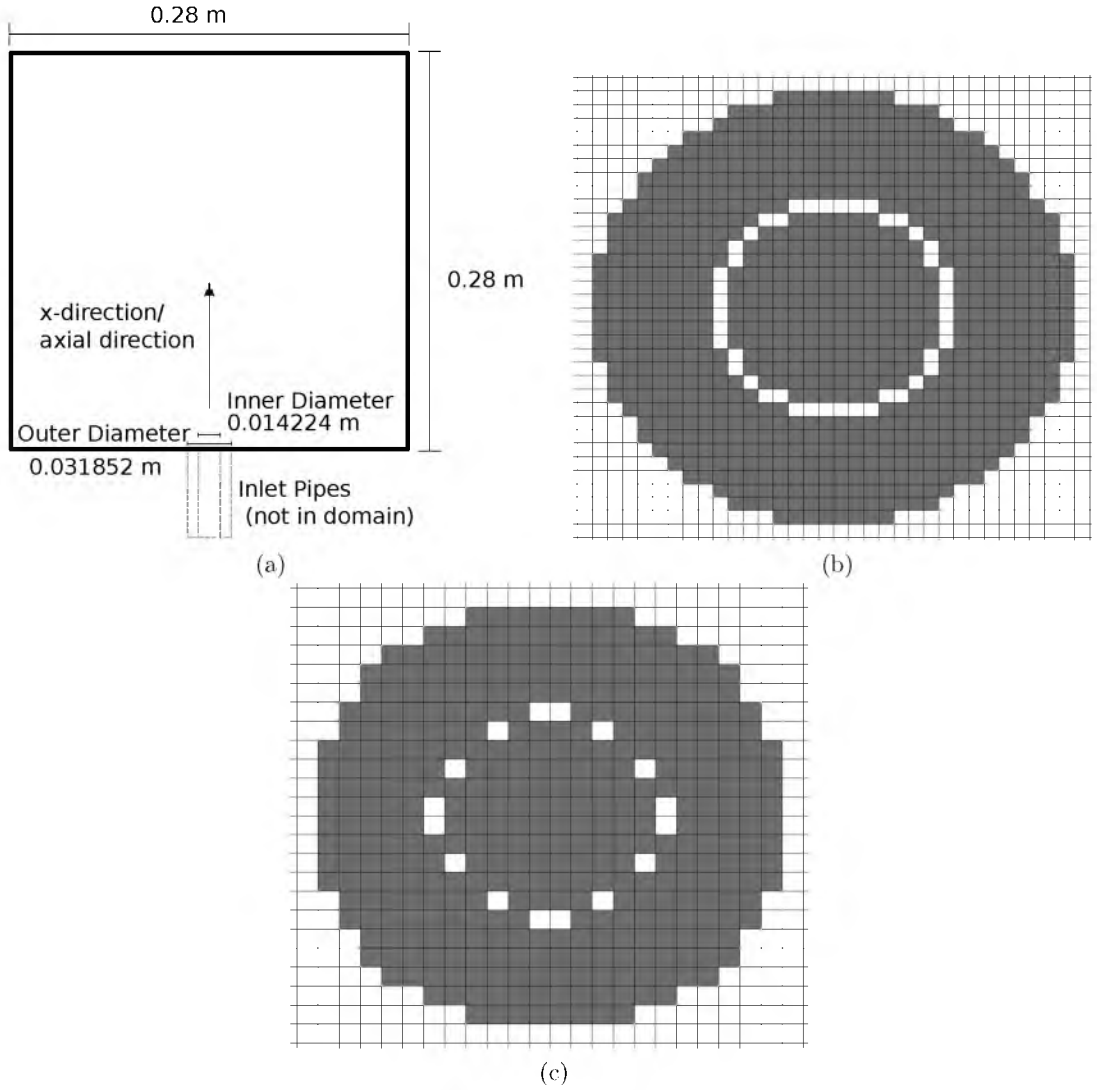

Figure 3.4: A center slice of the Cartesian computational domain (a); the inlet plane for the (b) high resolution and (c) low resolution cases. Here white represents wall cells and grey represents inlet cells.

3.5 Results and Discussion

The results here are separated into two sections, one for analyzing the axial centerline profiles, and one for analyzing the radially positioned velocity at axial locations. In order to clarify where the data at axial locations are in the flow field, Figure 3.5 is included for reference with the lines drawn on top of a slice of U velocity data from a simulation. The data for the centerlines are shown in Figure 3.6 to Figure 3.11, and the data for the downstream axial positions are shown in Figure 3.12 to Figure 3.19. Each centerline velocity plot is normalized by the initial velocity and each plot is normalized by the central inlet diameter. The isotropic $\langle u'u' \rangle$ data refer to the approximation that $\langle u'u' \rangle = \langle v'v' \rangle = \langle w'w' \rangle = 0.02 * U_0^2$

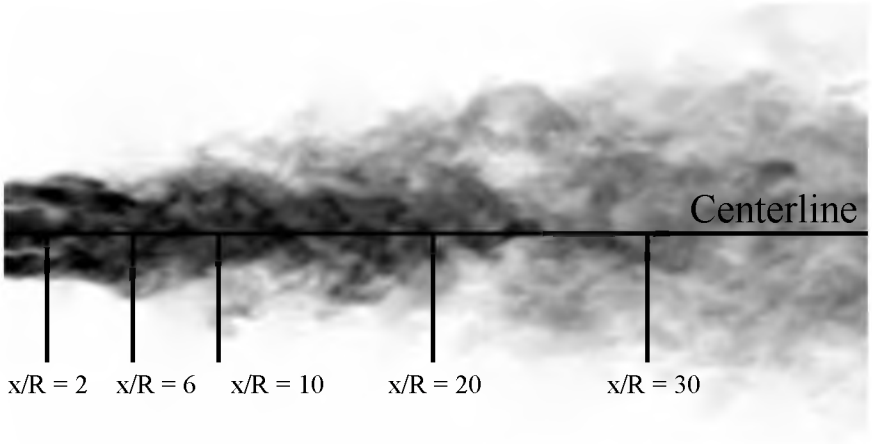

Figure 3.5: Lines showing where data are located, superimposed on a u-velocity data field.

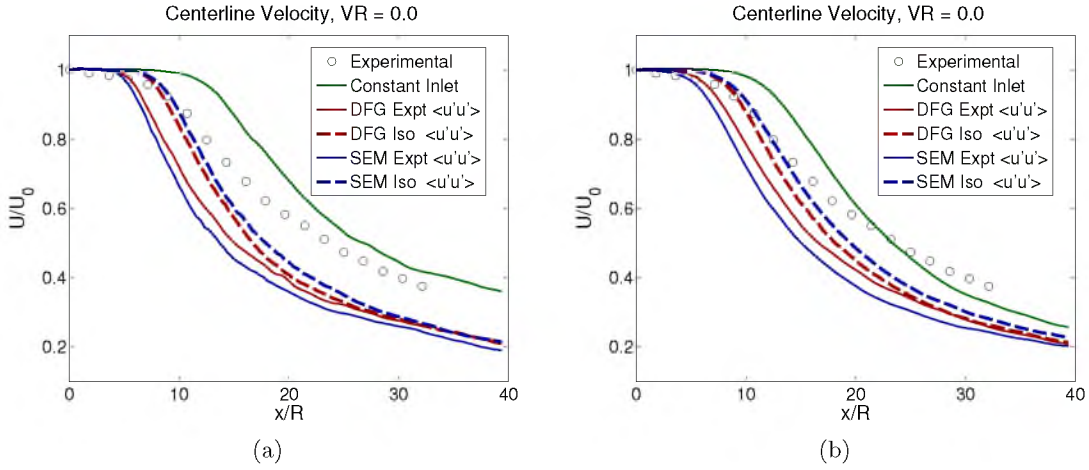

Figure 3.6: Velocity ratio 0.0, centerline normalized velocity for (a) high-resolution and (b) low-resolution cases. DFG = Digital Filter Generator, SEM = Synthetic Eddy Method.

over the entire inlet.

3.5.1 Centerline

Each of the figures (Figure 3.6 to Figure 3.11) show the lower and higher resolution simulation results side by side. The data are normalized by x/R in the axial direction. DFG refers to the data from using the digital-filter generation of the inlet and SEM refers to the data from using the synthetic eddy method. The simulation results for all three velocity ratio cases for the averaged velocity are shown in Figure 3.6 to Figure 3.8.

For the constant inlet in the velocity ratio 0.0 case, both resolutions show that the core region (the area before significant velocity decay occurs) is longer than in the experimental data. The implementation of the turbulent inlet improves the near-field simulation results

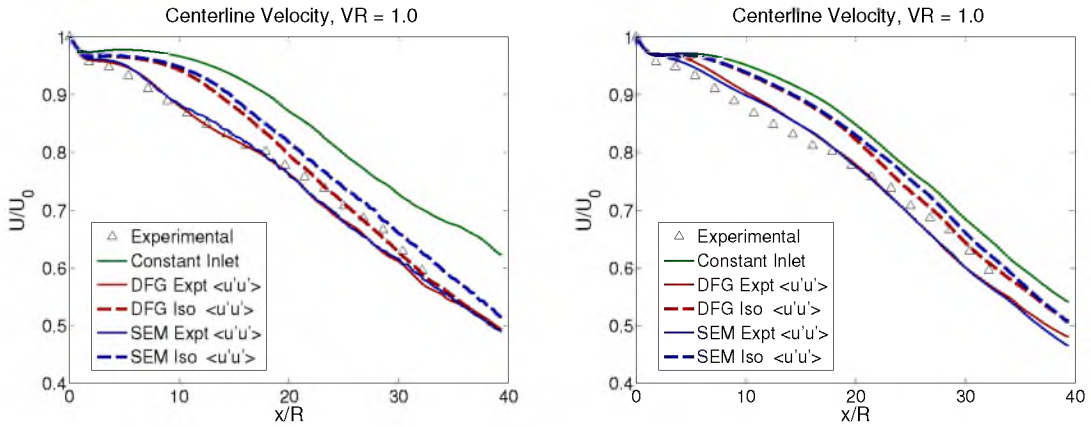

Figure 3.7: Velocity ratio 1.0, centerline normalized velocity for (a) high-resolution and (b) low-resolution cases. DFG = Digital Filter Generator, SEM = Synthetic Eddy Method.

in the core region, but the velocity decays much more rapidly once the core of the jet breaks up. The DFG and SEM inlets perform similarly in this case for both resolutions, with the SEM showing slightly more velocity decay with the experimental profile and slightly less decay than the DFG inlet with the isotropic fluctuation set. For this velocity ratio case, the low-resolution results show better agreement than the higher-resolution case. It is also interesting to see that the isotropic-fluctuation case matches the data a bit better for this case as the core breakup occurs later in the near field, and the SEM isotropic-fluctuation inlet closely matches experimental data up to a x/R of 15. However, in the far field both the turbulent inlet and the isotropic fluctuation cases decay down to the same velocity level.

For the case of a velocity ratio of 1.0, shown in Figure 3.7, using the turbulent inlet provided a significant increase in the accuracy of the averaged simulation results. The constant-velocity inlet contains a large core region where very little velocity decay occurs. The turbulent inlet data immediately begin to decay, due to the entrainment from the annular jet. When using the turbulent inlet, the simulation results are closer to the data at the far field region. In this case it is also seen that the higher resolution exhibits better results, which is to be expected. In this case the isotropic-fluctuation inlet does not behave as well as the velocity ratio 0.0 case in the near field. The data for the isotropic-fluctuation do decay enough to be close to the experimental results and the experimental profile inlet in the far field. The SEM and DFG inlets perform very closely with deviation only occurring in the far field region, where the SEM inlet shows less velocity decay for the isotropic-fluctuation case.

The averaged velocity for the velocity ratio case of 1.5 is shown in Figure 3.8. When

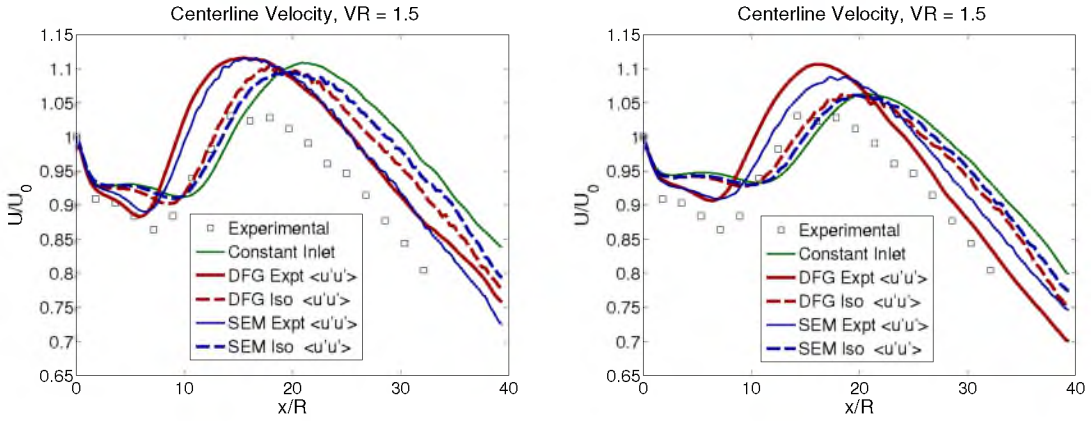

Figure 3.8: Velocity ratio 1.5, centerline normalized velocity for (a) high-resolution and (b) low-resolution cases. DFG = Digital Filter Generator, SEM = Synthetic Eddy Method.

looking at the data from the turbulent inlet, the near field region is more accurate than with the constant inlet and correctly shows the large decrease in velocity due to entrainment for the high-resolution case. The low-resolution case at least shows this decrease in velocity qualitatively better than the constant or isotropic-fluctuation inlets. The center region of the jet is where the inner shear layer approaches the jet centerline. Here the fluid from the central jet is mixed with the faster air from the annulus, causing an increase in the velocity. The two jets merge over a short region reaching a maximum before the decay begins. The DFG results show the location of the inner shear layer mixing closer to the correct axial location. These results also show the maximum-velocity peak occurs close to the correct axial position, but with a significantly higher value. The SEM cases shift the velocity peak slightly further downstream than the DFG cases, and do not show the same level of decrease in velocity in the near field for the experimental profile.

The data for the fluctuations have been normalized by dividing the RMS by the initial velocity in Figure 3.9 to Figure 3.11. The data for the velocity ratio of 0.0 are shown in Figure 3.9. The data for the fluctuations along the centerline show that the use of the turbulent inlet allows for the fluctuations to compare well in the near field region, but deviate significantly as the jet breakup occurs. Both the SEM and DFG inlets follow the same data trend, with the SEM inlet having slightly higher peaks in fluctuation values for an isotropic fluctuation inlet and slightly lower peaks for the experimental profile inlet. The isotropic-fluctuation case quickly reaches the same peak in fluctuation magnitude when the jet breaks up. When the constant inlet is used, the fluctuations take about ten radii downstream of the inlet to develop to the same magnitudes seen in the experimental data.

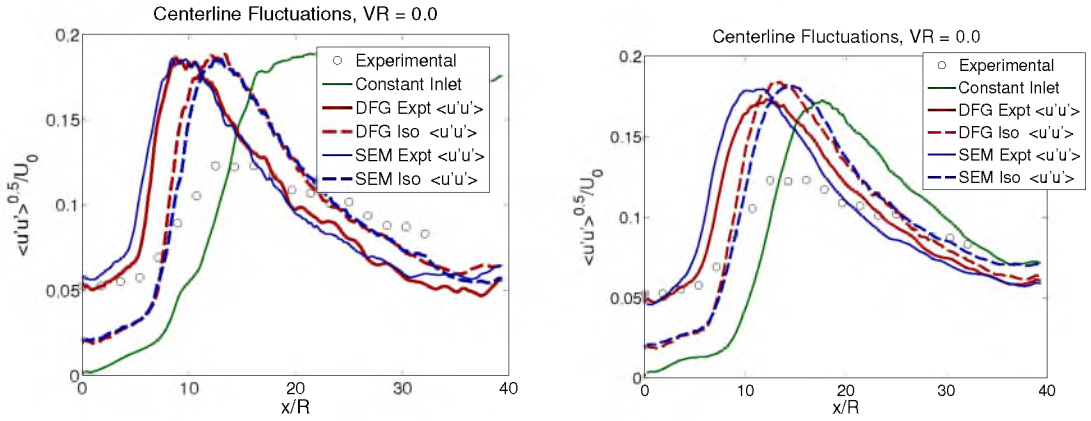

Figure 3.9: Velocity ratio = 0.0, centerline $\langle u'u' \rangle^{0.5}/U_0$ for (a) high-resolution and (b) low-resolution cases. DFG = Digital Filter Generator, SEM = Synthetic Eddy Method.

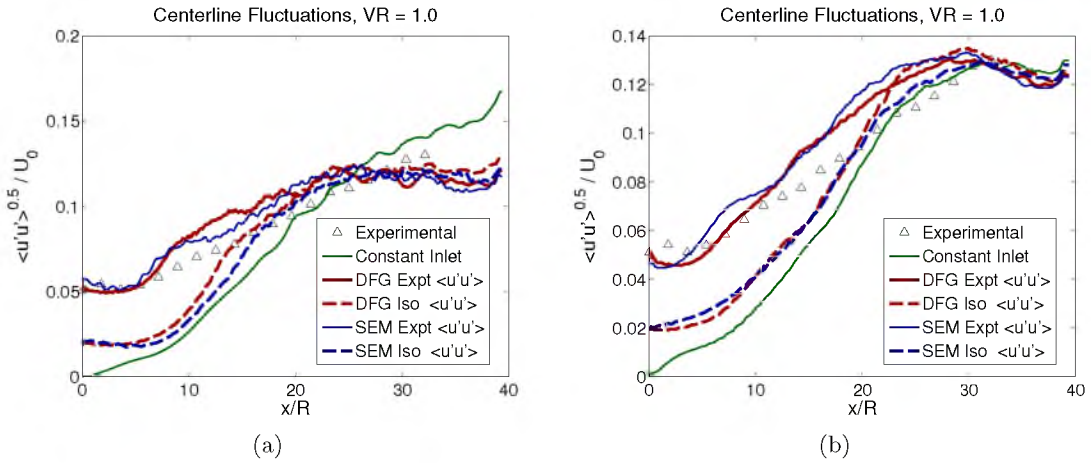

Figure 3.10: Velocity ratio = 1.0, centerline $\langle u'u' \rangle^{0.5}/U_0$ for (a) high-resolution and (b) low-resolution cases. DFG = Digital Filter Generator, SEM = Synthetic Eddy Method.

In the high-resolution case, the fluctuations for $\langle u'u' \rangle$ never decay back down to the level of experimental data. The $\langle v'v' \rangle$ results are omitted for conciseness, but follow the same trend seen in Figure 3.9.

The fluctuations for a velocity ratio of 1.0 in Figure 3.10 again show that it takes a significant length in the axial direction for the constant-velocity inlet to develop to the experimental level of fluctuations in its velocity profile. In the near field, the turbulent inlet methods show good agreement with experimental data. Unlike the velocity ratio 0.0 case, the fluctuations here do not peak unexpectedly high. In the far-field region, the data from all of the cases are fairly close to the experimental data.

The plots in Figure 3.11 show the results for the last case of velocity ratio 1.5. As

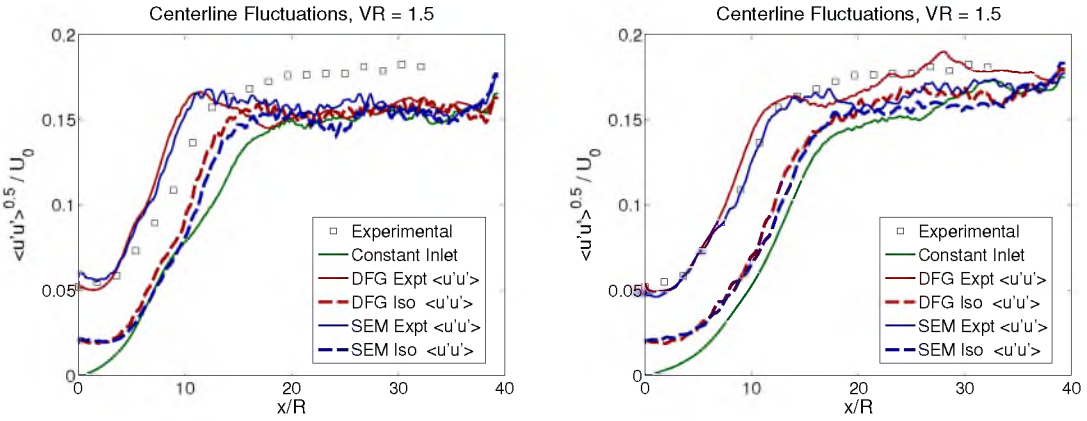

Figure 3.11: Velocity ratio = 1.5, centerline $\langle u'u' \rangle^{0.5}/U_0$ for (a) high-resolution and (b) low-resolution cases. DFG = Digital Filter Generator, SEM = Synthetic Eddy Method.

with the other cases, the fluctuation data show that the digital filter method increases the accuracy in the near field. In the low-resolution case, the results show better agreement with experimental data, while in the high-resolution case the fluctuations maintain a near constant value lower than the data. The results here also look similar to the velocity ratio 1.0 results in that the three inlets eventually maintain about the same level of fluctuations in the far-field region of the jet. For the isotropic-fluctuation inlet, the velocity ratio of 1.5 showed the least amount of change from the constant inlet. This likely due to the significantly lower fluctuations in the annular region, as shown in Figure 3.3.

3.5.2 Data at Axial Locations

The data from Budilarto also provide radially positioned velocity data downstream along the axial direction where comparisons can be made. The plots here are normalized to r/R for the radial direction and x/R for the axial direction. Each subfigure corresponds to data from the black lines shown in Figure 3.5.

In Figure 3.12, the velocity profiles are shown for the velocity ratio 0.0 case. In this plot the velocities shown are the raw values from the simulations. Due to the large gap in the data along the centerline decay this set of data do not give a good comparison and many of the plots show significantly lower values for the velocities.

These significant differences in the radial velocity profiles are due to the large decay along the centerline, as shown in Figure 3.6. To make these data relevant to the discussion, they need to be normalized to match the experimental profiles better. Each of the data sets in the plots is normalized by its current centerline velocity. The normalized u-velocity data

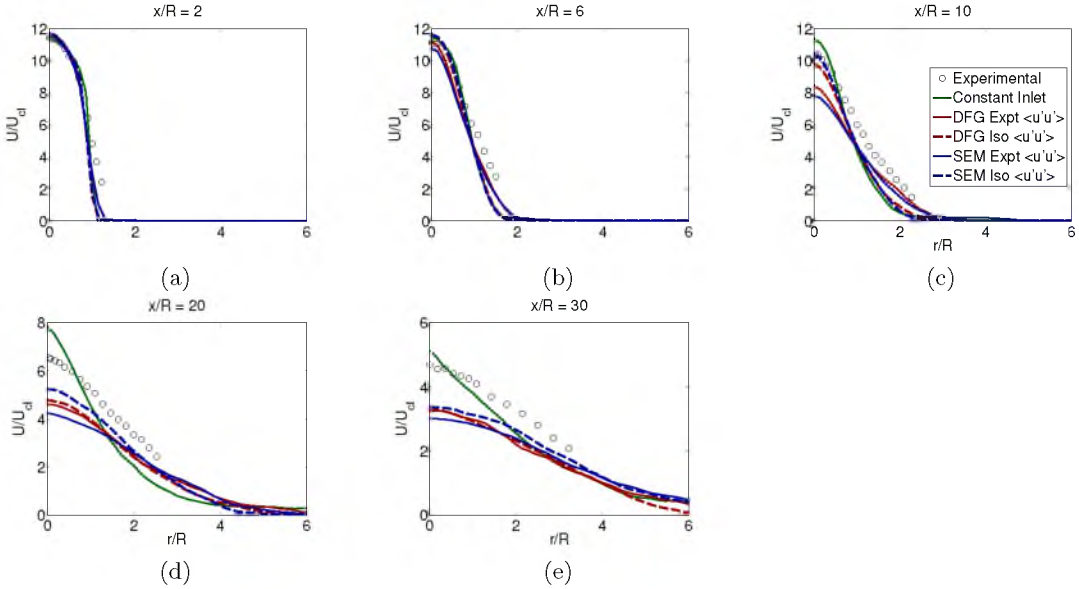

Figure 3.12: Velocity ratio = 0.0, downstream radial positioned velocity for high-resolution case. DFG = Digital Filter Generator, SEM = Synthetic Eddy Method.

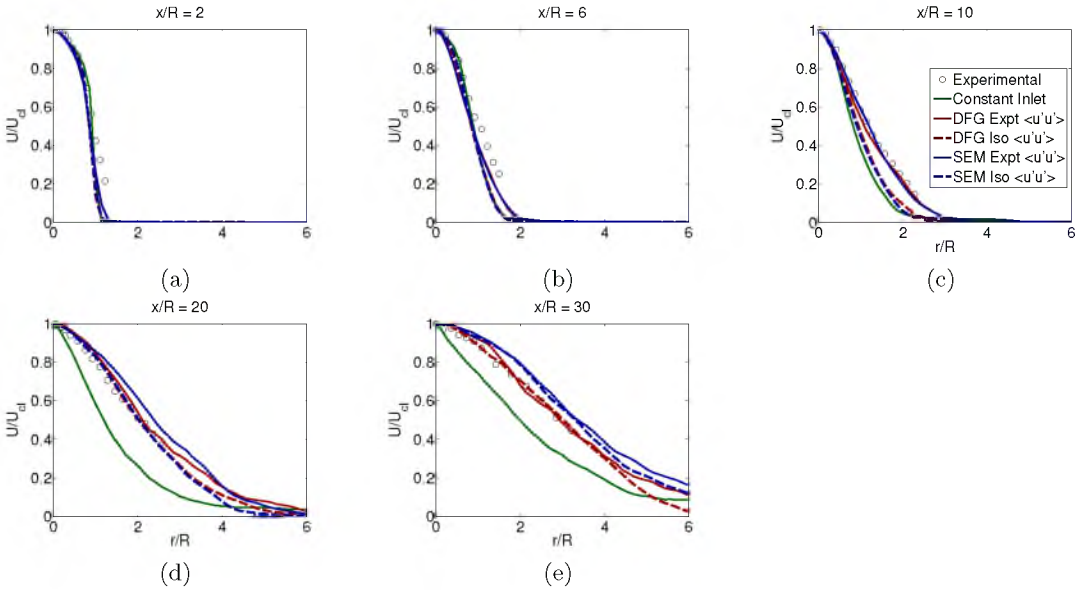

Figure 3.13: Velocity ratio = 0.0, downstream radial positioned normalized velocity for high-resolution case. DFG = Digital Filter Generator, SEM = Synthetic Eddy Method.

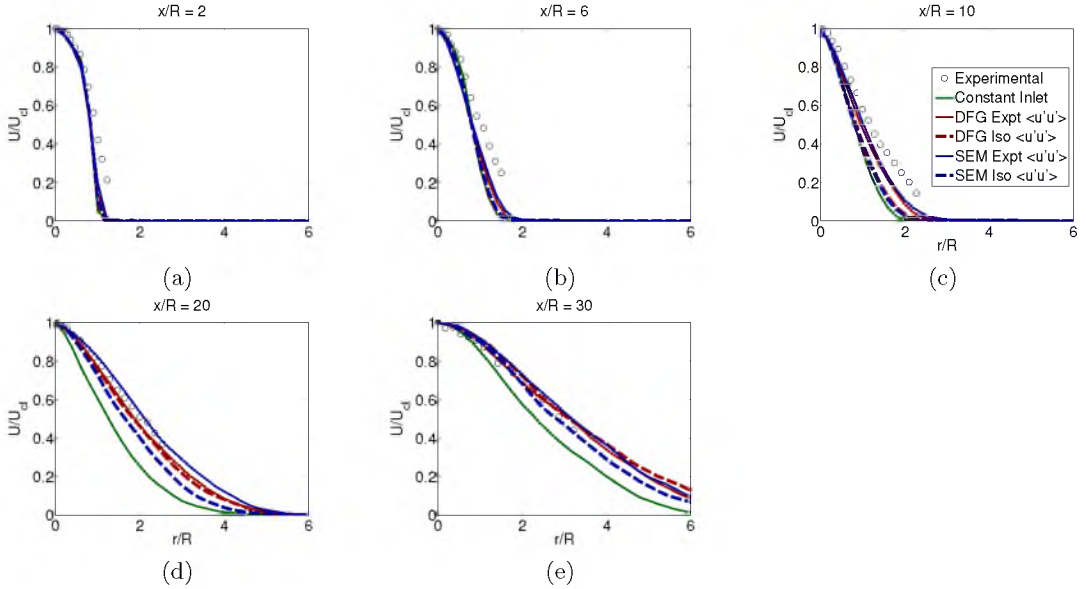

Figure 3.14: Velocity ratio = 0.0, downstream radial positioned normalized velocity for low-resolution case. DFG = Digital Filter Generator, SEM = Synthetic Eddy Method.

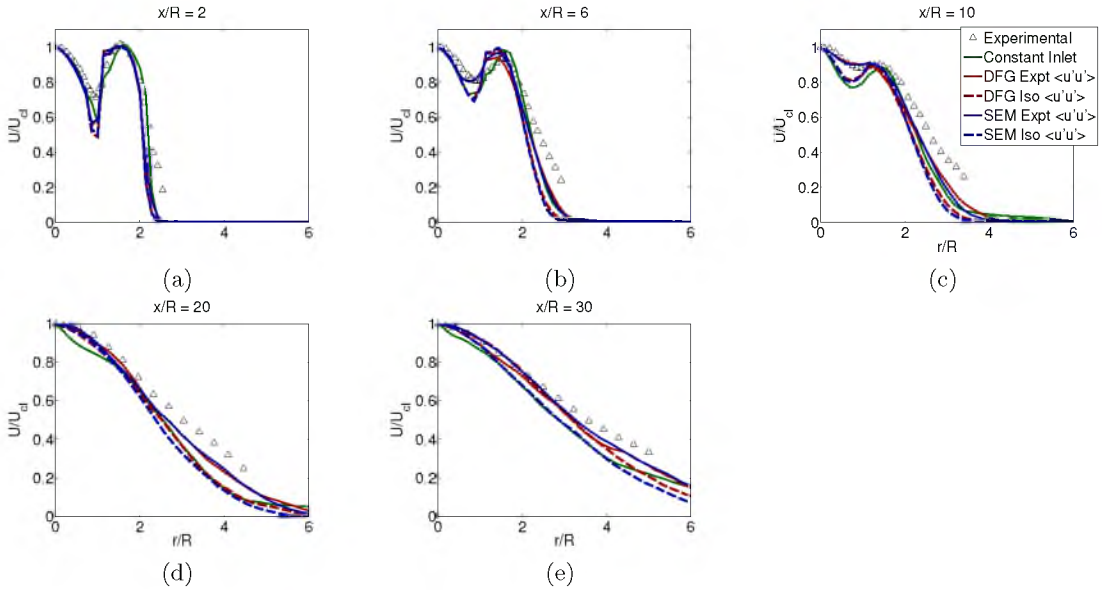

Figure 3.15: Velocity ratio = 1.0, downstream radial positioned normalized velocity for high-resolution case. DFG = Digital Filter Generator, SEM = Synthetic Eddy Method.

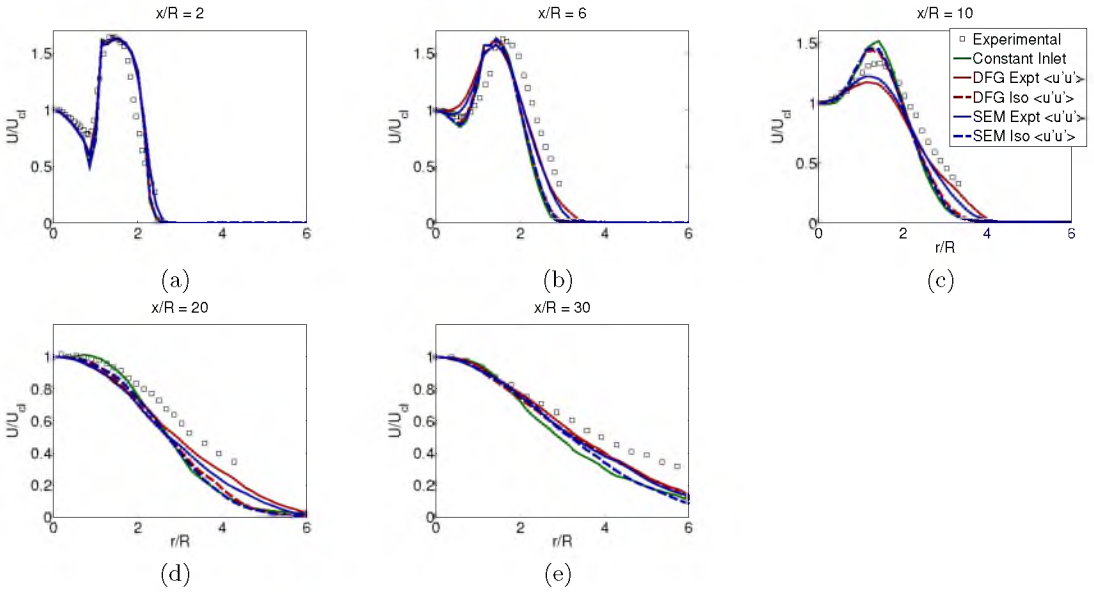

Figure 3.16: Velocity ratio = 1.5, downstream radial positioned normalized velocity for high-resolution case. DFG = Digital Filter Generator, SEM = Synthetic Eddy Method.

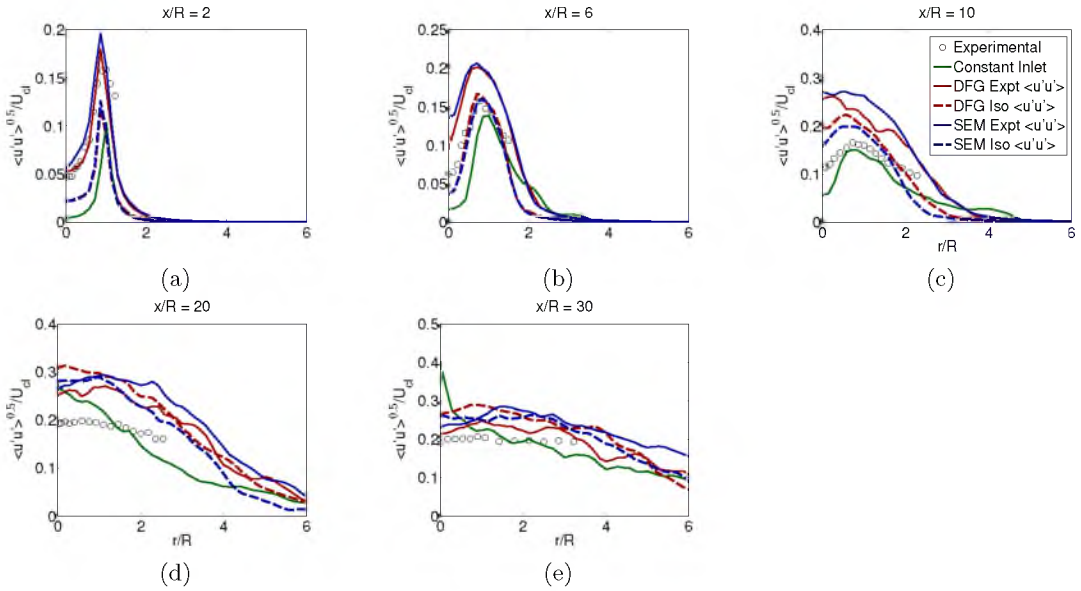

Figure 3.17: Velocity ratio = 0.0, downstream radial positioned velocity fluctuation, $\langle u'u' \rangle^{0.5}/U_0$, for high-resolution case. DFG = Digital Filter Generator, SEM = Synthetic Eddy Method.

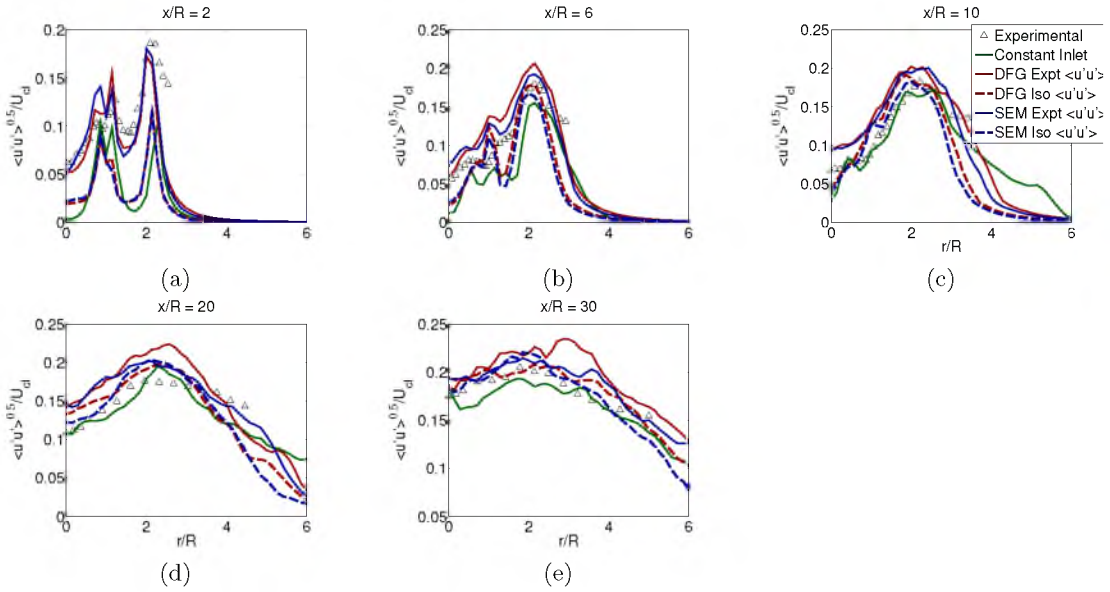

Figure 3.18: Velocity ratio = 1.0, downstream radial positioned velocity fluctuation, $\langle u'u' \rangle^{0.5}/U_0$, for high-resolution case. DFG = Digital Filter Generator, SEM = Synthetic Eddy Method.

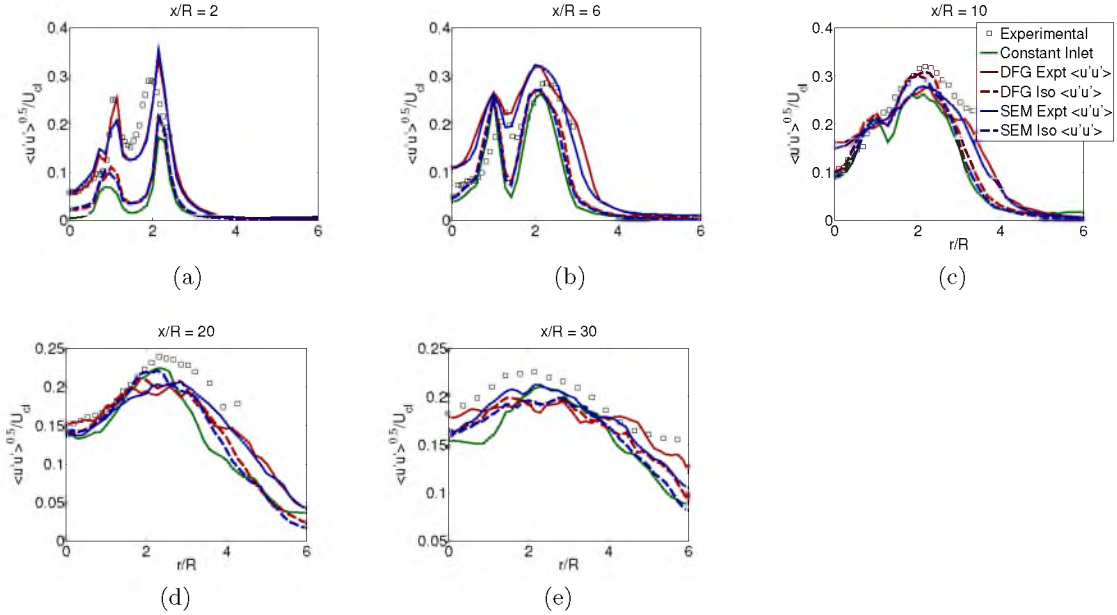

Figure 3.19: Velocity ratio = 1.5, downstream radial positioned velocity fluctuation, $\langle u'u' \rangle^{0.5}/U_0$, for high-resolution case. DFG = Digital Filter Generator, SEM = Synthetic Eddy Method.

at these locations for the velocity ratio of 0.0 are shown in Figure 3.13.

With the normalized velocity profile shown in Figure 3.13, the shape of the data from the DFG inlet simulation closely matches the shape of the expected profile for a developed self-preserving jet consistent with the experimental data once sufficient spatial distance has elapsed around $x/R = 10$. Without using the turbulent fluctuations, the "triangular" self-preserving shape does not develop. When using the 2% estimate, the velocity profile develops to match the experimental results further downstream at x/R of 20 and 30. In the early regions the DFG and SEM results are nearly identical, but the SEM velocities in the far field at x/R of 30 drift a bit higher than the DFG results.

Similar results are seen in the lower-resolution case, shown in Figure 3.14. Only when the turbulent inlets are used do the data show the development of proper jet spreading. However, at a lower resolution this only shows up down field at x/R of 20 and 30, with very little jet spreading in the early regions.

The normalized velocity profiles for the case at a velocity ratio of 1.0 are shown in Figure 3.15. The profiles at $x/R = 6$ and $x/R = 10$ show that the velocity dip in the shear region is too large compared to the experimental data when a constant inlet or isotropic-fluctuation inlet is used. The DFG and SEM experimental profile cases show this dip in the velocity correctly, and show nearly identical results up to the far-field region at x/R of 30. In the near-field region none of the inlet cases develop the jet spreading as quickly as the experimental data, which is surprising given that the velocity ratio 1.0 case matched the centerline data the best for the SEM and DFG cases with experimental fluctuation profiles. Further downstream at x/R of 20 and 30, the DFG and SEM with experimental profiles begin to spread wide enough to get close to matching the experimental data, while the other three cases only match the data in the region close to the center of the jet.

Figure 3.16 shows the normalized velocity profile for the last case with a velocity ratio of 1.5. For this case, the near-field region at x/R of 2 and 6 for all of the inlet cases are nearly identical, and do not capture the peak that is due to the annular flow well at $x/R = 6$, or show the jet spreading as wide as the experimental data. At $x/R = 10$ both the isotropic-fluctuation inlets and the constant inlet overshoot the outer flow of the jet, however, the DFG and SEM inlets with the experimental profile are not spread as wide as the experimental data. In the far-field region at $x/R = 20$, the constant inlet and isotropic fluctuation inlet actually match the experimental data better in the central region of the jet. However, outside of the central region the agreement is poor from both a quantitative and qualitative sense. The DFG and SEM inlets show a qualitative agreement with the jet

spreading, but the data are significantly lower in the actual velocity values.

The fluctuation profiles have been spatially normalized the same way in the x and r directions, and the values have been normalized by dividing the RMS by the centerline velocity. In the fluctuation profiles in Figure 3.17, the best agreement with the experimental results and the turbulent inlet are in the near field at $x/R = 2$, elsewhere there is only a qualitative agreement. The SEM and DFG inlets are nearly identical in the near-field region, but start to deviate at x/R of 10. The constant inlet data actually matched the experimental data better in the shear layer later downfield than the data sets from using one of the turbulent inlet methods, however, there is an unwanted behavior at the centerline with an increase in the fluctuations in the far-field region at x/R of 30. The isotropic-fluctuation case closely matches the turbulent inlet cases further downstream.

Figure 3.18 and Figure 3.19 show the fluctuation profiles for velocity ratios 1.0 and 1.5, respectively. Both of the velocity ratio cases show better agreement between the experimental data and the simulations with DFG and SEM experimental inlets in the early profile than with the constant inlet. Further downstream the constant-inlet and the isotropic-fluctuation cases have been given enough flow time to develop fluctuations, and all of the inlet cases generally have the same values. The figures here are for the higher-resolution case, similar trends are seen for lower resolution, as demonstrated in the earlier comparison between Figure 3.13 and Figure 3.14.

3.5.3 Assessment of Grid Resolution

The simulation results presented were used with constant grid spacing, which may be inaccurate for the conditions around the inlet of the domain. In order to assess the quality of the grid resolution used in this simulation, the ratio of the subgrid to the resolved turbulent energy scales was calculated, $\langle k_\tau \rangle / \langle \frac{1}{2} \tilde{u}_i \tilde{u}_i \rangle$. Here, a model for subgrid scale kinetic energy was used such that $\langle k_\tau \rangle = 2\nu_t \left| \tilde{S} \right|$ [184, 78]. The data presented here are for the VR = 1.0 case for both the high- and low-grid resolutions. The data for the ratio of subgrid to resolved turbulent kinetic energy are shown for the centerline, as well as at axial data at the same locations as the previous section in Figure 3.20.

The centerline data show that the central region of the jet is reasonably resolved, maintaining a ratio of at or below 0.2 between the subgrid and the resolved turbulent kinetic energy. This equates to about 17% of the turbulent kinetic energy on the resolved scale of the simulation. However, the ratios are very large in the near field region of the jet in the plots of the radial direction. The low resolution case shows some numerical noise outside the shear layer at x/R of 2, but the total magnitude of the energy is small, and this

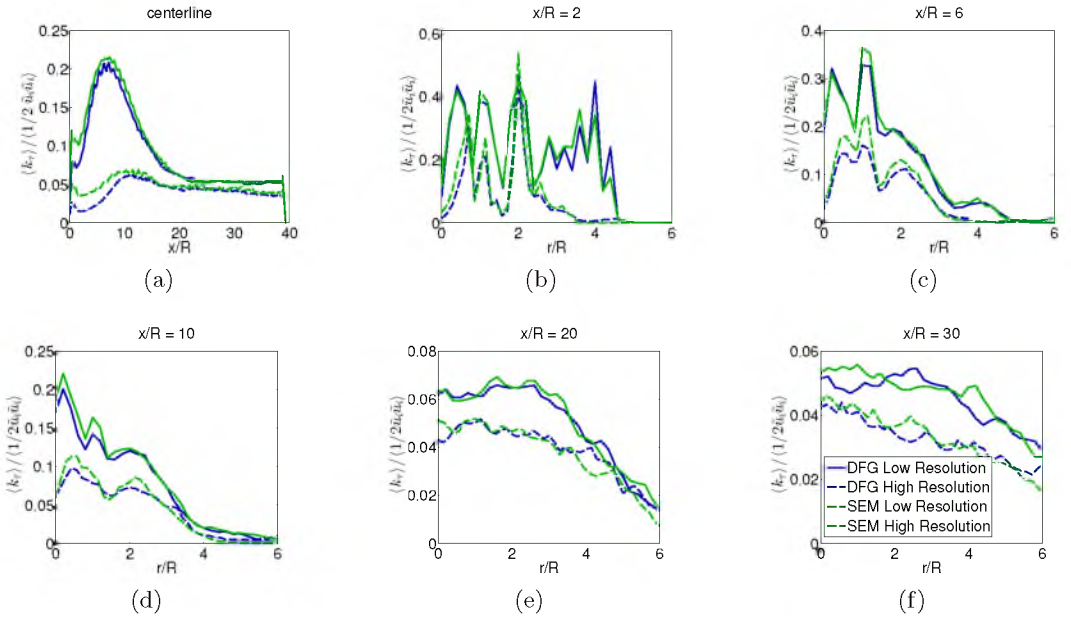

Figure 3.20: Ratio of subgrid scale kinetic energy to resolved turbulent kinetic energy, on the centerline (a) and various downstream locations (b-f). DFG = Digital Filter Generator, SEM = Synthetic Eddy Method.

likely has little effect on the simulation. In the far-field region of the jet past $x/R = 20$, the ratio is considerably smaller, as the decayed velocity in this region allows for a larger amount of the turbulent kinetic energy to be on the resolved scale of the simulation. Both the DFG and SEM inlets perform relatively the same throughout the domain. While the SEM data show slightly less resolved energy ratios, it is a minor difference that would likely be corrected with more time-steps averaged.

Figure 3.20 also includes the results for the higher resolution. As expected, when the grid resolution is improved the resolved turbulent kinetic energy is increased, and thus this ratio of subgrid scales to resolved scales is decreased for all of the profiles shown. A similar trend is seen with small values of 0.06 or less in the center of the jet and in the far field region, so these areas are reasonably resolved. The near-field region in the shear layer at $x/R = 2$ and 6 still shows very high ratios with this resolution, which means that the shear layer in this region is not as well resolved as the rest of the domain. The lack of resolved turbulent kinetic energy in this important shear region could propagate downfield and be responsible for some of the error in the results. When computational resources are available, improving the grid resolution further could increase the resolved turbulent kinetic energy of the simulation.

In addition to the kinetic energy resolution of the simulation, instantaneous vorticity

plots have been made to give a qualitative assessment of the turbulence downstream of the inlet. The vorticity is shown along a centerline plane in Figure 3.21 for the velocity ratio of 1.0 for the constant inlet case and the experimental profile case for the two turbulent inlet methods. This velocity ratio case was plotted because it showed the greatest improvement in the results when comparing the turbulent inlet methods to using a constant inlet. These correspond to the same plane as the previous velocity contour plot in Figure 3.5.

From these plots, it is seen that the largest vorticity values occur in the inner and outer shear layers for all of the cases. So even in the turbulent inlet cases, the majority of the turbulence in the flow is generated through the shear layer. Comparing the turbulent inlet cases with the constant inlet cases, it is clear that the core region of both the central jet and the annulus contain no turbulent structures until the shear layer instabilities propagate into the center of the jet, which occurs rather far downstream. However, both of the turbulent inlet cases show structured turbulence in the near field of the central jet and the annulus. When comparing the two resolutions for the constant inlet it is seen that the higher-resolution case takes further downfield to develop turbulent structures along the centerline. This is consistent with Figure 3.7 in that the higher-resolution case takes further

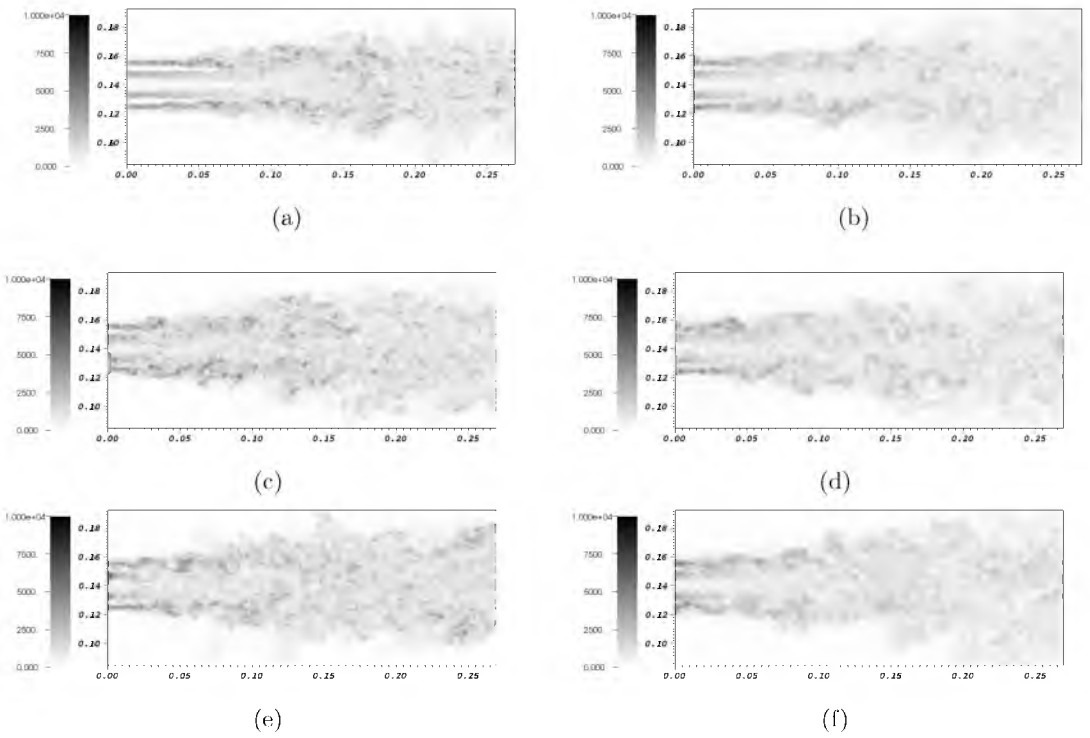

Figure 3.21: Vorticity contours for the VR = 1.0 case. Constant velocity for (a) high and (b) low resolutions, DFG for (c) high and (d) low resolutions, and SEM for (e) high and (f) low resolution.

downfield for the core region to start to show a decay in its velocity. The differences in the vorticity fields for the two turbulent inlet methods are relatively minor, and do not strongly support the strength of using one of these methods over the other.

3.5.4 Timing

In order to test the computational cost of the method, the time-steps for each simulation type were averaged. In addition, the time to load the table of pregenerated values into the CFD code and the time to generate the actual tables are listed in Table 3.1, where these timings are for the higher-resolution case. The number of realizations generated in the x-direction of the turbulent inlet was 5000, which is enough data for 10 flow-though times of the domain. For the total simulation time, over 20 hours were used for each simulation. The data are presented comparing the constant inlet profile to the digital-filter inlet and the synthetic-eddy method inlet, as well as a constant tophat profile, which has no table associated with it.

From the table, it is seen that the increase in the computational time of the simulation is about 2% for each time-step, which is an acceptable increase in terms of the computational cost. The increased computational cost is not from applying the inlet condition directly, but rather indirectly from a slightly stiffer linear solve in the pressure projection. On average, the linear solve was increased by 0.5 iterations per time-step. In terms of the table generation and loading, the 2-3 minutes required is an insignificant amount of time compared to the total simulation runtime. The SEM inlet has a slightly faster generation time than the DFG inlet, likely due the correlation summation occurring only nearby eddy locations rather than all random points. It should be noted that neither implementation here has undergone significant optimization as in Kempf et al. [77], so the timings could likely be improved. However, with the small generation time in the current implementation this was not a high priority, and the difference between the timings of each method is not a large concern when compared to the overall simulation time.

Table 3.1: Simulation timing.

Profile	Tophat	Constant	DFG	SEM
Table Generation (sec.)	-	0.05	157	73.9
Table Loading (sec.)	-	0.03	33.5	33.5
Average Time-step (sec.)	3.08	3.09	3.15	3.14

3.6 Conclusion

This study provides suitable evidence that the inlet methods used here can improve LES results for free-flow jet systems, even when used in under-resolved domains. The improvements here occurred best when applied to the velocity ratio 1.0 case. The most notable improvements to the accuracy are in the near field regions for the velocity fluctuations and the core regions of the jets for the averaged velocity fields. Beyond the near field, the results for the velocity ratio 1.5 case were only a qualitative match in the averaged velocity, but providing the correct location for the merging of the jets was seen. Using both the digital-filter method proposed by Klein et al. [79] and the synthetic-eddy method of Jarrin et al. [66], the CFD implementation of the inlet was done at a relatively low computational cost of the simulation.

Some error is still seen in the centerline velocity at the far-field regions for the jet for the velocity ratio 0.0 and 1.5 cases. The jet was investigated with two other subgrid models from Vreman [184] and Nicoud and Ducros [116], and neither improved the results. The error here could be due to the lack of resolved turbulent kinetic energy in the near-field shear layer. The ratio of subgrid to resolved energy was reasonably resolved for the center of the jet and in the far-field regions. If the resolution were increased further, the ratio would be improved and would likely affect the simulation results. The expected self-preserving shape of the jet in the far-field region also develops for all three of the velocity ratios when using the turbulent inlet, while this feature of the flow is absent when using a constant inlet. While some inaccuracies do occur, the qualitative features of the flow are much more inline with experimental results.

Using an isotropic-fluctuation inlet condition, which could be done without the availability of experimental data at the inlet, did provide some increase in accuracy to the results. Specifically, the development of the jet spreading for the velocity 0.0 case and the centerline data for the velocity 1.0 case were the best examples. The fluctuation profiles of the centerline were better than that of using just a constant inlet, but it still took some time while flowing downstream to develop to the same values of the fluctuations in the experimental data. However, for the velocity ratio 1.5 case the higher velocity in the outer jet likely contributed to the lack of significant improvement compared to the constant inlet for the normalized velocity comparisons. To employ the use of an isotropic-fluctuation inlet in the two synthetic methods used, the fluctuations would likely need to be ramped up from 2% when higher Reynolds numbers are used. The SEM and DFG methods showed very similar results throughout the data, and the differences that did occur were rather

minor. The computational cost for both methods was also minimal, so there is no distinct advantage between the two methods, however, the DFG method has slightly better results for the VR 1.5 case, and it will be used in other simulations in subsequent chapters.

CHAPTER 4

PRECIPITATION MODELING[1]

This section discusses the study of the precipitation reaction for calcium carbonate. The reaction is modeled with a mixture of two highly soluble salt streams of sodium carbonate and calcium chloride. The by-product of sodium chloride was deemed to be soluble enough to ignore its effects. This system was selected as a representation of dissolving carbon dioxide into a briny solution in order to perform carbon dioxide sequestration via mineralization. The research here consists of both an academic study with a simple geometry, as well as a study dealing with industrial pilot scale reactors. The CFD is done using ARCHES for the velocity and property scalar fields, and a coupling with the Wasatch codebase is used for the precipitate phase of the system [57, 159].

In the general sense, any two-step reaction can expressed as progression of reactants into intermediates into final products

$$\text{Reactants} \longrightarrow \text{Intermediates} \longrightarrow \text{Products}, \tag{4.1}$$

which can have different speeds between the reactions that can vary the timescales that need to be modeled in CFD. For the precipitation of calcium carbonate it is assumed that aqueous equilibrium chemistry occurs on the fastest scale and is simply modeled as an instantaneous reaction. The solid phase formation occurs much slower and is assumed to occur on the same scale as the CFD. For precipitation, the base Eq. (4.1) can be expressed as

$$\mathrm{Ca^{2+}(aq) + CO_3^{2-}(aq) \overset{fast}{\rightleftharpoons} CaCO_3(aq) \xrightarrow{slow} CaCO_3(s)}, \tag{4.2}$$

where the first reaction of reactants to intermediates is the equilibrium chemistry, and the second reaction of intermediates to products is the solid phase precipitation.

---

[1]Reprinted with permission from John Wiley and Sons. A.W. Abboud, B. Schroeder, T. Saad, S.T. Smith, D.D. Harris, and D.O. Lignell, *A numerical comparison of precipitating turbulent flows between large-eddy simulation and one-dimensional turbulence*, AIChE Journal, (2015), doi:10.1002/aic.14870.

4.1 Precipitation

The numerical model for the precipitate particles consists of transporting the particle size distribution (PSD). PSDs are commonly used in the crystallization community and have been shown to accurately represent populations of particles [21, 171, 62]. The PSD is adapted here to contain many of the complex source terms and is given by [152]

$$\frac{\mathrm{D}\eta(r)}{\mathrm{D}t} + \frac{\partial G(r)\eta(r)}{\partial r} = B(r) - D(r) + A(r) + \xi_{\text{mix}} \, . \tag{4.3}$$

Here η is the population balance, r is the internal coordinate of radius, $G(r)$ is the growth rate, $B(r)$ is the birth rate, $D(r)$ is the death rate, $A(r)$ is the aggregation rate, and ξ_{mix} is the source term that arises from the subgrid mixing model. For one dimension in the internal coordinates of the PBE, the statistical moments of the system are defined as

$$m_k = \int_0^\infty r^k \eta(r) \mathrm{d}r \, , \tag{4.4}$$

where m_k is the k^{th} moment of the system. Using QMOM, any unclosed moment of the system is estimated as a sum of the weights and abscissas as

$$m_k \cong \sum_\alpha^N w_\alpha r_\alpha^k \, . \tag{4.5}$$

This equation is exact for transported moments of the system, and is an approximation for unclosed moments. Eq. (4.3) can be easily transformed into a transport equation for the moments by multiplying by r^k and integrating, which results in

$$\frac{\mathrm{D}m_k}{\mathrm{D}t} + \int r^k \frac{\partial G(r)}{\partial r} \mathrm{d}r = \int r^k \left(B(r) - D(r) + A(r) + \xi_{\text{mix}} \right) \mathrm{d}r \, . \tag{4.6}$$

Each of the source terms in Eq. (4.6) will require some approximation or closure in order to solve the problem. The weights, w_i, and abscissas, r_i, in Eq. (4.5) are solved using the product-difference algorithm [56]. For each of the polymorphs, six moments are transported; this results in three abscissas and weights. Using a moment method requires closure of integral terms. For the closure of complex source terms, the quadrature method of moments is utilized [107].

In Schroeder et al. [165], a comprehensive modeling scheme for this precipitate system was developed. It was shown that this modeling scheme could reproduce the experimental results from Ogino et al. [121]. It should be noted that the model used here makes a few simplifications to avoid the effects of ion ratio [94, 170, 53, 14], pH levels [145, 157], the direct transformation of polymorphs [122, 162], nonclassical nucleation [52, 51], and molecular viscosity increases to the solution [61, 163]. A justification for this last assumption will

be shown later in this chapter. Due to the modularity of the model described here, more advanced physics can be substituted if desired.

The birth term of the system causes significant numerical problems as it creates a very large burst of particles at one point. To alleviate this, the LES domain is initialized with a wide distribution with a relatively low number density. This distribution was set as a uniform distribution with an average particle size of 500 nm, and a number density of 1.0×10^9 particles/m^3. This leads to the set of moments shown in Table 4.1. While this may seem like a densely populated system, the birth rates that occur in the system result in number densities for the polymorphs, which are many orders of magnitude greater than this initial distribution.

In the precipitation of calcium carbonate, there are four distinct solid phases at the temperature examined in this study. These phases are the amorphous phase – amorphous calcium carbonate (ACC); vaterite – a hexagonal crystalline structure; aragonite – an orthorhombic crystalline structure; and calcite – a trigonal hexagonal structure. For reference, SEM images of these phases in solution are shown in Ogino et al. [121].

4.1.1 Aqueous Phase

Two aqueous streams are mixed to model a more complex carbon dioxide mineralization reaction. These streams are aqueous sodium carbonate and calcium chloride. In this system an initial concentration of 0.03 M in each of the pure streams is used. At this low concentration, using Davies' correlations for activity coefficients has been shown to perform well [28]. For the timescales involved in this investigation, it is assumed that all of the aqueous phase reactions occur instantly. As the aqueous reactions occur many orders of magnitude faster than the LES time-steps, this is a good assumption. These aqueous phase equilibrium equations are solved for 10 of the major species in solution. The 10

Table 4.1: Initial values for the moments.

Moment	Initial value
m_0	1.0e9
m_1	5.0e11
m_2	3.333e14
m_3	2.5e17
m_4	2.0e20
m_5	1.667e23

species in the equilibrium calculation are: H_2O, H^+, OH^-, Ca^{2+}, $H_2CO_3^*$, HCO_3^-, CO_3^{2-}, $CaHCO_3^+$, $CaCO_3$ and $CaOH^+$. Previously, the OLI software had been utilized for these calculations, with over 75 species included in the equilibrium calculation [124]. However, for a consolidated scheme it was found to be easier and less computationally expensive to use the simple equilibrium calculation. At this low level of concentrations, little difference was seen in the supersaturation ratio results.

The supersaturation ratio for each polymorph is calculated based on the aqueous chemical activities and known solubilities for each polymorph, α, as $S_\alpha = [CaCO_3]/[CaCO_3]_{eq,\alpha}$ [144]. The solubility products and temperature correlations can be seen in Table 4.2. The aqueous chemistry is tabulated over mixture fraction and extent of reaction prior to running the CFD simulations to avoid the computational cost of solving the nonlinear system of equations at each grid point. In Figure 4.1, the two-dimensional space for the value of the supersaturation ratio over extent of reaction and mixture fraction is mapped out. The maximum supersaturation ratio that occurs here is a little over 1600 at a mixture fraction of 0.5. The extent of reaction variable is a scaled value from 0 to 1, where 0 represents that no solid phase has precipitated, and 1 represents that all of the solid phase has precipitated. The extent of reaction has a source term based on the change to the mass that has precipitated out in each time-step. The mixture fraction is set to 0 for the pure aqueous calcium chloride stream, and set to 1 for the pure aqueous sodium carbonate stream.

The solubilities of each of the polymorphs changes over temperature. These values can be found in the literature, and equations are listed in Table 4.2 [144]. The solubilities at room temperature are also included in this table. From these solubility values, it is easily seen that at room temperature ACC is the least stable precipitate, while calcite in the most stable.

Table 4.2: Solubility products for the polymorphs of calcium carbonate.

Polymorph	$-\log K_s$ at 25 °C	Temperature Correlation (T in K, t in °C)
ACC	6.40	$-\log K_s = 6.1987 + 0.005336t + 0.0001096t^2$
Vaterite	7.91	$-\log K_s = 172.1295 + 0.077993T - 3074.688/T - 71.595\log T$
Aragonite	8.34	$-\log K_s = 171.9773 + 0.077993T - 2903.293/T - 71.595\log T$
Calcite	8.48	$-\log K_s = 171.9065 + 0.077993T - 2839.319/T - 71.595\log T$

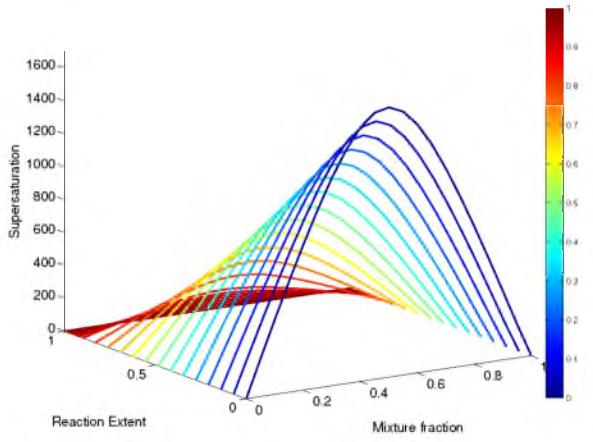

Figure 4.1: Plot showing the supersaturation ratio of calcite across the range of mixture fraction and extent of reaction values.

4.1.2 Birth

For the birth model, a homogeneous nucleation kernel is used with several correction terms [72]. The density function of the birth distribution is assumed to be a point function such that $B(r) = \delta(r - r_c)$. After integrating the source term in Eq. (4.3), the equation for the birth term results in

$$\int_0^\infty J\delta(r - r_c)r^k \mathrm{d}r = r_c^k * J, \tag{4.7}$$

where the critical radius of nucleation is given as [36]

$$r_c = \frac{2\sigma_T \nu}{RT\ln(S)}. \tag{4.8}$$

Here σ_T is the surface energy, ν is the molar volume, R is the gas constant, T is the temperature in Kelvin, and S is the supersaturation ratio. The Tolman length correction to the surface energy is utilized to account for size dependence of small particles on the nanoscale and is given by [175]

$$\sigma_T = \sigma_{\text{bulk}} + 1/2\sqrt{\sigma_{\text{bulk}}^2 - 0.8\ln(S)RT\sigma_{\text{bulk}} * r_1/\nu}. \tag{4.9}$$

In the birth term, the coefficient J represents the nucleation rate and is given by

$$J = zk_F N_1^2 \exp(\Delta G/K_b T)\ , \tag{4.10}$$

where ΔG is the Gibbs free energy of nucleation [71], k_B is the Boltzmann constant, z is the Zeldovich factor to account for differences from equilibrium [197], k_F is the reaction rate coefficient [72], T is the temperature and N_1 is the concentration of molecules in solution.

A more detailed description of the birth model can be found in Schroeder et al. [165]. The Gibbs free energy for a nucleating particle is given by

$$\Delta G = \frac{16\pi}{3}\frac{\nu^2\sigma_T^3}{K_b^2T^2\ln(S)^2} + K_bT\ln(S) - \sigma_T(36\pi\nu^2)^{1/3}, \tag{4.11}$$

where K_b is the Boltzmann constant. Then, the number of molecules in the nucleate particle is calculated as

$$i_c = \frac{32\pi}{3}\frac{\nu^2\sigma_T^3}{K_b^3T^3\ln(S)^3}. \tag{4.12}$$

Then the Zeldovich factor can be derived to calculate a correction for deviations from equilibrium [197]

$$z = \sqrt{\frac{\Delta G}{3\pi K_bTi_c^2}}, \tag{4.13}$$

in some cases ΔG can be less than zero, in which case z would be nonreal, when this occurs ΔG is set to 0, and z is set to 1. The reaction rate coefficient is calculated by [72]

$$k_F = D(48\pi^2\nu i_c)^{1/3}, \tag{4.14}$$

where ν is the molecular volume. The concentration of molecules in solution is calculated as

$$N_1 = N_AC_{eq}S. \tag{4.15}$$

Here N_A is the Avogadro number and C_{eq} is the equilibrium concentration of calcium carbonate. The combination of all these terms results in the overall nucleation rate in Eq. (4.10). The nucleation rates and sizes are dependent on the molecular volumes and the surface energies of the solid phases, these are listed in Table 4.3 and Table 4.4.

4.1.3 Growth

Many different mechanisms are possible for growth, comprehensive reviews can be found in Dirksen and Ring [36] and Lasaga [88]. For this study, all four polymorphs primarily utilize a diffusion-limited growth model, which is justified by the very large values for

Table 4.3: Molecular volumes.

Polymorph	Molar Volume (m^3/mol)
ACC	5.2677e-5
Calcite	3.693e-5
Aragonite	3.4159e-5
Vaterite	3.7627e-5

Table 4.4: Surface energy values for calcium carbonate polymorphs.

Polymorph	Theoretical Value (J/m^2)	Tuned Value (J/m^2)
ACC	–	0.056025
Calcite	0.16	0.176156
Aragonite	0.24	0.184666
Vaterite	0.22	0.147628

the supersaturation ratio in the system [73]. The diffusion-limited growth model has $1/r$ dependence, which, when integrated in the PBE requires closure of the -1^{st} and -2^{nd} moment. ACC, vaterite, and calcite are all assumed to be spherical such that the growth rate is given by

$$G(r) = \nu D C_{eq} * (S - \bar{S})/r. \tag{4.16}$$

Here, ν is the molar volume, D is the diffusion coefficient, S is the supersaturation ratio of the given polymorph, C_{eq} is the equilibrium concentration, and $\bar{S}$ is the Ostwald ripening term. For aragonite, a cylindrical diffusion model is assumed, which uses the same formula, except with an area to volume adjustment factor

$$G(r) = \frac{7}{6\ln(1/2)} * \nu D C_{eq}(\bar{S} - S)/r. \tag{4.17}$$

Ostwald ripening accounts for smaller particles dissolving faster than large ones. The Ostwald ripening term is derived from the Kelvin equation as [36, 119]

$$\bar{S} = \exp(2\sigma_T \nu / RTr). \tag{4.18}$$

Here, σ_T is the surface energy of the polymorph modified by the Tolman length scale [175], ν is the molar volume, R is the gas constant and T is the temperature. In the moment transport equations $\bar{S}$ requires closure in the growth model. The quadrature approximation is used such that

$$\bar{S} \approx \sum_{i}^{N} w_i \exp\left(\frac{2\sigma_T \nu}{RT r_i}\right). \tag{4.19}$$

However, if r_i is below a small cutoff value, then the value of the exponential is set to 1. At low supersaturation values, the growth mechanism switches from bulk diffusion to a kinetic dissolution mechanism. This model is responsible for the shrinking of particles to dissolve back into the solution to allow for more stable polymorphs to be prevalent in the long term [85]. This switch occurs when $S < \bar{S}$, where the growth is given by

$$G(r) = -k_s(S - \bar{S})^2. \tag{4.20}$$

Here, k_s is an empirical reaction rate constant for which values can be found in the literature for each of the various polymorphs [84, 83, 155]. This model has been shown to work for calcium carbonate polymorphs in the pH range used in this study at low supersaturation values [83]. Further details on the growth model used can be found in Schroeder et al. [165]. Other specific details exist in the literature for the growth rates of calcite [24], vaterite [4, 3], and other features such as spherical growth assumptions [12], and other morphological effects of the polymorphs in precipitation [3, 120].

4.1.4 Surface Energy

As the surface energy appears in the equations for critical radius and birth, as well as in the Gibbs free energy equation, raised to the power of 3, it is one of the most important parameters in the source terms of the PBEs. As a starting point, theoretical values could be used as calculated from molecular dynamics simulations [30]. However, there are two problems with this. The first is that data do not exist for ACC. The second is that the theoretical values are only calculated for the solid phases existing by themselves. The molecular dynamics do not account for the surface energy when the polymorphs are in an aqueous environment, and they do not account for the aqueous ions that would be present during precipitation. In Schroeder et al. [165], the surface energy parameters were tuned for all four polymorphs to adjust the model results to match experimental data across a range of temperatures. Since this study was able to match the experimental results quite well, the tuned surface energy values are used here. The tuned parameters here are taken to larger accuracy than molecular dynamics estimates because the birth rates are highly sensitive to these values. The values used are listed in Table 4.4 along with the theoretical values for reference.

With these values of the surface energy, the particles which nucleate are only a few nanometers in size. To account for the nanoscale precipitate particles, a correction of the surface energy is used [175]. The modified surface energy is given as

$$\sigma_T = \sigma_{\text{bulk}} * (1.0 - \delta_T/r). \tag{4.21}$$

Here, δ_T is the Tolman length, which is approximated by $0.2r_1$, where r_1 is the radius of one molecule. In the limit of large particles, the surface tension approaches the bulk value and $\bar{S}$ approaches 1.0. This equation can be used directly for the surface energy used in the Ostwald ripening formula in Eq. (4.18). For the critical radius of nucleation a short

derivation can be made to calculate the surface energy and the critical radius together. First, substitute the critical radius equation into Eq. (4.21)

$$\sigma_T = \sigma_{\text{bulk}} \left(1.0 - \frac{2\delta_T}{\frac{2\sigma_T \nu}{RT\ln(S)}} \right), \tag{4.22}$$

this can be rearranged and multiplied by σ_T to be put into quadratic form as

$$\sigma_T^2 - \sigma_{\text{bulk}}\sigma_T + \frac{\sigma_{\text{bulk}} RT \ln(S)\delta_T}{\nu} = 0. \tag{4.23}$$

This equation is then easily solvable with the quadratic formula to get the surface energy as

$$\sigma_T = \frac{\sigma_{\text{bulk}} \pm \sqrt{\sigma_{\text{bulk}}^2 - 4RT\ln(S)\delta_T/\nu}}{2}. \tag{4.24}$$

The negative root of the solution results in nonphysical surface energies, so only the positive root is used. This surface energy result can then be directly used in the Eq. (4.8) for the critical radius of nucleation as

$$r_c = \frac{\nu}{RT\ln(S)} \left(\sigma_{\text{bulk}} + \sqrt{\sigma_{\text{bulk}}^2 - 4RT\ln(S)\delta_T/\nu} \right). \tag{4.25}$$

4.1.5 Aggregation

To calculate the integrals resulting from the aggregation term, a quadrature approximation must be utilized. The aggregation kernel in its continuous form can be written as

$$A(r) = \frac{1}{2}\int_0^r \beta(r-\epsilon,\epsilon)\eta(r-\epsilon)\eta(\epsilon)\mathrm{d}\epsilon - \eta(r)\int_0^\infty \beta(r,\epsilon)\eta(\epsilon)\mathrm{d}\epsilon\,. \tag{4.26}$$

This kernel describes the frequency that particles with volume r and ϵ collide to form a new particle of size $r+\epsilon$, two terms are included for the death of the smaller colliding particles and the birth of the larger particle. The closure using QMOM is derived by Marchisio et al. [105] to be

$$A \approx 1/2 \sum_i^N w_i \sum_j^N w_j (r_i^3 + r_j^3)^{k/3} \beta_{ij}\psi_{i,j} - \sum_i^N r_i^k w_i \sum_j^N \beta_{ij}\psi_{i,j} w_j. \tag{4.27}$$

Here, β_{ij} is a frequency kernel and $\psi_{i,j}$ is a size dependent collision efficiency, k is dependent on the moment order. For Brownian aggregation, the frequency kernel can be expressed as

$$\beta_{ij,\text{Brownian}} = \frac{2K_b T}{3\rho}\frac{(r_i + r_j)^2}{r_i r_j}, \tag{4.28}$$

while for turbulent aggregation the kernel is given by

$$\beta_{ij,\text{Turbulent}} = \frac{4}{3}\left(\frac{3\pi\epsilon}{10\nu_{\text{fluid}}}\right)^{1/2}(r_i + r_j)^3. \tag{4.29}$$

Here, ν_{fluid} is the kinematic viscosity of the fluid and ϵ is the dissipation rate. The aggregation collision efficiency, $\psi_{i,j}$, is based on the size of the particles and on the current growth rate of the particles [90]

$$\psi_{i,j} = \frac{m_1}{1+m_1}, \tag{4.30}$$

where

$$m_1 = \begin{cases} G(r_i) \geq G(r_j) & \frac{LG(r_i)}{\rho\epsilon d^2} \\ \text{else} & \frac{LG(r_j)}{\rho\epsilon d^2} \end{cases}. \tag{4.31}$$

Here, d is the average particle diameter, $d = r_i + r_j$ and L is a length parameter. The G here is the growth rate of each of the colliding particles. Higher growth rates promote the aggregation of particles as the continued addition of molecules helps to bridge the particles together better.

4.1.6 Death

The dissolution death term is only calculated if the radius of the particles drops below a small r_{cutoff} value and the supersaturation value is lower than the Ostwald ripening term, $\bar{S}$. The death by dissolution term is calculated by

$$\text{Death}_i = \frac{-30kw_i}{\Delta t}, \tag{4.32}$$

with

$$k = 0.25(1 - \text{erf}(8 * (log(r_i/r_{\text{cutoff}}))) * (1 - \text{erf}(5 * \log(10^{-2.5}/w_i))) \,, \tag{4.33}$$

and requirements

$$\bar{S} > S \tag{4.34}$$

$$w_i > 1e-3 \text{ (arbitrary)} \tag{4.35}$$

$$r_i > 0 \tag{4.36}$$

$$r_i < 2r_{\text{cutoff}}. \tag{4.37}$$

If the requirements are not satisfied, then the death rate is simply set equal to zero. Dissolution causes numerical issues in QMOM closure problems, as some sets of moment values can cause an abscissa to be calculated as negative in the product difference algorithm. While the death term is not significant for the short timescales of the simulations presented, implementing it helps to maintain the numerical stability of the solution. This is a numerically empirical equation which selects a left boundary of the PSD and applies the death rate only to that section of the PSD. This type of method is mentioned in Yuan et al. [196], but the equation used here was internally developed.

4.1.7 Viscosity of Dispersions

In a particle laden flow, it is expected that the particle interaction would affect the flow of the system. In a near wall velocity profile, if a particle is assumed to be not rotating, then the velocity on opposite sides of the particle must be the same. The velocity gradient of the fluid across the particle is then reduced, and this reduced gradient can be modeled by an increase in the fluid viscosity [61]. Using a truncation of a Taylor's series expansion of the forces on the particle leads to a result known as Einstein's equation of viscosity of dispersions given by [61]

$$\mu = \mu_0(1 + 2.5\phi), \tag{4.38}$$

where μ_0 is the base viscosity of the fluid, and ϕ is the volume fraction of the particles in the dispersion. A similar force balance approach can be used to derive a modified form [166]

$$\mu = \mu_0(1 + 2.5\lambda\phi), \tag{4.39}$$

where λ empirically accounts for particle-particle interactions. In Schlomach et al. [163], it is shown that for high supersaturation ratios of calcium carbonate precipitation the relative viscosity of the dispersion is shown to increase with an increase in the volume fraction, along with a shear thinning effect. With a preliminary order of magnitude analysis, then the volume fraction of solids in solution can be calculated and an estimate of this effect can be made. In the short-time periods that will occur in LES, there will not be a significant amount of growth as in long-term models. If the study of Schroeder et al. [165] is used as a basis, then a rough estimate could be used with a number density of 1×10^{18} $\#/\mathrm{m}^3$ and a particle size of 100 nm. Then the volume fraction of particles per cubic meter can be calculated as

$$\phi \approx 1 \times 10^{18} \#/\mathrm{m}^3 * (100\mathrm{nm})^3 * (1 \times 10^{-9}\mathrm{m/nm})^3 * 4/3\pi = 0.0042\ . \tag{4.40}$$

If this value for the volume fraction of particles is used in Eq. (4.38), then the increase in the molecular viscosity of the system is only 1 %. This change is minor enough, especially when compared to the modeled turbulent viscosity in the LES flow, μ_t, that the change in molecular viscosity due to particle laden flow can be neglected.

4.1.8 Stokes Number

The formulation of the moment transport equations with one internal coordinate assumes that the particle velocity is equal to the velocity of the fluid phase. The validity of this

assumption is based on the particle size timescale relative to the timescale of the fluid flow. The Stokes number of the particles gives a relation for these timescales as

$$St = \frac{\tau_p U_0}{d_c} , \tag{4.41}$$

where τ_p is the relaxation time of the particle – essentially how fast the particle reacts to fluid flow around it – U_0 is the fluid velocity of the flow, and d_c is the characteristic dimension. The particle relaxation time is given by

$$\tau_p = \frac{\rho_p d_p^2}{18\mu_f} , \tag{4.42}$$

where ρ_p is the particle density, d_p is the particle diameter and μ_f is the fluid viscosity. For a rough calculation of the relaxation time assume the same parameters from the viscosity assumption in Subsection 4.1.7 with the radius of the particle equal to 100 nm, then $d_p = 200$ nm, and for the calcite polymorph, $\rho_p = 2711 kg/m^3$, and for water at room temperature the viscosity is $\mu_f = 8.9 \times 10^{-4} Pa \cdot s$. The value of the relaxation time is given by

$$\tau = \frac{2711 kg/m^3 * 200 \times 10^{-9} m}{18 * 8.9 \times 10^{-4} Pa \cdot s} = 1.69226 \times 10^{-4} s . \tag{4.43}$$

Now for the Stokes number evaluation assume the highest values used here, with $U_0 = 12$ m/s and $d_c = 0.0254$ m – these value are the highest that show up in the LES simulations that are discussed later. Then the Stokes number is equal to

$$St = \frac{1.69226 \times 10^{-4} s 12 m/s}{0.0254 m} = 0.07995 , \tag{4.44}$$

as this number meets the criteria for $St << 1$, the assumption that the precipitate particles follow the same streamlines of the fluid is valid.

4.1.9 Scalar Equations

There are two scalar equations that describe the evolution of the aqueous phase, the mixture fraction and the extent of reaction. The mixture fraction of the two streams defines the amount of mixing that has occurred on the macroscale. A mixture fraction of 1.0 refers to the stream of aqueous calcium chloride, while a mixture fraction of 0.0 refers to the stream of sodium carbonate. The extent of reaction defines how much of the solid phase has precipitated out of solution. It is scaled from 0.0 to 1.0, where 0.0 represents no solid precipitate, and 1.0 represents no ions left in solution to precipitate. The extent of reaction scalar has a source term to track this amount as

$$\eta_{\text{source}} = \omega_2 \frac{1}{\iota} \sum_{\alpha}^{M} \nu_\alpha \frac{4\pi}{3} \frac{dm_3}{dt}_{\text{source}} \tag{4.45}$$

where M is the number of polymorphs, and ι is a scaling constant to account for the maximum amount of solid precipitation. This adds up the rate change of the third moments of each of the polymorphs. By modifying these rates the volume is converted to a change in the moles of the system that are precipitated.

The following equation is used to calculate the diffusion rate of the aqueous ions in solution [72]

$$D = (T - 273) * 2.45 \times 10^{-11} + 4.94 \times 10^{-11} \ , \tag{4.46}$$

which at a room temperature of T = 25 ° C gives $D = 6.619 \times 10^{-10}$ m^2/s.

4.1.10 Subgrid Mixing

The subgrid mixing model that is used here relies on the calculation of the scalar variance. The scalar variance is a representation of how well the fluid streams are mixed on the subgrid scale of the LES. Given a mixture fraction in a cell, and the second moment of the mixture fraction, the scalar variance can be modeled as

$$\left\langle Z'^2 \right\rangle = \left\langle Z^2 \right\rangle - \left\langle Z \right\rangle^2 \ , \tag{4.47}$$

for a normalized value of the scalar variance – which is used in tabulation, not in precipitation – the maximum variance given the mixture fraction is then

$$\left\langle Z'^2 \right\rangle_{\text{max}} = \left\langle Z \right\rangle - \left\langle Z \right\rangle^2 \ . \tag{4.48}$$

The minimum value scalar variance value is 0. This leads to a minimum second moment value of

$$\left\langle Z^2 \right\rangle_{\text{min}} = \left\langle Z \right\rangle^2 \ , \tag{4.49}$$

and the maximum value of second moment is given by setting maximum variance to the actual variance, then

$$\left\langle Z^2 \right\rangle_{\text{max}} = \left\langle Z \right\rangle \ . \tag{4.50}$$

For the subgrid mixing model, it is assumed that three distinct environments exist in each cell. These environments each contain a different value of the mixture fraction between the two aqueous streams. There are three unknown weights for these environments, and three unknown mixture fractions. One could transport six moments of the mixture fraction to accomplish this, but each transport equation would need its own source terms to be

derived. An alternative that exists in the literature is transporting weights and abscissas of these distinct environments in a direct quadrature method of moments with interaction by exchange with the mean (DQMOM-IEM) approach [187]. A much simpler approach is used here by fixing a few parameters. The mixture fraction for each of the environments is fixed, so that environment 1 is set at mixture fraction of 0, environment 2 is set to the average mixture fraction $\langle Z \rangle$, and environment 3 is set to a mixture fraction of 1.

Three other constraints are then needed to solve the three unknown weights. The first is simply that the weights need to add to 1. The second is that the average of the three environments needs to equal the average mixture fraction. The last constraint is to have the environments match the given mixture fraction variance for the cell. In essence, the constraints are just the first three moments of the mixture fraction. These constraints in mathematical terms are

$$\omega_1 + \omega_2 + \omega_3 = 1 \tag{4.51}$$

$$\omega_1 * 0 + \omega_2 * \langle Z \rangle + \omega_3 * 1 = \langle Z \rangle \tag{4.52}$$

$$\omega_1 * 0^2 + \omega_2 * \langle Z \rangle^2 + \omega_3 * 1^2 = \left\langle Z'^2 \right\rangle \ , \tag{4.53}$$

which simplifies to

$$\omega_1 + \omega_2 + \omega_3 = 1 \tag{4.54}$$

$$\omega_2 * \langle Z \rangle + \omega_3 = \langle Z \rangle \tag{4.55}$$

$$\omega_2 * \langle Z \rangle^2 + \omega_3 = \left\langle Z'^2 \right\rangle \ . \tag{4.56}$$

These algebraic equations can then be used to calculate the weights of each of the environments. On the subgrid scale, these three distinct environments are: pure stream 1 of aqueous calcium chloride, pure stream 2 of aqueous sodium carbonate, and a mixed portion where the precipitation of calcium carbonate occurs. No reactions or precipitation occur in the pure stream environments. The mixture fraction and the scalar variance are calculated at each grid point. With the constraints of the three delta functions, analytical solutions are found for the weights of each of the three environments on the subgrid scale as

$$\omega_1 = \frac{\left\langle Z'^2 \right\rangle}{\langle Z \rangle} \ , \tag{4.57}$$

$$\omega_2 = \frac{\left\langle Z'^2 \right\rangle - \langle Z \rangle + \langle Z \rangle^2}{\langle Z \rangle^2 - \langle Z \rangle} \ , \tag{4.58}$$

$$\omega_3 = \frac{-\left\langle Z'^2 \right\rangle}{\langle Z \rangle - 1}. \tag{4.59}$$

The PBEs are only solved in the middle environment, ω_2. The moments in environments 1 and 3 are initialized to the same value as the rest of the domain with the values in Table 4.1 and are held constant throughout the simulation. The source term that appears in the PBE due to mixing environments 1 and 3 into the center is

$$\Xi_{\text{mix}} \equiv \int_0^\infty \xi_{\text{mix}} r^k dr, \tag{4.60}$$

$$\Xi_{\phi_{k,2},mix} = -\frac{\mathrm{d}\omega_1/\mathrm{d}t}{\omega_2}(\phi_{k,1} - \phi_{k,2}) - \frac{\mathrm{d}\omega_3/\mathrm{d}t}{\omega_2}(\phi_{k,3} - \phi_{k,2}). \tag{4.61}$$

Here $\phi_{k,i}$ represents the k^{th} moment for the i^{th} environment, so $\phi_{k,2}$ is the main solution variable, while $\phi_{k,1}$ and $\phi_{k,3}$ remain constant at the initialized value. The time derivative terms in Eq. (4.61) are given by

$$\frac{\mathrm{d}\omega_1}{\mathrm{d}t} = \frac{-\langle \chi_Z \rangle}{\langle Z \rangle}, \tag{4.62}$$

$$\frac{\mathrm{d}\omega_3}{\mathrm{d}t} = \frac{-\langle \chi_Z \rangle}{1 - \langle Z \rangle}. \tag{4.63}$$

Here χ_Z is the scalar dissipation rate. Figure 4.2 shows the graphical subgrid illustration and the corresponding probability density functions as discrete delta functions for an average mixture fraction of 0.5 with the scalar variance normalized by the maximum.

In order to calculate the scalar variance that is need for the calculations of the weights and the time derivatives of the weights, the second moment of the mixture fraction is required. To calculate the second moment of the mixture fraction, a transport equation is used given by

$$\frac{\mathrm{D}}{\mathrm{D}t}\left(\bar{\rho}\widetilde{Z^2}\right) = \frac{\partial}{\partial x_j}\left(\bar{\rho}(D_Z + D_t)\frac{\partial \widetilde{Z^2}}{\partial x_j}\right) - \bar{\rho}\chi_Z. \tag{4.64}$$

Here, D_Z and D_t are the molecular and turbulent diffusion coefficients, respectively. This equation requires the closure of the scalar dissipation rate, χ_Z, for the source term. This is implemented as an approximation based on the mixture fraction gradient [179]

$$\chi_Z \approx 2(D_Z + D_t)\frac{\partial Z}{\partial x_i}\frac{\partial Z}{\partial x_i}. \tag{4.65}$$

The model presented here is much more simple than the DQMOM-IEM approach [187]. Subsequently, it is much more computationally inexpensive. The methodology for solving the population balance shown here involves solving 24 scalar moment equations in total. This takes up more than 50 % of the total computational time. Incorporating the DQMOM-IEM approach with 2 environments would effectively double the computational cost for the moment transport equations. In addition, this simple model is shown to work well in a prior precipitation study [165].

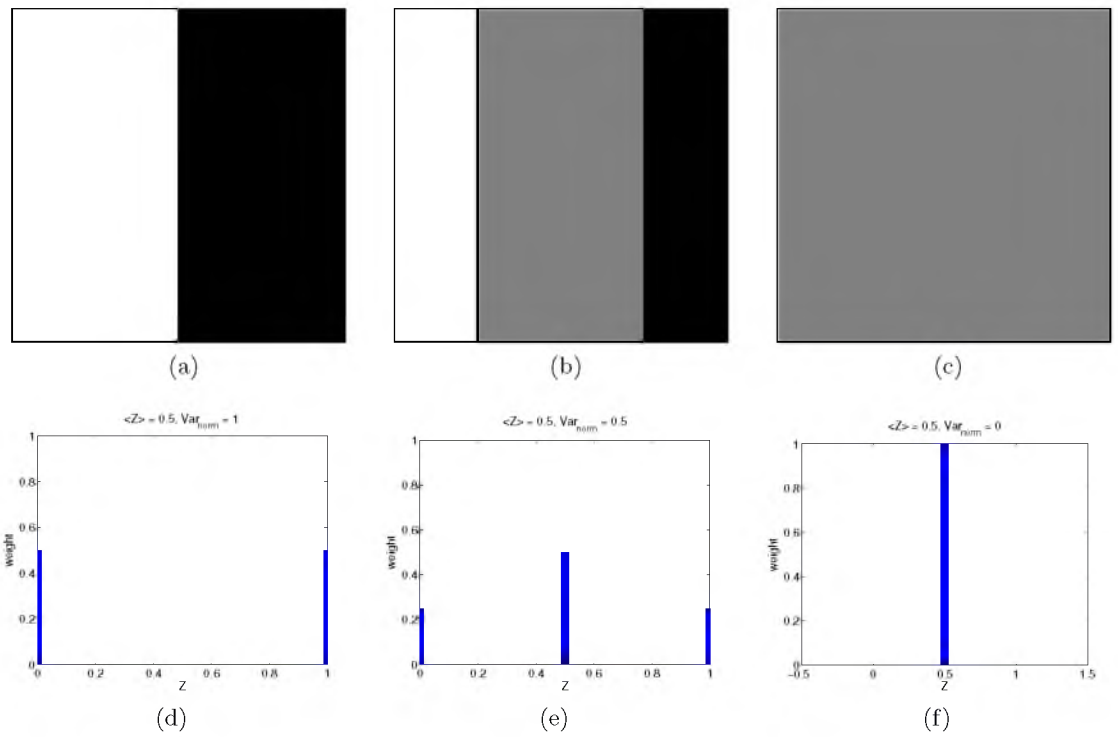

Figure 4.2: Illustration of the subgrid mixing model. Here (a-c) show the finite volume cell representation for a mixture fraction of 0.5, with varying scalar variance from 1 (unmixed) to 0 (fully mixed). The PDFs for each of these representations in shown in (d-f).

4.2 LES Configuration

The simulations carried out with the precipitation had a few main configurations. The first set of simulations was set up with a temporal jet. The flow setup used in this study is a turbulent mixing layer with periodic boundary conditions in all directions. The simulation's physical domain is 4 cm by 2 cm by 2 cm, with 8 million CFD grid points. The central jet is 1 cm wide. This central jet is initialized to a mixture fraction of 1, with a velocity of U_0, and the outer jet initialized to a mixture fraction of 0, and a velocity of $-U_0$. This setup was run at three different Reynolds numbers, 16,000, 64,000 and 128,000; this corresponds to U_0 values of 0.75 m/s, 3.0 m/s and 6.0 m/s. The goal was to try to change the selectivity of the polymorphs based on how quickly the two streams are mixed together. A slice of the initialized domain is shown in Figure 4.3.

By changing the Reynolds number so drastically, it may be possible to range from regions of the domain that are perfectly mixed down to a region that is so slowly mixed that the nucleation rates of the polymorphs are severely affected. Two of the most important polymorphs in the study are the ACC, which will form only early on in the reaction, and the calcite, which is the most stable polymorph in the long term. In Figure 4.4, the nucleation

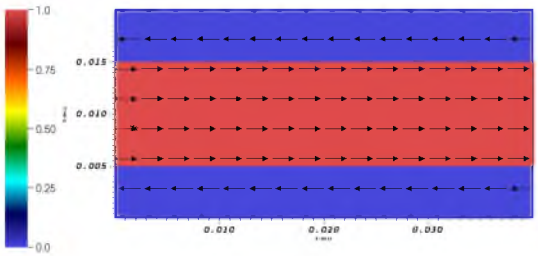

Figure 4.3: A two-dimensional slice of the intialized domain for the temporal jet configuration. The central jet is intialized with a velocity U_0 and mixture fraction of 1, while the outer jet has a velocity of $-U_0$ and mixture fraction 0.

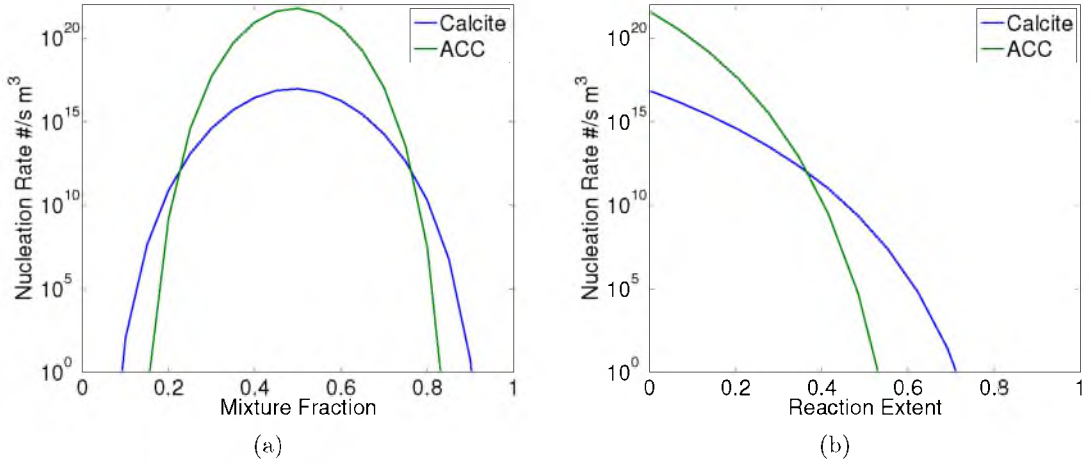

Figure 4.4: The nucleation rates for ACC and calcite plotted over the mixture fraction (a) and the extent of reaction (b).

of these two polymorphs is plotted as both a function of the mixture fraction and for the extent of reaction. The first plot shows that for the mixture fraction, ACC has a faster nucleation rate than calcite between 0.2 and 0.8, the second plot shows that for the extent of reaction ACC has a faster nucleation rate than calcite from 0 to 0.4. If the streams are mixed slow enough so that the mixture fraction remains on the fringes, it is possible enough calcite could be nucleated out of the system so that the extent of reaction is lowered before significant mixing occurs, and thus ACC would be less abundant than in a perfectly mixed system.

The other set of simulations for comparison of the precipitation model was for two different pilot scale reactors. The inlet mass flow rates to both of the reactors was set to 0.4985 kg/s at each inlet (0.9970 kg/s total flow rate) with an inlet Reynolds number of approximately 27,000. One reactor features two pipes mixing together in a coflow type configuration, then flowing over a static mixer; the geometry was adapted from details

provided by the Calera Corporation [18], which was a collaborative partner in the aqueous precipitation research. The second reactor is an impinging jet reactor with two streams in counter flow entering the reactor to create a mixing plane in the center. This reactor was adapted from Liu and Fox [96], but was scaled up significantly from the microscale reactor up to a pilot scale to match the flow rate of the first reactor. In the Liu and Fox paper, the inlets are on the order of millimeters, here the inlets are a couple centimeters across.

The geometry for the mixing pipes is shown in Figure 4.5. The second section of the pipes contains a static mixer to ensure that the incoming streams are fully mixed before the outlet is reached. Each of the inlet pipes has a diameter of $d = 0.235$ meters. The length from the inlet to the elbow is $6.4d$, from the elbow to the outlet is $11.8d$, with $9.4d$ as length of the static mixer. The pipe with the static mixer is about $1.1d$. The second inlet is rotated 45 degrees from the main alignment of the pipes. The domain consists of 1604 processors and 22 million cells.

The geometry for the impinging jet reactor is shown in Figure 4.6. As with the mixing pipes, the inlet pipe here has a diameter of $d = 0.235$ meters. The nondimensional sizing parameters used here are identical to one of the cases used in the Liu and Fox study [96], although here the size of the reactor is scaled up significantly. The diameter of the main mixing chamber is $D = 4.76d$ with a height of $2D$ and an outlet pipe of width $0.5D$. The domain here consists of 1136 processors and 15.7 million cells. It should be noted that this layout uses much fewer cells, the discrepancy here between the number of processors used is due to the notable dead space of wall cells in the mixing pipes near the angled pipe inlet.

The simulations with the pilot scale reactors use the digital filter generator inlet con-

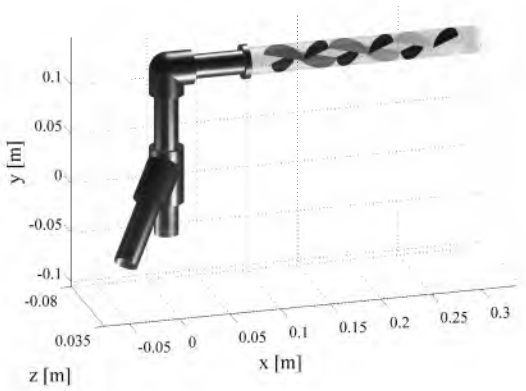

Figure 4.5: A three-dimensional representation of the geometry used for the mixing pipes reactor. The lower left pipes are the inlets, while the upper right pipe is the outlet. The area near the outlet pipe is where the static mixer is located.

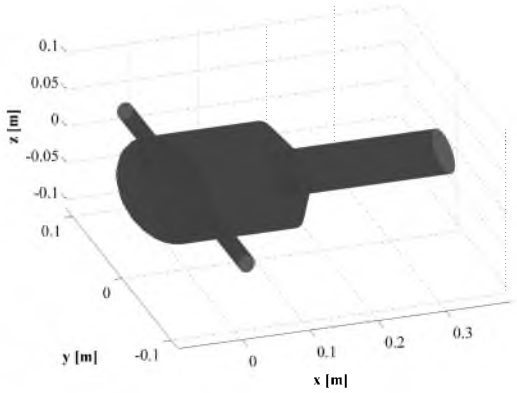

Figure 4.6: A three-dimensional representation of the geometry for the impinging jet reactor. The two smaller pipes are the inlets and the large pipe leading out of the tapered section is the outlet.

dition that was discussed in Chapter 3. This was because the short inlet sections of the pipe that occur before mixing begins do not allow for the proper development of turbulent flow prior to mixing of the streams. By using the turbulent inlet condition at the inlets, the flow can be more properly characterized, as the actual pilot reactors have long sections where turbulent flow would be developed. The length scale at the inlet was assumed to be $L = 1/4D$. As no experimental data exist for the reactor cases, the simple assumption of isotropic turbulence with $\langle u'u' \rangle = \langle v'v' \rangle = \langle w'w' \rangle = 0.02 * U_0^2$ was used. A slice of the inlet domain for the mixing pipes is shown in Figure 4.7. This figure highlights the turbulent structures of the flow field at the inlet plane, the figure is rescaled for each of the inlet velocities.

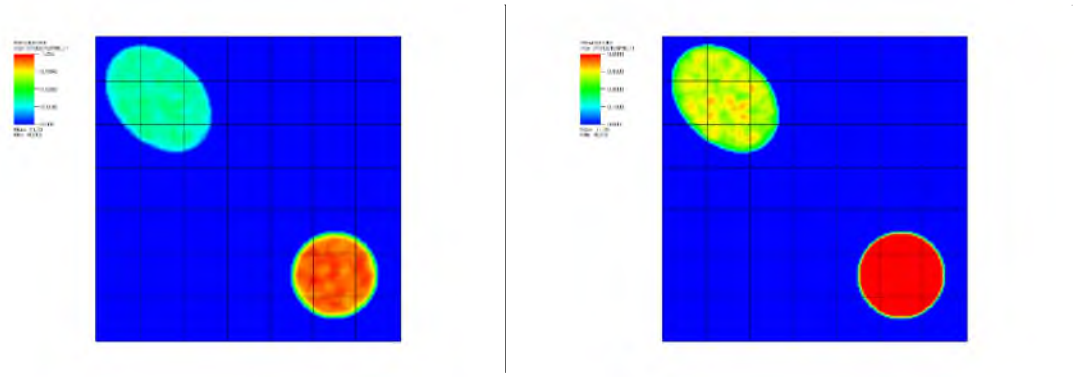

(a) (b)

Figure 4.7: The velocity for the mixing pipes reactor at the inlet plane. The data are rescaled to highlight the turbulent structures in the (a) vertical pipe and the (b) diagonal pipe.

4.3 Results and Discussion

The results of this will focus on the two sets of data. The first set is the hypothetical example of a periodic temporal jet. The goal of this section is to show how the resulting PSDs can be affected through changing the mixing rates of the system. The first part examines how the PSD is affected as mixing rates are increased by directly increasing the Reynolds number. The second part discusses the example of a pilot scale reactor for the system. This part will show how changing the mixing rate by altering the geometry of the system will affect the resulting PSDs.

4.3.1 Temporal Jet

This section discusses the results from the idealized temporal jet geometry. The temporal jet simulations are run for 48 hours of computational time to ensure the well-mixed state is achieved. As the temporal jet is initialized with no fluctuations it takes time for the velocity decay to occur. Eddys are formed slowly in the shear layer between the two jets, and these eddys grow to mix the jets together over the whole domain. After most of the domain is mixed together, the energy dissipates and the turbulent structures shrink in size again. The time evolution of the mixture fraction in a slice of the domain is shown in Figure 4.8, which illustrates this mixing effect. The smaller eddys are first formed in the shear layer of Figure 4.8(a), these smaller eddys continue to grow in Figure 4.8(b) and (c). Eventually, the length scale of the turbulent motion encompasses most of the domain and large scale macromixing occurs in Figure 4.8(d) through (f).

The data for the temporal jet that are examined are along the centerline of the domain. The data are spatially averaged for each time-step of the LES. In Figure 4.9, the velocity decay and the velocity fluctuations along the center of the domain are shown for all three cases. The cases are periodic with no force on the velocity, so the velocities all decay to 0 eventually, as the kinetic energy of the system is dissipated. As the Reynolds number is increased, the eddys that are shown in Figure 4.8 form more rapidly, which causes the velocity profile to start its decay quicker when disturbed. The graph in Figure 4.9 is logarithmically scaled in time on the x axis, so the decay rates between the cases vary widely. The middle Reynolds number case takes about two times as long to start to decay, and the low Reynolds number case takes nearly ten times longer when compared to the highest Reynolds number case. The velocity fluctuations start at zero and rapidly increase as the first eddys are advected into the centerline of the domain. As the kinetic energy of the system is dissipated these fluctuations decay away faster than they appear. The higher Reynolds number cases result in much higher maximum values in the velocity fluctuations.

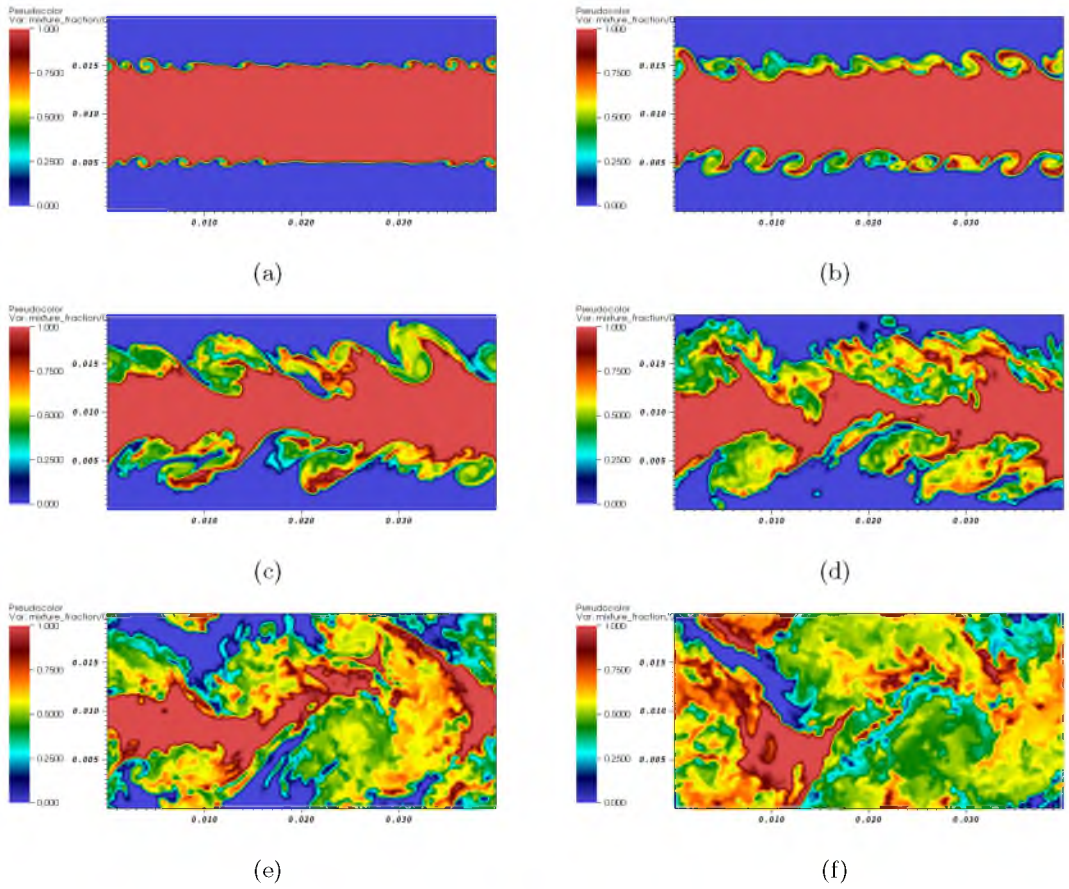

Figure 4.8: A slice of the domain that illustrates the mixing of the temporal jet domain. The time progress as (a) $t = 0.0125$s, (b) $t = 0.015$s, (c) $t = 0.02$s, (d) $t = 0.025$s, (e) $t = 0.03$s and (f) $t = 0.035$s. This is for the $U_0 = 6.0$ m/s case.

The peak in the velocity fluctuations occurs when the largest eddys of the system are still present, and correspond to the same time as the rapid drop in the centerline velocity. These velocity fluctuations also decay much more quickly in the larger Reynolds number cases. The larger eddys which form in the highest Reynolds number case cause the kinetic energy to decay from the system more rapidly.

In Figure 4.10, the mixture fraction and the fluctuations in the mixture fraction are shown along the domain centerline. As the domain is initialized to half at a mixture fraction of 0, and half at a mixture fraction of 1, the final state of the system is a mixture fraction of 0.5. These results start at the mixture fraction state 1.0 corresponding to pure aqueous calcium chloride. Similar to the velocity profiles, the mixture fraction profiles decay to the final rate quicker at the higher Reynolds numbers. Again, this is due to the eddys convecting the outer jet into the centerline, which occurs over a more rapid time period for higher Reynolds numbers. In the fluctuation profiles, an opposite trend is seen in the

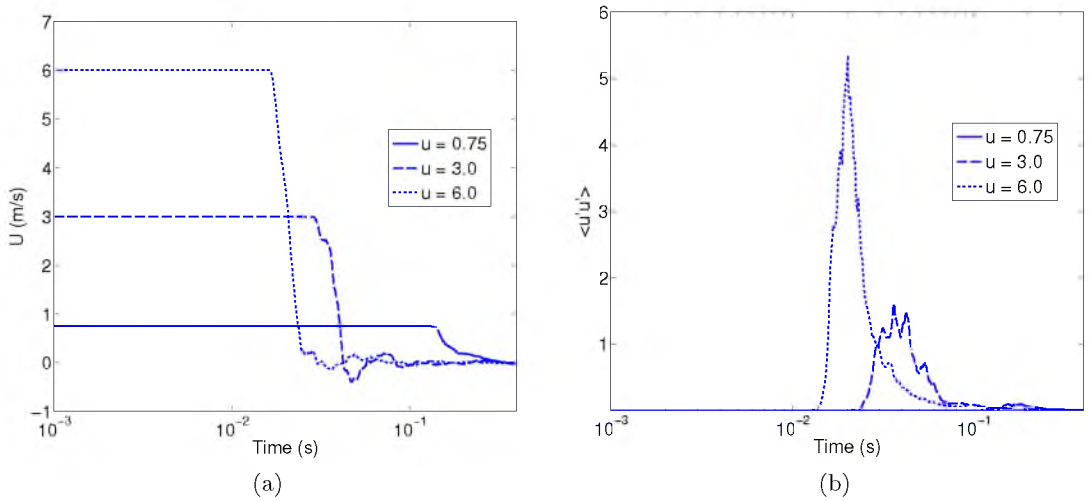

Figure 4.9: An averaged centerline of the velocity profile as it decays over time (a) and the velocity fluctuation profile (b) on the domain centerline. The x axis is on a logarithmic scale for the time.

magnitudes as compared to the velocity profiles. Increasing the Reynolds number shows a decrease in the variance of the mixture fraction. This is an intuitive result, as one would expect higher flow rates to mix more efficiently. The lowest Reynolds number also takes a long time for the mixture fraction variance to decay, nearly ten times larger than the high Reynolds number case. This large spike in the mixture fraction that occurs over the long period of time means that the low Reynolds number case remains the least well-mixed during the early mixing period when nucleation is important. The mixture fraction is one of the main scalars that determines the supersaturation ratio of the system, the faster mixing will directly lead to higher supersaturation ratios during the early nucleation period.

The vorticity of the same slice of the domain is shown in Figure 4.11. This shows the vorticity as the eddys form in the initial stages Figure 4.11(a), as well as the formation of vortex pairings seen in (b) and (c). These smaller turbulent formations combine and grow into the large scale structures seen in the later stages of the macromixing in (d) through (f). As the kinetic energy of the system dissipates the larger turbulent structures break down into smaller and smaller scale structures, shown in (g) and (h). At these later times the system is nearly well mixed in terms of the scalar mixture fraction. The small scale structures are residual and have little effect on the simulation as this point.

The zeroth moment – number density – results for all four of the polymorphs are shown in Figure 4.12. For all four of the polymorphs, increasing the Reynolds number of the system resulted in an increase in the number density of the nucleated particles. The faster mixing rates at higher Reynolds number lead to a higher supersaturation ratio in the shear layer,

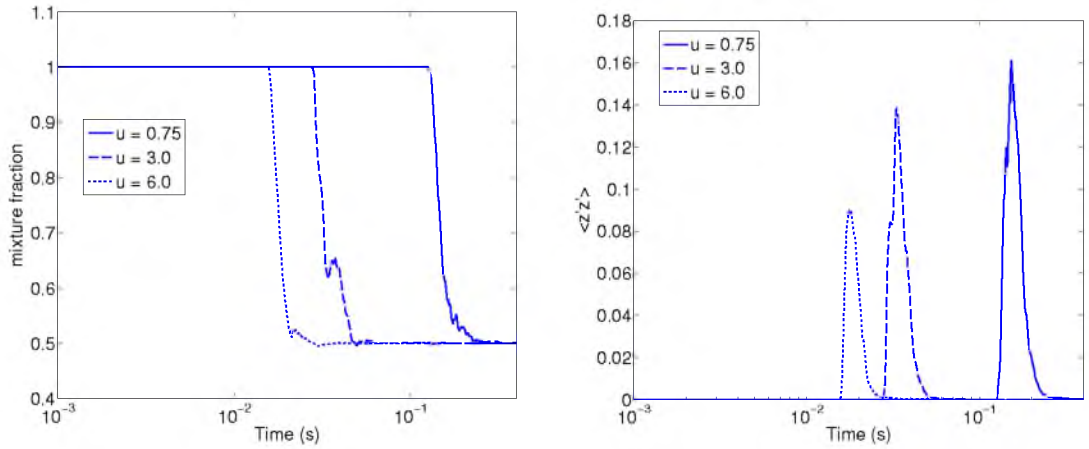

(a) (b)

Figure 4.10: An averaged centerline of the mixture profile as it decays over time (a) and the variance of the mixture fraction profile (b) along the domain centerline. The x axis is on a logarithmic scale for the time.

and therefore higher nucleation rates. This occurs due to the supersaturation dependence of Eq. (4.11). A higher supersaturation ratio leads to a lower stable Gibbs free energy of the nucleate particle. In turn, the lower Gibbs free energy leads to a higher nucleation rate in Eq. (4.10). The highest number density is for the ACC solid phase, which is expected from very low surface energy of this phase. Calcite and vaterite both had a fairly close number density, with vaterite being slightly higher, again from a lower surface energy at this temperature. Aragonite had the lowest number density, which is expected from its second lowest supersaturation ratio, and the highest surface energy, which impedes the nucleation. The range of Reynolds numbers used here was not significant enough to alter the polymorph selectivity for this aqueous concentration. The nucleation rate for ACC at this concentration is too high to overcome through the given mixing parameters. After the initial nucleation occurs the number density stops growing as the supersaturation ratio quickly drops to low levels.

The first moment for each of the polymorphs is shown in Figure 4.13. These moments are representative of the size of the particles in the system as they grow. The results for ACC show that this polymorph reaches a plateau in the first moment rather quickly. This plateau is arrived at as the supersaturation ratio of ACC quickly approaches 1.0 and growth is stopped. The vaterite and calcite plots here show a continued increase in the system as they grow. Aragonite also continues to grow at this state, but appears to do so much more slowly, as it has a low supersaturation ratio when compared to vaterite and calcite.

Using these two low order moments, the average radii for each of the polymorphs can be

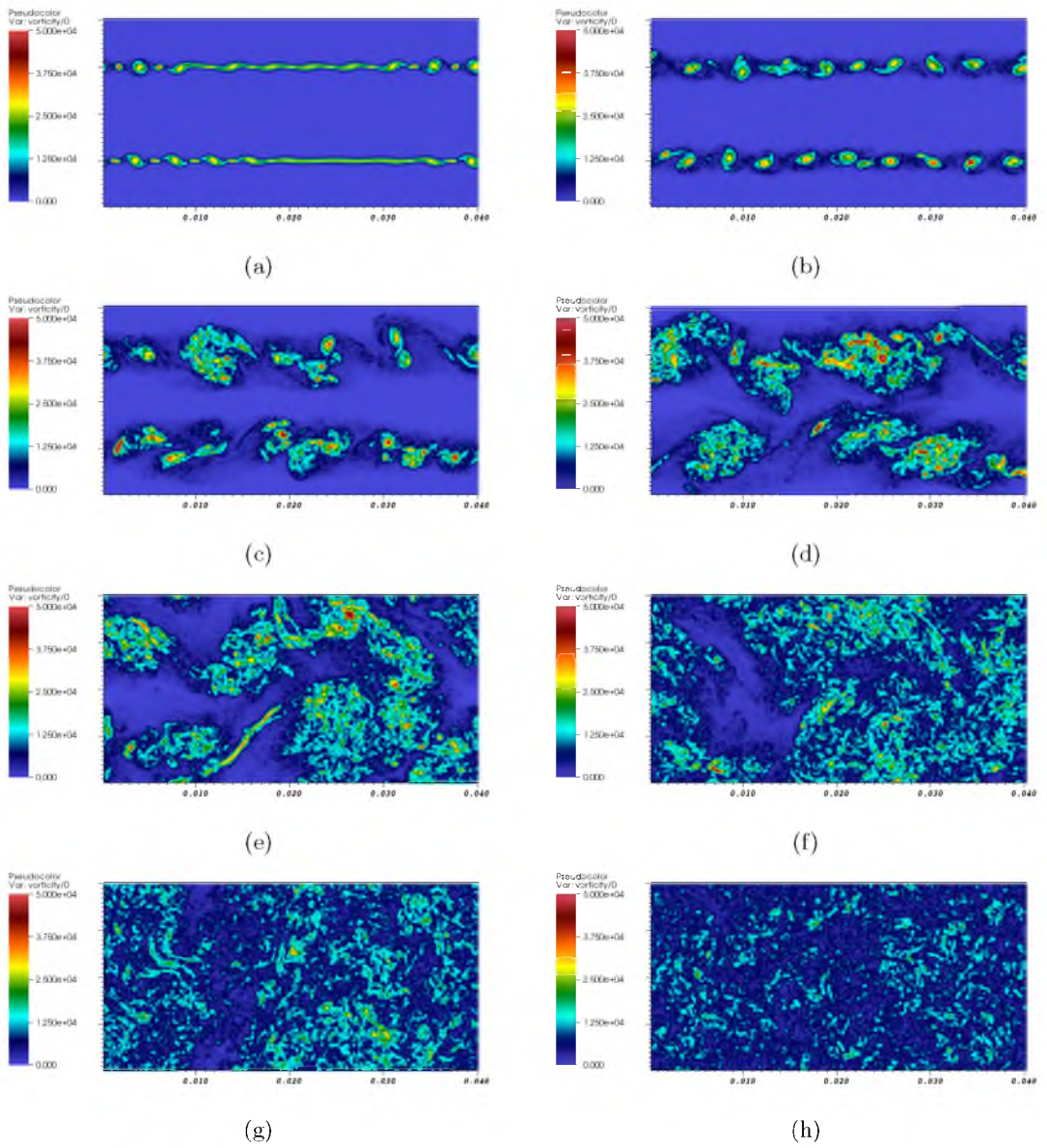

Figure 4.11: A slice of the domain that illustrates the mixing of the temporal jet domain by showing the vorticity develop in the shear layer. The time progress as (a) $t = 0.0125$s, (b) $t = 0.015$s, (c) $t = 0.02$s, (d) $t = 0.025$s, (e) $t = 0.03$s, (f) $t = 0.035$s, (g) $t = 0.04$s and (h) $t = 0.045$s. This is for the $U_0 = 6.0$ m/s case.

simply calculated as $r_{\text{ave}} = M_1/M_0$. The results of the radii for all four of the polymorphs are shown in Figure 4.14. As stated previously, the system was initialized with a wide distribution with a low number density, the initialized moments are found in Table 4.1. As shown by the previous plots, the initial distribution is orders of magnitude lower than the actual moments of the system, and have no effect on the results. However, this initial distribution leads to some numerical noise in the early time frames of the average radius

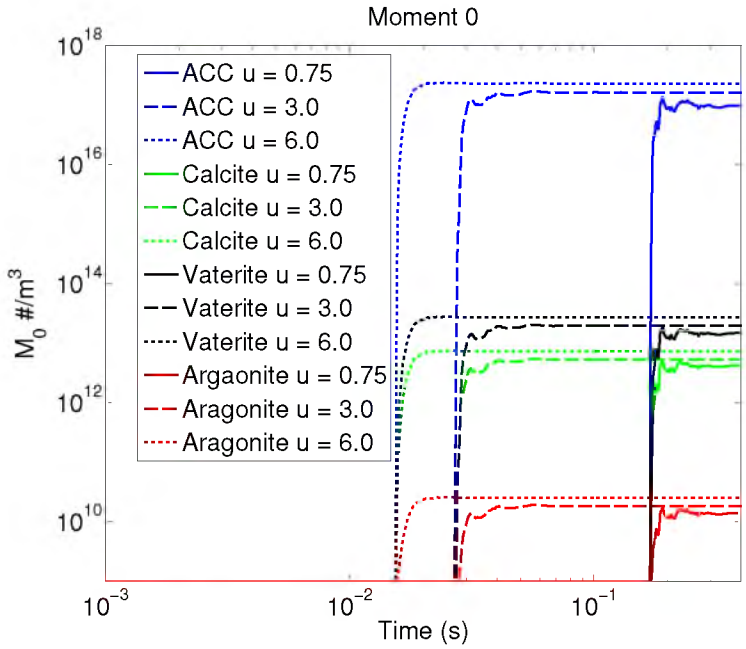

Figure 4.12: The zeroth moment (number density) of each of the four polymorphs of the system. Blue lines are ACC, green lines are calcite, black lines are vaterite, and red lines are aragonite. The solid lines refer to the $U_0 = 0.75$ m/s case, the dashed lines refer to the $U_0 = 3.0$ m/s case, and the dotted lines refer to the $U_0 = 6.0$ m/s case.

plots. The initial distribution used had an average radius of 500 nm, this caused large spikes to form in the plots. Once the noise from this initial size was dampened, the low point of each of the curves showed the nucleation radius for the polymorphs for each of the Reynolds number cases. The approximate nucleate size based on this analysis is shown in Table 4.5. After the nucleation event of the particles occurs, the increase in the average radius is due to the particles entering the growth phase of precipitation.

The values listed in Table 4.5 are only approximate values. As the nucleation would first occur in the turbulent shear layer, and not on the centerline, the actual nucleation values are probably lower, as some growth would start to occur. As shown in both the values in Table 4.5 and by the plots in Figure 4.14, the higher mixing rates of the temporal jet leads to a smaller nucleation size of the particles. This is due to the faster mixing rates reaching higher supersaturation ratios quicker, which in turn affects the critical radius of nucleation in Eq. (4.8). ACC has the lowest supersaturation ratio, but with the lowest surface energy of the polymorphs these particles nucleate smaller than aragonite particles. Calcite and vaterite have the first and second highest supersaturation ratios, respectively. As a result, these particles are the smallest nucleates. While calcite has a higher supersaturation ratio, the lower surface energy of vaterite evens out the effect so that the nucleate size of both

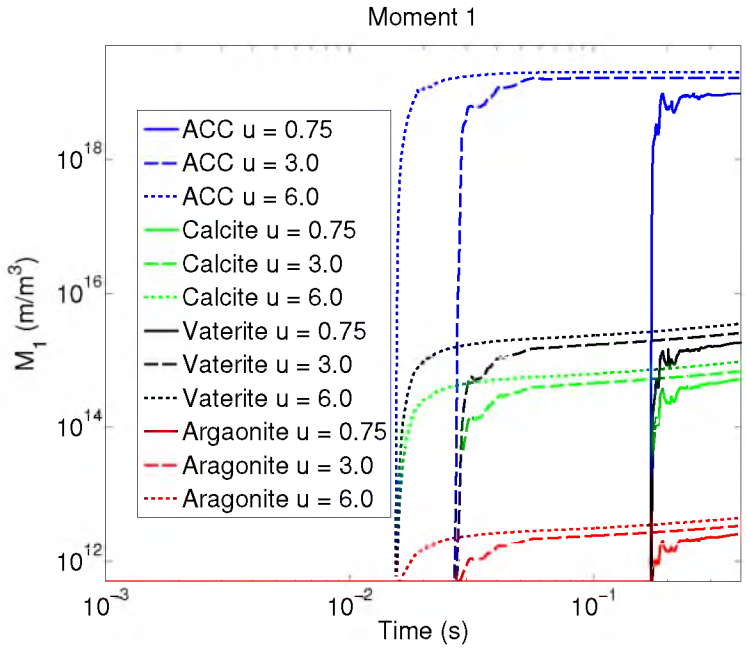

Figure 4.13: The first moment of each of the four polymorphs of the system. Blue lines are ACC, green lines are calcite, black lines are vaterite, and red lines are aragonite. The solid lines refer to the $U_0 = 0.75$ m/s case, the dashed lines refer to the $U_0 = 3.0$ m/s case, and the dotted lines refer to the $U_0 = 6.0$ m/s case.

these polymorphs is about the same.

After the initial nucleation of the polymorphs occur, the drop in supersaturation limits the birth of new particles and the polymorphs begin the major growth phase. In all three of the cases, the size of the ACC particles is shown to level off rather quickly. As this polymorph has the lowest supersaturation ratio, it quickly approaches 1.0 after nucleation and the growth of this phase stops. At longer timescales than what was simulated here, as the other three polymorphs continue to grow, eventually the supersaturation ratio of ACC would drop below 1.0. Then, the ACC phase would begin to dissolve back into solution [165]. In contrast, the calcite, vaterite and aragonite phases of the system continue to grow throughout the simulation. For the vaterite and calcite for the middle and the highest Reynolds number, the size of the particles becomes nearly indistinguishable. It is likely that at these high Reynolds numbers, the growth rate of these polymorphs has become reaction-rate limited, rather than mixing-rate limited.

While the initial nucleate sizes follow the trend that the higher Reynolds numbers lead to larger particles, the final sizes of the particles do not follow this trend. The lowest Reynolds numbers highlight this discrepancy the most. The cause for this could be due to the variance of the mixture fraction, shown in Figure 4.10 (b). This plot is on the log scale

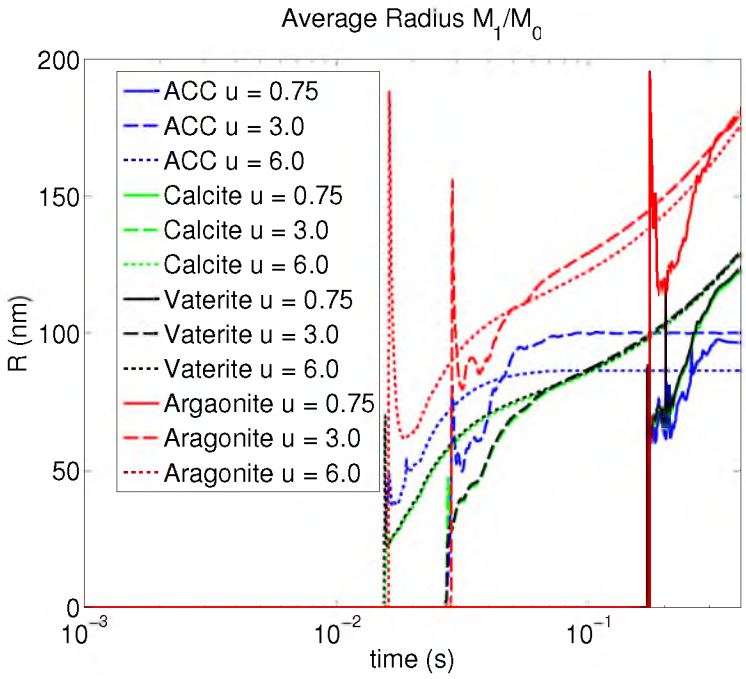

Figure 4.14: The average radius of each of the four polymorphs of the system. Blue lines are ACC, green lines are calcite, black lines are vaterite, and red lines are aragonite. The solid lines refer to the $U_0 = 0.75$ m/s case, the dashed lines refer to the $U_0 = 3.0$ m/s case, and the dotted lines refer to the $U_0 = 6.0$ m/s case.

Table 4.5: Approximate particle nucleate sizes (nm).

Case	ACC	Vaterite	Aragonite	Calcite
$U_0 = 0.75$	61	65	114	67
$U_0 = 3.0$	49	28	80	28
$U_0 = 6.0$	38	22	61	23

for the time axis, as such the length of time that the large mixture-fraction variance lasts is ten times longer at the lowest Reynolds number than the highest Reynolds number. While the average mixture fraction may be near 0.5, the large variance means that much of the central domain may not be at the well-mixed state. For example, half could be at 0.4 while half is at 0.6, which would lead to a vastly different value for nucleation and growth rates. Such large heterogeneity in the domain could be the cause of the nonintuitive results from the LES for the lowest Reynolds number.

It is possible that the inconsistencies here could be alleviated by further increasing the resolution of the LES. In Abboud et al. [1], it was shown that very high resolution one-dimensional turbulence simulations had a significantly lower value in the peak fluctuation

values, and did not show these inconsistencies with the lowest Reynolds number. The plot in Figure 4.15 shows the velocity and the fluctuations of the LES simulations at different grid resolutions for the highest Reynolds number case. As the grid resolution is increased, the data start to converge to a lower peak fluctuation value, and if the resolution were to be further increased, it is likely the fluctuation values would continue to decrease.

4.3.2 Pilot Scale Geometries

This section will discuss the two different geometries that were simulated using the ARCHES code. These geometries are of pilot scale industrial reactors. To achieve the steady state for the reactors, the simulations were run for more than 100 computational hours. The differences in the supersaturation ratio between the two reactors are highlighted in Figure 4.16. The still frames show that the mixing pipe reactor has a large region of high supersaturation over which the reaction and precipitation occurs. In contrast, the impinging jet reactor has a very small tight space in between the two jets where the reaction occurs in a very short plane. The difference in the supersaturation ratios between the two reactors is the main variable, which affects how particles are nucleated in each of the reactors.

The quickness of the mixing plays a large role in the supersaturation ratio and how fast the particles are nucleated. The differences in the two pilot reactors for the mixture fraction profile are shown in Figure 4.17. The impinging jets reactor has a very narrow region of mixing in the center of the jet plane, while the static mixing pipes requires a long drawn out time to mix thoroughly. It should be noted that the static mixer in the mixing pipes is

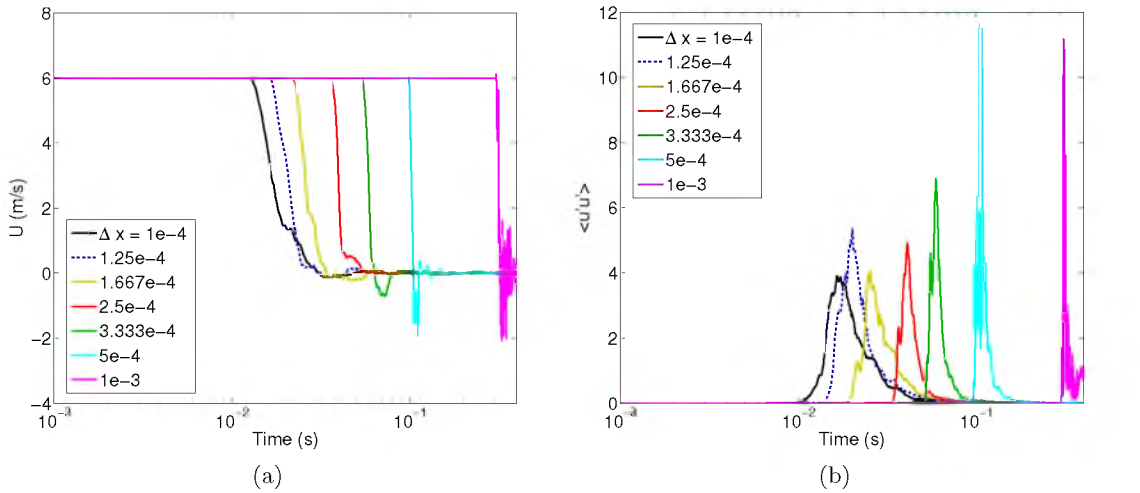

(a) (b)

Figure 4.15: The centerline velocity (a) and fluctuations (b) as the grid resolution of the LES is increased. The dotted blue line is the resolution at which the precipitation results were obtained.

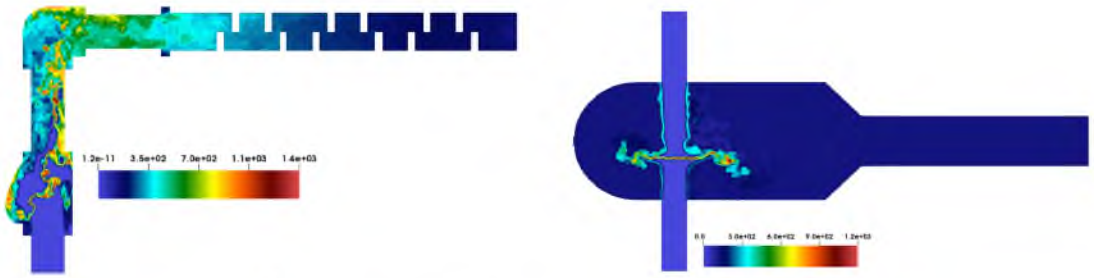

(a) (b)

Figure 4.16: The supersaturation ratio for calcite in the (a) mixing pipes and (b) impinging jet reactors.

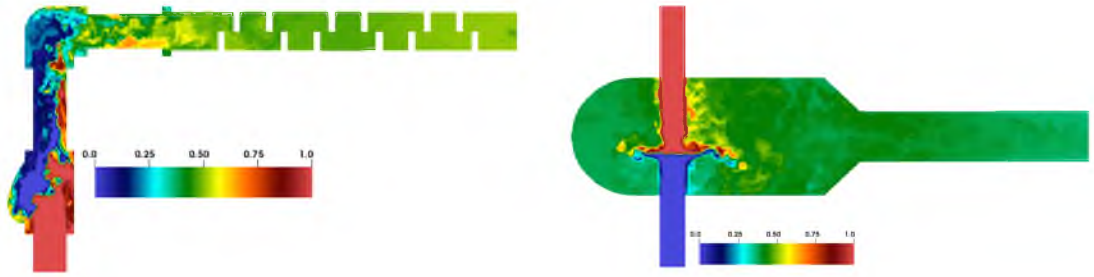

(a) (b)

Figure 4.17: The mixture fraction profile in the (a) mixing pipes and (b) impinging jet reactors.

far upstream from the initial fluid mixing section and not effective, as most of the mixing occurs prior to the flow entering this region.

The small region with a nearly 0.5 mixture fraction at the reaction plane in the impinging jets reactor leads to some of the highest values for supersaturation, as given by the plot in Figure 4.1. The averaged concentrations of each of the particles at the outlet of the geometries is shown in Table 4.6. These data are taken as a temporal- and spatially-averaged value over the outlet plane after steady state is reached. The zeroth moment in the table is represented as the particle concentration in terms of the number density per cubic meter. All of the polymorphs show an increase in the number density of more than 50 % in the impinging jets reactor when compared to the mixing pipes. The better mixing rate that occurs in the impinging jets as compared to the static mixer pipes results in higher number densities of particles at the outlet to the domain. This is consistent with the ideal geometry of the temporal jet, which showed faster mixing resulted in higher particle concentrations.

The data for the first moments of the polymorphs at the outlets of the pilot reactors are shown in Table 4.7. As before, these values are temporally- and spatially- averaged over the

Table 4.6: Average number density at reactor outlet (#/m^3).

Geometry	ACC	Vaterite	Aragonite	Calcite
Mixing Pipes	2.29e16	6.03e12	6.16e9	1.95e12
Impinging Jets	3.64e16	9.61e12	9.12e9	3.06e12
Percent Change	59%	59%	48%	57%

Table 4.7: Total size of suspension at reactor outlet (nm/m^3).

Geometry	ACC	Vaterite	Aragonite	Calcite
Mixing Pipes	3.58e18	9.94e14	1.61e12	3.18e14
Impinging Jet	4.53e18	2.13e15	3.39e12	8.41e14

outlet plane after steady state is reached. The first moment of the polymorphs is shown in the table in terms of nanometers per cubic meter, which is representative of the total size of the PSD.

Using the zeroth and first order moments of the system the average radii for each of the polymorphs at the outlet can be calculated. As with the temporal jet data, the average radii are calculated by dividing the first moment by the zeroth moment of each polymorph. These values are shown in Table 4.8 in units of nanometers.

For ACC, the better mixing that is promoted through the change in the geometry results in a much smaller average radius at the outlet in the impinging jet case. However, for other polymorphs this was not observed. Even though a higher number density was observed – as expected for better mixing cases – higher radii were seen for the other polymorphs. The main reason for this is the reaction time that is allowed for each case. The Reynolds numbers at the jet inlets are the same for both of the geometries, but the impinging pipes have a longer residence time by about four times more, due to the the size of the large chamber in between the impinging jets.

To examine the effect of the longer residence time, the outlet pipe of the impinging jets reactor is observed more closely. The average radius at the slice of the outlet is compared

Table 4.8: Average particle radius at reactor outlet (nm).

Geometry	ACC	Vaterite	Aragonite	Calcite
Mixing Pipes	156.83	164.86	260.71	163.13
Impinging Jets	124.86	221.58	367.45	275.19
Percent Change	-20.3%	34.4%	40.9%	68.7%

to a slice of the reactor upstream where the tapered portion begins. Table 4.9 shows the average radius of each of the polymorphs for these two planes of the impinging jets reactor. To illustrate where the data in Table 4.9 are taken from, a two-dimensional slice of the impinging jet is drawn in Figure 4.18. Here, the red line shows the upstream plane where data are taken, and the yellow line shows the outlet plane of the data. The figure also shows the formation of the ACC through nucleation occurring at the very sharp reaction plane where the supersaturation ratio is at its highest. After the nucleation occurs here the number density declines as this portion of the fluid is mixed into the other regions that are not as reactive.

These data show that the reaction is not yet complete as the more stable polymorphs are continuing to grow in this short region. Within the large chamber of the impinging jets reactor, the polymorphs have been given a significant time to continue growing after the nucleation. Furthermore, when the zeroth moment of ACC is examined it is 3.64×10^{16} at the upstream location and 3.48×10^{16} at the outlet. This shows that the reaction is starting to enter the first dissolution phase where ACC starts to dissolve back into the aqueous phase. This effect is shown in the zero dimensional modeling study by Schroeder et al. [165]. The average ACC size shows a slight increase, however, this is not due to the growth of the polymorph, but rather due to the death term in the PBE killing off the

Table 4.9: Average particle radius (nm) at reactor outlet and the tapered section for the impinging jet reactor.

Location	ACC	Vaterite	Aragonite	Calcite
Upstream Location	123.05	206.81	345.99	262.63
Outlet Plane	124.86	221.59	367.46	275.19

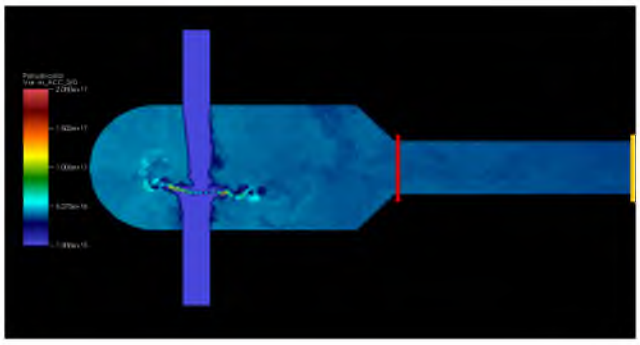

Figure 4.18: The number density of ACC in the impinging jet reactor in a two-dimensional slice at the center of the domain. Lines are drawn to show where data are taken for the averaging.

smaller particles as the ACC phase dissolves.

4.4 Conclusion

A framework using the Eulerian QMOM technique was developed for a set of precipitation reactions with a large number of physical models included to accurately represent all of the complex processes of the particles. The method was first applied to an idealized geometry of a temporal jet. Here, it was shown that while the selectivity of the polymorphs was not changed by the increase in Reynolds number, the effect of increasing the Reynolds number had a direct effect in improving the mixing rate of the system and decreasing the nucleate size of the polymorphs. Next, the method was applied to pilot scale flow reactors. It was shown that using the impinging jet reactor provided an increase in the number density of the particles when compared to the mixing pipes reactor. The framework for precipitate particles that was developed in the Wasatch codebase should be able to be generalized for any other precipitate flow system by simply changing the appropriate surface energy and supersaturation values to any arbitrary precipitating system. While presenting a comparison with some experimental data would have been a good addition to this chapter, data provided by the Calera Corporation [18] were not well suited for the short timescales of the CFD simulations.

CHAPTER 5

FLAMELET MODELING

This chapter will examine steady state flamelet modeling. The flamelet modeling approach is specific to nonpremixed combustion simulations. Part of the derivation of the flamelet equations relies on the nonpremixed formulation for laminar flames that specifies a mixture fraction between the oxygen and the fuel streams. A third-party software is used for its flamelet library capabilities. The output from this flamelet code is parsed and processed in a way to make it usable in the ARCHES codebase. The transformation used on the data from the flamelet library is nontraditional in terms of the current progress variable approach in literature. While no CFD simulations were run with these new flamelet tables, the postprocessed data and the method used to produce the tables are examined.

5.1 Flamelet Theory

Several flame studies have been conducted experimentally. Most notably, for the combustion of a methane-air flame, the work done by Sandia [9] has a vast quantity of information available to validate simulations. As shown in Pitsch et al. [141], using a postprocessed library can be used as a replacement for a coupled CFD and flamelet solver with little loss in accuracy when compared to the experimental results, at a much lower computational cost. Several other past studies have shown the use of a postprocessed flamelet model in conjunction with LES [143] and have included the use of a reaction progress variable [139, 65].

The main assumption for the flamelet models is that the chemical timescales are small enough that the reactions occur in a thin layer around the stoichiometric mixture. This assumption is valid as long as the reaction zone is thinner than the Kolmogorov eddy scale. The reaction zone is then laminar, and the only transport is diffusive transport which occurs normal to the surface of the stoichiometric mixture [140]. For the formulation of the flamelet model used here, it is assumed that the reaction has a two-step mechanism with a timescale separation between the first and second reactions, from the general Eq. (4.1) the reaction

can be expressed as

$$\text{Fuel} \xrightarrow{slow} \text{I} \xrightarrow{fast} \text{P}, \tag{5.1}$$

where I is representative of the intermediate species and P is representative of the final products. This reaction occurs with the opposite reaction speeds of the precipitation model in Eq. (4.2), here the first reaction is slow and considered to be on the timescale of CFD, while the second reaction is considered to be instantaneous with regards to the CFD timescale. Due to the input parameters required in the flamelet code, this reaction is represented as oxygen only reacting with the intermediates, and not with the fuel as

$$\begin{aligned} \text{Fuel} &\xrightarrow{slow} \text{I} \\ \text{I} + \text{O}_2 &\xrightarrow{fast} \text{P}, \end{aligned} \tag{5.2}$$

or for the specific combustion case with methane, here this is

$$\begin{aligned} \text{C}^* &\xrightarrow{slow} \text{CH}_4 \\ \text{CH}_4 + \text{O}_2 &\xrightarrow{fast} \text{P}. \end{aligned} \tag{5.3}$$

As this first reaction occurs on the timescale of the meso-mixing, the progress of the reaction is tracked through a scalar transport equation in the LES. The second reaction occurs much quicker and is on the subgrid scale of the LES, which makes it ideal to use a model such as a flamelet library. In this specific problem Fuel is referred to as C^*, the intermediate, I, is CH_4, and P, the products, represent the results from the flamelet code. In this representation of a combustion system, C^* is considered to be unreactive gaseous fuel. Methane is used here for the intermediate because it provides a simple test bed for the method, as the set of combustion reactions are much less complex than higher molecular weight hydrocarbons.

In this application of the flamelet model, the calculations were decoupled from the CFD solver and calculated a priori using a third-party flamelet library known as DARS [27]. DARS is a steady flamelet code. For the thermodynamics and reactions of the system, the GRI mech 3.0 is used, which consists of 53 species and 325 elementary reactions for the combustion of methane [167]. For the nonreactive (in terms of flamelet timescales) C^*, the thermodynamic properties of CH_4 are used in the calculations. Using DARS the data are output in terms of a radiation factor, the stoichiometric scalar dissipation rate, and the mixture fraction for each of the values of the reaction progress variable, Ξ. With the definition of the intermediate step of the reaction in Eq. (5.3), Ξ is the inverse extent of reaction variable for the first reaction step. DARS uses the standard flamelet transformation

to remove the problem from spatial dimensions, such that the mass fraction equations are given by

$$\rho\frac{\partial Y_i}{\partial \tau} = \rho\frac{\chi}{2}\frac{\partial^2 Y_i}{\partial Z^2} + \omega_i, \tag{5.4}$$

where Y_i is the mass fraction of each species i, χ is the scalar dissipation rate, ρ is the density, Z is the mixture fraction, τ is normalized time, and ω_i are species specific source terms. The mixture fraction is scaled from 0 to 1, where 0 is pure air stream and 1 is pure fuel stream. The enthalpy equation for the flamelet calculation is given by

$$\rho\frac{\partial h}{\partial \tau} = \rho\frac{\chi}{2}\frac{\partial^2 h}{\partial Z^2} - \dot{q}, \tag{5.5}$$

where h is the enthalpy and $\dot{q}$ consists of any appropriate heat flux terms. For the steady state flamelet approach, the time derivatives in Eq. (5.4) and Eq. (5.5) are set equal to zero. With DARS, the local scalar dissipation rates used at each value of the mixture fraction in the above equations are calculated with the inverse error function

$$\chi = \chi_{st}\exp(-2(\mathrm{erf}^{-1}(2Z-1))^2). \tag{5.6}$$

For the source term in the enthalpy equation in Eq. (5.5), DARS uses a radiation factor variable which is changed to get a wide array of possible temperature profiles for the system; this is set as a factor in front of the radiative heat flux term in the enthalpy equation as R_f

$$\dot{q} = R_f\sigma\epsilon(T^4 - T_0^4), \tag{5.7}$$

where σ is the Stefan-Boltzmann constant, ϵ is the emissivity, and T is the temperature in K. When the radiation factor is set to 0.0, then then heat flux is zero and the case is adiabatic. The set of equations is solved for all the of species present and DARS outputs the data so that they can be tabulated a priori to running a simulation using the flamelet model.

The typical steady state flamelet models based on the steady laminar flamelet model (SLFM) paramaterize the flamelet library space by the scalar dissipation rate of the system. The flamelet progress variable approach developed by Pierce and Moin [138, 139] uses a reaction progress variable instead. In this method, a transport equation is then required for the filtered reaction progress variable, the scalar transport equations for the mixture fraction and reaction progress variable are given by

$$\frac{\partial\bar{\rho}\tilde{Z}}{\partial t} + \nabla\cdot(\bar{\rho}\tilde{\mathbf{u}}\tilde{Z}) = \nabla\cdot(\bar{\rho}(D_z + D_t)\nabla\tilde{Z}) \tag{5.8}$$

$$\frac{\partial\bar{\rho}\tilde{C}}{\partial t} + \nabla\cdot(\bar{\rho}\tilde{u}\tilde{C}) = \nabla\cdot(\bar{\rho}(D_z + D_t)\nabla\tilde{C}) + \bar{\rho}\tilde{w}_C. \tag{5.9}$$

To account for the subgrid modeling in LES, the scalar variables of interest are obtained by integrating over the joint subgrid PDF of Z and C. This method is known as an assumed PDF method, for a given scalar variable, ϕ, this leads to

$$\tilde{\phi} = \int \phi(Z,C)\tilde{P}(Z,C)\mathrm{d}Z\mathrm{d}C. \tag{5.10}$$

For the subgrid PDF modeling in the progress-variable approach, a beta PDF is utilized for the mixture fraction, and a delta function is assumed for the reaction progress variable. While this method may not have the accuracy of a coupled unsteady flamelet model, the pretabulation is much more computationally inexpensive. The large advantage of using a progress variable approach is that the typical SLFM approach has no ability to account for ignition and extinction of the flame. This is demonstrated by the flamelet solution curve for the temperature in Figure 5.1. In Figure 5.1(a), the SLFM approach shows the curve for the temperature as the dissipation rate increases, and the large discontinuity that occurs for this extinction. On the other hand, in Figure 5.1(b) the typical "S-shaped curve" of diffusion flame theory is shown. This shows three regions of the flame: the steady burning branch, the unstable branch of partially extinguished states, and the complete extinction line [139]. The stable branch shows flame temperature decreasing with dissipation rate, as faster mixing increases reactant concentrations and dilutes product concentrations. The unstable branch shows where the flame is limited by kinetics, and the extinction line shows where the chemical kinetic rates are negligible [139].

Other flamelet methods include progress variable approaches first developed for premixed combustion systems, these include flamelet prolongation of intrinsic low-dimensional

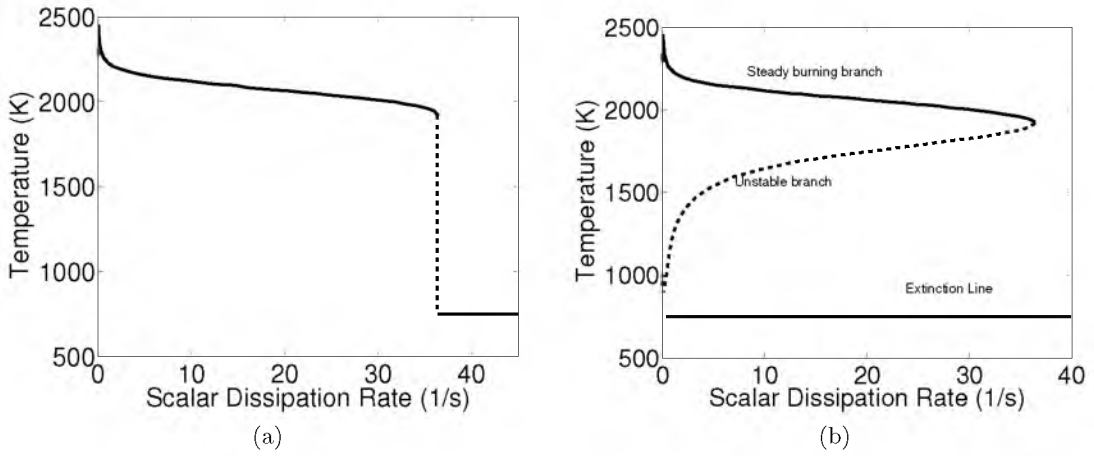

Figure 5.1: The typical "S-shaped curve" of a flamelet solution showing (a) typical steady state flamelet and (b) steady state flamelet with progress variable approach. These plots were created using data from Pierce and Moin [139].

manifold (FPI) [55, 40], and using flamelet-generated manifolds (FGM) [123]. Additional use of these methods has extended into partially premixed and nonpremixed cases [111, 183], as well as high dimensional space in reduced species variables [115]. In the formulation here, a different method of the tabulation is used than the method used in the reaction progress variable approach of Pierce and Moin [139]. The method still utilizes a variable for the reaction progress, but adds several other state variables to the tabulation. A new mixture fraction is defined, which is used to represent a reaction progress showing the amount of fuel available to react as

$$\eta = \frac{m_{\text{Fuel}}}{m_{\text{Fuel}} + m_I + m_{\text{Oxidizer}}}. \tag{5.11}$$

So that with this reaction progress definition, at $\eta = 0$, all of the fuel is available for the combustion as an intermediate, CH_4, and at $\eta_{\max}$ none of the fuel is available for combustion as all of it is C^*, where

$$\eta_{\max} = \frac{m_{\text{Fuel}} + m_I}{m_{\text{Fuel}} + m_I + m_{\text{Oxidizer}}}. \tag{5.12}$$

The data were then rearranged to fit around a normalized variable to track the enthalpy of the system, defined as the heat loss, γ, which is set as

$$\gamma = \frac{h_a - h}{h_s}, \tag{5.13}$$

where h_a is the adiabatic enthalpy, h is the current enthalpy, and h_s is the sensible enthalpy of the system. The heat loss is scaled from approximately -1 to 1. The sensible enthalpy is defined as the enthalpy of the given gaseous mixture at a reference temperature of 273 K. In order to get a complete range on the heat loss values, the radiation factor in Eq. (5.7) in the DARS code is changed significantly, with high resolution near -1 to 1, and low resolution to capture outlying data out to a radiation factor of -12 and 12.

The scalar data were tabulated for use in a lookup table by the ARCHES CFD code in terms of five independent variables, the mixture fraction, f, the scalar dissipation rate, χ_{st}, the scalar variance, $Z^{'2}$, the heat loss, γ and the reaction progress, η. For the scalar variance it is scaled from 0 to 1 based on the maximum value of the variance for the given value of Z in the cell.

An assumed PDF method is used for both the scalar dissipation rate and for the scalar variance for the subgrid state of the system. For the PDF of the scalar dissipation rate, a log-normal distribution was assumed so that

$$P(\chi_{st}) = \frac{1}{\chi_{st}\sigma\sqrt{2\pi}} \exp\left[\frac{-1}{2\sigma^2}(\ln(\chi_{st}) - \mu)^2\right], \tag{5.14}$$

where μ is calculated by

$$\mu = \ln(\langle \chi_{st} \rangle) - .5\sigma^2, \tag{5.15}$$

with the standard deviation of the PDF, σ, set equal to 3, based on the average of experimental studies stating its range from 2 to 4 [42]. For each value of Ξ there is a maximum $\langle \chi \rangle_{st}$ before extinction of the flame. At this point the DARS code fails to calculate a solution for the extinct flame. To remedy this, after this upper limit of the dissipation rate is reached a simple nonreactive mixing model was employed to calculate scalar quantities. The chemical state of the system at extinction is independent of the dissipation value [139].

For the PDF of the mixture fraction, a clipped Gaussian was used such that

$$\begin{aligned} P(Z) =& \frac{1}{2}\text{erfc}\left(\frac{\mu}{\sqrt{2\sigma^2}}\right) \times \delta(Z) + \frac{1}{2}\text{erfc}\left(\frac{1-\mu}{\sqrt{2\sigma^2}}\right) \times \delta(Z-1) \\ &+ \begin{cases} \frac{1}{\sqrt{2\pi\sigma^2}} \exp\left(\frac{-(Z-\mu)^2}{\sqrt{2\sigma^2}}\right) & 0 < Z < 1 \\ 0 & \text{otherwise.} \end{cases} \end{aligned} \tag{5.16}$$

During the tabulation of the data, instead of using a nonlinear solver to find μ and σ parameters the means and variances were tabulated in terms of these PDF parameters and used perform a reverse lookup of these values [168]. With these two PDFs defined the flamelet theory using the presumed PDF method can be used to evaluate the subgrid value for all of the dependent scalars as [134]

$$\langle \phi \rangle \left(\langle Z \rangle, \Xi, \langle \chi_{st} \rangle, \gamma, Z^{'2} \right) = \int_0^\infty \int_0^1 \phi(Z, \Xi, \chi_{st}, \gamma) P(Z, Z^{'2}) P(\chi_{st}) \mathrm{d}\chi_{st} \mathrm{d}Z. \tag{5.17}$$

This integration is done numerically using a two-dimensional trapezoid method, on approximately 2000 - 3000 total points. Due to limitations of the flamelet solver, not all of the relevant regions of the scalar dissipation rate in the PDF have solutions. As discussed before, when above the scalar dissipation extinction value, scalars are evaluated from a mixing model. However, at high values of χ_{st}, due to the pinching DARS exerts on the endpoints of mixture fraction space, getting a full range of heat loss space is impossible. For these cases the species mixture fractions from the adiabatic case were used, and the temperature was adjusted to solve the nonlinear equation for each heat loss value. In addition, there is difficulty in integrating the low end of the curve numerically, since the peak of the distribution changes orders of magnitude (note: mode = $\exp(\mu - \sigma^2)$), and exists below the low end of the χ_{st} space. There is not enough resolution in χ space for an exact PDF integration, so instead of employing the cumulative distribution function (CDF)

for this value it was simply evaluated by subtracting the known portion of the PDF from 1 (the defined integrated value for a PDF) as

$$1 - \int_{\chi_{\text{low}}}^{\chi_{\text{high}}} P(\chi)\mathrm{d}\chi, \tag{5.18}$$

with the integral using the numerical value. Furthermore, it was assumed that for all dependent variables below the low χ_{st} value, all ϕ are constant, which allows for the transformation of the integral in Eq. (5.17) to

$$\begin{aligned}\int_0^1 \int_0^\infty P(\chi)P(Z)\phi(\chi,Z)\mathrm{d}\chi\mathrm{d}Z = &\left(1 - \int_{\chi_{\text{low}}}^{\chi_{\text{high}}} P(\chi)\mathrm{d}\chi\right) \times \int_0^1 P(Z)\phi(\chi_{\text{low}},Z)\mathrm{d}Z \\ &+ \int_0^1 \int_{\chi_{\text{low}}}^{\chi_{\text{high}}} P(\chi)P(Z)\phi(\chi,Z)\mathrm{d}\chi\mathrm{d}Z\ .\end{aligned} \tag{5.19}$$

In the CFD code, the grid variable used for mixture fraction is not the same as the flamelet solution variable. DARS solves its mixture fraction as the combination of the two specified streams

$$Z = \frac{m_{\text{Fuel-stream}}}{m_{\text{Fuel-stream}} + m_{\text{Oxidizer-stream}}} = \frac{m_{\text{Fuel-inert}} + m_{\text{Fuel}} + m_{\text{I}}}{m_{\text{Fuel-inert}} + m_{\text{Fuel}} + m_{\text{I}} + m_{\text{Oxidizer}}}, \tag{5.20}$$

with $m_{\text{Fuel-stream}} = m_I + m_{\text{Fuel}} + m_{\text{Inert-in-fuel}}$. The inert in the fuel stream consists of trace amounts of nitrogen or carbon dioxide present. The grid variable for mixture fraction that is transported in the LES is defined as

$$f_p = \frac{m_{\text{I}}}{m_{\text{I}} + m_{\text{Fuel}} + m_{\text{Oxidizer}}}. \tag{5.21}$$

In combination with the reaction progress variable the look up variable for the flamelet library is defined with a transformation as

$$f = \frac{f_p}{1-\eta} = \frac{m_I}{m_I + m_{\text{oxidizer}}}. \tag{5.22}$$

The ARCHES code is set up to transport f_p and η as filtered scalar values. The data after the integration of the presumed PDF are remapped from Z and Ξ space onto these new f and η variables. Before the table lookup is performed in the LES algorithm, the f_p and η variables on the grid are used to calculate f. For the calculation of the scalar dissipation rate, an algebraic expression based on the mixture fraction gradient can be used so that

$$\chi \approx 2(D_{f_p} + D_t)\frac{\partial f_p}{\partial x_i}\frac{\partial f_p}{\partial x_i}, \tag{5.23}$$

where D_{f_p} and D_t are the molecular and turbulent diffusion coefficients, respectively. When calculating the scalar variance for the flamelet formulation, the same approach as the

precipitation subgrid model can be used. That is for the second moment of the mixture fraction to be added as a transport equation, and the scalar variance is then

$$\widetilde{f_p'^2} = \widetilde{f_p^2} - \widetilde{f_p}^2. \tag{5.24}$$

Unlike the precipitation formulation of the problem, here the variance will be scaled so that it can be tabulated from 0 to 1 across the given space. The variance is simply divided by the maximum variance for a given mixture fraction

$$\widetilde{f_p'^2}_{\text{norm}} = \frac{\widetilde{f_p'^2}}{\widetilde{f_p'^2}_{\text{max}}}, \tag{5.25}$$

where the maximum variance is given by

$$\widetilde{f_p'^2}_{\text{max}} = \widetilde{f}_p * (1 - \widetilde{f}_p). \tag{5.26}$$

The specific steps used to produce the table are listed in Appendix A. The data shown here are for a simple natural gas combustion case. The temperature of the fuel stream is 298 K and the air stream temperature is 290 K. The mass fractions for each stream are listed in Table 5.1 and Table 5.2, respectively.

5.2 Discussion

While no CFD simulations were run using this steady state flamelet technique, a brief analysis of the features and trends of the flamelet library will be included here. This section

Table 5.1: Mass fraction of the fuel stream.

Component	Mass Fraction
CH_4	0.928
C^*	0.0
C_2H_6	0.0253
C_3H_8	0.00265
N_2	0.02626
CO_2	0.01693

Table 5.2: Mass fraction of the air stream.

Component	Mass Fraction
O_2	0.2303
N_2	0.7488
H_2O	0.007183
Ar	0.01371

will also show plots for the justification of some of the assumptions that were made in constructing the library. The integrated data from the method should be usable in future ARCHES simulations.

As the inverse reaction extent Ξ is increased, the maximum value for which a stoichiometric dissipation rate arrives at a converged solution is decreased. This is due to the lack of combustible fuel available in the system, as higher Ξ values lead to high amounts of C^*. The system becomes too air rich and falls below its lower flammability limit. The highest Ξ value for which any solution converges is at 0.87. Above this limit it is assumed no reaction occurs, and a simple cold mixing model is used. The maximum χ_{st} value for converge is the extinction limit of the flame, a plot of this limit is shown in Figure 5.2. As less fuel is available for combustion, the extinction point in terms of the scalar dissipation rate is decreased, as the flammability has decreased; this decrease is shown to be rather linear up to the maximum converged Ξ value.

The PDF of the dissipation rate with a low value of the stoichiometric dissipation rate set at $\chi_{st} = 5$ is shown in Figure 5.3. The first plot in Figure 5.3(a) shows the full PDF with the mean of 5 marked in a dotted line. The peak of the PDF is very near the axis here. The second plot in Figure 5.3(b) shows the PDF zoomed into this peak region, where the mode is located. The lowest χ_{st} value that is converged is at 0.037, most of the peak of this PDF lies below the converged region of the dissipation rate space. When integrated, the

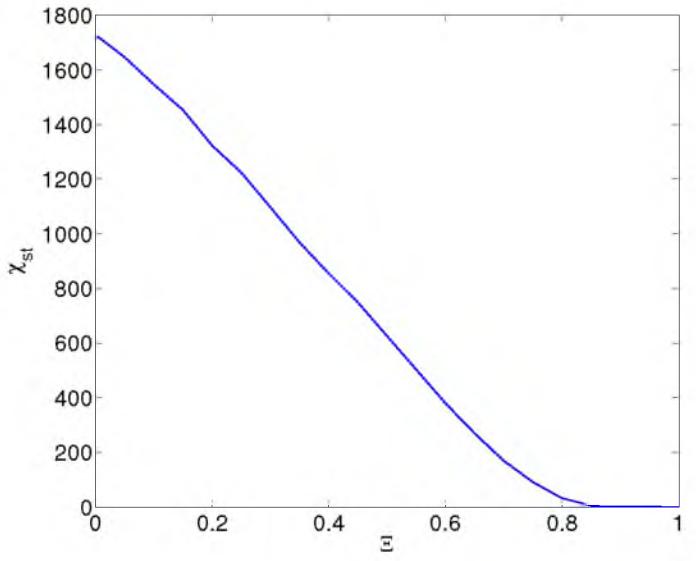

Figure 5.2: A plot showing the extinction value for the dissipation rate as a function of the inverse extent of reaction.

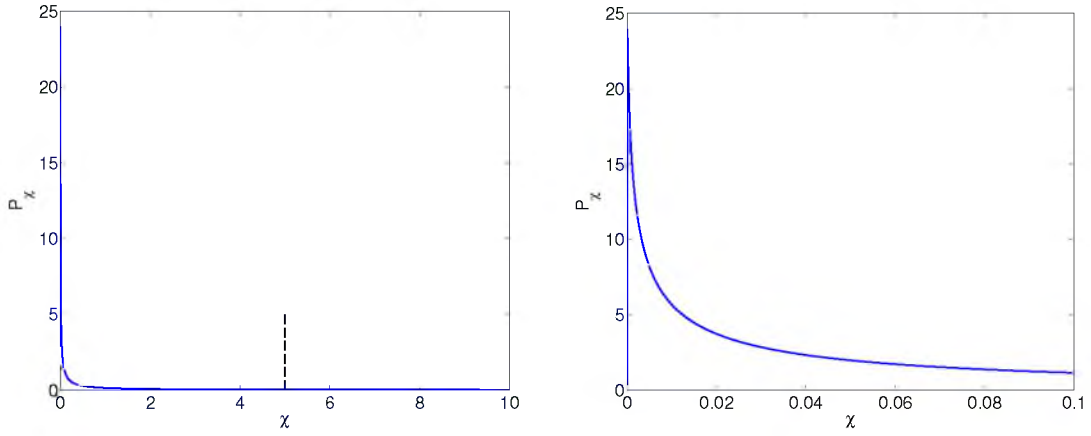

Figure 5.3: The PDF of the scalar dissipation rate with average $\chi_{st} = 5$, shown with full PDF (a), zoomed region near the PDF peak (b).

region here consists of 29% of the total area of the PDF. If this region is not accounted for, then the integrated total mass fractions do not add up anywhere close to 1.0. The solution to the problem that is used here is to assume that below the minimum value of χ_{st} any further flamelet solution converges to the same value. This assumption is mathematically highlighted in the formulation of Eq. (5.18) and Eq. (5.19).

A similar plot for the PDF is shown in Figure 5.4 for a much higher rate of dissipation, set to $\chi_{st} = 1000$. Similar to the previous plot, Figure 5.4(a) shows the full PDF with a dotted line to highlight the mean dissipation rate. At this higher mean, the region with the peak in the PDF shown in Figure 5.4 (b) is at least higher than the converged χ_{st} of the system. However, the peak still appears magnitudes lower than the mean dissipation rate. This leads to a very coarse grid in terms of the numerical integration. The unresolved region here consists of about 5% of the PDF area, and would still lead to a summation of the mass fractions to be less than 1. To resolve this the mass fractions are renormalized by the total to ensure that this does not occur.

For the above assumptions to work out for the integration of the PDF, and for the integrations in Eq. (5.18) and Eq. (5.19) to work, the solution to the PDEs for the flamelet must converge to the same solution as the dissipation rate approaches χ_{low}. A plot of this is shown in Figure 5.5 for two of the main variables in the system, the mass fractions of oxygen and of methane. The plot is the adiabatic case for radiation factor with a 0 value set for Ξ. Each of the plots show the variable in mixture fraction space as the scalar dissipation rate is changed. The black line on the plot shows the flamelet solution at the lowest scalar dissipation rate, and the arrow shows the trend for a decrease in the scalar dissipation rate.

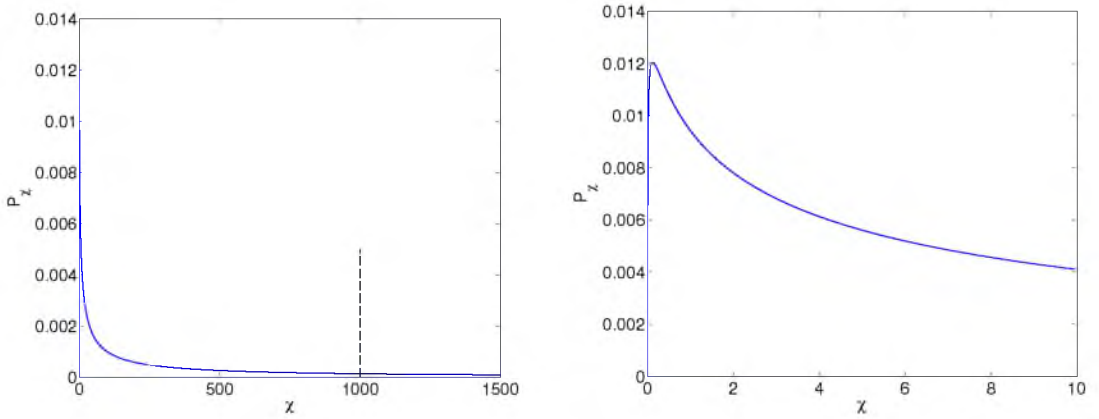

(a) (b)

Figure 5.4: The PDF of the scalar dissipation rate with average $\chi_{st} = 1000$, shown with full PDF (a), zoomed region near the PDF peak (b).

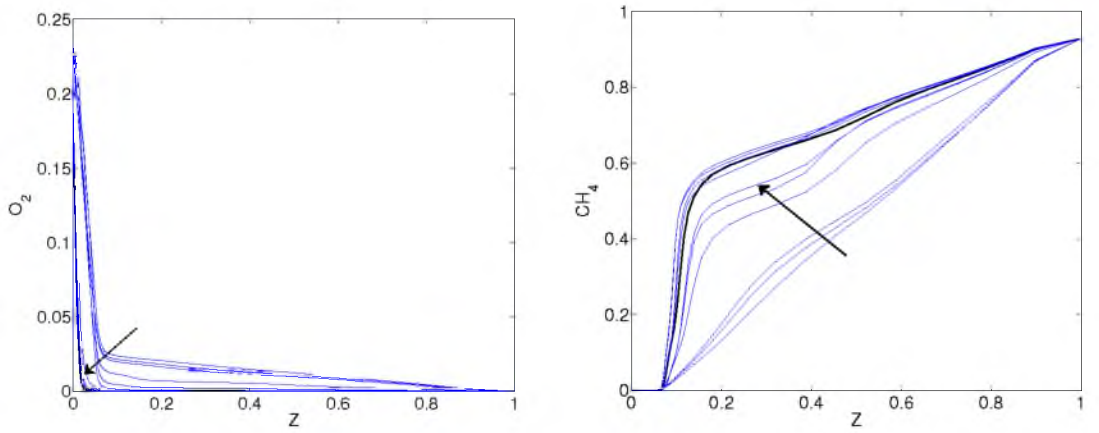

(a) (b)

Figure 5.5: The plots show the mass fraction of O_2 (a) and CH_4 (b) over the mixture fraction space of a flamelet solution. The scalar dissipation rate is decreased in the direction of the arrow in each plot, the black line is the solution for the lowest dissipation rate.

The plots for both of these variables converge to the solution for the lowest converged scalar dissipation rate, so the assumption made in these integrals should be valid.

For the radiation factor tuning, it was found that not all of the grid space that is desired for the normalized heat loss is covered. One reason for this is that the end points of the mixture fraction space are fixed to the specified input temperature. This does not allow for any change in the heat loss space at the end points, which consequently results in a pinched region near the endpoints with very poor heat loss coverage. This pinching effect is easily seen when the heat loss space is plotted as in Figure 5.6. This shows the heat loss as a function of mixture fraction in the x-axis, and as a function of the radiation factor in

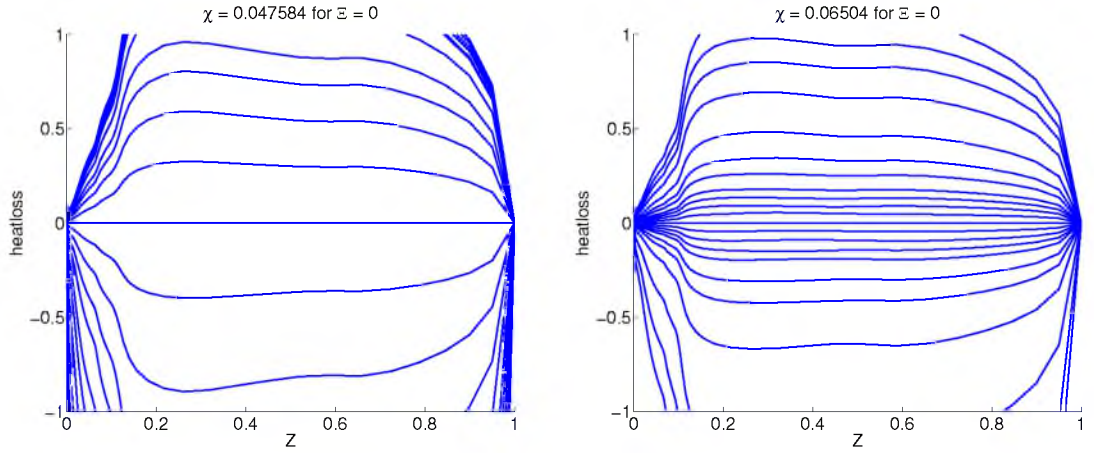

(a) (b)

Figure 5.6: The heat loss coverage for two low values of the dissipation rate, the areas near $Z = 0$ and $Z = 1$ are pinched due to DARS clipping.

the direction of the arrow. To fill in this gap in coverage from the DARS code, the Matlab parsing script takes the nearest converged flamelet solution at the given mixture fraction and keeps the exact same mass fraction of the components. Then, a nonlinear solver is set up to solve for the temperature of this given composition for unresolved areas for the heat loss space.

The heat loss coverage from the radiation factor tuning becomes worse as the scalar dissipation rate of the system in increased. The heat loss coverage for two higher values of the dissipation rate is shown in Figure 5.7. Even at the largest radiation factors of -12 and 12 the outlying data fail to reach the minimum and maximum of the heat loss in prettyreffig:HL2(a). The same process as before is followed, where a nonlinear solver is used to find the temperature to meet the gaps in heat loss. At an even higher value for the dissipation rate, there fails to be any variance in the heat loss space at all in the system in prettyreffig:HL2(b). This is likely due to the diffusion-like term, that contains the scalar dissipation rate in Eq. (5.5) becoming orders of magnitude larger than the heat flux, so that the change in heat flux through the radiation factor has no effect.

With these assumptions made, and the gaps in the flamelet data filled in with the justified results, the flamelet table is constructed for the five independent scalar variables. These are the mixture fraction, extent of reaction, the scalar variance, the scalar dissipation, and the heat loss. A few surfaces of dependent variables varying across these are plotted here. The first plot in Figure 5.8 shows the enthalpy of the system as it changes over the scalar variance and mixture fraction space.

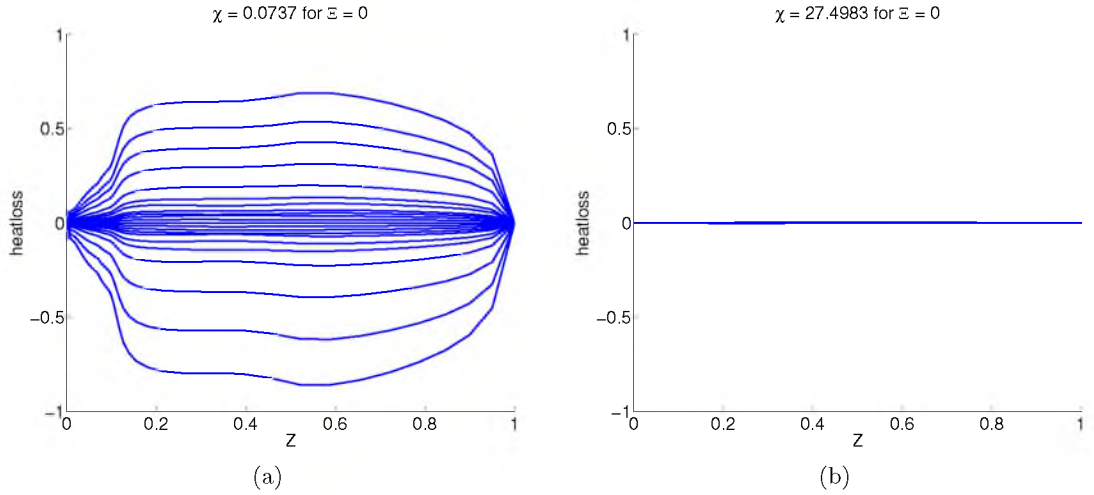

(a) (b)

Figure 5.7: The heat loss coverage for two high values of the dissipation rate. Here the heat loss coverage is limited due to the fast "diffusion" rate of the PDE.

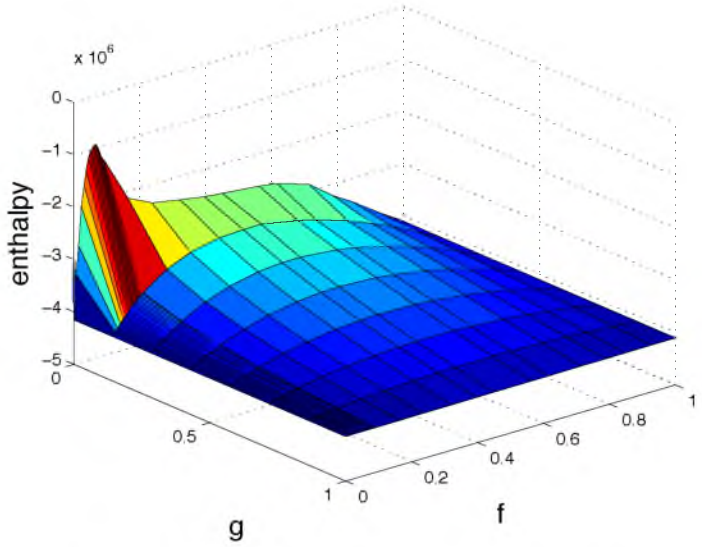

Figure 5.8: The enthalpy of the flamelet solution over scalar variance and mixture fraction. Mixture fraction is varied on the x-axis, and variance is changed on the y-axis.

This plot shows the large spike in the enthalpy near the stoichiometric point of the reaction. The largest change in enthalpy from the reaction occurs in the mixture fraction space here. The other direction shows the scalar variance. At zero scalar variance the plot is unchanged from the base case, as the mixture is assumed to be perfectly mixed at the subgrid level. At a scalar variance of 1, the subgrid mixture is assumed to be completely unmixed, and the result appears as a simple cold mixing between the two streams. Even a

small portion of the domain being unmixed in the variance causes a sharp drop off for the enthalpy of the system.

The next plot in Figure 5.9 shows the temperature variation over the same independent parameters of mixture fraction and scalar variance. The plot of the temperature shows the highest temperature in near the stoichiometric mixture fraction, just like the enthalpy, for the zero scalar variance case. At the scalar variance of 1, the cold mixing case is shown where the temperature only varies between the initial temperatures of the two streams. As with the enthalpy, even a small increase of scalar variance causes a steep drop in the profile. The reason for this sharp decline near the peak, and the shift of the temperature peak to towards the center of mixture fraction space, is because the plot is shown with the normalized scalar variance. At a normalized variance of 0.125, then near $Z = 0.2$ the variance is 0.78, while near $Z = 0.5$ the variance is 0.5. This results in more of the clipped Gaussian PDF existing in the unmixed delta functions for mixture fractions away from the center.

The next plot in Figure 5.10 shows the enthalpy again over mixture fraction, but the other independent variable is the heat loss. This plot shows the effect of remapping the enthalpy space onto the normalized heat loss variable utilized in the code. The centerline at a heat loss of zero shows no change in the enthalpy over changing the mixture fraction. The largest change in the enthalpy as a function of heat loss occurs near the stoichiometric

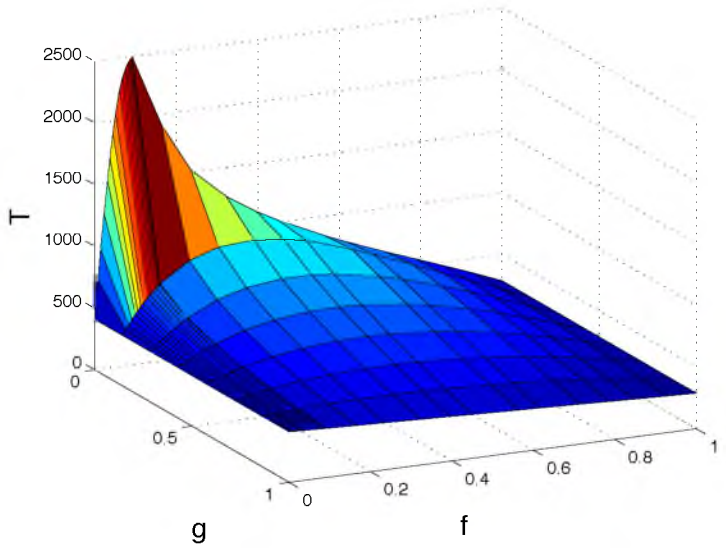

Figure 5.9: The temperature of the flamelet solution over scalar variance and mixture fraction. Mixture fraction is varied on the x-axis, and variance is changed on the y-axis.

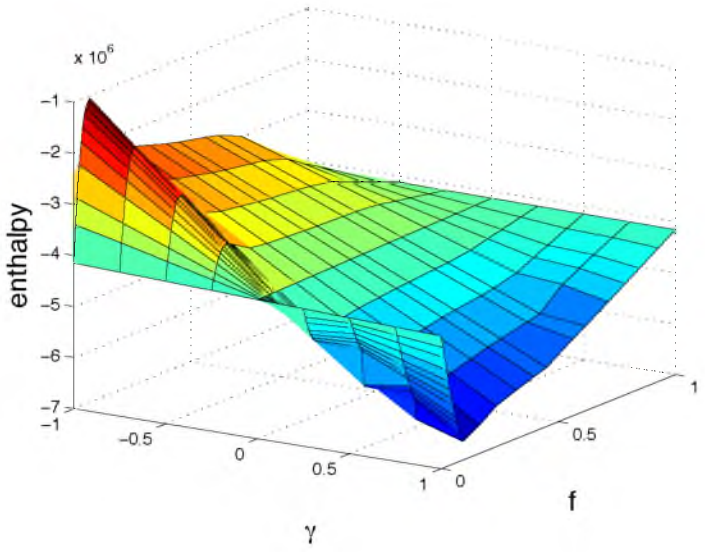

Figure 5.10: The enthalpy of the flamelet solution over heat loss and mixture fraction. Mixture fraction is varied on the x-axis, and heat loss is changed on the y-axis.

point. At this point where the reaction is the most efficient, the largest gain in enthalpy is seen when approaching a negative heat loss value, and the most enthalpy is lost as it approaches a heat loss of 1.

The plot in Figure 5.11 corresponds to the same independent variables, but again plots the temperature. This plot shows a similar peak to the enthalpy plot at the lowest value for the heat loss. As the heat loss is increased the peak in the temperature profile decreases in value, which is the expected result of the normalized heat loss variable. The shifting peak in temperature in mixture fraction space as a heat loss of 1 is approached is likely due to a shift in the calculations, as higher heat loss values had poorer convergence.

The plot in Figure 5.12 shows the formation of NO as a function of the heat loss and mixture fraction. The peak in the formation of NO appears near the stoichiometric point, but slightly more towards the air stream side of the mixture fraction where O_2 is in excess. As the heat loss of the system is correlated to the enthalpy, an increase in the heat loss leads to higher temperatures of the flamelet solution. This in turn leads to higher formation of thermal NO formation during the combustion of the methane [198, 89, 39].

The plot in Figure 5.13 shows NO_2 over the same independent variables. As with the formation of NO, this peak occurs to the right of the stoichiometric point due to the excess O_2 required. However, the width is much narrower and shifted further to the right, as more oxygen is required for the reaction. The amount present is also two orders of magnitude

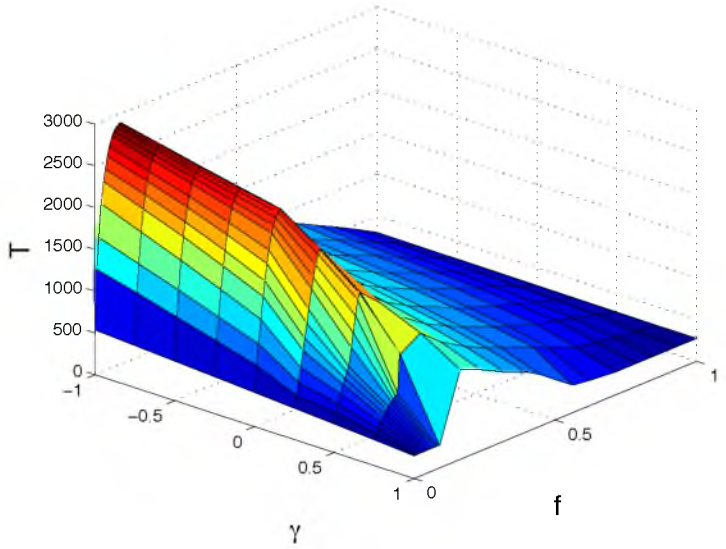

Figure 5.11: The temperature of the flamelet solution over heat loss and mixture fraction. Mixture fraction is varied on the x-axis, and heat loss is changed on the y-axis.

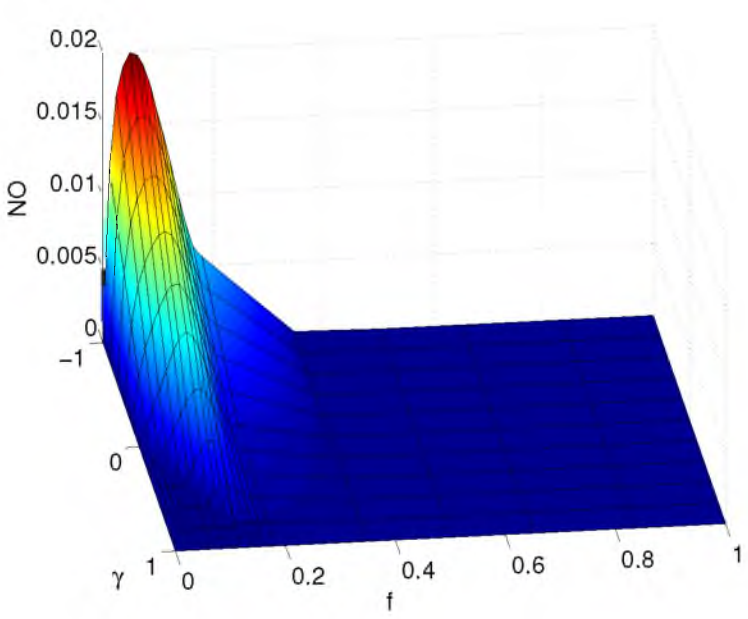

Figure 5.12: The formation of NO for the flamelet solution over mixture fraction and heat loss. Mixture fraction is varied across the x-axis and heat loss is changed on the y-axis.

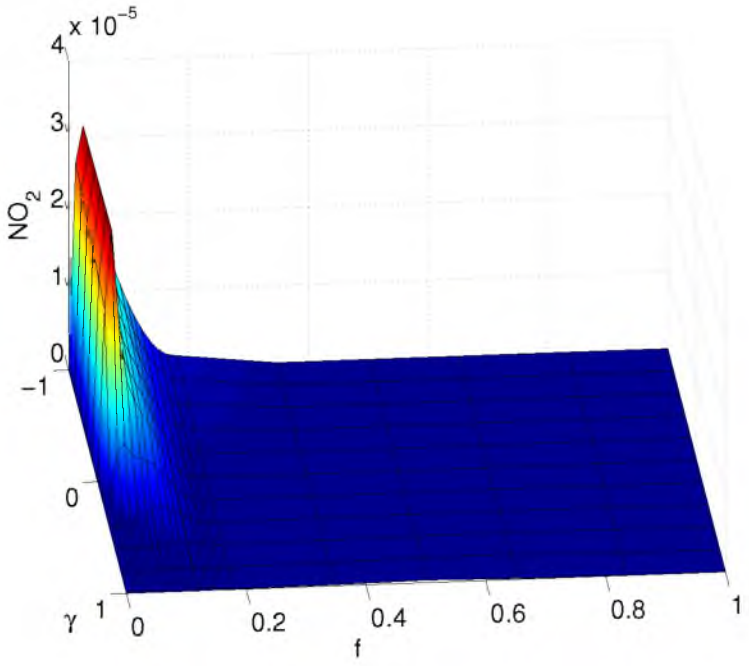

Figure 5.13: The formation of NO_2 for the flamelet solution over mixture fraction and heat loss. Mixture fraction is varied across the x-axis and heat loss is changed on the y-axis.

lower, as the reaction follows the Zeldovich model, which produces NO before NO_2 [198]. The formation of NO_2 reaches a steep cliff in the descending slope as the temperature is lowered. It is likely that the reaction's activation energy crosses a threshold that makes the NO_2 reaction unfavorable quicker than the NO reaction becomes unfavorable.

5.3 Conclusion

A method was developed to utilize the DARS flamelet code for use in CFD simulations. The method builds a library based on five independent variables that are transported in the CFD code. Various insufficiencies in the convergence of the flamelet code were handled through either cold mixing solutions or through approximations with nonlinear solves, based on the situation. The method adds additional parameters to traditional flamelet modeling techniques, and the some of the important resulting dependent variables are plotted. The method here was shown for natural gas as an application, but with a different set of inlet parameters and reaction mechanisms, the method should be adaptable to any gaseous combustion system.

CHAPTER 6

CONDITIONAL QUADRATURE METHOD OF MOMENTS

This chapter will discuss a moment method that is specifically developed for multivariate problems that can exhibit physical crossing of the quadrature nodes, the conditional quadrature method of moments (CQMOM). The method will be outlined as it exists in the literature for a three internal coordinate case. Then, the derivation for the fourth and higher dimensions of internal coordinates will be shown, followed by the handling of source terms. A few test cases are included that will highlight the proper treatment of particle trajectory crossing in the ARCHES codebase. This is followed by a comparison of simulation data with experimental data for an inert particle case.

6.1 DQMOM

A brief overview of the direct quadrature method of moments (DQMOM) will be presented here. This is another type of moment method developed that makes it possible to directly track the evolution of the PBEs. The method requires the solution of the transport equations for the weights and weighted abscissas instead of the moments of the PBE. Recall the quadrature approximation for the NDF can be expressed as a combination of N Dirac functions

$$\eta(\xi;t) = \sum_{\alpha=1}^{N} \omega_\alpha(t)\delta(\xi - \xi_\alpha(t)). \tag{6.1}$$

If Eq. (6.1) is inserted into the PBE in Eq. (4.3) and the convective term is ignored for now, then it can be expressed as

$$\sum_{\alpha=1}^{N} \frac{\partial}{\partial t}\left(\omega_\alpha \delta(\xi - \xi_\alpha)\right) = S(\xi;t), \tag{6.2}$$

where $S(\xi;t)$ is the lumped together source terms of the PBE. Using the product rule for derivatives this equation can be rearranged to

$$\sum_{\alpha=1}^{N} \delta(\xi - \xi_\alpha)\frac{\mathrm{d}\omega_\alpha}{\mathrm{d}t} - \sum_{\alpha=1}^{N} \delta^{'}(\xi - \xi_\alpha)\omega_\alpha\frac{\mathrm{d}\xi_\alpha}{\mathrm{d}t} = S(\xi;t). \tag{6.3}$$

Now consider the product rule for the derivative of $\omega_\alpha\xi_\alpha$

$$\frac{\mathrm{d}\omega_\alpha\xi_\alpha}{\mathrm{d}t} = \omega_\alpha\frac{\mathrm{d}\xi_\alpha}{\mathrm{d}t} + \xi_\alpha\frac{\mathrm{d}\omega_\alpha}{\mathrm{d}t}, \tag{6.4}$$

which can be rearranged to

$$\omega_\alpha\frac{\mathrm{d}\xi_\alpha}{\mathrm{d}t} = \frac{\mathrm{d}\omega_\alpha\xi_\alpha}{\mathrm{d}t} - \xi_\alpha\frac{\mathrm{d}\omega_\alpha}{\mathrm{d}t}. \tag{6.5}$$

This can be substituted into Eq. (6.3) to give

$$\sum_{\alpha=1}^{N} \delta(\xi - \xi_\alpha)\frac{\mathrm{d}\omega_\alpha}{\mathrm{d}t} - \sum_{\alpha=1}^{N} \delta^{'}(\xi - \xi_\alpha)\left(\frac{\mathrm{d}(\omega_\alpha\xi_\alpha)}{\mathrm{d}t} - \xi_\alpha\frac{\mathrm{d}\omega_\alpha}{\mathrm{d}t}\right) = S(\xi;t). \tag{6.6}$$

Using the following substitutions

$$\frac{\mathrm{d}\omega_\alpha}{\mathrm{d}t} = a_\alpha; \quad \frac{\mathrm{d}(\omega_\alpha\xi_\alpha)}{\mathrm{d}t} = b_\alpha, \tag{6.7}$$

the equation can be rewritten as

$$\sum_{\alpha=1}^{N} \delta(\xi - \xi_\alpha)a_\alpha - \sum_{\alpha=1}^{N} \delta^{'}(\xi - \xi_\alpha)(b_\alpha - \xi_\alpha a_\alpha) = S(\xi;t), \tag{6.8}$$

and this can be rearranged into

$$\sum_{\alpha=1}^{N} \Big(\delta(\xi - \xi_\alpha) + \delta^{'}(\xi - \xi_\alpha)\Big)a_\alpha - \sum_{\alpha=1}^{N} \delta^{'}(\xi - \xi_\alpha)b_\alpha = S(\xi;t). \tag{6.9}$$

Recall the equation for the moments shown in Eq. (4.4), using this equation in combination with the rules of integration for Dirac functions yields two identities

$$\int_0^\infty \xi^k\delta(\xi - \xi_\alpha)\mathrm{d}\xi = \xi_\alpha^k \tag{6.10}$$

$$\int_0^\infty \xi^k\delta^{'}(\xi - \xi_\alpha)\mathrm{d}\xi = -k\xi_\alpha^{k-1}. \tag{6.11}$$

Now, multiplying Eq. (6.9) by ξ^k and integrating from 0 to ∞ makes it possible to use the identities to obtain

$$(1-k)\sum_{\alpha=1}^{N} \xi_\alpha^k a_\alpha + k\sum_{\alpha=1}^{N} \xi_\alpha^{k-1} b_\alpha = \int_0^\infty S(\xi;t)\xi^k d\xi \approx \bar{S}_k^{(n)}, \tag{6.12}$$

which is a linear system and can be solved for a_α and b_α, using the values for the weights and abscissas of the quadrature nodes. Here, $\bar{S}_k$ is the moment transform of the source term that is evaluated with the quadrature approximation for the k^{th} order moment. This

source term would consist of the summation of all source terms for the particles, such as the birth, death and aggregation kernels from Chapter 4. This set of linear systems is used to represent the evolution of $2N$ moments of order $m_0, m_1, m_2, \ldots, m_{2N-1}$ where N is the number of quadrature nodes used. This requires solving the following set of transport equations

$$\frac{\mathrm{d}w_1}{\mathrm{d}t} = a_1, \ldots, \frac{\mathrm{d}w_N}{\mathrm{d}t} = a_N; \; \frac{\mathrm{d}(w_1\xi_1)}{\mathrm{d}t} = b_1, \ldots, \frac{\mathrm{d}(w_N\xi_N)}{\mathrm{d}t} = b_N. \tag{6.13}$$

Solving this set of equations requires setting up a linear system from the summations in Eq. (6.12) for $k = 0, 1, 2, \ldots, 2N-1$, which results in

$$\begin{bmatrix} 1 & \ldots & 1 & 0 & \ldots & 0 \\ 0 & \ldots & 0 & 1 & \ldots & 1 \\ -\xi_1^2 & \ldots & -\xi_N^2 & 2\xi_1 & \ldots & 2\xi_N \\ \vdots & \vdots & \vdots & \vdots & \vdots & \vdots \\ -2(1-N)\xi_1^{2N-1} & \ldots & -2(1-N)\xi_N^{2N-1} & (2N-1)\xi_1^{2N-2} & \ldots & (2N-1)\xi_N^{2N-2} \end{bmatrix} \times$$
$$\begin{bmatrix} a_1 \\ \vdots \\ a_N \\ b_1 \\ \vdots \\ b_N \end{bmatrix} = \begin{bmatrix} \bar{S}_0 \\ \bar{S}_1 \\ \vdots \\ \bar{S}_{2N-2} \\ \bar{S}_{2N-1} \end{bmatrix}. \tag{6.14}$$

Solving this matrix gives all of the a_α and b_α values, from which the time evolution of the weights and the abscissas of the distribution can be calculated. If two of the quadrature nodes are identical, then the determinant of the matrix is null, and the linear system becomes singular. The main source of unstable simulations in DQMOM is in the event of these identical nodes. Perturbation of the nodes can be used to over come the singularity [101]. For the extension of the DQMOM method for spatially heterogeneous problems, a small change is made to the source term matrix of Eq. (6.14) to become

$$\begin{bmatrix} \bar{S}_0 \\ \bar{S}_1 \\ \vdots \\ \vdots \\ \bar{S}_{2N-2} + \bar{C}_{2N-2} \\ \bar{S}_{2N-1} + \bar{C}_{2N-1} \end{bmatrix}, \tag{6.15}$$

where the correction term, $\bar{C}_k$, is given by

$$\bar{C}_k = k(k-1)\sum_{\alpha=1}^{N}\left(w_\alpha \xi_\alpha^{k-2} D_x \frac{\partial \xi_\alpha}{\partial t}\frac{\partial \xi_\alpha}{\partial t}\right). \tag{6.16}$$

This correction term is only present when a spatial gradient of the quadrature nodes is present, and when a diffusion mechanism is involved. If particles are sufficiently large

then the diffusion, D_x, is set as zero and the correction term also becomes zero. This linear system is solved for a_α and b_α, which are then used in the transport equations for the weights and weighted abscissas as

$$\frac{\partial w_\alpha}{\partial t} + \frac{\partial}{\partial x_i}(u_{p,i} w_\alpha) - \frac{\partial^2}{\partial x_i^2}(D_x w_\alpha) = a_\alpha \tag{6.17}$$

$$\frac{\partial (w_\alpha \xi_\alpha)}{\partial t} + \frac{\partial}{\partial x_i}(u_{p,i}(w_\alpha \xi_\alpha) - \frac{\partial^2}{\partial x_i^2}(D_x w_\alpha \xi_\alpha) = b_\alpha. \tag{6.18}$$

This derivation of DQMOM is the same form shown in Marchisio and Fox [102]. A similar derivation can be made for the extension to multivariate problems. The method has been shown to work in many past simulations such as soot formation [200, 201], fluidized beds [38, 37], coal combustion [129, 130] and other applications [101, 43]. However, the formulation of the method in ARCHES is not able to properly solve the particle trajectory crossing for the general case.

A simple case is set up for the particle trajectory crossing with DQMOM. The case is 1.2 m by 1.2 m in x and y space with a periodic condition set in the z direction, with a resolution of 100 by 100 by 2. Two inlets are located on the x-minus face with one environment in each. Both are set to an x velocity of 1.0 m/s, and the y velocities are set to 1 m/s and -1 m/s. A slice of this domain at steady state is shown in Figure 6.1. This case is set up with no particle-fluid interactions, and no particle-particle interactions such as collisions.

This can be mitigated if the particle trajectory crossing is known a priori by initializing the weights of the inlet streams such that the representations of the PBE exist in separate environments before crossing. While this may work for simple cases, in actual simulations

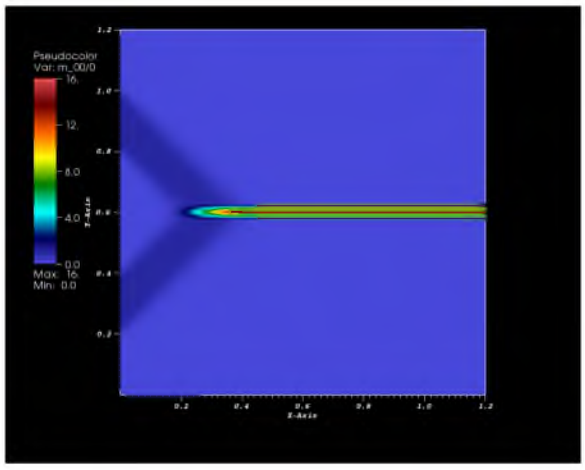

Figure 6.1: A two-dimensional slice of the domain showing the particle trajectory crossing problem with DQMOM. The inlets are intialized with the same environemnts populated, when the particles jets meet the y-velcoities are simply averaged.

this is often not the case, as the complex flows will result in particle trajectory crossings in areas of the domain that are not known a priori. Even knowing the outcome of a case a priori, if the particle trajectory crossing is determined by the geometry of the walls, rather than the geometry of the inlets, then adjusting the inlet environments would not mitigate this effect when DQMOM is used. A simple case is set up for particles hitting a wall in a channel flow. A channel is setup with height of 0.5 m and width of 2.0 m with periodic condition in the z-dimension, the resolution used is 120 by 30 by 2. The inlet is set with a x-velocity of 1.0 m/s and a y-velocity of 1.0 m/s, so it is pointed toward the wall in the y-plus direction. The result of this simple simulation at steady state is shown in Figure 6.2 for a slice of this two-dimensional domain.

As the particles hit the wall, the zero-velocity Dirichlet condition for the y-direction velocity causes no rebound from the wall to occur. Instead, the particles accumulate in the one flow cell next to the wall, and no other cells near the wall contain particles. These particles are then convected in the x-direction along this one cell next to the wall towards the outlet. There is no adaptive way in DQMOM to deal with particles bouncing away from the wall when the internal coordinates contain the velocities. These two cases highlight one of the numerical issues of DQMOM, this ineffectiveness has led to further development of moment methods, and the main method demonstrated in this chapter, CQMOM, can adapt to solve this problem.

6.2 CQMOM Theory

In Chapter 4 with the precipitation modeling with QMOM, a monovariate approach was used with the internal coordinate set as only the radius, r. In CQMOM, multiple internal coordinates are used for all of the properties of the system, the internal coordinates will be represented in this section by ξ_i for the i^{th} internal coordinate.

The number of moments that are required to be transported for CQMOM depend on

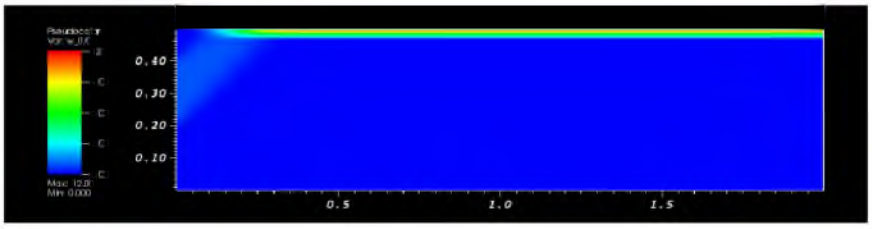

Figure 6.2: A two-dimensional slice of the simulation showing particles interacting with the wall with the DQMOM model. As particles hit the wall, they do not bounce off and accumulate in the cell next to the wall.

the number of quadrature nodes used for each internal coordinate, the total is given by

$$n_{\text{moments}} = 2N_1 + \sum_{i=2}^{M} N_1 \left(\prod_{j=2}^{i} N_j \right) (2N_i - 1). \tag{6.19}$$

Here, N_i is the number of quadrature nodes used for the i^{th} internal coordinate. The derivation for CQMOM revolves around the use of basic probability axiom for conditional probability. This axiom states that for a given joint probability distribution, $\eta(x, y)$, the PDF can be expressed as the multiplication of the conditional probability with the marginal probability as

$$\eta(x, y) = \eta(x|y)\eta(x) = \eta(y|x)\eta(x). \tag{6.20}$$

If this is applied to a joint probability function of an arbitrary number of internal coordinates, M, then the generic NDF of $\eta(\boldsymbol{\xi})$ can be rearranged to

$$\eta(\xi_M|\xi_1, \xi_2, \ldots, \xi_{M-1}) = \frac{\eta(\boldsymbol{\xi})}{\eta(\xi_1, \xi_2, \ldots, \xi_{M-1})}, \tag{6.21}$$

which is the conditional probability distribution of ξ_M given that all other internal coordinates $(\xi_1, \xi_2, \ldots, \xi_{M-1})$ are fixed. By definition, the number density of the conditional probability distribution is fixed to 1, and the denominator can be defined by integrating out the M^{th} internal coordinate

$$\eta(\xi_1, \xi_2, \ldots, \xi_{M-1}) = \int_{\Omega_{\xi_M}} \eta(\boldsymbol{\xi}) \mathrm{d}\xi_M. \tag{6.22}$$

Analogous to Eq. (6.21) a conditional density function for the $(M-1)^{\text{th}}$ internal coordinate can be defined as

$$\eta(\xi_{M-1}|\xi_1, \xi_2, \ldots, \xi_{M-2}) = \frac{\eta(\xi_1, \xi_2, \ldots, \xi_{M-1})}{\eta(\xi_1, \xi_2, \ldots, \xi_{M-2})}. \tag{6.23}$$

From here is should be straight forward that smaller and smaller subsets of internal coordinates can be conditioned down to ξ_1 and then the number density function can be set equivalent to

$$\begin{aligned} \eta(\boldsymbol{\xi}) =& \eta(\xi_M|\xi_1, \xi_2, \ldots, \xi_{M-1})\eta(\xi_{M-1}|\xi_1, \xi_2, \ldots, \xi_{M-2}) \\ & \times \cdots \times \eta(\xi_4|\xi_3, \xi_2, \xi_1)\eta(\xi_3|\xi_2, \xi_1)\eta(\xi_2|\xi_1)\eta(\xi_1) \end{aligned} \tag{6.24}$$

These equalities are used as the basis for deriving the method to calculate the quadrature nodes for the multivariate number density function. The CQMOM method uses the conditioning as a way to quickly prescribe quadrature nodes for the closure problem. The

conditioning allows for several small matrices to be solved for the closure quadrature nodes, rather than a complex nonlinear system that is required in multivariate QMOM. As a quick demonstration, consider a two-dimensional normal distribution given by the standard equation

$$\eta(\xi_1,\xi_2) = \frac{1}{2\pi\sigma_x\sigma_y\sqrt{(1-\rho^2)}} \exp\left(\frac{-1}{2(1-\rho^2)}\left(\frac{(\xi_1-\mu_x)^2}{\sigma_x^2} + \frac{(\xi_2-\mu_y)^2}{\sigma_y^2}\right)\right), \qquad (6.25)$$

and let $\mu_x = \mu_y = 5.0$, $\rho = 0.25$, $\sigma_x = 0.5$ and $\sigma_y = 1.0$. The rendering of this distribution in space is shown in Figure 6.3.

The PDF should be calculated the same way regardless of the order of the conditioning that is used via Eq. (6.20). The two permutation calculations for this moment set yield the two sets of abscissas seen in Figure 6.4. The black dots are the positions of the abscissas u_1, u_2, and the red dots show the abscissas that are used for the conditional quadrature.

If it is set that $N_1 = N_2 = 4$, then a total of 16 abscissas will be calculated. One permutation of CQMOM will require 32 moments of the 48 optimal moment set, and if both permutations are calculated, then the full 48 optimal moment set will be required; this full set can be found in Fox [46].

For a distribution that contains no covariance between the variables, the order of the conditioning would have no effect on the quadrature nodes calculated. With no covariance, the variables are entirely independent and the marginal PDFs are not effected.

For illustration purposes, the calculation for CQMOM in three dimensions is also included in Figure 6.5. Here a three-dimensional normal distribution was again used with the same means. The red dots and lines are the initial quadrature nodes, the blue ones are the quadrature nodes conditioned on the first dimension, and the black dots are the final conditional quadrature nodes.

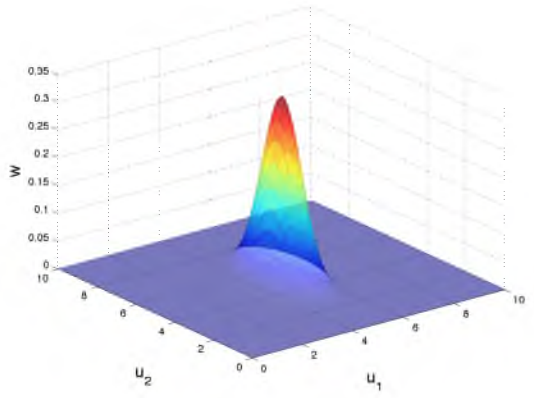

Figure 6.3: Two-dimensional normally distributed PBE.

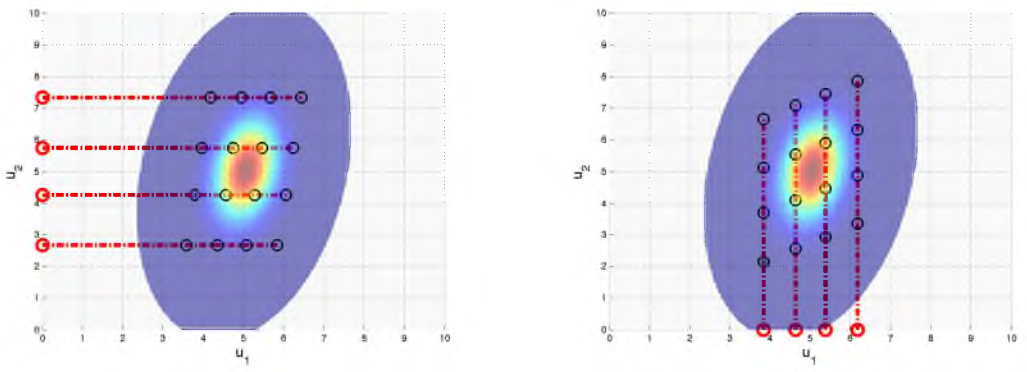

(a) (b)

Figure 6.4: Two-dimensional quadrature nodes showing red dots for the first dimension quadrature nodes, and black dots for the quadrature nodes in the second internal coordinate.

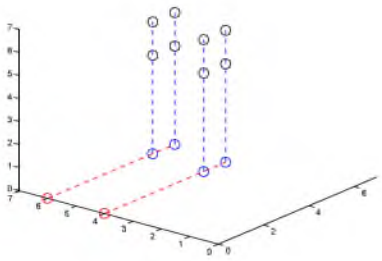

Figure 6.5: Three-dimensional quadrature nodes showing red dots for the first internal coordiante, blue dots for the second, and black dots for the final internal coordinate.

6.2.1 CQMOM for Kinetic Modeling

First, consider the case when all passive scalars of the particles are constant, and the only internal coordinates in the PBE are the particle velocities. Then, the PBE transport equation is given as

$$\frac{\partial \eta(t,\mathbf{x},\mathbf{u})}{\partial t} + u_i \frac{\partial \eta(t,\mathbf{x},\mathbf{u})}{\partial x_i} = 0 \,. \tag{6.26}$$

Note that the definition of the moments for a multivariate case are

$$m_{i,j,k} = \iiint u_1^i u_2^j u_3^k \eta(t,\mathbf{x},\mathbf{u}) \mathrm{d}u_1 \mathrm{d}u_2 \mathrm{d}u_3 = 0 \,. \tag{6.27}$$

Multiplying equation Eq. (6.26) over the first internal coordinate, u_1, and integrating yields a moment transport equation of the form

$$\frac{\partial m_{1,0,0}}{\partial t} + \frac{\partial m_{2,0,0}}{\partial x_1} + \frac{\partial m_{1,1,0}}{\partial x_2} + \frac{\partial m_{1,0,1}}{\partial x_3} = \iiint S(\xi_1,\xi_2,\xi_3)\xi_1^i \xi_2^j \xi_3^k \mathrm{d}\xi_1 \mathrm{d}\xi_2 \mathrm{d}\xi_3 \,, \tag{6.28}$$

where the convective terms have been converted into moments. From this equation, it can be seen that the generalized transport equation for the velocities of the particles is not a

closed moment transport equation, as the u_1 transport is dictated by the $i+1^{\text{th}}$ moment, the u_2 transport is dictated by the $j+1^{\text{th}}$ moment and u_3 is dictated by $k+1^{\text{th}}$ moment. In general terms the moment transport equation for three internal coordinates of velocity is given by

$$\frac{\partial m_{i,j,k}}{\partial t}+\frac{\partial m_{i+1,j,k}}{\partial x_1}+\frac{\partial m_{i,j+1,k}}{\partial x_2}+\frac{\partial m_{i,j,k+1}}{\partial x_3}=\iiint S(\xi_1,\xi_2,\xi_3)\xi_1^i\xi_2^j\xi_3^k \mathrm{d}\xi_1\mathrm{d}\xi_2\mathrm{d}\xi_3 \ . \quad (6.29)$$

Thus, the moment transport equations will require closure. In multivariate QBMM, a summation of point distributions is used to estimate the PBE as

$$\eta(\boldsymbol{\xi})=\sum_{\alpha}^{N}\omega_\alpha\delta(\boldsymbol{\xi}-\boldsymbol{\xi}_\alpha) \ , \quad (6.30)$$

where N is the total number of abscissas for the quadrature. Note that the rest of this derivation is done for arbitrary internal coordinates, so $\mathbf{u}$ has been substituted for $\boldsymbol{\xi}$. The unclosed moments of the system can be estimated with the quadrature weights and abscissas as

$$m_{i,j,k}=\sum_{\alpha}^{N}\omega_\alpha\xi_{1,\alpha}^i\xi_{2,\alpha}^j\xi_{3,\alpha}^k \ . \quad (6.31)$$

The case of Eq. (6.21) for fixing $M=3$ for the three internal coordinates of the system (representing the velocities) is given by

$$\eta(\boldsymbol{\xi})=\eta(\xi_3|\xi_1,\xi_2)\eta(\xi_1,\xi_2)=\eta(\xi_3|\xi_1,\xi_2)\eta(\xi_2|\xi_1)\eta(\xi_1) \ . \quad (6.32)$$

Here, ξ_1 would correspond to u, ξ_2 would correspond to v and ξ_3 would correspond to w. Now, the procedure for calculating these quadrature nodes will be laid out. First, a few definitions are required. The conditional moments for the second dimension of the internal coordinates are defined as

$$\langle\xi_2^j\rangle|(\xi_1)\equiv\int\xi_2^j\eta(\xi_2|\xi_1)\mathrm{d}\xi_2 \ . \quad (6.33)$$

This represents the j^{th} conditional moment of the ξ_2 internal coordinate, conditioned on the value of a quadrature node of ξ_1. Similarly, the conditional moments for the third dimension of the internal coordinates can be defined as

$$\langle\xi_3^k\rangle|(\xi_1,\xi_2)\equiv\int\xi_3^k\eta(\xi_3|\xi_1,\xi_2)\mathrm{d}\xi_3 \ . \quad (6.34)$$

This represents the k^{th} conditional moment of the ξ_3 internal coordinate, conditioned on the values of a quadrature node for a given set of ξ_1 and ξ_2. Then it follows from using the properties of conditional probability that the mixed moments can be set as

$$m_{i,j,0}=\iint\xi_1^i\xi_2^j\eta(\xi_1,\xi_2)\mathrm{d}\xi_2\mathrm{d}\xi_1=\int\xi_1^i\langle\xi_2^j\rangle|(\xi_1)\eta(\xi_1)\mathrm{d}\xi_1 \ , \quad (6.35)$$

and

$$m_{i,j,k} = \iiint \xi_1^i \xi_2^j \xi_3^k \eta(\xi_1, \xi_2, \xi_3) \mathrm{d}\xi_1 \mathrm{d}\xi_2 \mathrm{d}\xi_3 = \iint \xi_1^i \xi_2^j \langle \xi_3^k \rangle | (\xi_1, \xi_2) \eta(\xi_1, \xi_2) \mathrm{d}\xi_1 \mathrm{d}\xi_2 \ . \quad (6.36)$$

Here, i, j, k are the moment orders of each of the internal coordinates. The method here is only for the conditioning order in Eq. (6.32), other permutations of the conditioning will be the same, but with different orders for the internal coordinates. The first step is to use the pure moments of the first variable, $m_{i,0,0}$ with $i = 0, \ldots, 2N_1 - 1$, to calculate the N_1 quadrature nodes for ξ_1. Here, the adaptive Wheeler algorithm [189] from Yuan and Fox [195] will be used for the quadrature calculation of the internal coordinates so that a approximation for $\eta(\xi_1)$ is

$$\eta(\xi_1) = \sum_{\alpha_1}^{N_1} \omega_{\alpha_1} \delta(\xi_1 - \xi_{1;\alpha_1}) \ , \quad (6.37)$$

using this equation in Eq. (6.35) gives an approximation for the mixed moments as

$$m_{i,j,0} = \sum_{\alpha_1}^{N_1} \omega_{\alpha_1} \xi_{1;\alpha_1}^i \langle \xi_2^j \rangle | (\xi_{1;\alpha_1}) \ . \quad (6.38)$$

For simplicity, define $\langle \xi_2^j \rangle_{\alpha_1} \equiv \langle \xi_2^j \rangle | (\xi_{1;\alpha_1})$; this denotes the N_1 unknown j^{th} order moments. If all of the mixed moments in terms of only ξ_1 and ξ_2 ($m_{i,j,0}$) are known, then a linear system to solve for the conditional moments can be constructed from Eq. (6.38) as

$$\mathbf{V}_1 \mathbf{R}_1 \begin{bmatrix} \langle \xi_2^j \rangle_1 \\ \langle \xi_2^j \rangle_2 \\ \vdots \\ \langle \xi_2^j \rangle_{N_1} \end{bmatrix} = \begin{bmatrix} m_{0,j,0} \\ m_{1,j,0} \\ \vdots \\ m_{N_1-1,j,0} \end{bmatrix} \ . \quad (6.39)$$

This matrix system needs to be solved for each set of second dimensional moments from $j = 1, ..., 2N_2 - 1$. Here, N_2 is the maximum number of quadrature nodes needed to reconstruct the conditional probability function $\eta(\xi_2|\xi_1)$. The right hand side for each of the matrices will require a total of $N_1 \times (2N_2 - 1)$ moments to be defined. The coefficient matrices are defined by

$$\mathbf{V}_1 = \begin{bmatrix} 1 & \cdots & 1 \\ \xi_{1;1} & \cdots & \xi_{1;N_1} \\ \vdots & & \vdots \\ (\xi_{1;1})^{N_1-1} & \cdots & (\xi_{1;N_1})^{N_1-1} \end{bmatrix} \text{ and } \mathbf{R}_1 = \begin{bmatrix} \omega_1 & & \\ & \ddots & \\ & & \omega_{N_1} \end{bmatrix} \ . \quad (6.40)$$

This linear system can then be solved using the Rybicki algorithm for the conditional moments [148]. These conditional moments can then be used to construct the two-dimensional distribution as

$$\eta(\xi_1, \xi_2) = \sum_{\alpha_1}^{N_1} \sum_{\alpha_2}^{N_2} \omega_{\alpha_1} \omega_{\alpha_1;\alpha_2} \delta(\xi_1 - \xi_{1;\alpha_1}) \delta(\xi_2 - \xi_{2;\alpha_1;\alpha_2}) \ . \quad (6.41)$$

Now, for each of the α_1 nodes, one-dimensional quadrature with the Wheeler algorithm [189] is executed on these second dimensional moments to find the conditional weights $\omega_{\alpha_1,\alpha_2}$ and conditional abscissas $\xi_{2;\alpha_1,\alpha_2}$. Even though it is not calculated, the zeroth moments $\langle \xi_2^0 \rangle_{\alpha_1}$ are equal to 1 based on the definition of a conditional number density function. At this point, if the problem were two-dimensional the necessary information needed to close the unknown moments is obtained. For higher numbers of internal coordinates, the algorithm is repeated with slight additions.

Using the equation in Eq. (6.41) in Eq. (6.36) yields a summation for the three-dimensional moments as

$$m_{i,j,k} = \sum_{\alpha_1}^{N_1} \sum_{\alpha_2}^{N_2} \omega_{\alpha_1} \omega_{\alpha_1,\alpha_2} \xi_{1;\alpha_1}^{i} \xi_{2;\alpha_1,\alpha_2}^{j} \langle \xi_3^k \rangle_{\alpha_1,\alpha_2} \ . \tag{6.42}$$

Here the $N_1 \times N_2$ unknown k^{th} order conditional moments $\eta(\xi_3|\xi_1,\xi_2)$ are represented by $\langle \xi_3^k \rangle_{\alpha_1,\alpha_2}$, where $\langle \xi_3^k \rangle_{\alpha_1,\alpha_2} \equiv \langle \xi_3^k \rangle | (\xi_{1;\alpha_1}, \xi_{2;\alpha_1,\alpha_2})$. Now a new variable is used for clarity, ζ, defined as

$$\zeta_{\alpha_1;j,k} = \sum_{\alpha_2}^{N_2} \omega_{\alpha_1,\alpha_2} \xi_{2;\alpha_1,\alpha_2}^{j} \langle \xi_3^k \rangle_{\alpha_1,\alpha_2} \ , \tag{6.43}$$

substituting this into Eq. (6.42) yields

$$m_{i,j-1,k} = \sum_{\alpha_1}^{N_1} \omega_{\alpha_1} \xi_{1,\alpha_1}^{i} \zeta_{\alpha_1;j,k} \ . \tag{6.44}$$

With this expression a linear system can be constructed to solve for each ζ as

$$\mathbf{V}_1 \mathbf{R}_1 \begin{bmatrix} \zeta_{1;j,k} \\ \zeta_{2;j,k} \\ \vdots \\ \zeta_{N_1;j,k} \end{bmatrix} = \begin{bmatrix} m_{0,j-1,k} \\ m_{1,j-1,k} \\ \vdots \\ m_{N_1-1,j-1,k} \end{bmatrix} \ . \tag{6.45}$$

The linear system in Eq. (6.45) has to be solved multiple times for each $j = 1, ..., N_2$ and for each $k = 1, ..., 2N_3 - 1$. Here, N_3 is number number of quadrature nodes in the third internal coordinate to reconstruct $\eta(\xi_3|\xi_1,\xi_2)$. Then, with all ζ known, Eq. (6.43) can be used to solve the conditional abscissas, with a linear system that must be solved for every value of α_1

$$\mathbf{V}_{2;\alpha_1} \mathbf{R}_{2;\alpha_1} \begin{bmatrix} \langle \xi_3^k \rangle_{\alpha_1,1} \\ \langle \xi_3^k \rangle_{\alpha_1,2} \\ \vdots \\ \langle \xi_3^k \rangle_{\alpha_1,N_2} \end{bmatrix} = \begin{bmatrix} \zeta_{\alpha_1;1,k} \\ \zeta_{\alpha_1;2,k} \\ \vdots \\ \zeta_{\alpha_1;N_2,k} \end{bmatrix} \ , \tag{6.46}$$

where

$$\mathbf{V}_{2;\alpha_1} = \begin{bmatrix} 1 & \cdots & 1 \\ \xi_{2;\alpha_1,1} & \cdots & \xi_{2;\alpha_1,N_2} \\ \vdots & & \vdots \\ (\xi_{2;\alpha_1,1})^{N_2-1} & \cdots & (\xi_{2;\alpha_1,N_2})^{N_2-1} \end{bmatrix} \text{ and } \mathbf{R}_{2;\alpha_1} = \begin{bmatrix} \omega_{\alpha_1,1} & & \\ & \ddots & \\ & & \omega_{\alpha_1,N_2} \end{bmatrix} . \quad (6.47)$$

As before, this set of linear systems can be solved with the Rybicki algorithm [148]. This system must be solved for each $\alpha_1 = 1, ..., N_1$ and for each $k = 1, ..., 2N_3 - 1$. This will result in the conditional moments, $\langle \xi_3^k \rangle_{\alpha_1,\alpha_2}$, for the third internal coordinate of $\eta(\xi_3|\xi_1, \xi_2)$. These conditional moments will then be used in the adaptive Wheeler algorithm to solve for the conditional weights $\omega_{\alpha_1,\alpha_2,\alpha_3}$ and conditional abscissas $\xi_{3;\alpha_1,\alpha_2,\alpha_3}$, so that the full reconstruction of the PBE for three internal coordinates is expressed as

$$\eta(\boldsymbol{\xi}) = \sum_{\alpha_1}^{N_1} \sum_{\alpha_2}^{N_2} \sum_{\alpha_3}^{N_3} \omega_{\alpha_1} \omega_{\alpha_1,\alpha_2} \omega_{\alpha_1,\alpha_2,\alpha_3} \delta(\xi_1 - \xi_{1;\alpha_1}) \delta(\xi_2 - \xi_{2;\alpha_1,\alpha_2}) \delta(\xi_3 - \xi_{3;\alpha_1,\alpha_2,\alpha_3}) \ . \quad (6.48)$$

6.2.2 CQMOM Convection Scheme

The number of nodes required for each dimension of the quadrature (N_1, N_2, N_3) will determine the moments required for the system. For the three-dimensional problem, there are six possible permutations for the conditioning. The other five are straight forward to adapt the above set of equations to solve. For kinetic equations of the particles, all six permutations will be used. With all six permutations it will be necessary to transport a total of $4N_1N_2N_3$ moments, these moments are the full optimal moment set of the system. Based on the internal-coordinate dimensions and number of quadrature nodes the set of moments that are required can be found in Fox [46].

If the permutations are listed as $(1, 2, 3)$ representing $\eta(u_3|u_1, u_2)\eta(u_2|u_1)\eta(u_1)$, then the permutations giving the x_1 component of kinetic energy are (1,2,3) and (1,3,2), the x_2 component given by (2,1,3) and (2,3,1) and the x_3 component uses (3,1,2) and (3,2,1). Using these permutations gives eight different combinations that can control all three directions of the kinetic-energy flux. For the spatial fluxes in the quadrature method, a flux-splitting algorithm is proposed by Yuan and Fox [196], where the moments are updated in each spatial direction separately

$$\mathbf{M}^n \xrightarrow{x_1 \text{ direction}} \mathbf{M}_1^* \xrightarrow{x_2 \text{ direction}} \mathbf{M}_2^* \xrightarrow{x_3 \text{ direction}} M_3^* \ , \quad (6.49)$$

here $\mathbf{M}$ is the set of moments and $\mathbf{M}_3^*$ is the set of moments for one of the eight possible combinations of the quadrature permutations. Each of the eight combinations must be

transported in this way, so that there is a set of M^* for each combination K. Then the updated optimal moment set for the next time-step is

$$\mathbf{M}^{n+1} = \frac{1}{K}(\mathbf{M}_1 + \cdots + \mathbf{M}_K) \ , \tag{6.50}$$

and the convection term for the next time-step is then

$$\mathbf{M}_k^1 = \mathbf{M}_k^* - \frac{\Delta t}{\Delta x}\left[\mathbf{G}_x^+(N,U,V,W_k^1) - \mathbf{G}_x^-(N,U,V,W_k^1)\right] \ , \tag{6.51}$$

where the flux function $\mathbf{G}$ is from Vikas et al. [182]. In two dimensions, there are two permutations of CQMOM both of which can control the energy flux in x_1 and x_2 directions, which results in four combinations to use in the convective transport.

This concept of using a flux splitting algorithm is to adjust for the differences made by the quadrature approximation. Depending on the order of the conditional internal coordinates and the covariance between variables, different values for the quadrature nodes will be calculated. The reconstruction of quadrature nodes into the moments will yield slightly different results. For example, the two-dimensional PDF shown earlier with four quadrature nodes in each direction yields the differences in Table 6.1 for the higher order moment calculations needed for convective transport. These moments are calculated using the same normal distribution as shown in Figure 6.4. The highest error here is only 0.01 %; in order to correct for this small difference in the calculation, the convective flux would have to be calculated four times for the two-dimensional case. For a three-dimensional case, the computational work for the convective flux would have to be increased by eight times. With such a small difference in the values, this is a large amount of computational time to contribute to correcting such a small difference. In addition, using every permutation of the CQMOM method would nearly double the transported moment equations as well. For a large scale computation that the ARCHES code is typically used for, this computational expense cannot be justified. The implementation in the ARCHES codebase uses only one permutation of the CQMOM method.

Table 6.1: CQMOM permutation error.

Moment	$m_{0,8}$	$m_{8,0}$	$m_{4,4}$	$m_{5,4}$	$m_{4,5}$	$m_{8,1}$	$m_{1,8}$	
% change	5.57e-4	4.21e-6	5.74e-8	7.73e-6	2.91e-5	7.49e-5	2.92e-3	
Moment	$m_{6,4}$	$m_{4,6}$	$m_{8,2}$	$m_{2,8}$	$m_{7,4}$	$m_{4,7}$	$m_{8,3}$	$m_{3,8}$
% change	6.79e-5	4.412e-4	2.51e-4	6.11e-3	3.31e-4	3.44e-3	6.08e-4	1.03e-2

Both first-order upwind and a specialized Roe minmod scheme for pseudo second order spatial discretization have been implemented into the ARCHES codebase. In general, the set of convective fluxes for a set of moments, $\mathbf{F}_{\text{conv}}$ can be given by

$$\mathbf{F}_{\text{conv}} = \mathbf{G}^{+} - \mathbf{G}^{-}, \tag{6.52}$$

here $\mathbf{G}$ denotes the fluxes at the plus and minus faces of a cell given by

$$\mathbf{G}^{+} = G(\mathbf{M}_{i+1/2,l}, \mathbf{M}_{i+1/2,r}) \tag{6.53}$$

$$\mathbf{G}^{-} = G(\mathbf{M}_{i-1/2,l}, \mathbf{M}_{i-1/2,r}), \tag{6.54}$$

here $\mathbf{M}$ is the set of transported moment equations, the function G is

$$\mathbf{G}(\mathbf{M}_l, \mathbf{M}_r) = \mathbf{H}^{+}(\mathbf{M}_l) + \mathbf{H}^{-}(\mathbf{M}_r), \tag{6.55}$$

with

$$\mathbf{H}^{+} = \sum_{\alpha}^{N} \omega_{\alpha,l} \max(u_{\alpha,l}, 0) \begin{pmatrix} 1 \\ u_{\alpha,l} \\ u_{\alpha,l}^2, \\ u_{\alpha,l}^3 \\ \vdots \end{pmatrix} \tag{6.56}$$

$$\mathbf{H}^{-} = \sum_{\alpha}^{N} \omega_{\alpha,r} \min(u_{\alpha,r}, 0) \begin{pmatrix} 1 \\ u_{\alpha,r} \\ u_{\alpha,r}^2, \\ u_{\alpha,r}^3 \\ \vdots \end{pmatrix} . \tag{6.57}$$

This definition is for a set of moments with one internal coordinate. Expanding the formulation to multiple coordinates is straight forward, the elements of the matrix are simply expanded to contain the other abscissas raised to the power of the respective i, j, k moments that are transported

$$\begin{pmatrix} 1 \\ u_{\alpha,l} \\ u_{\alpha,l}^2, \\ u_{\alpha,l}^3 \\ \vdots \end{pmatrix} \longrightarrow \begin{pmatrix} 1 \\ u_{\alpha,l}^i v_{\alpha,l}^j w_{\alpha,l}^k \\ u_{\alpha,l}^i v_{\alpha,l}^j w_{\alpha,l}^k \\ u_{\alpha,l}^i v_{\alpha,l}^j w_{\alpha,l}^k \\ \vdots \end{pmatrix} . \tag{6.58}$$

For other spatial directions, the max and min functions are just applied to the v and w velocities for the y- and $z-$ directions. For the first order scheme, the weights and abscissas

are assumed to be constant across a cell, this is a step-wise function that for the i^{th} cell is expressed as

$$\mathbf{N}^n_{i-1/2,r} = \mathbf{N}^n_i, \quad \mathbf{N}^n_{i+1/2,l} = \mathbf{N}^n_i, \tag{6.59}$$

where $\mathbf{N}$ is the set of weights and abscissas. For the second order scheme, a minmod slope limiter is used. For the i^{th} cell this can be written as

$$\mathbf{N}^n_{i-1/2,r} = \mathbf{N}^n_i - \frac{\Delta x}{2}\delta\mathbf{N}_i \tag{6.60}$$

$$\mathbf{N}^n_{i+1/2,l} = \mathbf{N}^n_i - \frac{\Delta x}{2}\delta\mathbf{N}_i, \tag{6.61}$$

with

$$\delta\mathbf{N}_i = \text{minmod}\left(\frac{\mathbf{N}^n_i - \mathbf{N}^n_{i-1}}{\Delta x}, \frac{\mathbf{N}^n_{i+1} - \mathbf{N}^n_i}{\Delta x}\right), \tag{6.62}$$

where the minmod function is given by

$$\text{minmod}(x,y) = \text{sign}(x)\left(\frac{1+\text{sign}(xy)}{2}\right)\min(|x|,|y|). \tag{6.63}$$

and the sign function is

$$\text{sign}(x) = \begin{cases} -1 & x < 0 \\ 0 & x = 0 \\ 1 & x > 0 \end{cases}. \tag{6.64}$$

To highlight the difference in the spatial discretization schemes, a simple jet is convected using each of the methods. The domain is the same size as the earlier DQMOM demonstration, except only one jet is used. The steady state profile is shown in Figure 6.6. This figure shows the wide spreading that the first order spatial scheme undergoes as numerical diffusion, while the pseudo-second order scheme maintains a tighter profile of the jet. Wall interactions are also developed in the code for the CQMOM method.

At the wall a restitution coefficient, ϵ_w, can be prescribed, which accounts for kinetic energy lost due to the impact with the wall. When $\epsilon_w = 1$, this is a perfectly elastic collision and no momentum is lost. For an x-direction wall the boundary condition is given by [182]

$$\begin{bmatrix} \omega_\alpha \\ u_\alpha \\ v_\alpha \\ w_\alpha \end{bmatrix}_{\text{wall}} = \begin{bmatrix} \omega_\alpha/\epsilon_w \\ -\epsilon_w u_\alpha \\ v_\alpha \\ w_\alpha \end{bmatrix}_{\text{interior}}. \tag{6.65}$$

Adapting this for y- and z- direction walls simply requires changing which internal coordinate ϵ_w is applied to. For some physical models, various particles may be expected to deposit on walls. Adapting the wall interaction boundary condition to account for this

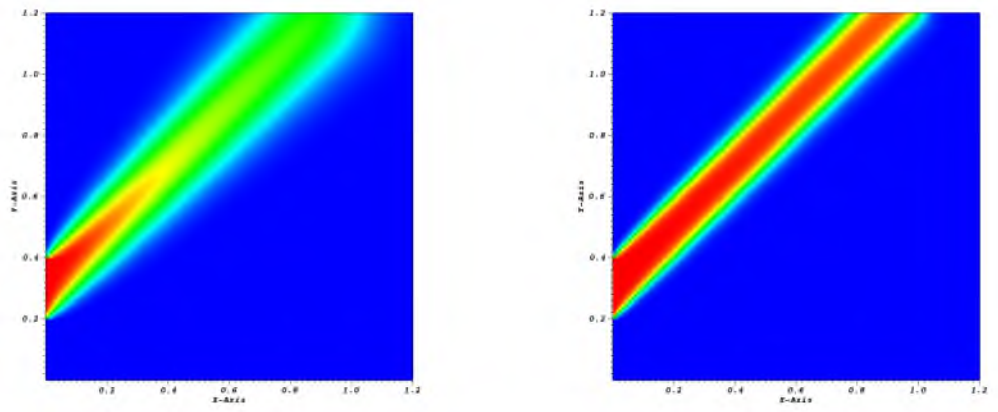

(a) (b)

Figure 6.6: A two-dimensional slice of a particle jet transported with (a) the first order CQMOM scheme and (b) the pseudo-second order scheme.

effect is rather straightforward. The reflecting particles are just multiplied by the fraction of particles that do reflect

$$\begin{bmatrix} \omega_\alpha \\ u_\alpha \\ v_\alpha \\ w_\alpha \end{bmatrix}_{\text{wall}} = \begin{bmatrix} (1-f_{\text{stick}})\omega_\alpha/\epsilon_w \\ -\epsilon_w u_\alpha \\ v_\alpha \\ w_\alpha \end{bmatrix}_{\text{interior}} , \tag{6.66}$$

here f_{stick} is the fraction of particles which hit the wall that are deposited. Models for f_{stick} will vary based on the physical process for various particles, models for coal are available in the literature [186, 15].

6.2.3 Extension for the Addition of Multiple Scalars as Internal Coordinates

The extension of CQMOM to a fourth dimension of internal coordinates is rather straight forward. An equation for the fourth dimension moments can be created and a similar procedure to the one used in Subsection 6.2.1 can be developed. First, start with the equation for the fourth-dimensional moments

$$m_{i,j,k,l} = \iiiint \xi_1^i \xi_2^j \xi_3^k \xi_4^l \eta(\xi_1,\xi_2,\xi_3,\xi_4) \mathrm{d}\xi_1 \mathrm{d}\xi_2 \mathrm{d}\xi_3 \mathrm{d}\xi_4 , \tag{6.67}$$

the quadrature approximation for these fourth order moments is given by

$$\begin{aligned} \eta(\xi_1,\xi_2,\xi_3,\xi_4) = & \sum_{\alpha_1}^{N_1}\sum_{\alpha_2}^{N_2}\sum_{\alpha_3}^{N_3}\sum_{\alpha_4}^{N_4} \omega_{1;\alpha_1}\omega_{2;\alpha_1,\alpha_2}\omega_{3;\alpha_1,\alpha_2,\alpha_3}\omega_{4;\alpha_1,\alpha_2,\alpha_3,\alpha_4} \times \\ & \delta(\xi_1-\xi_{1;\alpha_1})\delta(\xi_2-\xi_{2;\alpha_1,\alpha_2})\delta(\xi_3-\xi_{3;\alpha_1,\alpha_2,\alpha_3})\delta(\xi_4-\xi_{4;\alpha_1,\alpha_2,\alpha_3,\alpha_4}) . \end{aligned} \tag{6.68}$$

Now, define the conditional fourth dimension moments similar to before

$$\langle \xi_4^l \rangle | (\xi_1, \xi_2, \xi_3) = \int \xi_4^l \eta(\xi_4 | \xi_3, \xi_2, \xi_1) \mathrm{d}\xi_4 \ , \tag{6.69}$$

which describes the l^{th} conditional moment of ξ_4 conditioned on set values for ξ_1, ξ_2, ξ_3. Now, for simplicity define this as

$$\langle \xi_4^l \rangle_{\alpha_1,\alpha_2,\alpha_3} \equiv \langle \xi_4^l \rangle | (\xi_1, \xi_2, \xi_3). \tag{6.70}$$

The total number density of the system can be expressed as

$$\eta(\xi_1, \xi_2, \xi_3, \xi_4) = \eta(\xi_4 | \xi_3, \xi_2, \xi_1) \eta(\xi_1, \xi_2, \xi_3) \ . \tag{6.71}$$

Combining this with the quadrature node approximation, the definition of the conditional moment, and multiplying by the internal coordinates gives an equation for the quadrature reconstruction of the fourth-dimensional moments

$$m_{k_1,k_2,k_3,k_4} = \sum_{\alpha_1}^{N_1} \sum_{\alpha_2}^{N_2} \sum_{\alpha_3}^{N_3} \omega_{1;\alpha_1} \omega_{2;\alpha_1,\alpha_2} \omega_{3;\alpha_1,\alpha_2,\alpha_3} \xi_{1;\alpha_1}^{k_1} \xi_{2;\alpha_2}^{k_2} \xi_{3;\alpha_3}^{k_3} \langle \xi_4^{k_4} \rangle_{\alpha_1,\alpha_2,\alpha_3} \ . \tag{6.72}$$

With the correct moments, and the prior quadrature nodes known, the conditional fourth order moments can be calculated here similar to the previous method. As before, a new temporary variable is created, Ξ, defined by

$$\Xi_{\alpha_1,\alpha_2;k_3,k_4} = \sum_{\alpha_3}^{N_3} \omega_{\alpha_1,\alpha_2,\alpha_3} \xi_{3;\alpha_3}^{k_3} \langle \xi_4^{k_4} \rangle_{\alpha_1,\alpha_2,\alpha_3} \ . \tag{6.73}$$

Substituting this in to Eq. (6.72) gives

$$m_{k_1,k_2-1,k_3-1,k_4} = \sum_{\alpha_1}^{N_1} \sum_{\alpha_2}^{N_2} \omega_{1;\alpha_1} \omega_{2;\alpha_1,\alpha_2} \xi_{1;\alpha_1}^{k_1} \xi_{2;\alpha_2}^{k_2} \Xi_{\alpha_1,\alpha_2;k_3,k_4} \ , \tag{6.74}$$

and a new value for ζ is set as

$$\zeta_{\alpha_1;k_2,k_3,k_4} = \sum_{\alpha_2}^{N_2} \omega_{\alpha_1,\alpha_2} \xi_{2;\alpha_2}^{k_2} \Xi_{\alpha_1,\alpha_2;k_3,k_4} \ . \tag{6.75}$$

Then substituting this definition of ζ into Eq. (6.74) yields

$$m_{k_1,k_2-1,k_3-1,k_4} = \sum_{\alpha_1}^{N_1} \omega_{\alpha_1} \xi_{1;\alpha_1}^{k_1} \zeta_{\alpha_1;k_2,k_3,k_4} \ . \tag{6.76}$$

From here the method can be solved with a set of linear systems as before. A Vandermonde matrix is constructed from Eq. (6.76) as

$$\boldsymbol{V}_1 \boldsymbol{R}_1 \begin{bmatrix} \zeta_{1;k_2,k_3,k_4} \\ \zeta_{2;k_2,k_3,k_4} \\ \vdots \\ \zeta_{N_1;k_2,k_3,k_4} \end{bmatrix} = \begin{bmatrix} m_{0,k_2-1,k_3-1,k_4} \\ m_{1,k_2-1,k_3-1,k_4} \\ \vdots \\ m_{N_1-1,k_2-1,k_3-1,k_4} \end{bmatrix} . \tag{6.77}$$

Here, $\mathbf{V}_1$ and $\mathbf{V}_2$ have the same definitions as before. This set of matrices is then solved to get all ζ values by looping $k_2 = 1, \ldots, N_2$, $k_3 = 1, \ldots, N_3$, and $k_4 = 1, \ldots, 2N_4 - 1$. With

all the ζ values calculated, then these can be used in Eq. (6.73) to solve for all of the Ξ values. Each node in the first internal coordinate needs to solve this new set of matrices for each first-dimensional node, $\alpha_1 = 1 \ldots N_1$

$$\boldsymbol{V}_{2;\alpha_1}\boldsymbol{R}_{2;\alpha_1}\begin{bmatrix}\Xi_{\alpha_1,1;k_3,k_4}\\ \Xi_{\alpha_1,2;k_3,k_4}\\ \vdots \\ \Xi_{\alpha_1,N_2;k_3,k_4}\end{bmatrix} = \begin{bmatrix}\zeta_{\alpha_1;1,k_3,k_4}\\ \zeta_{\alpha_1;2,k_3,k_4}\\ \vdots \\ \zeta_{\alpha_1;N_2,k_3,k_4}\end{bmatrix}, \tag{6.78}$$

for each α_1 this is solved for $k_3 = 1, \ldots, N_3$ and $k_4 = 1, \ldots, 2N_4 - 1$. With all the Ξ values calculated, then the conditional moments of the fourth internal coordinate can be calculated for each α_1, α_2 node using Eq. (6.75) in a Vandermonde form as

$$\boldsymbol{V}_{3;\alpha_1,\alpha_2}\boldsymbol{R}_{3;\alpha_1,\alpha_2}\begin{bmatrix}\langle\xi_4^{k_4}\rangle_{\alpha_1,\alpha_2,1}\\ \langle\xi_4^{k_4}\rangle_{\alpha_1,\alpha_2,2}\\ \vdots \\ \langle\xi_4^{k_4}\rangle_{\alpha_1,\alpha_2,N_3}\end{bmatrix} = \begin{bmatrix}\Xi_{\alpha_1,\alpha_2;1,k_4}\\ \Xi_{\alpha_1,\alpha_2;2,k_4}\\ \vdots \\ \Xi_{\alpha_1,\alpha_2;N_3,k_4}\end{bmatrix}, \tag{6.79}$$

with

$$\mathbf{V}_{3;\alpha_1,\alpha_2} = \begin{bmatrix}1 & \cdots & 1\\ \xi_{3;\alpha_1,\alpha_2,1} & \cdots & \xi_{3;\alpha_1,\alpha_2,N_3}\\ \vdots & & \vdots \\ (\xi_{3;\alpha_1,\alpha_2,1})^{N_3-1} & \cdots & (\xi_{3;\alpha_1,\alpha_2,N_3})^{N_3-1}\end{bmatrix}$$

$$\text{and } \mathbf{R}_{3;\alpha_1,\alpha_2} = \begin{bmatrix}\omega_{\alpha_1,\alpha_2,1} & & \\ & \ddots & \\ & & \omega_{\alpha_1,\alpha_2,N_3}\end{bmatrix}. \tag{6.80}$$

For each quadrature node α_1, α_2 this set of matrices needs to be solved for $k_4 = 1, \ldots, 2N_4 - 1$. With the conditional moments solved for, each set can be run through the Wheeler algorithm as before to find the final quadrature nodes for the fourth internal coordinate.

After this, one could conceivably continue adding in additional temporary variables to solve sets of linear systems as the internal coordinate dimensionality is increased ad nauseum. However, this presents two major problems. First, the number of operations required for the CQMOM inversion from moments to quadrature nodes increases substantially for each dimension added. Secondly, the number of transport equations also increases quite substantially. If it is assumed that each $N_i = 2$, then each additional internal coordinate more than doubles the required moments transported via Eq. (6.19), and for $N_i = 3$ each additional coordinate nearly triples the required transported equations; the number of moment transport equations required are listed in Table 6.2.

Table 6.2: Transported moments required for $N_i = 2$ and $N_i = 3$.

Internal Coordinates	2	3	4	5	6	7
Transported Moments $N_i = 2$	10	22	46	94	190	382
Transported Moments $N_i = 3$	21	66	201	606	1821	5466

In order to prevent this exponential increase in the number of required moment transport equations, the assumption can be made that for any extra internal coordinates added to the system, $N_i = 1$. This greatly decreases the computational time from the CQMOM inversion, and reduces the number of moments required to be transported. To extend this to M-dimensional internal coordinate space, consider the case with $N_1 = 2$, $N_i = 1$ $i \geq 2$. As before, the quadrature nodes are calculated for the first internal coordinate with the Wheeler algorithm. Now consider the Vandermonde matrix for the second internal coordinate

$$\begin{bmatrix} 1 & 1 \\ \xi_{1;1} & \xi_{1;2} \end{bmatrix} \begin{bmatrix} \omega_1 & \\ & \omega_2 \end{bmatrix} \begin{bmatrix} \langle \xi_2 \rangle_1 \\ \langle \xi_2 \rangle_2 \end{bmatrix} = \begin{bmatrix} m_{0,1,0} \\ m_{1,1,0} \end{bmatrix} . \tag{6.81}$$

After solving this equation for the conditional moments, the weights and quadrature nodes for the second internal coordinate have the trivial answer of $\xi_{2;1} = \langle \xi_2 \rangle_1$, $\xi_{2;2} = \langle \xi_2 \rangle_2$, and $\omega_{2;1} = \omega_{2;2} = 1$. This is due to the definition of the conditional PDF having a zeroth moment of 1. Continuing this example, now consider the Vandermonde matrix that is required for the next internal coordinate

$$\boldsymbol{V}_1 \boldsymbol{R}_1 \begin{bmatrix} \zeta_{1;1,1} \\ \zeta_{2;1,1} \end{bmatrix} = \begin{bmatrix} m_{0,0,1} \\ m_{1,0,1} \end{bmatrix} , \tag{6.82}$$

with the zeta values known the next linear system to solve for each α_1 becomes a trivial equation of

$$\boldsymbol{V}_2 \boldsymbol{R}_2 \left[\langle \xi_3 \rangle_{\alpha_1,1} \right] = [1] \left[\langle \xi_2 \rangle^0_{\alpha_1,1} \right] \left[\langle \xi_3 \rangle_{\alpha_1,1} \right] = \left[\zeta_{\alpha_1;1,1} \right] , \tag{6.83}$$

which easily simplifies to

$$\langle \xi_3 \rangle_{\alpha_1,1} = \zeta_{1;\alpha_1,1}. \tag{6.84}$$

From here, it should be readily apparent that for any higher number of internal coordinates the $\boldsymbol{V}$ and $\boldsymbol{R}$ matrices continue to equate to 1. Thus any additional conditional moments can be set equal to the appropriate ζ value, provided that the initial matrix in Eq. (6.81) is filled with the correct moments. With this restriction, any higher order internal coordinate with only one node is only conditioned on the first internal coordinate. Mathematically, the PDF could be rewritten slightly as

$$\eta(\boldsymbol{\xi}) = \eta(\xi_M|\xi_1)\eta(\xi_{M-1}|\xi_1)\dots\eta(\xi_2|\xi_1)\eta(\xi_1), \tag{6.85}$$

this of course only holds for the specific example, and any extension places the conditioning on the highest internal coordinate with more than one node. In the method that was developed in the ARCHES codebase, up to the fourth internal coordinate may be specified with any number of quadrature nodes, the restriction $N_i = 1$ only comes into place for $i \geq 5$. The low number of internal coordinates was only used to show the derivation with more brevity. With four internal coordinates allowed to have more than one quadrature node Eq. (6.85) would be expressed as

$$\begin{aligned}\eta(\boldsymbol{\xi}) =& \eta(\xi_M|\xi_4,\xi_3,\xi_2,\xi_1)\eta(\xi_{M-1}|\xi_4,\xi_3,\xi_2,\xi_1)\eta(\xi_{M-2}|\xi_4,\xi_3,\xi_2,\xi_1) \\ &\times\cdots\times\eta(\xi_4|\xi_3,\xi_2,\xi_1)\eta(\xi_3|\xi_2,\xi_1)\eta(\xi_2|\xi_1)\eta(\xi_1)\ .\end{aligned} \tag{6.86}$$

It should be noted that the derivation for the calculation of the quadrature nodes shown here, no assumption of the properties of the internal coordinates was made. This also applies to the first three internal coordinates that were previously used in kinetic modeling section. The calculation of the quadrature nodes for CQMOM has no dependency on whether the internal coordinates are velocities or other passive scalar properties, and has no explicit dependency on ordering of the internal coordinates.

6.2.4 Source Terms for Particle Modeling

With the implementation of a full three-dimensional kinetic equation of CQMOM into the LES code, appropriate momentum source terms need to be added into the moment transport equations. For terms that do not affect the birth or death rate of particles, the source terms in Eq. (6.26) can be expressed as

$$S(\xi_1,\xi_2,\xi_3,\dots) = \sum_{i=1}^{M}\frac{\partial G_i(\boldsymbol{\xi})\eta(\boldsymbol{\xi})}{\partial\xi_i}. \tag{6.87}$$

When the integral is applied, then the source term for the first internal coordinate of the moment $m_{i,j,k,\dots}$ is

$$S(\xi_1,\xi_2,\xi_3,\dots)_1 = \int\cdots\int\xi_1^i\xi_2^j\xi_3^k\cdots\frac{\partial G_i(\boldsymbol{\xi})\eta(\boldsymbol{\xi})}{\partial\xi_i}\mathrm{d}\xi_1\mathrm{d}\xi_2\mathrm{d}\xi_3\cdots, \tag{6.88}$$

using integration by parts over the first internal coordinate yields

$$= -i\int\cdots\int\xi_1^{i-1}\xi_2^j\xi_3^k\cdots G_i(\boldsymbol{\xi})\eta(\boldsymbol{\xi})\mathrm{d}\xi_1\mathrm{d}\xi_2\mathrm{d}\xi_3\cdots. \tag{6.89}$$

For simple source terms this could be expressed as a function of an integer moment – i.e., if G_1 was constant this term would be equal to $-iG_1m_{i-1,j,k,\dots}$ – for complex source

terms a quadrature approximation would be required. In Pedel et al. [129, 130, 131], there are two momentum source terms to be included in the simulation of inert particles: particle drag and the gravitational source. The gravitational source term is

$$\frac{\mathrm{d}\mathbf{u}_p}{\mathrm{d}t} = \mathbf{g}\frac{\rho_p - \rho_g}{\rho_p} \ , \tag{6.90}$$

since this is in terms of $\frac{\mathrm{d}\xi_i}{\mathrm{d}t}$, the acceleration is the equivalent to a growth term – seen in Chapter 4 – for the velocity, and exists in the PBE as $\partial(\mathrm{d}u/\mathrm{d}t)\eta(u,t)/\partial u$. Then in one dimension multiplying this by u_1^i and integrating over the domain yields an expression in terms of the moment as

$$\int u_1^i \mathbf{g}\frac{\rho_p - \rho_g}{\rho_p}\eta(u_1)\mathrm{d}u_1 = -\int i u_1^{i-1}\mathbf{g}\frac{\rho_p - \rho_g}{\rho_p}\eta(u_1)\mathrm{d}u_1 = -i m_{i-1} g_1 \frac{\rho_p - \rho_g}{\rho_p} \ . \tag{6.91}$$

The first step in the above equation results from applying an integration by parts method to the integral. This equation is dependent on the $i-1^{\text{th}}$ moment, and thus would be unclosed for a given set of moments. This requires the quadrature approximation to calculate the source term. The drag model used is empirical based on the Reynolds number for the typical size regime of coal particles [168]. It is given in terms of an acceleration term as

$$\frac{\mathrm{d}u_i}{\mathrm{d}t} = \frac{f_{\text{drag}}}{\tau_p}(u_{g,i} - u_{p,i}) \ , \tag{6.92}$$

if the same method used in Eq. (6.91) is applied to the drag term, then for a moment source term it becomes

$$\frac{\mathrm{d}m_i}{\mathrm{d}t} = -i\frac{f_{\text{drag}}}{\tau_p}(m_{i-1}u_g - m_i) \ , \tag{6.93}$$

which as before relies on the $i-1^{\text{th}}$ moment, and requires a closure approximation. In the drag equation, the particle relaxation time, τ_p, is given by

$$\tau_p = \frac{\rho_p d_p^2}{18\mu_g} \ , \tag{6.94}$$

and the drag coefficient, f_{drag}, is given by

$$f_{\text{drag}} = \begin{cases} 1 + 0.15Re^{0.687} & \text{if } Re < 994; \\ 0.0183Re & \text{if } Re > 994. \end{cases} \tag{6.95}$$

Here, the limits of the Reynolds number have been changed slightly from conventional literature to make the transition between the two correlations smoother. The Reynolds number used in Eq. (6.95) is the relative Reynolds number, defined as

$$Re_r = \frac{|U_g - U_p| d_p \rho_g}{\mu_g} \ . \tag{6.96}$$

The corresponding gas-coupled form is the opposite force applied as the surface area of the particles on the gas multiplied by the ratio of the densities summed over all of the quadrature nodes

$$\frac{\mathrm{d}u_{g,i}}{\mathrm{d}t} = \sum_{\alpha}^{N} \frac{\mathrm{d}u_{p,i}}{\mathrm{d}t}_{\alpha} \omega_\alpha \frac{\rho_p}{\rho_g} \frac{\pi}{6 d_p^3}. \tag{6.97}$$

Any general source term can be used with the quadrature approximation, regardless if the source term is applied to the internal velocity coordinates or to any of the scalars in the system. As long as the source term can be expressed in the general form of $\mathrm{d}\xi_i/\mathrm{d}t$ – an acceleration or growth term – then the source term for the $i, j, k...$ moment can be expressed as

$$m_{ijk\cdots k_M,\text{source}} = i \sum_{\alpha}^{N} \omega_\alpha \mathrm{d}\xi_{p,1}/\mathrm{d}t_\alpha \xi_{1,\alpha}^{i-1} \xi_{2,\alpha}^{j} \xi_{3,\alpha}^{k} \times \cdots \times \xi_{M,\alpha}^{k_M}. \tag{6.98}$$

Note that this form assumes that this source term is applied to the first internal coordinate. For each internal coordinate source term, the exponent with the -1 is changed to that internal coordinate and the coefficient in front of the summation is changed to that internal coordinate's exponent for the corresponding moment. The framework that has been built into the ARCHES codebase should allow for the easy addition of more scalar internal coordinates for the modeling of physical systems.

6.3 CQMOM Simulations

For the validation of the CQMOM portion of the code, several test cases have been run to verify that the code is implemented correctly. Some of these include simple periodic tests, along with flows that exhibit no fluid-particle interaction to ensure that particle trajectory crossing is working as intended. After the verification of the CQMOM, working validation cases were developed to compare CQMOM simulation results to experimental data of inert particle flows. The validation cases include both monodisperse and poly disperse inert particle flows. For the monodisperse case, the three velocities are used as the only internal coordinates. For the polydisperse case, the diameter is added as an internal coordinate and a few different moment configurations are tested.

6.3.1 CQMOM Tuning Parameters

This is a brief discussion of the various tuning parameters that have been implemented into the ARCHES codebase in order to maintain numerical stability of the CQMOM convection. The parameters were tuned empirically until suitable values were found that kept physical cases from resulting in unrealizable moment space.

Two of these parameters are the same ones used in the adaptive Wheeler algorithm of Yuan and Fox [195]. The first of these is e_{abs}, which sets a limit on the ratio between the largest and the smallest abscissas. The second of these is $r_{\min}$, which sets a limit on ratio between the maximum and minimum weight values. If either of these parameters is not met, then the number of quadrature nodes is reduced by 1, and the Wheeler algorithm is run again. This helps limit poor abscissas values from being calculated in the far tails of the distribution.

In the implementation in the ARCHES code, a few additional parameters were added to maintain realizable moment space. The first is a $m_{0,\min}$, which dictates the minimum value of the number density for the quadrature nodes to be calculated; if the zeroth moment is below this value all abscissas and weights are set to zero. The second is a clipping on the individual abscissa, for both high and low values, $\xi_{i,\max}$ and $\xi_{i,\min}$. If a quadrature node is lower than this value and the abscissa value is outside of the clip parameters, rather than being clipped, the quadrature node weight and abscissa are set to zero. If any clipping occurs, then the new quadrature nodes are used to reconstruct new values for the moments at the updated time-step. The third parameter is a limit on the minimum weight of the abscissa, $\omega_{\min}$, for calculating the convective flux. Below this limit the flux is calculated to be zero. As long as the minimum values here are orders of magnitude lower than the number density of the flow, there should be very little impact on the simulation. These are in place to prevent areas away from the main flow from having some numerical diffusion cause an unrealizable moment set.

6.3.2 CQMOM Verification Cases

The first test case looks at a two-quadrature node case where two jets are coming from different walls. One is from the x-direction and one is from the y-direction. Each jet is initialized with a point distribution so that only one environment exists with a number density $m_{00} = 1.0$. The case here is periodic in z with 1 m by 1 m dimensions in x and y with a coarse mesh of 20 by 20 by 2 cells. The two streams are allowed to cross in the center where the adaptive method calculates two separate environments. This is the simplest case that can be run to demonstrate that the implementation of the method has been done correctly. The case also demonstrates that the adaptive method has been adjusted so that a zero mean value can be handled, even when the advection direction is not the primary conditioned variable. The number density profile is shown in Figure 6.7.

This system uses two quadrature nodes in u and one node in v, which results in the following transported moments for the $v|u$ permutation: $m_{00}, m_{10}, m_{20}, m_{30}, m_{01}, m_{11}$. In

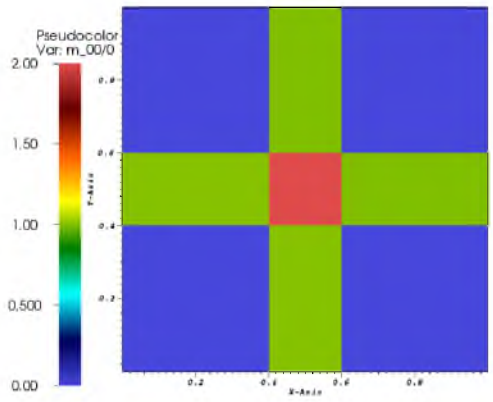

Figure 6.7: A slice showing the zeroth moment (number density) of the two-dimensional particle trajectory crossing case after steady state has been achieved.

Figure 6.8, the weights for the steady state are shown. As the inlets are initialized with only point distributions, the area near the inlet contains only weight 1. When the two streams of particles cross in the center, the adaptive CQMOM algorithm results in the calculation of two separate environments. After crossing, there is no cross-contamination between the environments, and the streams exist with only one environment for a point distribution, again.

A similar test case is setup with four quadrature nodes with two nodes in u and two in v; this adds four moments to the prior set: $m_{02}, m_{03}, m_{12}, m_{13}$. The case is 1.2 m by 1.2 m in x and y space with a periodic condition set in the z-direction, the resolution is 100 by 100 by 2. This has two inlets on the same face, with each initialized as a distribution rather

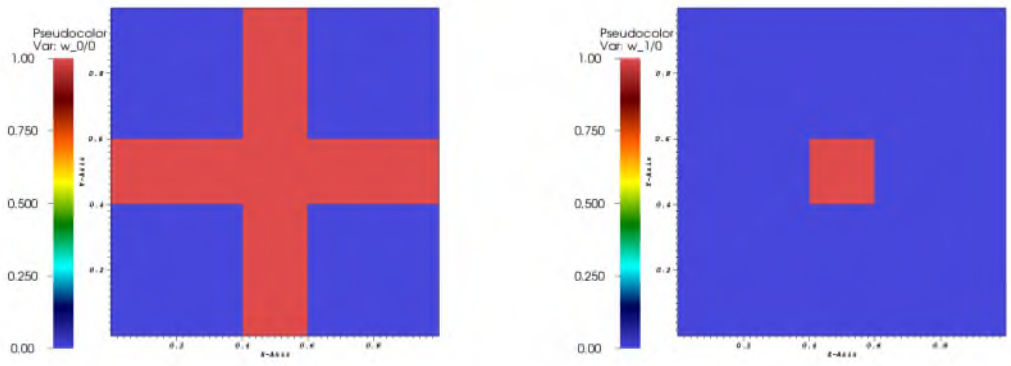

(a) (b)

Figure 6.8: A slice of the-two dimensional particle trajectory crossing case showing the two weights of the system after steady state has been achieved.

than a point. This case has geometry and velocities identical to the DQMOM case shown earlier. The jets cross diagonally and both x- and y- direction momentum are maintained. A steady state slice of this is shown in Figure 6.9.

A test case was setup to demonstrate particle wall interactions. A channel is setup with height of 0.5 m and width of 2.0 m with a periodic condition in the z-dimension, the resolution used is 120 by 30 by 2. The inlet used has an average velocity of 1.0 m/s in both x and y with a variance of 0.0001. The wall restitution coefficient is changed to show how it impacts the wall-normal velocity. The first case uses a wall restitution coefficient of $\epsilon_w = 1.0$, corresponding to an elastic collision, and the second uses a wall restitution coefficient arbitrarily set to $\epsilon_w = 0.75$. Each time the particles hit the wall the v-velocity is decreased by 25 %. The number density for these cases is shown in Figure 6.10.

The last test case demonstrates particle trajectory crossing for CQMOM convection in all three spatial dimensions. This case is run in a cubic 1.0 m^3 box with a resolution of 100 cells in each physical dimension, resulting in 1 million cells in the domain. The x-face has four inlets on it which are aimed towards the center of the domain to cross at the same point. The values for these inlets are listed in Table 6.3; each of these inlets is circular with a radius of 0.1 meters, and an average u-velocity of 1.0 m/s.

This simulation is run for 2000 time-steps to achieve the steady state solution to the moment transport equations. In Figure 6.11, a three-dimensional rendering of the steady state solution of these four jets crossing is shown.

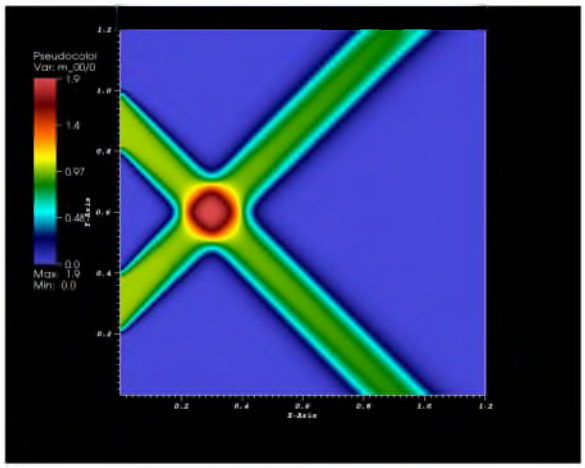

Figure 6.9: A two-dimensional slice of the two-dimensional particle trajectory crossing case showing the zeroth moment (number density) after steady state has been achieved.

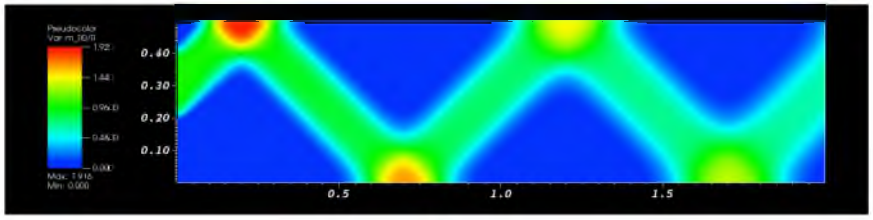

(a)

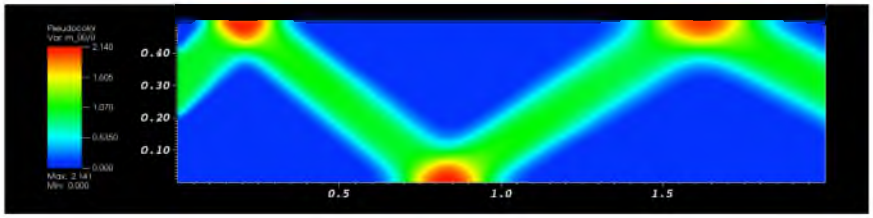

(b)

Figure 6.10: Wall interactions in a channel flow system. (a) shows a restitution coefficient of 1.0 – an elastic collision, (b) shows a restitution coefficient of 0.75 where the particles lose v-velocity as they bounce off the walls.

Table 6.3: Inlet conditions used for three-dimensional CQMOM example.

	center y(m)	center z(m)	ave V(m/s)	ave W(m/s)
inlet 1	0.25	0.25	1.0	1.0
inlet 2	0.75	0.25	1.0	-1.0
inlet 3	0.25	0.75	-1.0	1.0
inlet 4	0.75	0.75	-1.0	-1.0

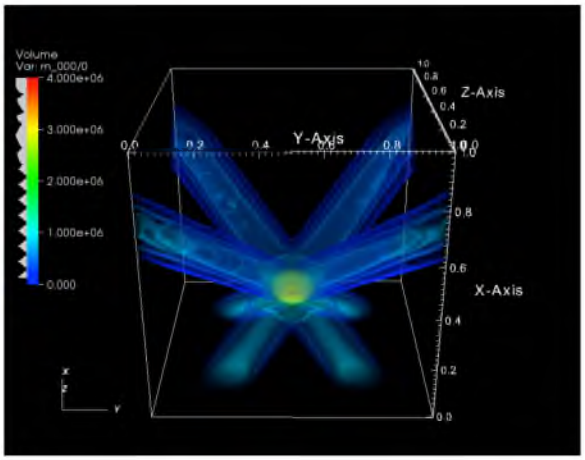

Figure 6.11: A rendering of the three-dimensional particle trajectory crossing case after steady state has been achieved.

6.3.3 CQMOM Validation Cases

For the validation of the CQMOM, the literature data from Budilarto [16] were used. The cases are very similar to the ones that were examined in the section of turbulent inlets in Chapter 3 with the same geometry and velocity ratio cases. The difference is in the inclusion of particles. In the cases here, the central nozzle jet is injected with particles – but not the annular flow. The particles that are injected are 2500 kg/m^3. This is analogous to coal burners, with the interior jet containing fuel, and the exterior jet as the oxidizer stream.

The flows here used the digital filter generator for the inlet condition [79]. As shown in Section 3.5, this type of inlet has a slightly better result in some cases, such as velocity ratio of 1.5, than the synthetic eddy method. The marginal difference in the computational cost to generate the inlet is neglected. The fluctuation level at the inlet was set to the fluctuations from the experimental data, rather than an isotropic 2% of velocity inlet profile; as shown, this is significantly better in the single phase flow cases.

The data in Budilarto [16] have two different particle sizes that are utilized at all three of the velocity ratios. The average for these particle size distributions is 25 μm and 70 μm. For the 70 μm cases, it was assumed that the particle size is monodisperse. Pedel et al. utilizes this assumption in a previous DQMOM particle study [131]. With the utility that is built into the particle models, this assumption allows for the particle diameter to be removed as an internal coordinate of the system, which decreases the moment transport equations required – and thus reduces the cost of the simulation. For the 25 μm case, a polydisperse distribution will be used, which will require the inclusion of the diameter as an internal coordinate.

These cases all have the two-way physical coupling between the fluid and the particle phases enabled. The source terms used are the drag model of Eq. (6.92) and Eq. (6.97), and the gravity force from Eq. (6.90). All the cases will be run using a slightly higher resolution than those from Chapter 3. The domain size is the same 0.28 meter cubic box, but the grid resolution has been increased to 300 by 300 by 300 for a total of 27 million cells run on 1728 processors.

The 70 μm size particle case will be discussed first. Here, the accuracy in increasing the number of quadrature nodes is examined. For each of the velocity ratios, two different numbers of quadrature nodes are used. For the first case, eight total quadrature nodes are used, with two internal coordinates in each dimension and the conditional set up as w conditioned on v, u conditioned on u. This leads to the set of moment transport equations

in Table 6.4. For the second case, only four total quadrature nodes are used. Two nodes are used in the u coordinate, two in the v coordinate and only one in w. This reduces the number of transported moments from 22 to 14, and halves the computational work that is required in the calculation of the convection and source terms. This set of transport equations are listed in Table 6.5.

The moments are initialized with a constant u velocity of 9.6 m/s. The total number density is the same as used in previous studies of $1.3e9$ $\#/\mathrm{m}^3$ [131]. A point distribution is used for the v and w velocities with nodes of -0.328 and 0.328. A second case is used with a small perturbation to the particle u-velocity using values of ± 0.1 of the base; this may help avoid some singularities in the matrices when calculating the weights and abscissas of the system.

A smaller case is run to test the effect of using four versus eight quadrature nodes. The resolution for this case is 100^3 over the same physical size of the domain. The plot in Figure 6.12 shows the centerline averaged particle velocity data for the two different number of nodes for two of the velocity ratio cases. As seen here, there is only a minor difference in the simulation results when the number of quadrature nodes is increased. The plot in Figure 6.13 shows the centerline data for the time-averaged fluid velocities for the same case. As with the particle velocities there is very little change in these results when the number of quadrature nodes is increased from four to eight.

Table 6.4: Moments used for eight quadrature node CQMOM.

m_{000}	m_{100}	m_{200}	m_{300}
m_{010}	m_{110}		
m_{020}	m_{120}		
m_{030}	m_{130}		
m_{001}	m_{002}	m_{003}	
m_{101}	m_{102}	m_{103}	
m_{011}	m_{012}	m_{013}	
m_{111}	m_{112}	m_{113}	

Table 6.5: Moments used for four quadrature node CQMOM.

m_{000}	m_{100}	m_{200}	m_{300}
m_{010}	m_{110}		
m_{020}	m_{120}		
m_{030}	m_{130}		
m_{001}	m_{101}	m_{011}	m_{111}

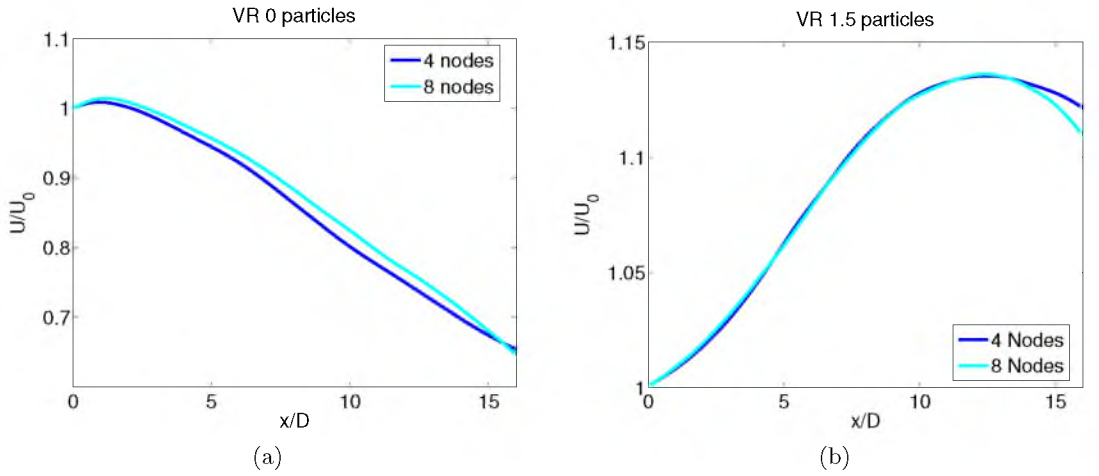

Figure 6.12: The centerline data for the time-averaged particle velocities using four versus eight total quadrature nodes. (a) shows the VR = 0.0 case and (b) shows the VR = 1.5 case.

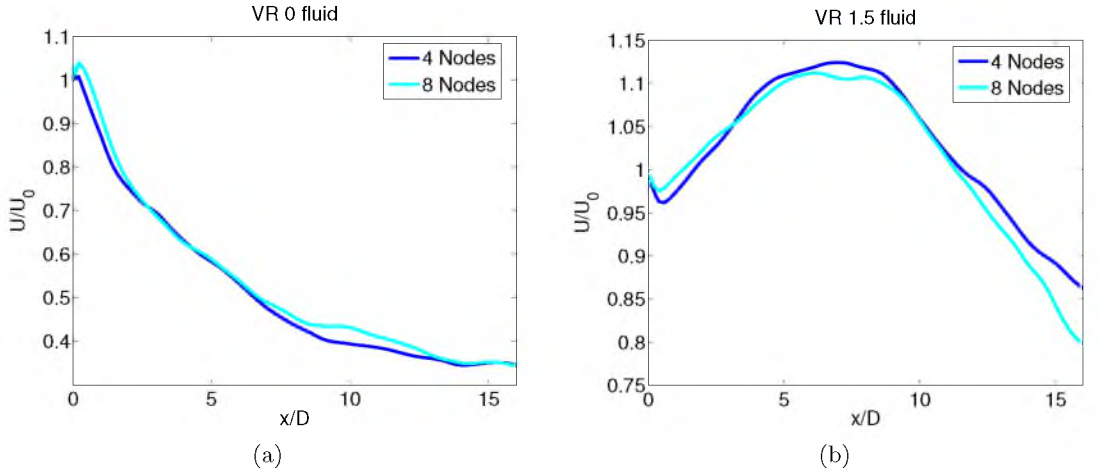

Figure 6.13: The centerline data for the time-averaged fluid velocities using four versus eight total quadrature nodes. (a) shows the VR = 0.0 case and (b) shows the VR = 1.5 case.

The main reason for this comparison is that in Yuan and Fox [195] and other prior QBMM studies, it is recommended to use a minimum of two quadrature nodes per internal coordinate. The overall timing of using the two different number of quadrature nodes was compared. The results for both the average timing per patch and the maximum timing is shown in Figure 6.14. The five major Uintah tasks that involve CQMOM are shown. These tasks include the convective flux calculation, the moment source term calculation, the inversion of moments into weights and abscissas, the calculation of individual sources, and the correction term for stability.

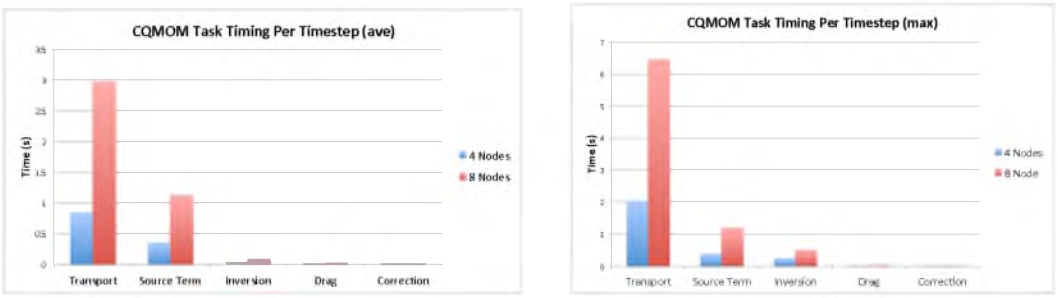

(a) (b)

Figure 6.14: The Uintah task timing for the five major components of the CQMOM transport equations. (a) shows the average over all patches, (b) shows the maximum.

The timing here shows that the computational cost of increasing the number of nodes from four to eight increases nearly three-fold. This is mostly due to the additional transport equations, however, that would only account for about two times of the cost. The additional computational cost comes from the summation terms that exist in both the convective flux equations and in the moment source term equation. As the number of quadrature nodes double, the work done to calculate both of these terms for the transport equations that are already included is doubled, and this accounts for the rest of the increase in the computational cost. Because of this vast increase in computational cost for little change in simulation results, it is justifiable to use four total quadrature nodes for the rest of the simulations performed. A few other conclusions about the timing can be made. The tuning parameters for the stability shown in Subsection 6.3.1 are very negligible in terms of the cost. In addition, the moment inversion technique is much cheaper than the actual transport of the moment equations. For further improvement of the speed of CQMOM, the convection calculation and the source term calculation are the main areas that should be examined.

Tests to compare using the perturbation of the first internal coordinate to the case with using a constant value for the first internal coordinate were conducted. These two cases were run at the higher resolution case with 27 million total cells. The base jet case with a velocity ratio of 0.0 was used for the comparison. The centerline time-averaged particle and fluid velocities are shown in Figure 6.15.

In Table 6.6, a list of three different ways to initial the first conditional internal coordinate, in this case the u-velocity, is shown. Each case uses the same nodes for the v- and w- velocities with different initializations for the u-velocity. The first case shows initializing with a constant velocity in u; this results in a loss of information in the last internal coordinate as only zero velocity is calculated for w. The second case applies the perturbation

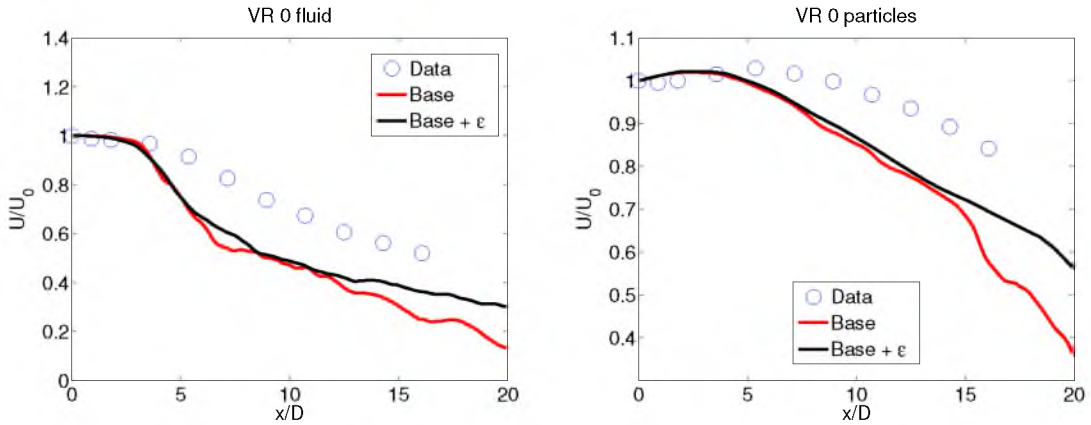

Figure 6.15: The time-averaged centerline data for the fluid velocity (a) and the particle velocity (b) for the VR = 0.0 high-resolution case.

to initial nodes alternating the ±0.1, and results in the CQMOM algorithm returning the exact value of the nodes back. The difference between these two initializations is shown graphically in Figure 6.16. The third case still applies the perturbation, but use −0.1 for the first two, and +0.1 for the second two. Even with the perturbation applied, this third case results in the loss of information in the last internal coordinate of the system, which highlights one of the intricacies of CQMOM, in that careful specification of inlet conditions should be a high priority. It may be possible to use full normal or uniform distributions rather than a summation of point distributions to initialize moments in CQMOM in order to avoid these singularities. The downside to this would be that the exact values of the abscissas would not be easy to specify to specific values. The benefit to using a summation of point distributions is that the Wheeler algorithm is guaranteed to return the exact nodes from which moments are fed.

The data in this plot show that during the early portion of the jet, the particle velocity is nearly identical in the two cases. Once the core of the jet begins to break up downstream the base case starts to differ from the perturbated case, slightly at first, and then proceeds to diverge significantly in the very far-field region of the jet. The data for the fluid velocity show a similar trend, where the near-field region of the jet is unaffected by the type of initialization. However, as before when the core region of the jet breaks up the base case deviates slowly at first and then completely diverges form the perturbated case in the far-field region. A reason for this could be the loss of data that occurs when the first internal coordinate is represented by a point distribution. The adaptive method immediately forces the total number of quadrature nodes to two, and several high order mixed moments are

Table 6.6: Initialized order of quadrature nodes.

initial $u_{p,y}$	0.328	0.328	-0.328	-0.328
initial $u_{p,z}$	0.328	-0.328	0.328	-0.328
initial $u_{p,x}$ case 1	9.6	9.6	9.6	9.6
resulting ω_α	6.5e8	6.5e8	0.0	0.0
resulting $u_{p,y}$	-0.328	0.328	0.0	0.0
resulting $u_{p,z}$	0.0	0.0	0.0	0.0
initial $u_{p,x}$ case 2	9.59	9.61	9.59	9.61
resulting ω_α	3.25e8	3.25e8	3.25e8	3.25e8
resulting $u_{p,y}$	-0.328	0.328	-0.328	0.328
resulting $u_{p,z}$	0.328	0.328	-0.328	-0.328
initial $u_{p,x}$ case 3	9.59	9.59	9.61	9.61
resulting ω_α	6.5e8	6.5e8	0.0	0.0
resulting $u_{p,y}$	0.328	-0.328	0.0	0.0
resulting $u_{p,z}$	0.0	0.0	0.0	0.0

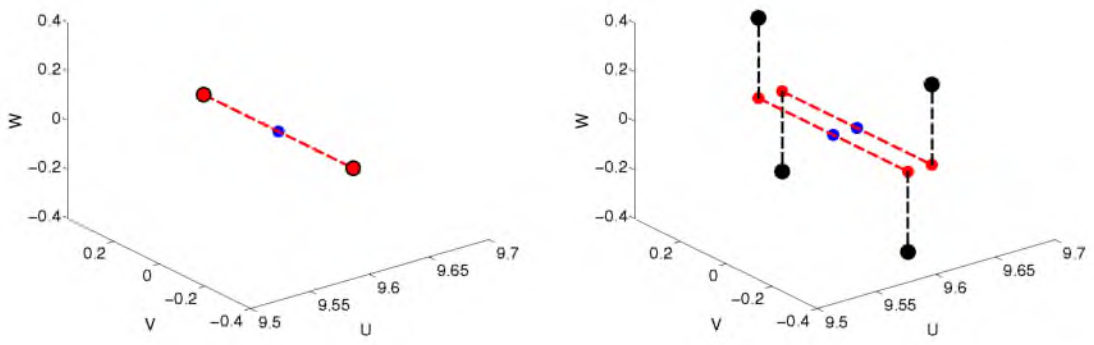

Figure 6.16: Graphical representation of the initialized nodes of the system. (a) corresponds to no perturbation, and (b) corresponds to the case with perturbation of the u-velocity nodes.

unused in the calculation of the nodes, and subsequent convective transport of those nodes. In the near-field region, the particles are likely moving at a similar enough speed so that the loss of this data is inconsequential. As the shear region breaks up the core of the jet and particles begin to spread out, and the loss of the data in the quadrature nodes may play a role in the discrepancies here. While neither simulation case is particularly close to the experimental data after initial jet break-up occurs, the perturbated case shows the closest agreement in the far-field region.

The centerline time-averaged data for all three of the velocity ratio cases is shown in Figure 6.17. For all three cases the fluid velocity in the near-field region shows good

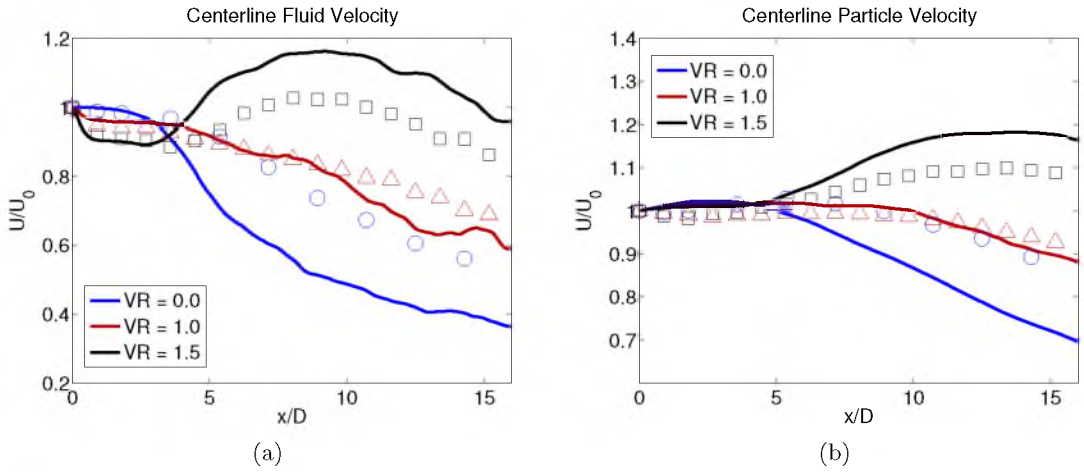

Figure 6.17: The time-averaged centerline data for the fluid velocity (a) and the particle velocity (b) for all of the velocity ratio cases. Lines show the simulation results and the markers show the respective experimental results.

agreement with the experimental data, including the dip in velocity for the VR = 1.5 case from the entrainment of the central jet. The VR = 1.0 case performs the best across most of the range of the jet, but does start to show poor results in the far-field region. The simulation data from the VR = 1.5 case overshoots the experimental data, but maintains the trend in the downfield location where the peak velocity is reached from the merging of the annular flow. The base VR = 0.0 case shows the least amount of agreement with the experimental data set, as the decay is widely overestimated. These results are fairly consistent with those of the turbulent inlets shown in Chapter 3 in terms of which cases performed the best in the LES code.

For the particle velocity data shown in Figure 6.17, the results for all three cases again show relatively good agreement with the experimental data in the near-field region. For the VR = 0.0 case, the simulation data again show poor agreement with the experimental data, as the velocity decays at a much faster rate. The VR = 1.0 case matches the experimental data quite well, without the inconsistency in the far-field region that was seen in the fluid velocity. The data from the VR = 1.5 case again show the experimental data overshoot the maximum velocity peak in the far-field region. However, the data from the VR = 1.5 case do match the downfield location peak, and also show the lack of decay in the near jet region, as the large particles have a slow relaxation time and are not constrained as much as the fluid flow.

The time-averaged data for the three velocity ratio cases for the fluctuations of the velocity are shown in Figure 6.18. The results for the simulation velocity fluctuation data

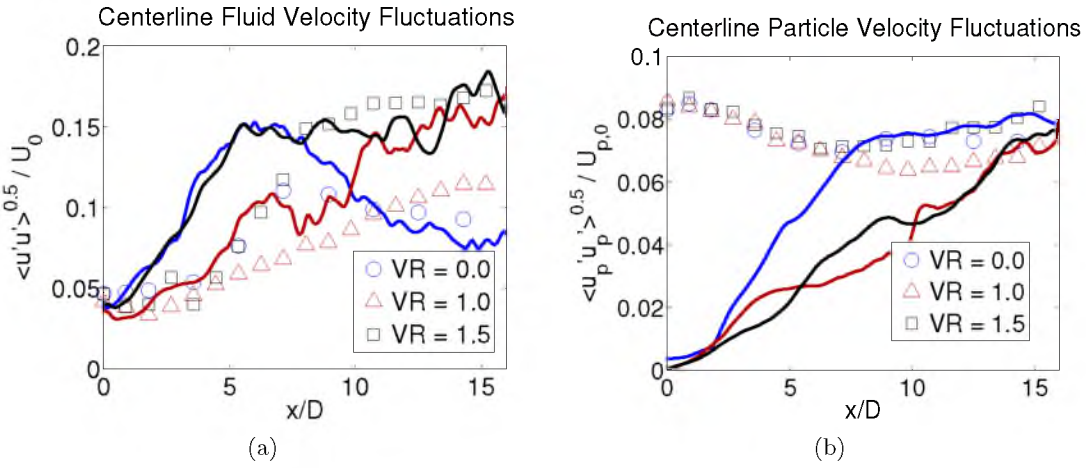

Figure 6.18: The time-averaged centerline data for the fluid velocity fluctuations (a) and the particle velocity fluctuations (b) for all of the velocity ratio cases. Lines show the simulation results and the markers show the respective experimental results.

show considerable difference than the experimental data. For the fluid velocity fluctuations, the VR = 0.0 vase spikes very high early on in the simulation, although qualitatively it does begin to decay down after the core of the jet breaks down, and does reach experimental values in the far-field region. Overall, the VR = 1.0 case shows higher values in the simulation for the fluctuations than the experimental data, but it does follow the same qualitative trend with a near constant increase in the value. The case with VR = 1.5 spikes very early on in the simulation fluctuation data, but in the far field region it appears to start to level out at a similar value to the experimental data.

For the particle velocity fluctuations in Figure 6.18, significant differences in the data between the experimental data and the simulation data exist. In order to keep consistency with the specifications of Pedel et al. [131], the initial velocity for the particles was set to a constant value for the VR = 1.0 and VR = 1.5 cases shown here. For the VR = 1.0 only a small perturbation of the inlet was used, as shown previously, which is the reason the inlet is slightly different than the other velocity ratio cases. The fluctuations in the particle velocity eventually develop to the experimental values, but it takes nearly the full domain do to so for the VR = 1.0 and 1.5 cases, and about half of the domain to develop for the VR = 0.0 case. A three-dimensional rendering of the particles spreading out is shown in Figure 6.19 for the VR = 0.0 case.

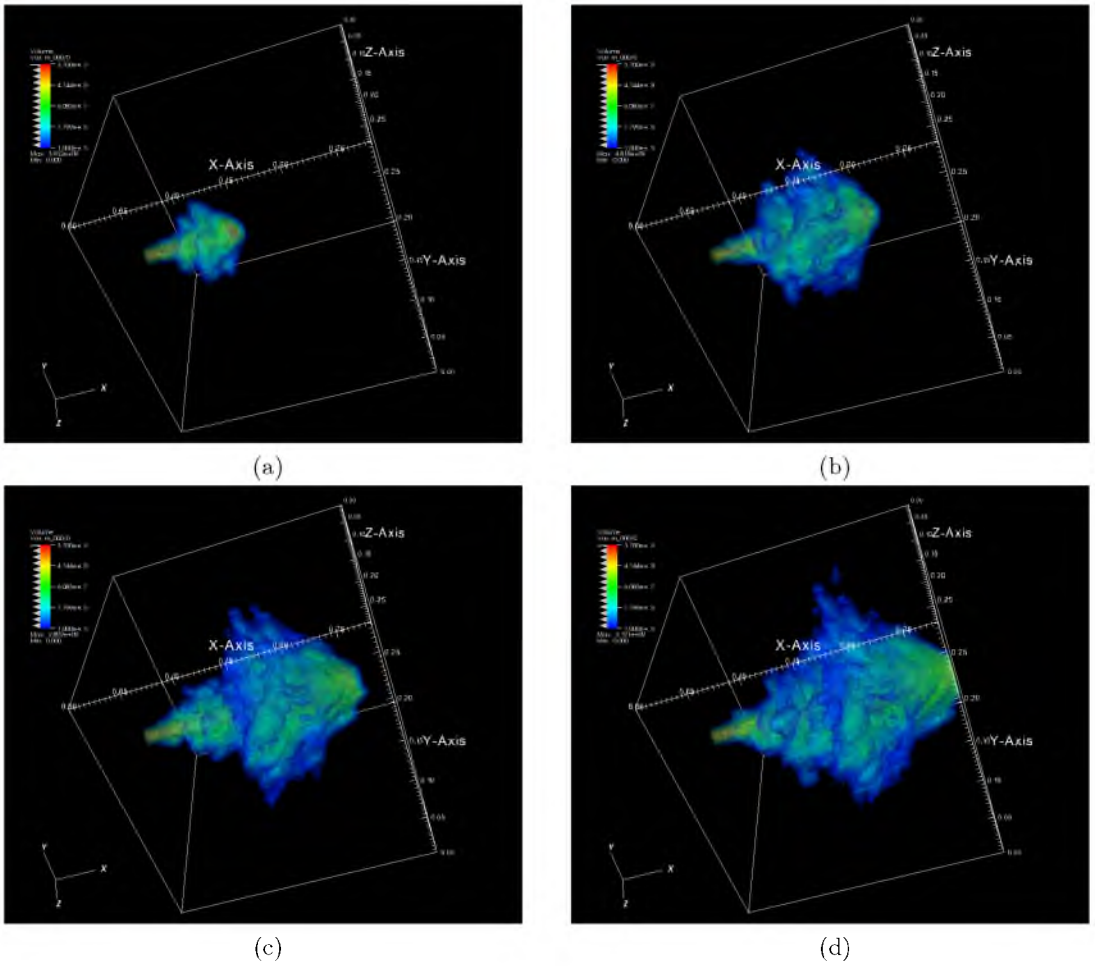

Figure 6.19: A three-dimensional rendering of the evolution of the particle jet. This shows times at (a) $t = 0.015$s, (b) $t = 0.03$s, (c) $t = 0.045$s, (d) $t = 0.06$s.

6.3.4 CQMOM Validation Cases with Diameter

For the 25 μm case, the diameter is now included as an internal coordinate. There are two possibilities for this expansion to use a scalar as an internal coordinate. One is that the scalar can be used as the first conditioned internal coordinate, and the second is that is can be used as the final conditioned internal coordinate. Both of these cases will be examined in comparison to the experimental data to get a better understanding of which case leads to better results. The specification for the 25 μm case is done with a perturbation so that the exact initial nodes are recovered after the CQMOM algorithm, as discussed and shown in Table 6.6.

As shown in Figure 6.12, four nodes provides adequate accuracy in the simulation results when compared to the simulation case with eight quadrature nodes. As such, only four quadrature nodes will be utilized for the 25 μm cases. To state more explicitly: the first

case is set up with w conditioned on v, u, d; conditioned on u, d; conditioned on d. If the same approach is used such that two quadrature nodes are used in the first and second coordinates and one quadrature node is used for the higher coordinates, this results in four total quadrature nodes. The resulting set of transport equations required is then 18 moments, these are listed in Table 6.7. For the second case d is conditioned on w, v, u; conditioned on v, u; conditioned on u. The same set of moments is utilized, but the order of the internal coordinates is changed here. These cases will be referred to as "scalar-conditioned"(SC) and "velocity-conditioned"(VC), respectively. For the initialization of the moments the small particles are assumed to be close to the average of the fluid flow, where the u-velocity is set as 11.6 ± 0.01 m/s, and the v- and w-velocities are set as 0.0 ± 0.0001. These nodes have been initialized in the correct order to return the same values through the CQMOM inversion algorithm, as demonstrated in Table 6.6. The radius nodes are set to 20 μm and 30 μm.

In addition, one possible alternative set up for the moments was considered. This set up would utilize all four quadrature nodes in the radius for the first internal coordinate. This may provide an advantage in that the PSD can be better represented by having a wide array of radius nodes specified. The moments that are required for transport in this case are shown in Table 6.8. The velocity values to initialize these moments are the same used in the SC and VC cases. Here, the extra dimensionality in the first internal coordinate is taken advantage of to improve the number of radii nodes to include both larger and smaller particle sizes. The radius nodes used for this case are 14 μm, 20 μm, 30 μm and 34 μm. This will be referred to as the SC-4 case.

In order to provide a simple proof of concept of the method applied to a combination of scalar and velocity internal coordinates, the cases were first run at the smaller resolution with a 100 by 100 by 100 grid size for the domain. The case plotted is for VR = 0.0, as before the digital filter generator of Chapter 3 is used, with a new generation of turbulent inlet data based on the 25 μm experimental data set. The moments were initialized as constant

Table 6.7: Moments used for four quadrature node CQMOM with diameter.

m_{0000}	m_{1000}	m_{2000}	m_{3000}
m_{0100}	m_{1100}		
m_{0200}	m_{1200}		
m_{0300}	m_{1300}		
m_{0010}	m_{1010}	m_{0110}	m_{1110}
m_{0001}	m_{1001}	m_{0101}	m_{1101}

Table 6.8: Moments if four radius nodes used.

m_{0000}	m_{1000}	m_{2000}	m_{3000}	m_{4000}	m_{5000}	m_{6000}	m_{7000}
m_{0100}	m_{1100}	m_{2100}	m_{3100}				
m_{0010}	m_{1010}	m_{2010}	m_{3010}				
m_{0001}	m_{1001}	m_{2001}	m_{3001}				

across the inlet domain, which does not account for spatial variation of the particle velocities at the inlet which is seen [16, 131].

The results for the particle and fluid velocities for this low resolution test are shown in Figure 6.20. The low resolution of the simulations here show rather poor results for all three of the cases in both of the profiles. While the rate of velocity decay is about the same slope, the simulations here fail to show the core region of the jet maintaining a high velocity in the near-field region. However, there are a few things to note here for future use. The SC and VC cases show reasonable agreement with each other, and unlike the eight-node and four-node cases in the previous section, there is no distinct advantage to using either case based on the information of this plot. The SC-4 case shows the largest deviation from the others, particularly as the flow is further downstream. The SC-4 case does not allow for a full particle trajectory crossing to occur. While particles from different environments are capable of crossing, for two particles of the same radius it is not possible with this configuration of the moments, and this could be the main source of error which causes the SC-4 case to deviate far from the others.

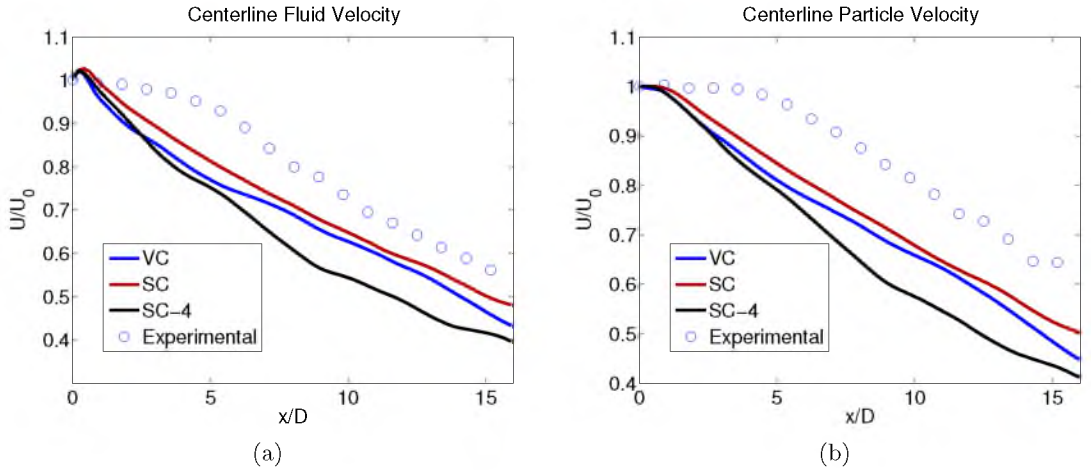

(a) (b)

Figure 6.20: The time-averaged centerline data for the fluid velocity (a) and the particle velocity (b) for the VR = 0.0 case. Lines show the simulation results and the markers show the experimental results.

The agreement of the SC and VC cases is not quite as close as the cases utilizing four and eight quadrature nodes, and a further investigation of these cases is done. A two-dimensional slice of the domains showing the zeroth moment and the average radius is shown in Figure 6.21. Both cases show the width of the jet as fairly narrow in the number density plots in Figure 6.21(a) and (b). When looking at the average radius plots in Figure 6.21(c) and (d), both cases show high average radius of particles at the very fringes between where it drops to a value of zero completely. This occurs due to some numerical dispersion, and the primary goal of the tuning parameters in Subsection 6.3.1 is to avoid this numerical noise. The noise occur in areas with a very small number density, as observed by comparing the average radius contour to the number density contour, and it should have little effect on the overall simulation. The large difference between the two is that the VC case shows that the main section of the jet has nearly the same average particle size across the slice. The SC case shows the spreading of different particle sizes, larger particle sizes are in the central jet, and further from the central jet smaller particles are located.

Intuitively, the results of the SC case should be closer to actual physical data. The smaller particles are transported to the edges of the jet by eddies, as the relaxation time of small particles adapts to the fluid streamlines faster. The larger particles have more inertia and are not as easily convected from the center portion of the jet. The limitation of only one quadrature node for the radius in the VC case can cause the general averaging seen in those results. In cases where particles of different sizes enter the same cell with the velocities, the CQMOM algorithm with only one node of the radius will average these two values. When the velocities are different, the radius should be preserved.

While the SC case appears to be the best case going forward with CQMOM for future uses, there is a limitation that one must consider. As with the SC-4 case, if the velocities are not allowed to have more than one quadrature node, then the particle trajectory crossing – one of the main advantages of CQMOM – will not be possible to simulate. If additional scalars are added to the list of internal coordinates, it is likely that they may be dependent on or at least highly correlated with the radius. In this case, at least one of the velocities should be included early in the conditional splitting of the PBE. The best way to split the PBE and order the internal coordinates would likely be to use radius as the first, the velocities as the second, third and fourth, and any additional scalars after that. Mathematically, the splitting of the PBE into conditionals would be expressed as

$$\eta(\boldsymbol{\xi}) = \eta(\boldsymbol{\xi}|u,v,w,r)\eta(w|u,v,r)\eta(v|u,r)\eta(u|r). \tag{6.99}$$

The first two simulation cases – SC and VC – were run again at the higher grid resolution

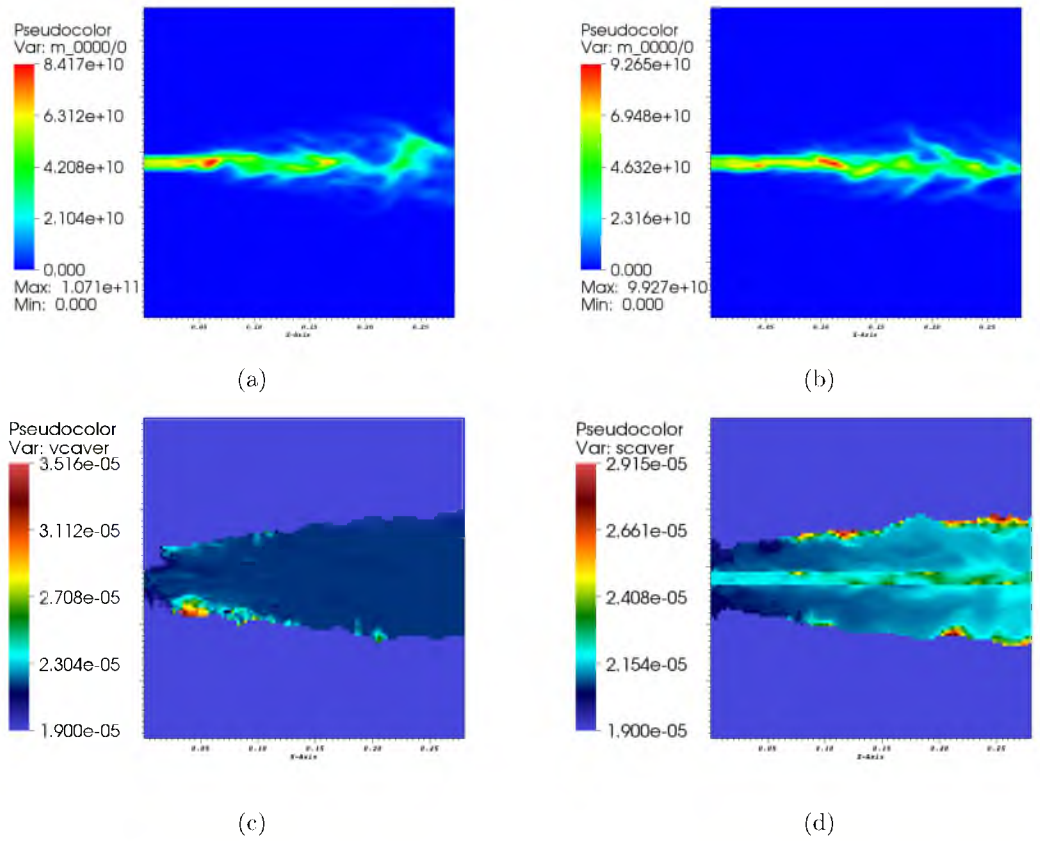

Figure 6.21: A two-dimensional slice of the domain at the centerline showing the zeroth moment for VC (a) and SC (b) cases, along with the average radius for the VC (c) and SC (d) cases.

that was used in the monodisperse case. The SC-4 case was not run, as the results were significantly worse than the other two cases, and it was regarded as a poor option. The results for the fluid and particle velocities at the centerline of the jet are shown in Figure 6.22. These cases show a large improvement over the previous under resolved case. For the particle velocity, both cases show nearly identical agreement with experimental data in the near-field region. As the core of the jet breaks up, the two cases start to deviate slightly, but still show very good agreement with the experiment throughout the rest of the domain. For the fluid velocity, both cases are nearly identical to each other in the near-field region, however, they do overestimate the region before significant velocity decay occurs a little bit. In the far-field region, the SC case shows more decay in the velocity profile than the VC case, which is more in line with the experimental data.

The results for the fluid and particle velocity fluctuations are shown in Figure 6.23. For the fluid velocity fluctuations, both methods perform nearly the same in the near-field region up to about halfway downstream, and match experimental data well here. Further

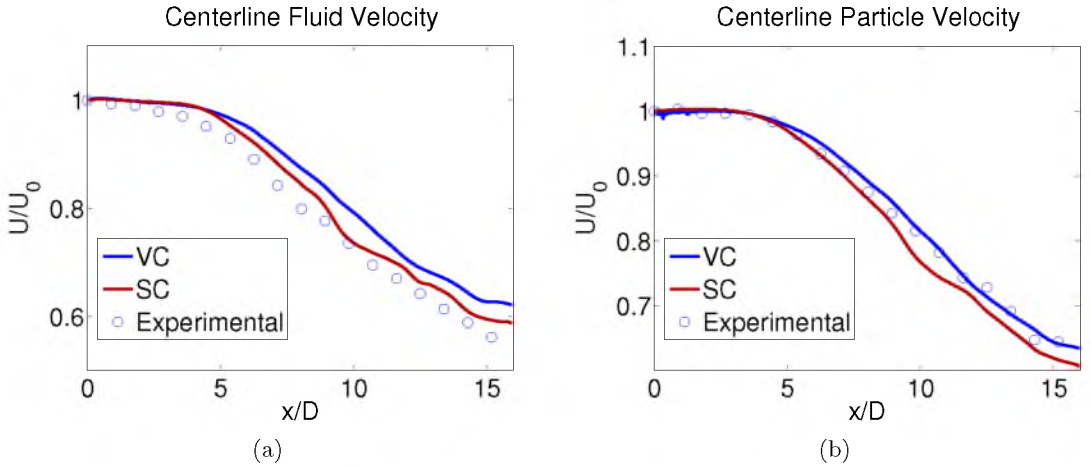

Figure 6.22: The time-averaged centerline data for the fluid velocity (a) and the particle velocity (b) for the VR = 0.0 case with a high grid resolution. Lines show the simulation results and the markers show the experimental results.

downstream near a x/D of 10, the SC case has a spike in its level of fluctuations that is inconsistent with the experimental data. In this region, the fluctuation levels in VC case stay relatively the same, which is more consistent with the experimental results. For the particle velocity fluctuations, there is little agreement with the results in the near-field region. As with the monodisperse case, this is due to the initialization. The small ± 0.01 perturbation was not sufficient to characterize the inlet fluctuations of the particles. In addition, the near-field region shows some unexplained noise in the fluctuation levels for the VC case. Further downstream, the particles in both simulations begin to develop fluctuations that are of the same magnitude of those in the experiments. The VC case matches the experimental data the best in the far-field region, while the SC case overestimates the fluctuation levels slightly in this region. Overall, the SC case appears to capture the averaged velocities better than the VC case, but the opposite occurs for the results of the velocity fluctuations.

A two-dimensional slice of the domains showing the zeroth moment and the average radius for these high resolution cases is shown in Figure 6.24. The zeroth moment of the particles in Figure 6.24(a) and (b) is focused on the center of the jet, and does not break up significantly until half the domain is covered. Even at the higher resolution, numerical noise occurs near the fringe areas of the jet where large average radii are calculated. However, as with the low resolution cases, this noise is far enough from the central jet and has such a low number density, it should have little effect on the simulations. For the VC case, the noise appears to be worse than in the lower resolution case in Figure 6.21(c). At this higher resolution, both cases maintain the same behavior seen with the previous cases. The SC

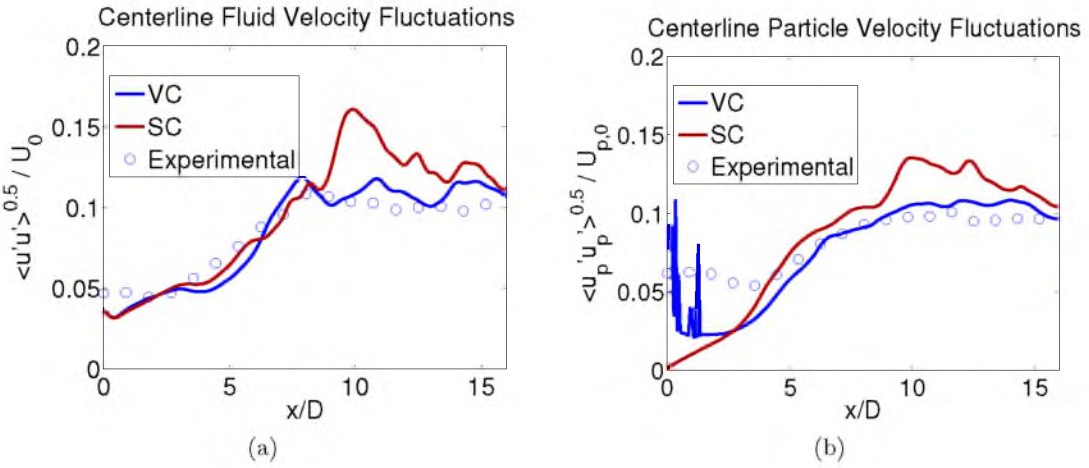

Figure 6.23: The time-averaged centerline data for the fluid velocity fluctuations (a) and the particle velocity fluctuations (b) for the VR = 0.0 case with a high grid resolution. Lines show the simulation results and the markers show the experimental results.

case shows the core of the jet containing larger average particles as those particles adapt to the fluid flow slower. The VC case still shows the bulk of the jet as one average particle size when the resolution is increased.

Near the inlet region, the VC case shows much more noise in the radius profile than the SC case. The number density cutoff that is used to plot the radius is five orders of magnitude less than the core particle flow. The noise in the VC case may be significant in that the average radius is calculated to be higher than the node of 30 μm in some areas. If the quadrature nodes of the VC case were expanded such that $N_i = 2$ for all of the internal coordinates, it is possible that the spreading of different size particles could be captured. However, this would require more than a four times increase in the computational cost as the total quadrature nodes would increase to 16, and the total number of transport equations would increase to 46, and this cost is not desirable for large-scale simulations.

6.3.5 CQMOM Scalar Test

While no simulations were run for a full coal combustion case, the methodology from the scalar extension shown in Subsection 6.2.3 should be applicable to that problem, as well as any other multivariate distribution with well-behaved internal coordinate source terms. For ill-conditioned source terms, derivations using the quadrature approximation could likely be made and adapted to fit here. In order to show that the extension of CQMOM into M-dimensional internal coordinate space is valid, a simple test case will be set up.

This test case will be the stand-in parameters for a coal combustion case consisting of the three velocities for particles, and four scalar components of the system. The scalar

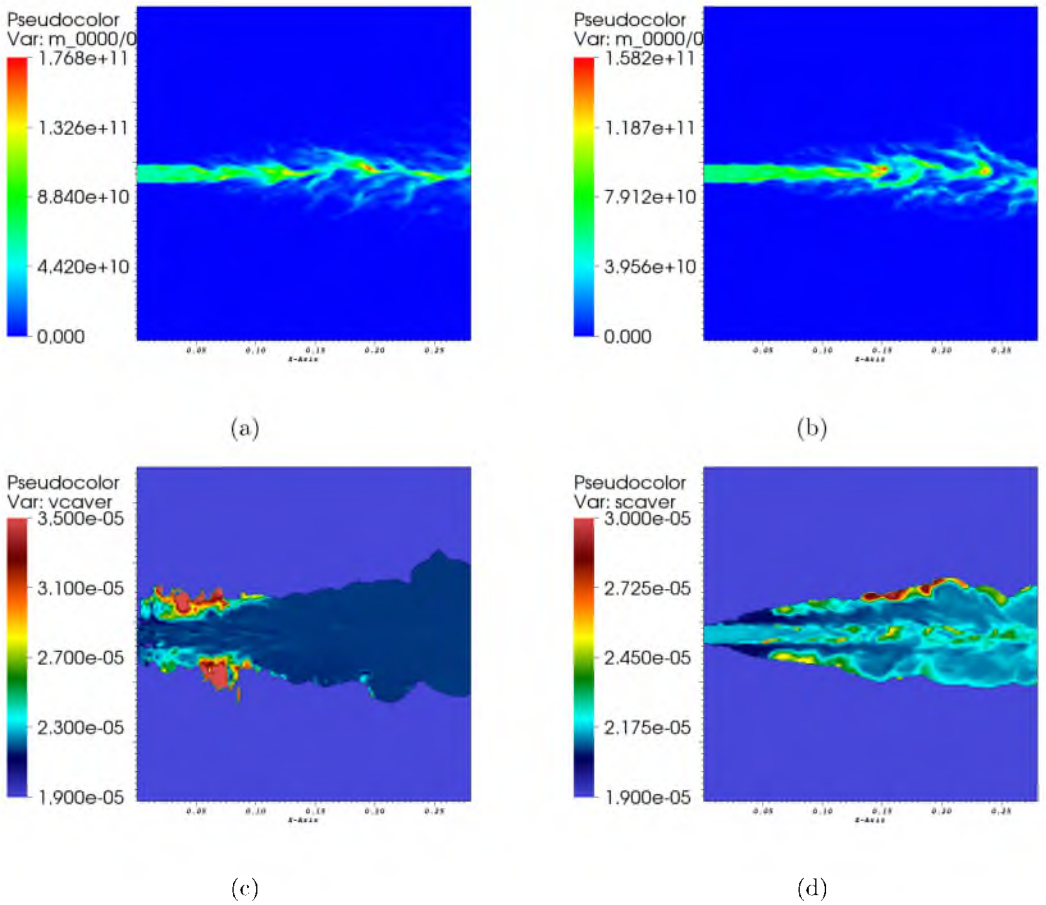

Figure 6.24: A two-dimensional slice of the domain at the centerline showing the zeroth moment for VC (a) and SC (b) resolved cases, along with the average radius for the VC (c) and SC (d) cases.

components in the case of coal would be particle diameter, coal mass, char mass and particle temperature. The values used are entirely arbitrary, and should not be interpreted as actual physical parameters to be used in coal simulation. The values were selected over a wide array of magnitudes to show the quadrature nodes can be preserved without scaling. The values used to initialize the system are listed in Table 6.9.

As was shown previously, adequate results for particle transport were achieved with only four total quadrature nodes. The test case here will again use four total quadrature nodes, with two nodes in the u-velocity and two nodes in the v-velocity, with one node in the w-velocity and the rest of the scalar internal coordinates. This results in 30 total moment transport equations, which are listed in Table 6.10. It should be noted that for the same number of quadrature nodes and internal coordinates, a DQMOM approach would require 32 transport equations. Thus, the approximate cost of CQMOM in the context here with

Table 6.9: Initialized values for internal coordiantes in seven-dimensional CQMOM.

variable	ϵ	node 1	node 2	node 3	node 4
u	0.01	$2-\epsilon$	$2-\epsilon$	$2+\epsilon$	$2+\epsilon$
v	0.01	$1-\epsilon$	$1+\epsilon$	$1-\epsilon$	$1+\epsilon$
w	0.01	$1-\epsilon$	$1-\epsilon$	$1+\epsilon$	$1+\epsilon$
Radius	1.0	$10-\epsilon$	$10+\epsilon$	$10-\epsilon$	$10+\epsilon$
Coal Mass	0.0001	$0.01+\epsilon$	$0.01-\epsilon$	$0.01+\epsilon$	$0.01-\epsilon$
Char Mass	0.0001	$0.001+\epsilon$	$0.001+\epsilon$	$0.001-\epsilon$	$0.001-\epsilon$
Temperature	10.0	$300+\epsilon$	$300+\epsilon$	$300-\epsilon$	$300-\epsilon$

Table 6.10: Moments used for four quadrature node CQMOM with seven internal coordinates.

$m_{0000000}$	$m_{1000000}$	$m_{2000000}$	$m_{3000000}$
$m_{0100000}$	$m_{1100000}$		
$m_{0200000}$	$m_{1200000}$		
$m_{0300000}$	$m_{1300000}$		
$m_{0010000}$	$m_{1010000}$	$m_{0110000}$	$m_{1110000}$
$m_{0001000}$	$m_{1001000}$	$m_{0101000}$	$m_{1101000}$
$m_{0000100}$	$m_{1000100}$	$m_{0100100}$	$m_{1100100}$
$m_{0000010}$	$m_{1000010}$	$m_{0100010}$	$m_{1100010}$
$m_{0000001}$	$m_{1000001}$	$m_{0100001}$	$m_{1100001}$

only one permutation of the quadrature nodes requires about the same number of equations.

A three-dimensional rendering of this jet is shown in Figure 6.25(a). This shows the jet as it diagonally travels through the domain. The simulation is a simple 1 m^3 box with the same resolution as used in the earlier test case, with 100 cells in each dimension run on 125 processors. As the jet travels diagonally it is spread slightly, both due to the variance in the velocity initialization and due to some numerical diffusion. To actually observe the scalar transport of the seven internal coordinates, a two-dimensional plane of the simulation will be shown. The zeroth moment of the plane on the centerline of the domain is shown in Figure 6.25(b).

In figure Figure 6.26, the first three internal coordinates are shown along a slice of the domain. These coordinates are the u-, v-, and w-velocities. Each row in the figure corresponds to an internal coordinate, (a-d) for u-velocity, (e-h) for v-velocity, and (i-l) for w-velocity. As this is a test case, no drag is included so the particles flow in the same direction as initialized. Some "speckles" do appear, but these are in areas far away from the main flow field given by the zeroth moment in Figure 6.25. The values for the quadrature

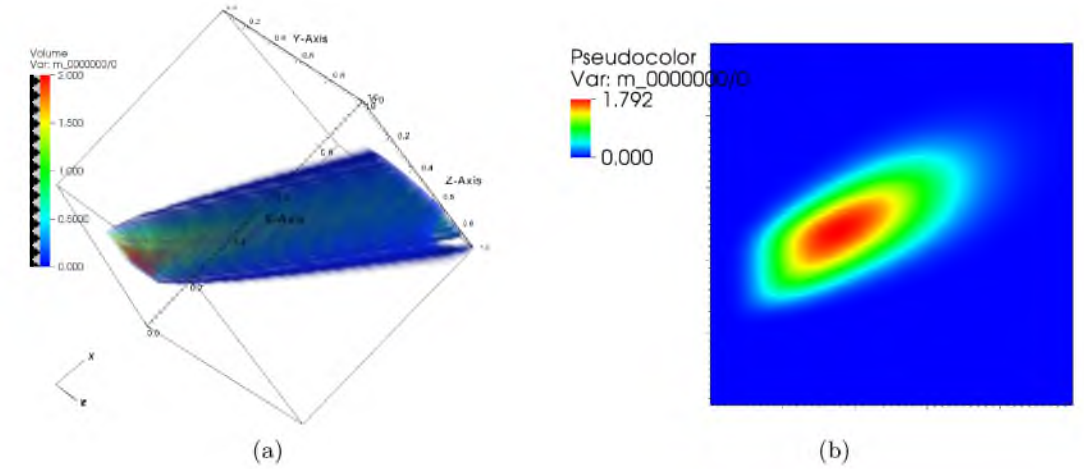

(a) (b)

Figure 6.25: A three-dimensional rendering of the zeroth moment of the jet (a) and a two-dimensional slice in the center of the domain (b).

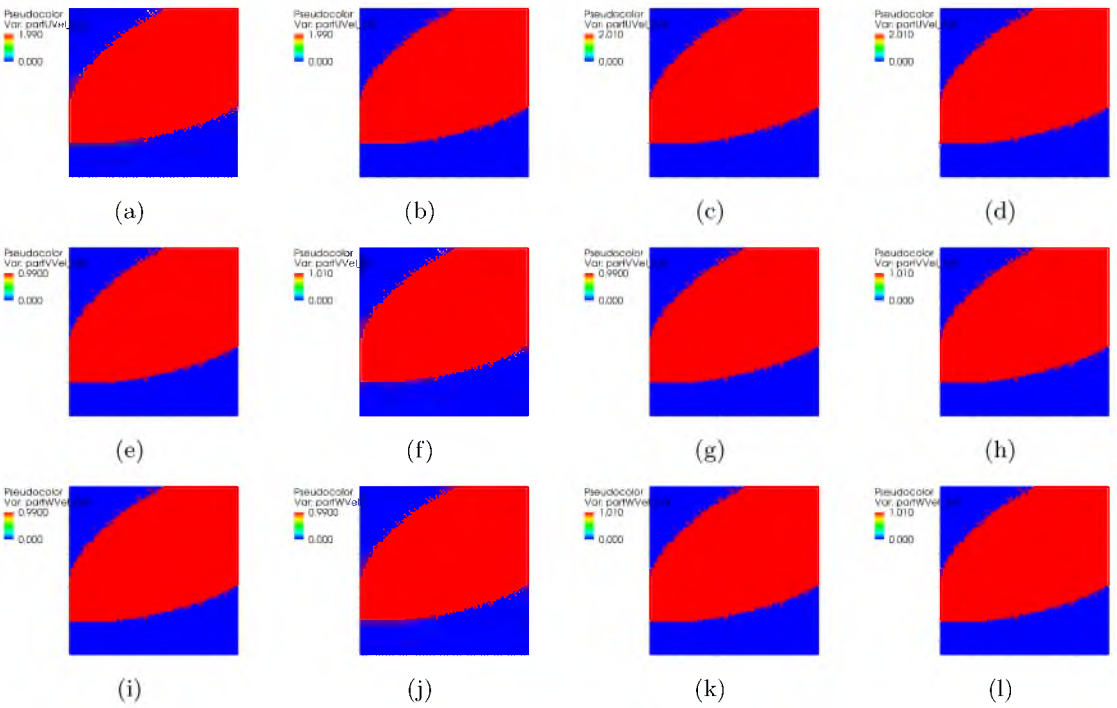

(a) (b) (c) (d)

(e) (f) (g) (h)

(i) (j) (k) (l)

Figure 6.26: A two-dimensional slice of the domain showing velocity transport in CQMOM with seven internal coordinates. The coordinates shown here are: (a-d) u-velocity, (e-h) v-velocity, and (i-l) w-velocity.

nodes correspond to the initialized nodes in Table 6.9.

The remaining internal coordinates are all of the coal-specific scalars of the system, these are shown in Figure 6.27. As before, each row corresponds to a different internal coordinate, (a-d) is the radius, (e-h) is the coal mass, (i-l) is the char mass, and (m-p) is the temperature. As with the velocities, the quadrature nodes here are preserved as the moments are convected across the domain and continue to match the values in Table 6.9. The "speckles" present from the velocities are still present here. These are very small values for the number density that are not near the main flow of the system.

The internal coordinates that were shown vary several orders of magnitude. The highest average internal coordinate values is 300, and the lowest is 0.001 so the change across the variables is five orders of magnitude. In the perturbation of ϵ, the range is varied from 10 to

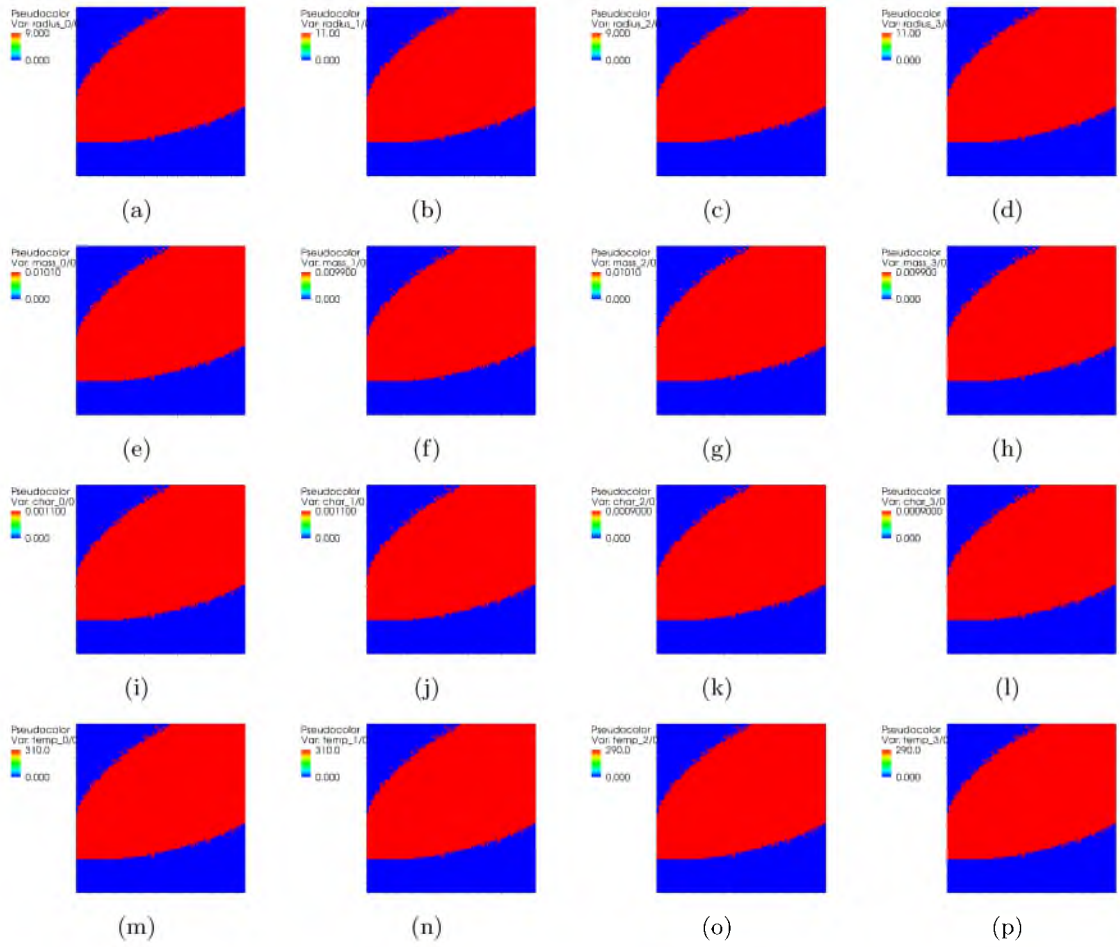

Figure 6.27: A two-dimensional slice of the domain showing scalar transport in CQMOM with seven internal coordinates. The coordinates shown here are: (a-d) radius, (e-h) mass, (i-l) char, and (m-p) temperature.

0.0001, again with five orders of magnitude in change. The transport of the moments for the problem were the unscaled values, so the CQMOM algorithm can handle the quadrature approximation with these large differences in the internal coordinates. In addition, the CQMOM algorithm can deal with any arbitrary number of internal coordinates; here, seven are shown as this number has been used in past coal combustion simulations. The CQMOM framework developed here should be adaptable to any other particle systems, as long as the source terms can be modeled in a similar method to that shown in Subsection 6.2.4.

6.4 Conclusion

A new moment method termed CQMOM for use in disperse particle flow was outlined here. The method was shown to have good results in simple particle trajectory crossing examples when compared to the older method of DQMOM. In combination with the turbulent inlet condition of Chapter 3, validation cases were set up for comparison with experimental data. The first case used large particles with a monodisperse assumption so that only three internal coordinates for size were used. An extension of the method was created to extend to four dimensions of internal coordinates; this extension was then used for the next validation case using polydisperse particles so that the diameter was included as an internal coordinate. Further extension of CQMOM was made with a constriction on the number of quadrature nodes added for higher than four coordinates; this extension should work for any arbitrary number of internal coordinates. This was shown to preserve the initial nodes in an example transport problem using seven internal coordinates that would be representative of a coal combustion simulation. A full coal combustion simulation should be possible using CQMOM, as long as the appropriate source terms are developed and implemented.

Some of the discrepancies with comparisons with the experimental data could be due to some of the approximations that were taken in the implementation. The first major approximation was to ignore all of the extra permutations and combinations of the conditional splitting of the PBE for the kinetic modeling. In the prior specification of the method, it was stated that for three velocities six permutations must be used in eight different combinations of the transport. This is highly undesirable for a full CFD implementation, as the computational cost would be too high. If the CQMOM method were the same cost as DQMOM, it would require more than an eight times increase over the current implementation. The second approximation that may contribute to the error is the handling of the source term. Prior studies apply the source terms directly to the nodes, then do a full

moment reconstruction after the abscissas are updated. As with the kinetic modeling, this would cause an increase in the computational cost, albeit probably not as severe. The lack of variance in the inlet particle velocity could also be another area of error, as the proper value for the variance is not developed until significantly far downstream.

CHAPTER 7

CONCLUDING REMARKS

In order to improve inlet conditions in LES flows, a turbulent inlet condition was implemented into the ARCHES codebase. The inlet was implemented as a standalone executable to produce a table prior to running a simulation. This implementation allows for easy verification that first- and second-order statistics are preserved. The two methods for the synthetic inlet condition both showed improvement in the flow field when compared to a constant inlet velocity case. In particular, the fluctuations in the velocity field that could not be obtained when using a constant inlet led to the proper development of turbulence within the core region of the jet, which improved the core jet breakup. The implementation of the method in the ARCHES codebase should be adaptable for further use in LES simulations with any geometric configuration.

The precipitation of calcium carbonate was modeled using QMOM. Two separate sets of simulations were run. The first set of simulations involved a simplified geometry. Using higher Reynolds numbers to improve the mixing rates resulted in smaller radii in the particle size distributions of all of the polymorphs. The high order of magnitude that the ACC polymorph exhibits did not allow for any selectivity between the different polymorphs with the concentration values used here. The second set of simulations utilized industrial pilot scale reactors. The turbulent inlet flow condition was used in these geometries to improve the inlet conditions of the truncated domains. The two reactors were set to the same inlet Reynolds number and flow rate to be able to make solid conclusions on the mixing. The impinging jets reactor was shown to produce a higher number density of the particles than in the mixing pipes reactor. The impinging jets reactor did produce larger particles, which were due to the longer residence time.

A method was used to set up a library for flamelet modeling to represent subgrid scales in gaseous combustion. Output from a flamelet code was parsed and remapped onto new definitions for the extent of reaction and mixture fraction for combustion of natural gas. A presumed PDF method was used for the subgrid modeling, with a clipped Gaussian

distribution used for the mixture fraction, and a log-normal distribution used for the scalar dissipation rate. The flamelet library was shown to produce expected results as the heat loss was varied, the temperature and enthalpy of the curve varied nearly linearly due to the normalization. As the scalar variance was varied the system reaches a nonmixed state at maximum variance. The heat loss showed an increase in the thermal production of minor species of NO and NO_2 as it, and therefore the temperature was increased. As the method only requires a reaction mechanism for the fuel along with thermodynamic properties of the species, and inlet conditions of fuel and oxidation streams, it should be adaptable for any LES subgrid modeling of combustion systems.

A framework was developed for multiphase flow using CQMOM. The CQMOM framework developed here was utilized to show improvement in particle trajectory crossing problems when compared to DQMOM. The CQMOM framework was also used to demonstrate its use in inert particle flow problems by comparisons with experimental data. The simulations here also utilized the turbulent inlet condition with the same parameters used previously. In the monodisperse cases, only moderate agreement with the experimental data was seen. The CQMOM framework has been shown to be extendable to an arbitrarily large number of internal coordinates. As long as models are developed for the rate change for any scalar internal coordinate, then it should be easy to adapt CQMOM to be usable for coal combustion, or any other disperse particle flow application.

There are several areas of this research that are original contributions to the field. For the turbulent inlet case, this particular study is the first to compare the two synthetic eddy methods used here to experimental data to examine the improvement of simulations over using a constant inlet for coaxial flow jets in such detail. For the precipitation study, the modeling of a complex precipitate that has multiple competing solid phase reactions is an addition to the field. For flamelets, the work here has extended previous formulations of the model to account for more variations in local effects. For CQMOM, the implementation of the technique with velocity internal coordinates into an LES code is the first such study. In addition, the extension of the CQMOM inversion algorithm into M-dimensional internal coordinate space is a novel technique that will allow for the modeling of complex particle flows.

Some of the work presented here has been published in the literature. Chapter 3 discussed the implementation of turbulent inlet conditions into the ARCHES codebase. This work has been published in its entirety in Abboud and Smith [2]. Chapter 4 discussed research of the precipitation of calcium carbonate. The formulation of the model and the

simulations with the temporal jet geometry have been published in Abboud et al. [1]. The study focused on the comparison of these LES results with results from a one-dimensional turbulence code.

The recommendations for future research in the areas that were discussed in this dissertation are as follows. For the turbulent inlet research, the digital filter method could be used in other ARCHES simulations to improve the flow conditions. The method was presented for constant density cases, some modifications may be required for variable density inlets. For the precipitation research, an aspect that could be studied is lowering the concentration condition that was used; this may provide a way for the simulations to show better selectivity between the different polymorphs. For the flamelet research, the tabulated data could be run in the LES code for comparisons with experimental data. The results of a CFD simulation could also be compared with results using the current combustion models in ARCHES of the equilibrium model and the rate-controlled constrained equilibrium model. For the CQMOM research, the M-dimensional extension for the method should make it easily adaptable to use for modeling coal combustion and comparison with the current DQMOM model in ARCHES. Simulating coal combustion with the CQMOM model should only require the implementation of appropriate source terms for the scalars. A few improvements could also be made to the CQMOM code. Currently, wall interaction only works for flat walls in the Cartesian framework, it would be desirable to allow for the method to interact correctly with diagonal walls. It may also be interesting to investigate initializing the moments at the inlet with continuous distributions rather than point distributions.

APPENDIX A

DARS FLAMELET ALGORITHM/STEPS

This appendix outlines the specific steps used to produce a table for use in the ARCHES codebase using the flamelet modeling from DARS. Consider the generic chemical reaction

$$C^* \longrightarrow I + O_2 \longrightarrow P$$

where C^* is essentially the component of fuel that is nonreactive, I is the reactive intermediate, O_2 is the oxidizer, and P is the set of products.

1. DARS GUI
   (a) Use the DARS Flamelet library to create four preliminary files needed to begin a simulation
      i. This case uses only one radiation factor R_f – this appears in enthalpy equation as $R_f * \sigma * (T^4 - T_a^4)$
      ii. Use a mixture fraction of 100 points
      iii. Define fuel and oxidizer streams
         A. Fuel stream has C^* with a value of 0.0 mass fraction
      iv. Four files are generated
         A. FlameUserSettings.txt – Contains the RF used for simulation
         B. GasComposition.txt – Contains the fuel and oxidizer stream information
         C. InputRedKinMec.txt
         D. InputRedKinTherm.txt
2. Running DARS from script files
   (a) Loop over all reaction extents in XI.txt (0.0 to 1.0)
   (b) Loop over all radiation factors in RF.txt (-12.0 to 12.0)

(c) Change the value of C^* and CH_4 in the GasComposition.txt file

(d) Change the value of RF in the FlameUserSettings.txt file

(e) Run chamble.exe (DARS solver for each setting)

i. The runDARS.sh script accomplishes this with the sed utility

(f) Result

i. This gives XI folders for each value from 0.0 to 1.0

ii. Each XI folder contains RF folders for each value from -12.0 to 12.0

iii. Each RF folder contains many data files numbered by the χ_{st} value up to the blowout

(g) Gather only the SV and Yp files to be used in the table

i. SV files contain the information of state space variables (T, density, enthalpy, molecular weight, etc.) as a function of mixture fraction

ii. Yp files contain the mass fraction information of the species in the kinetic file as a function of mixture fraction

iii. Easy collection of these files can be done with the scripts gatherData.sh and ResultsFilter.sh

3. Matlab table parsing

(a) Use the DARSParse.m file to open all of the files created by DARS and parse the data into a multidimensional array

(b) Calculate the sensible heat (h_s) from the adiabatic case (RF = 0.0) for each value of XI

(c) Calculate χ if not found in the table (as of 2012 it should be a table variable)

(d) Find a global value for $\chi_{\max}$ and $\chi_{\min}$ to be used over all of the table

(e) Find h_s and H_a to include in the table

(f) Find the heat loss value for each point as $\gamma = \frac{H_a - H}{h_s}$

(g) Do interpolation to construct one grid of scalar dissipation and mixture fraction space across all XI

i. This maps out a heat loss space, then finds the data from the RF values to interpolate onto this space

(h) Fill out empty values of heat loss and dissipation in the table

i. For high missing values of χ use cold mixing result – blowout has occurred

ii. For low missing values of χ copy the next highest value

iii. High/low missing values of heat loss use closest converged values mass fraction composition, then adjust temperature and iterate until heat loss value is matched

(i) Save a text file with information, using MATLAB integration tools is too slow from here

4. C++ Integration

(a) Calculate the equations for the joint presumed PDFs of mixture fraction and scalar dissipation rate

(b) This is done using int.exe (raw code in DARSIntegrate.cc/h)

(c) Mixture fraction PDF

i. A Clipped Gaussian PDF is used

ii. The μ and σ parameters are pretabulated as a function of the average and variance in ClippGaussParams.txt

(d) Scalar dissipation rate PDF

i. $f_{\chi^*} = \frac{1}{\sigma(2\pi)^{1/2}} \frac{1}{\chi^*} \left[-\frac{1}{2\sigma^2}(\ln(\chi^* - \mu)^2\right]$

ii. μ is related to the mean value of χ^*

iii. and σ is related to the standard deviation

iv. From experimental work $\sigma = [2, 4]$ – used 3

v. Get range of values for $\langle\chi\rangle$

vi. Determine the value of μ for each χ

vii. $\langle\chi^*\rangle = \exp(\mu + 0.5\sigma^2 - \mu = \ln\langle\chi^*\rangle - 0.5\sigma^2$

(e) Use the joint mixture fraction and dissipation rate PDF result to get the averaged value for each $\langle\phi\rangle$ (variables of interest)

(f) $f_{z,\chi} = f_z f_{\langle\chi^*\rangle}$

(g) $\langle\phi\rangle \int_0^1 \int_0^\infty \phi f_{z,\chi} d\chi dz$

(h) Trapezoidal integration of 2-3000 points

(i) Output these data tabulated over all relevant parameters

5. Matlab table creation

   (a) Load the text file from the C++ integration

   (b) Construct a space in η and f_p space

   (c) Interpolate the ξ and z space onto these new values

   (d) $\eta = \frac{C^*}{I+C^*+O_2}$

   (e) $f = \frac{I}{I+O_2}$

   (f) Create a five-dimensional table text file in ARCHES readable format

      i. $\phi = \phi(\eta, f, g, \gamma, \chi)$

   (g) Save all the data as a .mat file; this can be loaded to plot graphs

6. ARCHES/LES

   (a) $\langle \chi \rangle = C_{\tau,SKE} \frac{\left\langle Z'^2 \right\rangle k^{1/2}}{\Delta}$

   (b) $C_{\tau,SKE} = 2$

   (c) $\left\langle Z'^2 \right\rangle = 2(D_Z + D_t)\frac{\partial Z}{\partial x_i}\frac{\partial Z}{\partial x_i}$ (one model)

APPENDIX B

CODE ALGORITHM TO DETERMINE REQUIRED MOMENTS IN CQMOM

```
void CQMOMInversion( const int& M, const vector<int>& N_i)
{
  cout << "List of required moments" << endl;
  for (int i = 0; i < N_i[0]*2; i++ ) {
    cout << "m_" << i << endl;
  }
  if (M == 1) {
    return;
  }
  // loop over each k_2 1,...,2N2-1
  // 0th moment for all conditional = 1
  for (int k = 1; k < 2*N_i[1]; k++) {
    for (int i=0; i < N_i[0]; i++) {
      cout << "m_" << i << k << endl;
    }
  }
  if (M == 2) {return;}

  // start the 3D quadrature method
  for (int k3 = 1; k3 < 2*N_i[2]; k3++) {
    for (int k2 = 0; k2 < N_i[1]; k2++) {
      // loop through all combinations of k_2/k_3 for zeta values
      for (int i = 0; i < N_i[0]; i++) {
        cout << "m_" << i << k2 << k3 << endl;
```

```
    }
  }
}
if ( M == 3 ) {return;}

// start the 4D quadrature
for (int k2 = 0; k2 < N_i[1]; k2++ ) {
  for (int k3 = 0; k3 < N_i[2]; k3++ ) {
    for (int k4 = 1; k4 < 2*N_i[3]; k4++ ) {
      for (int k1 = 0; k1 < N_i[0]; k1++) {
        cout << "m_" << k1 << k2 << k3 << k4 << endl;
      }
    }
  }
}
if ( M == 4 ) {return;}

// after M = 4, limit internal coordinates to 1 per direction
for (int m = 5; m <= M; m++) {
  // all the steps in the 4D quadrature need to be repeated
  // but with  different moment sets based on m
  for (int k2 = 0; k2 < N_i[1]; k2++ ) {
    for (int k3 = 0; k3 < N_i[2]; k3++ ) {
      for (int k4 = 0; k4 < N_i[3]; k4++ ) {
        for (int k1 = 0; k1 < N_i[0]; k1++) {
          cout << "m_" << k1 << k2 << k3 << k4;
          for (int i = 5; i <= m; i++) {
            int product;
            if (i == m) {
              product = 1;
            } else {
              product = 0;
            }
            cout << product;
```

```
            }
            cout << endl;
          }
        }
      }
    }
  }
  return;
}
```

REFERENCES

[1] A. W. Abboud, B. Schroeder, T. Saad, S. T. Smith, D. D. Harris, and D. O. Lignell, *A numerical comparison of precipitating turbulent flows between large-eddy simulation and one-dimensional turbulence*, AIChE Journal, (2015). doi: 10.1002/aic.14870.

[2] A. W. Abboud and S. T. Smith, *Large eddy simulation of a coaxial jet with a synthetic turbulent inlet*, International Journal of Heat and Fluid Flow, 50 (2014), pp. 240–253.

[3] J.-P. Andreassen, *Formation mechanism and morphology in precipitation of vaterite - nano-aggregation or crystal growth?* Journal of Crystal Growth, 274 (2005), pp. 256–264.

[4] J.-P. Andreassen and M. J. Hounslow, *Growth and aggregation of vaterite in seeded-batch experiments*, AIChE Journal, 50 (2004), pp. 2772–2782.

[5] S. V. Apte, K. Mahesh, P. Moin, and J. C. Oefelein, *Large-eddy simulation of swirling particle-laden flows in a coaxial-jet combustor*, Interantional Journal of Multiphase Flow, 29 (2003), pp. 1311–1331.

[6] K. Askselvoll and P. Moin, *Large-eddy simulation of turbulent confined coannular jets*, Journal of Fluid Mechanics, 315 (1996), pp. 387–411.

[7] M. H. Baba-Ahmadi and G. R. Tabor, *Inlet conditions for large eddy simulation of gas-turbine swirl injectors*, AIAA Journal, 47 (2008), pp. 1782–1790.

[8] ——, *Inlet conditions for LES using mapping and feedback control*, Computers and Fluids, 38 (2009), pp. 1299–1311.

[9] R. S. Barlow and J. H. Frank, *Effects of turbulence on species mass fractions in methane/air jet flames*, in Twenty-Seventh Symposium on Combustion, Pittsburgh, 1998, The Combustion Institute, pp. 1087–1095.

[10] G. Batchelor, *The Theory of Homogeneous Turbulence*, Cambridge University Press, Cambridge, 1953.

[11] P. Batten, U. Goldberg, and S. Chakravarthy, *Interfacing statistical turbulence closures with large eddy simulation*, AIAA Journal, 42 (2004), pp. 485–492.

[12] R. Beck and J.-P. Andreassen, *The onset of spherulitic growth in crystallization of calcium carbonate*, Journal of Crystal Growth, 312 (2010), pp. 2226–2238.

[13] M. Berzins, J. Luitjens, Q. Meng, T. Harman, C. Wight, and J. Peterson, *Uintah: A scalable framework for hazard analysis*, in TeraGrid Conference, ACM, 2010, p. 3.

[14] J. N. Bracco, A. G. Stack, and C. I. Steefel, *Upscaling calcite growth rates from the mesoscale to the macroscale*, Environmental Science and Technology, 47 (2013), pp. 7555–7562.

[15] A. Brink, D. Lindberg, M. Hupa, M. de Tejada, M. Paneru, M. Jorg, and G. Scheffnecht, *Predicting deposit build-up in oxy-fuel and air fired pulverized coal combustion*, in Impacts of Fuel Quality, Snowbird, UT, October 2014.

[16] S. Budilarto, *An Experimental Study on Effects of Fluid Aerodynamics and Particle Size Distributions in Particle Laden Jet Flows*, PhD thesis, Purdue University, 2003.

[17] A. Buffo, M. Vanni, D. L. Marchisio, and R. O. Fox, *Multivariate quadrature-based moments methods for turbulent polydisperse gasliquid systems*, International Journal of Multiphase Flow, 50 (2013), pp. 41–57.

[18] Calera Corporation, 2012. 485 Alberto Way Suite 210 Los Gatos, CA 95032.

[19] F. H. Champagne and I. J. Wygnanski, *An experimental investigation of coaxial turbulent jets*, International Journal of Heat and Mass Transfer, 14 (1971), pp. 1445–1464.

[20] J. C. Cheng, R. D. Vigil, and R. O. Fox, *A competitive aggregation model for flash nanoprecipitation*, Journal of Colloid and Interface Science, 351 (2010), pp. 330–342.

[21] P. Chiang, M. D. Donohue, and J. L. Katz, *A kinetic approach to crystallization from ionic solution: II. crystal nucleation*, Journal of Colloid and Interface Science, 100 (1988), pp. 203–211.

[22] N. A. Chigier and J. M. Beer, *The flow region near the nozzle in double concentric jets*, Journal of Fluids Engineering, 86 (1964), pp. 797–804.

[23] A. Chorny and V. Zhdanov, *Turbulent mixing and fast chemical reaction in the confined jet flow at large schmidt number*, Chemical Engineering Science, 68 (2012), pp. 541–554.

[24] A. P. Collier and M. J. Hounslow, *Growth and aggregation rates for calcite and calcium oxalate monohydrate*, AIChE Journal, 45 (1999), pp. 2298–2305.

[25] P. J. Colucci, F. A. Jaberi, P. Givi, and S. B. Pope, *Filtered density function for large eddy simulation of turbulent reacting flows*, Physics of Fluids, 2 (1998), pp. 499–515.

[26] A. W. Cook and J. J. Riley, *Subgrid-scale modeling for turbulent reacting flows*, Combustion and Flame, 112 (1998), pp. 593–606.

[27] DARS, 2012. CD adapco.

[28] C. W. Davies, *Ion Association*, Butterworth, London, 1962.

[29] S. M. de Bruyn Kops, J. J. Riley, G. Kosály, and A. W. Cook, *Investigation of modeling for non-premixed turbulent combustion*, Flow, Turbulence and Combustion, 60 (1998), pp. 105–122.

[30] N. H. de Leeuw and S. C. Parker, *Surface structure and morphology of calcium carbonate polymorphs calcite, aragonite, and vaterite: An atomistic approach*, The Journal of Physical Chemistry B, 102 (1998), pp. 2914–2922.

[31] J. D. de St Germain, J. McCorquodale, S. Parker, and C. Johnson, *Uintah: A massively parallel problem solving environment*, in High-Performance Distributed Computing, The Ninth International Symposium, IEEE, 2000, pp. 33–41.

[32] O. Desjardins, R. O. Fox, and A. Villedieu, *A quadrature-based moment closure for the william spray equation*, in Proceedings of the Summer Program, Center for Turbulence Research, Stanford, CA, 2006.

[33] O. Desjardins, R. O. Fox, and P. Villedieu, *A quadrature-based moment method for dilute fluid-particle flows*, Journal of Computational Physics, 227 (2008), pp. 2514–2539.

[34] L. di Mare, M. Klein, W. P. Jones, and J. Janicka, *Synthetic turbulence inflow conditions for large eddy simulation*, Physics of Fluids, 18 (2006).

[35] R. B. Diemer and J. H. Olson, *A moment methodology for coagulation and breakage problems: Part 1analytical solution of the steady-state population balance*, Chemical Engineering Science, 57 (2002), pp. 2193–2209.

[36] J. Dirksen and T. Ring, *Fundamentals of crystallization: Kinetic effects on particle size distributions and morphology*, Chemical Engineering Science, 46 (1991), pp. 2389–2427.

[37] R. Fan and R. O. Fox, *Segregation in polydisperse fluidized beds: Validation of a multi-fluid model*, Chemical Engineering Science, 63 (2008), pp. 272–285.

[38] R. Fan, D. L. Marchisio, and R. O. Fox, *Application of the direct quadrature method of moments to polydisperse gas–solid fluidized beds*, Powder Technology, 139 (2004), pp. 7–20.

[39] C. P. Fenimore, *Formation of nitric oxide in premixed hydrocarbon flames*, in International Symposium on Combustion, vol. 13, Elsevier, 1971, pp. 373–380.

[40] B. Fiorina, O. Gicquel, L. Vervisch, S. Carpentier, and N. Darabiha, *Approximating the chemical structure of partially premixed and diffusion counterflow flames using FPI flamelet tabulation*, Combustion and Flame, 140 (2005), pp. 147–160.

[41] T. H. Fletcher, A. R. Kerstein, R. J. Pugmire, M. S. Solum, and D. M. Grant, *Chemical percolation model for devolatilization. 3. direct use of carbon-13 nmr data to predict effects of coal type*, Energy & Fuels, 6 (1992), pp. 414–431.

[42] R. O. Fox, *Computational Models for Turbulent Reacting Flows*, Cambridge University Press, Cambridge, 2003.

[43] ——, *Bivariate direct quadrature method of moments for coasgulation and sintering of particle populations*, Journal of Aerosol Science, 37 (2006), pp. 1562–1580.

[44] ——, *A quadrature-based third-order moment method for dilute gas-particle flows*, Journal of Computational Physics, 227 (2008), pp. 6313–6350.

[45] ——, *Higher-order quadrature-based moment methods for kinetic equations*, Journal of Computational Physics, 228 (2009), pp. 7771–7791.

[46] ——, *Optimal moment sets for multivariate direct quadrature method of moments*, Industrial and Engineering Chemistry Research, 48 (2009), pp. 9686–9696.

[47] M. Frenklach and S. J. Harris, *Aerosol dynamics modeling using the method of moments*, Journal of Colloid and Interface Science, 118 (1987), pp. 252–261.

[48] S. K. Friedlander, *Dynamics of aerosol formation by chemical reaction**, Annals of the New York Academy of Sciences, 404 (1983), pp. 354–364.

[49] E. Gavi, D. L. Marchisio, and A. A. Barresi, *CFD modelling and scale-up of confined impinging jet reactors*, Chemical Engineering Science, 62 (2007), pp. 2228–2241.

[50] E. Gavi, L. Rivautella, D. L. Marchisio, M. Vanni, A. A. Barresi, and G. Baldi, *CFD modelling of nano-particle precipitation in confined impinging jet reactors*, Chemical Engineering Research and Design, 85 (2007), pp. 735–744.

[51] D. Gebauer and H. Cölfen, *Prenucleation clusters and non-classical nucleation*, Nano Today, 6 (2011), pp. 564–584.

[52] D. Gebauer, A. Völkel, and H. Cölfen, *Stable prenucleation calcium carbonate clusters*, Science, 322 (2008), pp. 1819–1822.

[53] T. A. Gebrehiwet, G. D. Redden, Y. Fujita, M. S. Beig, and R. W. Smith, *The effect of the co3 2-to ca2+ ion activity ratio on calcite precipitation kinetics and sr2+ partitioning*, Geochemical Transactions, 13 (2012), p. 1.

[54] M. Germano, U. Piomelli, P. Moin, and W. H. Cabot, *A dynamic subgrid-scale eddy viscosity model*, Physics of Fluids A: Fluid Dynamics, 3 (1991), pp. 1760–1765.

[55] O. Gicquel, N. Darabiha, and D. Thévenin, *Laminar premixed hydrogen/air counterflow flame simulations using flame prolongation of ILDM with differential diffusion*, Proceedings of the Combustion Institute, 28 (2000), pp. 1901–1908.

[56] R. G. Gordon, *Error bounds in equilibrium statistical mechanics*, Journal of Mathematical Physics, 9 (1968), pp. 655–663.

[57] J. Guilkey, T. Harman, J. Luitjens, J. Schmidt, J. Thornock, J. D. de St Germain, S. Shankar, J. Peterson, C. Brownlee, C. Reid, T. Saad, and J. Beckvermit, *Uintah User Guide*, 2013.

[58] R. Gunawan, I. Fusman, and R. D. Braatz, *High resolution algorithms for multidimensional population balance equations*, AIChE Journal, 50 (2004), pp. 2738–2749.

[59] V. S. Gururajan, T. F. Wall, R. P. Gupta, and J. S. Truelove, *Mechanisms for the ignition of pulverized coal particles*, Combustion and Flame, 81 (1990), pp. 119–132.

[60] E. Hassel, S. Jahnke, N. Kornev, I. Tkatchenko, and V. Zhdanov, *Large-eddy simulation and laser diagnostic measurements of mixing in a coaxial jet mixer*, Chemical Engineering Science, 61 (2006), pp. 2907–2912.

[61] P. C. Hiemenz and R. Rajagopalan, *Principles of Colloid and Surface Chemistry, Revised and Expanded*, vol. 14, CRC Press, New York, 1997.

[62] J. Hostomsky and A. G. Jones, *Calcium-carbonate crystallization, agglomeration and form during continuous precipitation from solution*, Journal of Physics D, 24 (1991), pp. 165–170.

[63] M. J. Hounslow, R. L. Ryall, and V. R. Marshall, *A discretized population balance for nucleation, growth, and aggregation*, AIChE Journal, 34 (1988), pp. 1821–1832.

[64] H. M. Hulburt and S. Katz, *Some problems in particle technology: A statistical mechanical formulation*, Chemical Engineering Science, 19 (1964), pp. 555–574.

[65] M. Ihme, C. M. Cha, and H. Pitsch, *Prediction of local extinction and re-ignition effects in non-premixed turbulent combustion using a flamelet/progress variable approach*, in Proceedings of the Combustion Institute, vol. 30, pp. 793 – 800.

[66] N. Jarrin, S. Benhamadouche, D. Laurence, and R. Prosser, *A synthetic-eddy-method for generating inflow conditions for large-eddy simulations*, International Journal of Heat and Fluid Flow, 27 (2006), pp. 585–593.

[67] N. Jarrin, R. Prosser, J.-C. Uribe, S. Benhamadouche, and D. Laurence, *Reconstruction of turbulent fluctuations for hybrid rans/les simulations using a synthetic-eddy method*, International Journal of Heat and Fluid Flow, 30 (2009), pp. 435–442.

[68] N. Jarrin, J.-C. Uribe, R. Prosser, and D. Laurence, *Synthetic inflow boundary conditions for wall bounded flows*, in Advances in Hybrid RANS-LES Modelling, Springer, Berlin, 2008, pp. 77–86.

[69] B. K. Johnson and R. K. Prud'homme, *Chemical processing and micromixing in confined impinging jets*, AIChE Journal, 49 (2003), pp. 2264–2282.

[70] D. Jung, S. Gamard, and W. K. George, *Downstream evolution of the most energetic modes in a turbulent axisymmetric jet at high reynolds number. Part 1. The near-field region*, Journal of Fluid Mechanics, 514 (2004), pp. 173–204.

[71] D. Kashchiev, *Nucleation: Basic Theory with Applications*, Butterworth-Heinemann, Oxford, 2000.

[72] D. Kashchiev and G. M. van Rosmalen, *Review: Nucleations in solutions revisited*, Cyrstal Research and Technology, 38 (2003), pp. 555–574.

[73] J. Kawano, N. Shimobayahi, M. Kitamura, K. Shinoda, and N. Aikawa, *Formation process of calcium carbonate from highly supersaturated solution*, Journal of Crystal Growth, (2002), pp. 419–423.

[74] A. Keating, U. Piomelli, E. Balaras, and H.-J. Kaltenbach, *A priori and a posteriori tests of inflow conditions for large-eddy simulation*, Physics of Fluids, 16 (2004), pp. 4696–4712.

[75] A. Kempf, W. Malalasekera, K. Ranga-Dinesh, and O. Stein, *Large eddy simulations of swirling non-premixed flames with flamelet models: A comparison of numerical methods*, Flow, Turbulence and Combustion, 81 (2008), pp. 523–561.

[76] A. Kempf, A. Sadiki, and J. Janicka, *Prediction of finite chemistry effects using large eddy simulation*, Proceedings of the Combustion Institute, 29 (2002), pp. 1979–1985.

[77] A. M. Kempf, S. Wysocki, and M. Pettit, *An efficient, parallel low-storage implementation of kleins turbulence generator for LES and DNS*, Computers and Fluids, 60 (2012), pp. 58–60.

[78] J. Kim and H. Choi, *Large eddy simulation of a circular jet: Effect of inflow conditions on the near field*, Journal of Fluid Mechanics, 620 (2009), pp. 383–411.

[79] M. Klein, A. Sadiki, and J. Janicka, *A digital filter based generation of inflow data for spatially developing direct numerical or large eddy simulations*, Journal of Computational Physics, 186 (2003), pp. 652–665.

[80] ——, *Investigation of the influence of the reynolds number on a plane jet using direct numerical simulation*, International Journal of Heat and Fluid Flow, 24 (2003), pp. 785–794.

[81] A. N. Kolmogorov, *Foundations of the Theory of Probability*, Chelsea Publishing Co., 1950.

[82] N. Kornev, V. Zhdanov, and E. Hassel, *Study of scalar macro- and microstructures in a confined jet*, International Journal of Heat and Fluid Flow, 29 (2008), pp. 665–674.

[83] D. Kralj, L. Brecevic, and J. Kontrec, *Vaterite growth and dissolution in aqueous solution iii. Kinetics of transformation*, Journal of Crystal Growth, 177 (1997), pp. 248–257.

[84] D. Kralj, L. Brecevic, and A. E. Nielsen, *Vaterite growth and dissolution in aqueous solution i. Kinetics of crystal growth.*, Journal of Crystal Growth, 104 (1990), pp. 793–800.

[85] ——, *Vaterite growth and dissolution in aqueous solution ii. Kinetics of dissolution*, Journal of Crystal Growth, 143 (1994), pp. 269–276.

[86] S. Kumar and D. Ramkrishna, *On the solution of population balance equations by discretization i. A fixed pivot technique*, Chemical Engineering Science, 51 (1996), pp. 1311–1332.

[87] ——, *On the solution of population balance equations by discretization iii. Nucleation, growth and aggregation of particles*, Chemical Engineering Science, 52 (1997), pp. 4659–4679.

[88] A. C. Lasaga, *Kinetic Theory in the Earth Sciences*, Princeton University Press, Princeton, 1998.

[89] G. A. Lavoie, J. B. Heywood, and J. C. Keck, *Experimental and theoretical study of nitric oxide formation in internal combustion engines*, Combustion Science and Technology, 1 (1970), pp. 313–326.

[90] T. L. Liew, J. P. Barrick, and M. J. Hounslow, *A micro-mechanical model for the rate of aggregation during precipitation from solution*, Chemical Engineering Technolology, 26 (2003), pp. 282–285.

[91] D. O. Lignell, J. H. Chen, and H. A. Schmutz, *Effects of damköhler number on flame extinction and reignition in turbulent non-premixed flames using DNS*, Combustion and Flame, 158 (2011), pp. 949–963.

[92] D. O. Lignell, J. H. Chen, and P. J. Smith, *Three-dimensional direct numerical simulation of soot formation and transport in a temporally evolving nonpremixed ethylene jet flame*, Combustion and Flame, 155 (2008), pp. 316–333.

[93] D. O. Lignell, G. C. Fredline, and A. D. Lewis, *Comparison of one-dimensional turbulence and direct numerical simulations of soot formation and transport in a nonpremixed ethylene jet flame*, Proceedings of the Combustion Institute, (2014).

[94] Y.-P. Lin and P. C. Singer, *Effects of seed material and solution composition on calcite precipitation*, Geochimica et Cosmochimica Acta, 69 (2005), pp. 4495–4504.

[95] F. Lince, D. L. Marchisio, and A. A. Barresi, *Smart mixers and reactors for the production of pharmaceutical nanoparticles: Proof of concept*, Chemical Engineering Research and Design, 87 (2009), pp. 543–549.

[96] Y. Liu and R. O. Fox, *CFD predictions for chemical processing in a confined impinging jets reactor*, AIChE Journal, 52 (2006), pp. 731–744.

[97] T. S. Lund, X. Wu, and K. D. Squires, *Generation of turbulent inflow data for spatially-developing boundary layer simulations*, Journal of Computational Physics, 140 (1998), pp. 233–258.

[98] C. Y. Ma, X. Z. Wang, and K. J. Roberts, *Morphological population balance for modeling crystal growth in face directions*, AIChE Journal, 54 (2008), pp. 209–222.

[99] P. Marchal, R. David, J. P. Klein, and J. Villermaux, *Crystallization and precipitation engineering i. An efficient method for solving population balance in crystallization with agglomeration*, Chemical Engineering Science, 43 (1988), pp. 59–67.

[100] D. L. Marchisio, *Large eddy simulation of mixing and reaction in a confined impinging jets reactor*, Computers and Chemical Engineering, 33 (2009), pp. 408–420.

[101] D. L. Marchisio and R. O. Fox, *Solution of population balance equations using the direct quadrature method of moments*, Journal of Aerosol Science, 36 (2005), pp. 43–73.

[102] D. L. Marchisio and R. O. Fox, *Multiphase Reacting Flows: Modeling and Simulation*, vol. 492, Springer, Berlin, 2007.

[103] ——, *Computational Models for Polydisperse Particulate and Multiphase Systems*, Cambridge University Press, London, 2013.

[104] D. L. Marchisio, R. D. Vigil, and R. O. Fox, *Implementation of the quadrature method of moments in CFD codes for aggregation-breakage problems*, Chemical Engineering Science, 58 (2003), pp. 3337–3351.

[105] D. L. Marchisio, R. D. Vigil, and R. O. Fox, *Quadrature method of moments for aggregation-breakage processes*, Journal of Colloid and Interface Science, 258 (2003), pp. 322–334.

[106] B. J. McCoy, *A new population balance model for crystal size distributions: Reversible, size-dependent growth and dissolution*, Journal of Colloid and Interface Science, 240 (2001), pp. 139–149.

[107] R. McGraw, *Description of aerosol dynamics by the quadrature method of moments*, Aerosol Science and Technology, 27 (1997), pp. 255–265.

[108] R. McGraw and J. H. Saunders, *A condensation feedback mechanism for oscillatory nucleation and growth*, Aerosol Science and Technology, 3 (1984), pp. 367–380.

[109] R. McGraw and D. L. Wright, *Chemically resolved aerosol dynamics for internal mixtures by the quadrature method of moments*, Journal of Aerosol Science, 34 (2003), pp. 189–209.

[110] D. Merrick, *Mathematical models of the thermal decomposition of coal: 2. Specific heats and heats of reaction*, Fuel, 62 (1983), pp. 540 – 546.

[111] J.-B. Michel, O. Colin, and D. Veynante, *Modeling ignition and chemical structure of partially premixed turbulent flames using tabulated chemistry*, Combustion and Flame, 152 (2008), pp. 80–99.

[112] K. Miura, *A new and simple method to estimate f (e) and k0 (e) in the distributed activation energy model from three sets of experimental data*, Energy & Fuels, 9 (1995), pp. 302–307.

[113] F. Montomoli and S. Eastwood, *Implementation of synthetic turbulence inlet for turbomachinery LES*, Computers and Fluids, 46 (2011), pp. 369–374.

[114] H. Muhr, R. David, J. Villermaux, and P. H. Jezequel, *Crystallization and precipitation engineering-vi. Solving population balance in the case of the precipitation of silver bromide crystals with high primary nucleation rates by using the first order upwind differentiation*, Chemical Engineering Science, 51 (1996), pp. 309–319.

[115] P.-D. Nguyen, L. Vervisch, V. Subramanian, and P. Domingo, *Multidimensional flamelet-generated manifolds for partially premixed combustion*, Combustion and Flame, 157 (2010), pp. 43–61.

[116] F. Nicoud and F. Ducros, *Subgrid-scale stress modelling based on the square of the velocity gradient tensor*, Flow, Turbulence and Combustion, 62 (1999), pp. 183–200.

[117] A. Nielsen, *Kinetics of Precipitation*, Pergamon Press Ltd., New York, 1964.

[118] S. Niksa and A. R. Kerstein, *Flashchain theory for rapid coal devolatilization kinetics. 1. Formulation*, Energy & Fuels, 5 (1991), pp. 647–665.

[119] C. Noguera, B. Fritz, A. Clemant, and A. Baronnet, *Nucleation, growth, and aging scenarios in closed systems i: A unified mathematical framework for precipitation, condensation, and crystallization.*, Journal of Crystal Growth, 297 (2006), pp. 180–186.

[120] C. Noiriel, C. I. Steefel, L. Yang, and J. Ajo-Franklin, *Upscaling calcium carbonate precipitation rates from pore to continuum scale*, Chemical Geology, 318 (2012), pp. 60–74.

[121] T. Ogino, T. Suzuki, and K. Sawada, *The formation and transformation mechanism of calcium carbonate in water*, Geochimica et Cosmochimica Acta, 51 (1987), pp. 2757–2767.

[122] T. Ogino, T. Suzuki, and K. Sawada, *The rate and mechanism of polymorphic tranformation of calcium carbonate in water*, Journal of Crystal Growth, 100 (1990), pp. 159–167.

[123] J. v. Oijen and L. D. Goey, *Modelling of premixed laminar flames using flamelet-generated manifolds*, Combustion Science and Technology, 161 (2000), pp. 113–137.

[124] OLI Systems, Inc., 2012. 240 Cedar Knolls Road Suite 301 Cedar Knolls NJ 07927.

[125] M. Olsson and L. Fuchs, *Large eddy simulation of the proximal region of a spatially developing circular jet*, Physics of Fluids, 8 (1996), pp. 2125–2137.

[126] C. Pantano, S. Sarkar, and F. A. Williams, *Mixing of a conserved scalar in a turbulent reacting shear layer*, Journal of Fluid Mechanics, 481 (2003), pp. 291–328.

[127] S. Parker, *A component-based architecture for parallel multi-physics PDE simulation*, in Computational Science, ICCS, 2002, pp. 719–734.

[128] A. Passalacqua, R. O. Fox, R. Garg, and S. Subramaniam, *A fully coupled quadrature based moment method for dilute to moderately dilute fluid particle flows*, Chemical Engineering Science, 65 (2010), pp. 2267–2283.

[129] J. Pedel, J. N. Thornock, and P. J. Smith, *Large eddy simulation of pulverized coal jet flame ignition using the direct quadrature method of moments*, Energy and Fuels, 26 (2012), pp. 6686–6694.

[130] ——, *Ignition of co-axial turbulent diffusion oxy-coal jet flames: Experiments and simulations collaboration*, Combustion and Flame, 160 (2013), pp. 1112–1128.

[131] J. Pedel, J. N. Thornock, S. T. Smith, and P. J. Smith, *Large eddy simulation of polydisperse particles in turbulent coaxial jets using the direct quadrature method of moments*, International Journal of Multiphase Flow, 63 (2014), pp. 23–38.

[132] N. Peters, *Local quenching due to flame stretch and non-premixed turbulent combustion*, Combustion Science and Technology, 30 (1983), pp. 1–17.

[133] ——, *Laminar diffusion flamelet models in non-premixed turbulent combustion*, Progress in Energy and Combustion Science, 10 (1984), pp. 319–339.

[134] ——, *Turbulent Combustion*, Cambridge University Press, Cambridge, 2000.

[135] P. Petersson, M. Larson, and L. Jonsson, *Development of a turbulent jet generated by a mixer in weak co-flow and counter-flow*, International Journal of Heat and Fluid Flow, 21 (2000), pp. 1–10.

[136] M. Petitti, M. Vanni, D. L. Marchisio, A. Buffo, and F. Podenzani, *Simulation of coalescence, break-up and mass transfer in a gas-liquid stirred tank with CQMOM*, Chemical Engineering Journal, 228 (2013), pp. 1182–1194.

[137] C. Pierce and P. Moin, *Method for generating equilibrium swirling inflow conditions*, AIAA Journal, 36 (1998), pp. 1325–1327.

[138] ——, *Progress-variable approach for large eddy simulation of turbulent combustion*, tech. rep., Dept. Mech. Eng., Stanford Univ., 2001.

[139] ——, *Progress-variable approach for large-eddy simulation of non-premixed turbulent combustion*, Journal of Fluid Mechanics, 504 (2004), pp. 73–97.

[140] H. Pitsch, *Large-eddy simulation of turbulent combustion*, Annual Review of Fluid Mechanics, 38 (2006), pp. 453–482.

[141] H. Pitsch, M. Chen, and N. Peters, *Unsteady flamelet modeling of turbulent hydrogen-air diffusion flames*, in Twenty-Seventh Symposium on Combustion, Pittsburgh, 1998, The Combustion Institute.

[142] H. Pitsch and M. Ihme, *An unsteady/flamelet progress variable method for LES of nonpremixed turbulent combustion*, in Aerospace Sciences Meeting and Exhibit, Reno, Jan 2005, AIAA.

[143] H. Pitsch and H. Steiner, *Large-eddy simulation of a turbulent piloted methane/air diffusion flame (sandia flame d)*, Physics of Fluids, 12 (2000).

[144] L. N. Plummer and E. Busenburg, *The solubilities of calcite, aragonite, and vaterite in co2-h2o solutions between 0 and 90 c, and an evaluation of the aqueous model for the system caco3-co2-h2o*, Geochimica et Cosmochimica Acta, 46 (1982), pp. 1011 – 1040.

[145] O. S. Pokrovsky, S. V. Golubev, J. Schott, and A. Castillo, *Calcite, dolomite and magnesite dissolution kinetics in aqueous solutions at acid to circumneutral ph, 25 to 150 c and 1 to 55 atm pco2: New constraints on co2 sequestration in sedimentary basins*, Chemical Geology, 265 (2009), pp. 20–32.

[146] S. B. Pope, *Turbulent Flows*, Cambridge University Press, Cambridge, 2000.

[147] S. E. Pratsinis, *Simultaneous nucleation, condensation, and coagulation in aerosol reactors*, Journal of Colloid and Interface Science, 124 (1988), pp. 416–427.

[148] W. H. Press, S. A. Teukolsky, W. T. Vetterling, and B. P. Falnnery, *Numerical Recipes in Fortran 77: The Art of Scientific Computing*, Cambridge University Press, London, 1992.

[149] N. Punati, J. C. Sutherland, A. R. Kerstein, E. R. Hawkes, and J. H. Chen, *An evaluation of the one-dimensional turbulence model: Comparison with direct numerical simulations of co/h2 jets with extinction and reignition*, Proceedings of the Combustion Institute, (2010).

[150] V. Raman and H. Pitsch, *Large-eddy simulation of a bluff-body-stabilized non-premixed flame using a recursive filter-refinement procedure*, Combustion and Flame, 142 (2005), pp. 329–347.

[151] D. Ramkrishna, *Population Balances*, Academic Press, 2000.

[152] A. Randolph and M. A. Larson, *Theory of Particulate Processes*, Academic Press, New York, 1971.

[153] J. J. Riley and P. A. McMurty, *The use of direct numerical simulation in the study of turbulent chemically reacting flows*, Turbulent Reactive Flows, (1989), pp. 486–514.

[154] J. J. Riley, R. W. Metcalfe, and S. A. Orszag, *Direct numerical simulations of chemically reacting mixing layers*, Physics of Fluids, 29 (1986), pp. 406–422.

[155] C. S. Romanek, J. W. Morse, and E. L. Groassman, *Aragonite kinetics in dilute solutions*, Aquatic Geochemistry, 17 (2011), pp. 339–356.

[156] D. E. Rosner, R. McGraw, and P. Tandon, *Multivariate population balances via moment and Monte Carlo simulation methods: An important sol reaction engineering bivariate example and mixed moments for the estimation of deposition, scavenging, and optical properties for populations of nonspherical suspended particles*, Industrial and Engineering Chemical Research, 42 (2003), pp. 2699–2711.

[157] E. Ruiz-Agudo, C. V. Putnis, C. Rodriguez-Navarro, and A. Putnis, *Effect of ph on calcite growth at constant ratio and supersaturation*, Geochimica et Cosmochimica Acta, 75 (2011), pp. 284–296.

[158] T. Saad, A. W. Abboud, S. T. Smith, and T. A. Ring, *A class of exact solutions for population balances with arbitrary internal coordinates*, AIChE Journal, (2015). doi: 10.1002/aic.14739.

[159] T. Saad, J. C. Sutherland, A. Biglari, and A. W. Abboud, *Wasatch Documentation*, 2013.

[160] P. Sagaut, *Large Eddy Simulation for Incompressible Flows*, Springer, Berlin, 2006.

[161] M. Sakiz and O. Simonin, *Numerical experiments and modelling of non-equilibrium effects in dilute granular flows*, in International Symposium on Rarefied Gas Dynamics, 1999.

[162] K. Sawada, *Mechanism of crystallization and transformation of calcium carbonates*, Pure and Applied Chemistry, 69 (1997), pp. 921–928.

[163] J. Schlomach, K. Quarch, and M. Kind, *Investigation of precipitation of calcium carbonate at high supersaturations*, Chemical Engineering and Technology, 29 (2006), pp. 215–220.

[164] J. U. Schluter, H. Pitsch, and P. Moin, *Large eddy simulation in flow conditions for coupling with reynolds-averaged flow solvers*, AIAA Journal, 42 (2004), pp. 478–84.

[165] B. B. Schroeder, D. D. Harris, S. T. Smith, and D. O. Lignell, *Theoretical framework for multiple-polymorph particle precipitation in highly supersaturated systems*, Crystal Growth & Design, 14 (2014), pp. 1756–1770.

[166] R. Simha, *A treatment of the viscosity of concentrated suspensions*, Journal of Applied Physics, 23 (1952), pp. 1020–1024.

[167] G. P. Smith, D. M. Golden, M. Frenklach, N. W. Moriarty, B. Eiteneer, M. Goldenberg, C. T. Bowman, R. K. Hanson, S. Song, W. C. G. Jr, V. V. Lissianksi, and Z. Qin, *Gri mech 3.0*.

[168] L. D. Smoot and P. J. Smith, *Coal Combustion and Gasification*, Plenum Press, New York, 1985.

[169] J. Spinti, J. Thornock, E. Eddings, P. Smith, and A. Sarofim, *Heat transfer to objects in pool fires*, in Transport Phenomena in Fires, WIT Press, Southampton, UK, 2008.

[170] A. G. Stack and M. C. Grantham, *Growth rate of calcite steps as a function of aqueous calcium-to-carbonate ratio: Independent attachment and detachment of calcium and carbonate ions*, Crystal Growth & Design, 10 (2010), pp. 1409–1413.

[171] C. Steefal and P. van Cappellan, *A new kinetic approach to modeling water-rock interaction: The role of nucleation, precursors, and ostwald ripening*, Geochimica et Cosmochimica Acta, 54 (1990), pp. 2657–2677.

[172] G. R. Tabor and M. H. Baba-Ahmadi, *Inlet conditions for large eddy simulation: A review*, Computers and Fluids, 39 (2010), pp. 553–567.

[173] G. I. Taylor, *The spectrum of turbulence*, in Proceedings of the Royal Society of London A: Mathematical, Physical and Engineering Sciences, vol. 164, The Royal Society, 1938, pp. 476–490.

[174] I. Tkatchenko, N. Kornev, S. Jahnke, G. Steffen, and E. Hassel, *Performanaces of LES and RANS models for simulation of complex flows in a coaxial jet mixer*, Flow, Turbulence and Combustion, 78 (2007), pp. 111–127.

[175] R. Tolman, *The effect of droplet size on surface tension*, Journal of Chemical Physics, 17 (1948), pp. 333–337.

[176] Uintah, 2013. unitah.utah.edu. Accessed 1/1/2015.

[177] U.S. Environmental Protection Agency, *Inventory of U.S. greenhouse gas emissions and sinks: 1990-2013*, tech. rep., 2015.

[178] I. Valente, E. Celasco, D. L. Marchisio, and A. A. Barresi, *Nanoprecipitation in confined impinging jets mixers: Production, characterization and scale-up of pegylated nanospheres and nanocapsules for pharmaceutical use*, Chemical Engineering Science, 77 (2012), pp. 217–227.

[179] P. Vedula, P. K. Yeung, and R. O. Fox, *Dynamics of scalar dissipation in isotropic turbulence: A numerical and modelling study*, Journal of Fluid Mechanics, 433 (2001), pp. 29–60.

[180] I. Veloudis, Z. Yang, J. J. McGuirk, G. J. Page, and A. Spencer, *Novel implementation and assessment of a digital filter based approach for the generation of LES inlet conditions*, Flow, Turbulence and Combustion, 79 (2007), pp. 1–24.

[181] V. Vikas, Z. J. Wang, and R. O. Fox, *Realizable high-order finite-volume schemes for quadrature-based moment methods applied to diffusion population balance equations*, Journal of Computational Physics, 249 (2013), pp. 162–179.

[182] V. Vikas, Z. J. Wang, A. Passalacqua, and R. O. Fox, *Realizable high-order finite-volume schemes for quadrature-based moment methods*, Journal of Computational Physics, 230 (2011), pp. 5328–5352.

[183] A. Vreman, B. Albrecht, J. Van Oijen, L. De Goey, and R. Bastiaans, *Premixed and nonpremixed generated manifolds in large-eddy simulation of sandia flame d and f*, Combustion and Flame, 153 (2008), pp. 394–416.

[184] A. W. Vreman, *An eddy-viscosity subgrid-scale model for turbulent shear flow: Algebraic theory and applications*, Physics of Fluids, 16 (2004), pp. 3670–3681.

[185] B. Vreman, B. Geurts, and H. Kuerten, *Large-eddy simulation of the turbulent mixing layer*, Journal of Fluid Mechanics, 1997 (1997), pp. 357–390.

[186] P. M. Walsh, A. N. Sayre, D. O. Loehden, L. S. Monroe, J. M. Beér, and A. F. Sarofim, *Deposition of bituminous coal ash on an isolated heat exchanger tube: Effects of coal properties on deposit growth*, Progress in Energy and Combustion Science, 16 (1990), pp. 327–345.

[187] L. Wang and R. O. Fox, *Comparison of micromixing models for CFD simulation of nanoparticle formation*, AIChE Journal, 50 (2004), pp. 2217–2232.

[188] P. Wang, X. S. Bai, M. Wessman, and J. Klingman, *Large eddy simulation and experimental studies of a confined turbulent swirling flow*, Physics of Fluids, 16 (2004).

[189] J. C. Wheeler, *Modified moments and gaussian quadratures*, Rocky Mountain Journal of Mathematics, 4 (1974), pp. 287–296.

[190] D. L. Wright, R. McGraw, and D. E. Rosner, *Bivariate extension of the quadrature method of moments for modeling simultaneous coagulation and sintering of particle populations*, Journal of Colloid an dInterface Science, 236 (2001), pp. 242–251.

[191] I. Wygnanski and H. Fiedler, *Some measurements in the self-preserving jet*, J. of Fluid Mech., 38 (1969), pp. 577–612.

[192] K. Yamamoto, T. Murota, T. Okazaki, and M. Taniguchi, *Large eddy simulation of a pulverized coal jet flame ignited by a preheated gas flow*, Proceedings of the Combustion Institute, 33 (2011), pp. 1771 – 1778.

[193] C. Yoon and R. McGraw, *Representation of generally mixed multivariate aerosols by the quadrature method of moments: I. Statistical foundation*, Journal of Aerosol Science, 35 (2004), pp. 561–576.

[194] ——, *Representation of generally mixed multivariate aerosols by the quadrature method of moments: II. Aersol dynamics*, Journal of Aerosol Science, 35 (2004), pp. 577–598.

[195] C. Yuan and R. O. Fox, *Conditional quadrature method of moments for kinetic equations*, Journal of Computational Physics, 230 (2011), pp. 8216–8246.

[196] C. Yuan, F. Laurent, and R. O. Fox, *An extended quadrature method of moments for population balance equations*, Journal of Aerosol Science, 51 (2012), pp. 1–23.

[197] J. B. Zeldovich, *Theory of the formation of a new phase cavitation*, Journal of Experimental and Theoretical Physics, 12 (1942), pp. 525–538.

[198] Y. B. Zeldovich, *The oxidation of nitrogen in combustion explosions*, Acta Pysichochimica USSR, 21 (1946), pp. 577–628.

[199] V. Zhdanov, N. Kornev, E. Hassel, and A. Chrony, *Mixing of confined coaxial flows*, International Journal of Heat and Mass Transfer, 49 (2006), pp. 3942–3956.

[200] A. Zucca, D. L. Marchisio, A. A. Barresi, and R. O. Fox, *Implementation of the population balance equation in CFD codes for modelling soot formation in turbulent flames*, Chemical Engineering Science, 61 (2006), pp. 87–95.

[201] A. Zucca, D. L. Marchisio, M. Vanni, and A. A. Barresi, *Validation of bivariate DQMOM for nanoparticle processes simulation*, AIChE Journal, 53 (2007), pp. 918–931.